

THE UNIVERSITY OF READING

**The Mineral Dust Cycle**  
**at the**  
**Last Glacial Maximum and Present Day**

A thesis submitted for the degree of Doctor of Philosophy

Department of Meteorology

Daniel J. Lunt

**December 2001**

**Declaration**

I confirm that this is my own work and the use of all material from other sources has been properly and fully acknowledged.

Daniel Lunt

## **Abstract**

Ice-core and ocean-core data, point to a global increase in mineral dust deposition at the Last Glacial Maximum (LGM), 21,000 years ago, relative to the present day. Previous dust models, attempting to simulate this increase, have either failed to do so, or have not agreed with data pointing to a Patagonian origin of Antarctic dust, and an Asian origin of Arctic dust.

Firstly, a simple model for investigating the transport of dust to ice-core sites is described. It is shown that changes to transport alone, are not sufficient to explain the increase in LGM dust deposition at polar latitudes; however, the provenance of dust can be related to its transport.

Secondly, a new dust cycle model is described, which in many ways is an improvement on previous models. The sensitivities of the model are tested under present day conditions, case studies of dust storms are carried out, and results from a 10-year integration are compared to deposition data and surface concentration measurements. In these tests, the model performs very well; however, there is a high sensitivity to certain parameters which are poorly constrained by observations.

Running under LGM conditions, the observed increases in dust deposition are not well simulated by the model, nor is the provenance of Antarctic dust. The sensitivity studies suggest ways in which the model-data comparison can be improved, within the uncertainties of the parameterisations. Implementing these changes leads to a much improved agreement with data. Analysis of the results shows that globally, the 29% increase in atmospheric dust loading at the LGM, is due to a spatially varying combination of increased winds, and decreased vegetation. However, the lifetime of LGM dust is slightly less, being 5.8 days compared to 5.9 days at the present day. The relatively large increases in deposition over Antarctica can be attributed to decreased LGM precipitation over the Southern Ocean. At Dome C, Antarctica, where data point to a Patagonian provenance of LGM dust, the model is predicting that 72% of the dust is Patagonian in origin.

Future work should focus on the radiative effects of dust, and on extending the work to other time periods.

## **Acknowledgements**

I would like to thank my supervisor, Paul Valdes, for providing many an entertaining and interesting discussion, for devising such a fascinating project, and for enabling me to attend several sunny conferences.

Thanks to everyone in the Department of Meteorology, for making my time here so enjoyable; special thanks go to my buddy, Marc - one day he may make my dream 5 a side team.

Thanks to my housemates, Ian, Dan and Phil, for providing me with Tight Fit, a bed, council tax, and much banter.

Thanks to Em, for providing lots of encouragement and understanding, and for being brave in coming to France with me.

Finally, thanks to Mum, Dad, George, Mumma and Puppa, and Gran, for supporting me in all sorts of ways; I couldn't have done it without you.

## Contents

<b>1</b>	<b>Introduction</b>	<b>1</b>
1.1	The Dust Cycle Today . . . . .	1
1.1.1	Sources of Dust . . . . .	2
1.1.2	Sinks of Dust . . . . .	6
1.2	The Radiative Effects of Dust . . . . .	7
1.2.1	Direct radiative effects . . . . .	7
1.2.2	Indirect radiative effects . . . . .	11
1.3	The Climate and Dust Cycle at the Last Glacial Maximum . . . . .	14
1.3.1	The role of Milankovitch forcing in climate change . . . . .	14
1.3.2	The climate of the LGM . . . . .	16
1.3.3	Dust Records of the LGM: the DIRTMAP dataset . . . . .	19
1.3.4	Possible reasons for changes in dust deposition . . . . .	21
1.4	Previous Work on LGM Dust Cycle Modelling . . . . .	22
1.4.1	Joussaume . . . . .	22
1.4.2	Genthon . . . . .	24
1.4.3	Andersen . . . . .	25
1.4.4	Reader . . . . .	26
1.4.5	Mahowald . . . . .	26
1.4.6	Summary . . . . .	28
1.5	Aims of this study, and plan of the thesis . . . . .	28
<b>2</b>	<b>Transport of Dust to Ice-Core Sites</b>	<b>30</b>

2.1	Introduction . . . . .	30
2.2	Model Description . . . . .	31
2.2.1	The General Circulation Model: HadAM3 . . . . .	32
2.2.2	The Trajectory Model: OFFLINE . . . . .	34
2.2.3	Model Setup . . . . .	35
2.3	Results . . . . .	38
2.3.1	Trajectory Densities . . . . .	38
2.3.2	Trajectory Counting . . . . .	45
2.4	Conclusions . . . . .	48
2.5	Discussion . . . . .	50
<b>3</b>	<b>The Dust Model</b>	<b>52</b>
3.1	Introduction . . . . .	52
3.2	Modelling the Transport of Dust . . . . .	53
3.2.1	TOMCAT simulation of advection: The Prather Scheme . . . . .	55
3.2.2	TOMCAT simulation of convection: The Tiedke Scheme . . . . .	58
3.2.3	TOMCAT simulation of vertical diffusion: The Louis Scheme . . . . .	58
3.2.4	Testing transport in the dust model . . . . .	59
3.3	Modelling the Sources of Dust . . . . .	62
3.3.1	Influences of Vegetation on Source Strength . . . . .	63
3.3.2	The Particle Size Distribution of Parent Soils . . . . .	69
3.3.3	Entrainment of Dust by the Surface Wind . . . . .	74
3.4	Modelling the Sinks of Dust . . . . .	83
3.4.1	Wet Deposition of Dust . . . . .	83
3.4.2	Dry Deposition of Dust . . . . .	90

3.5	Further Improvements to the Dust Model . . . . .	93
3.5.1	Gusts . . . . .	93
3.5.2	Effect of snow cover . . . . .	96
3.6	Summary of results from one-year integration . . . . .	97
3.7	Conclusions . . . . .	99
<b>4</b>	<b>Modelling the Present Day Dust Cycle</b>	<b>100</b>
4.1	Introduction . . . . .	100
4.2	Sensitivity Studies . . . . .	101
4.2.1	Vegetation Sensitivity Study . . . . .	101
4.2.2	Entrainment Study . . . . .	108
4.2.3	Deposition Study . . . . .	114
4.2.4	Advection and Resolution Study . . . . .	115
4.3	Case Studies . . . . .	120
4.3.1	Model setup . . . . .	120
4.3.2	Asia; April 1998 . . . . .	121
4.3.3	North Africa; September 1998 . . . . .	123
4.3.4	Summary of case studies . . . . .	125
4.4	10 year integration . . . . .	126
4.4.1	The experimental setup . . . . .	126
4.4.2	The model results . . . . .	129
4.4.3	Comparison with observations . . . . .	136
4.5	Discussion and Conclusions . . . . .	144
<b>5</b>	<b>Modelling the LGM dust cycle</b>	<b>148</b>

5.1	Introduction . . . . .	148
5.2	The ten year experiment . . . . .	149
5.2.1	Model Setup . . . . .	149
5.2.2	The modelled dust concentration . . . . .	151
5.2.3	Analysis of source regions . . . . .	153
5.2.4	The modelled lifetime of dust . . . . .	156
5.2.5	Comparison with DIRTMAP . . . . .	158
5.2.6	Deposition in the ten year experiment . . . . .	161
5.2.7	Provenance of dust in the ten year experiment . . . . .	164
5.2.8	Summary of results from the ten year LGM experiment . . . . .	165
5.3	Experiments with an increased scavenging coefficient, and a new moisture parameterisation . . . . .	166
5.4	Conclusions . . . . .	172
<b>6</b>	<b>Conclusions</b>	<b>174</b>
6.1	Principal Findings . . . . .	174
6.2	Summary of Results . . . . .	174
6.2.1	Analysis of transport . . . . .	175
6.2.2	Dust cycle modelling . . . . .	175
6.3	Future Work . . . . .	177
6.3.1	Extending the trajectory work . . . . .	177
6.3.2	Improvements to the dust model . . . . .	179
6.3.3	Suggestions for improved observations . . . . .	182
6.3.4	Extending the dust cycle modelling work . . . . .	183
<b>A</b>	<b>Empirical expression for the collision efficiency, <math>E</math></b>	<b>186</b>

**B Resistance analogue approach to dry deposition**

**187**

---

# CHAPTER 1

## Introduction

Entrained by the surface wind, from arid regions, into the atmosphere, dust particles can be transported over thousands of kilometres. During their residence in the atmosphere, they interact directly with short and long-wave radiation, and indirectly through interactions with clouds and other aerosols. Once deposited, dust particles can provide a source of nutrients to marine and continental ecosystems, perhaps leading to climate change over much longer timescales. Changes in climate can in turn lead to changes in the global dust cycle.

Dust is clearly an important component of the earth system.

However, despite this, very little quantitative information is known of the effects of dust on climate, or of the effects of climate on dust. Reasons for this include a relative lack of observations of global dust concentrations and size distributions, and difficulties involved in modelling the global dust cycle. This thesis addresses some of the problems with dust cycle modelling, with particular emphasis on the uncertainties involved, comparison with observations, and understanding why dust has varied in previous states of the earth system, especially the Last Glacial Maximum, 21,000 years ago.

In this introductory chapter, the present day dust cycle is described, and the climatic effects of dust discussed. Records of dust deposition over the past 21,000 years are presented, and previous work in the field of dust cycle modelling is reviewed. Finally, the aims of the thesis are outlined.

### 1.1 The Dust Cycle Today

Pye (1987) defines dust as the suspension of solid particles in a gas, or a deposit of such particles. There are several types of atmospheric dust: cosmic dust, volcanic dust, dust from industrial emissions, and dust which originates from sediments and soils. Throughout this thesis, dust refers to the last of these, mineral dust.

The following sections explain the different processes involved in the dust cycle, focusing on the sources and sinks of dust. Much of this section is based on the works of Bagnold (1941) and Pye (1987).

### 1.1.1 Sources of Dust

#### Potential source regions of dust

Sources of dust often consist of particles with a wide range of radii. Particles are commonly categorised by their radii into three types: sand ( $r > 25\mu\text{m}$ ), silt ( $25\mu\text{m} > r > 1\mu\text{m}$ ) and clay ( $1\mu\text{m} > r$ ) (Sumner, 1998). These types can be further refined into coarse and fine fractions. In general, it is clay and fine-silt which make up the majority of dust in suspension in the atmosphere; larger particles fall out very quickly under the action of gravity. At large distances from any source regions, for example over the equatorial Pacific or Antarctica, the majority of wind-blown dust is clay (Steffensen, 1997). However, soils consisting of a large fraction of clay are not strong sources of dust, as the surface can become crusted, and resistant to erosion by the wind (Gillette *et al.*, 1982). Therefore, the most efficient dust sources tend to be soils with a large silt content (Pye, 1987).

Silt particles are produced via a number of mechanisms, including chemical weathering, abrasion of sand particles during strong wind events, or abrasion in rivers and lakes, and the movement of glaciers over rocks. Pye (1987) identifies several natural terrain types which act as major sources of dust, and which typically consist of relatively large amounts of silt. Among these regions are dried-up lake beds, unvegetated loess where wind-blown dust has been deposited over thousands of years, glacial outwash plains at the margins of ice-sheets at high latitudes, and certain dunefields with a relatively high silt content.

The global distribution of dust sources is very inhomogeneous, due to variations in terrain type over small spatial scales. In the Sahara, satellite imagery shows that much of the wind-blown dust originates from the area of the Bodele depression, northeast of Lake Chad (Prospero, 1999), a region which is a dried-up lake bed. Similarly, in Australia, the centre of strongest dust storm activity is in the region of Lake Eyre, another dried-up lake, and the Simpson desert (McTainsh and Pitblado, 1987).

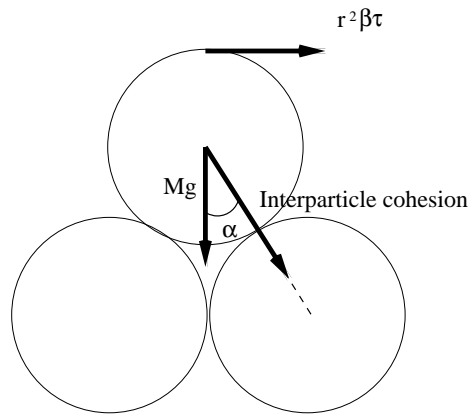


**Figure 1.1:** Schematic showing the forces associated with wind shear, gravity, and inter-particle cohesion, acting on a particle of mass  $M$ , and radius  $r$ , resting on a bed, in a windstream characterised by a friction velocity  $u^*$ .  $\beta$  is a constant, and the wind shear,  $\tau = \rho_a u^{*2}$ .

A potential dust source is one which could emit dust, given a reasonable wind strength. Such areas have little or no vegetation, and a plentiful supply of particles of a size which can be entrained. Unfortunately, there are no global observations of potential dust sources. Satellite imagery, and other observations, such as dust-storm frequency, have the disadvantage that they include effects such as wind strength and soil moisture.

Therefore, one of the problems in dust modelling is defining the potential source regions of dust, and assigning them relative magnitudes. This problem is addressed in section 3.3.

### Entrainment and flux of dust

By making measurements in wind tunnels and in the desert, Bagnold (1941) showed that the roughness length of a surface is typically  $1/30$  the size of particles making up the surface. By slowly increasing the wind strength in a wind tunnel lying over a sandy bed, he also found that above a certain value of the friction velocity,  $u^*$ , the particles in the bed begin to move. The onset of movement occurs at a threshold friction velocity,  $u_t^*$ , which depends on the size of the particles in the bed.

Dust particles are mobilised when the forces acting on them due to the surface wind, pulling them away from the bed, are stronger than the forces keeping them on the bed. Bagnold considered the balance of forces acting on an exposed particle of radius  $r$ , density  $\rho_p$ , and mass  $M$ , supported at an angle  $\alpha$  by the particles beneath it, in a windstream characterised by the friction velocity  $u^*$ ; the situation shown in figure 1.1. The surface drag acting on the particle,  $\tau$  is given by  $\tau = \rho_a u^{*2}$ , where

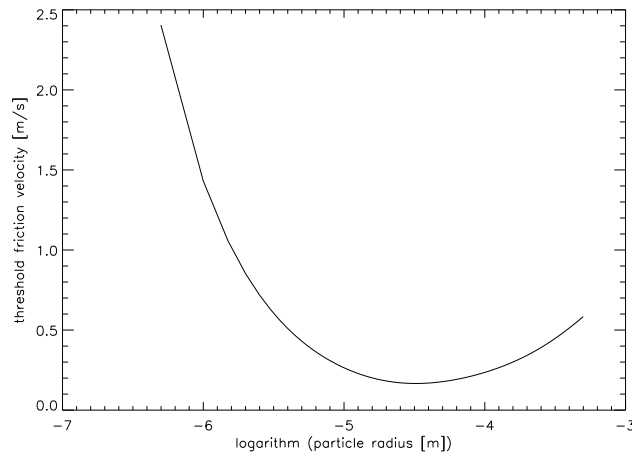


**Figure 1.2:** Threshold friction velocity,  $u_t^*$ , as a function of particle radius, as calculated by Marticorena and Bergametti (1995), based on observational work by Iversen and White (1982).

$\rho_a$  is the density of air, and the force is  $\beta r^2 \tau$ , where  $\beta$  is a constant depending on the geometry. The turning moment of this force is given by  $\beta r^3 \tau \cos \alpha$ .  $Mg$  is the force of gravity acting on the particle,  $Mg = (4/3)\pi r^3 \rho_p g$ , and its moment is  $Mgr \sin \alpha$ . Equating the moments leads to an expression for the threshold friction velocity,  $u_t^*$ :

$$u_t^* = A \sqrt{\frac{\rho_p}{\rho_a} g r} \quad (1.1)$$

In wind tunnel experiments, with a range of monotonic sized particles, Bagnold found the dimensionless parameter  $A$  to be constant over a wide range of particle sizes, resulting in a square root dependence of threshold wind speed on particle size. However, he observed that for small particle sizes, with radius  $r < 80 \mu\text{m}$ , the threshold velocity increases with decreasing particle size. Iversen and White (1982) suggested that this upturn in the friction velocity is due to inter-particle cohesion forces, which are relatively stronger between smaller particles than between large particles, and which Bagnold neglected in his analysis. More recently, based on work by Iversen and White (1982), Marticorena and Bergametti (1995) have constructed a semi-empirical equation for  $u_t^*(r)$ , over a wide range of particle radii, which has good agreement with observations carried out in wind tunnels over soil beds consisting of uniform particle size. Their results are shown in figure 1.2, for the particle size range over which their equation is valid. However, little work has been carried out on quantifying the effects of a bed consisting of a range of particle sizes.

Bagnold postulated that particles are entrained into the air by rolling and then bouncing. Others have observed that particles are lifted into the air by pressure differences between the top and bottom of

the grain (Bisal and Nielsen, 1962). These pressure differences can arise from fluctuations due to eddy motion, or the fact that the wind velocity is sheared, leading to a decrease in static pressure at the top of the grain. In all these cases, particles are entrained into the air, and then fall back down to the surface, where they collide with other particles in the bed. They may then eject other particles into the flow. This process of particles rising and then falling is known as saltation. Once saltation is initiated, it can be maintained at a lower windspeed than the initial threshold.

The action of saltating particles removes kinetic energy from the wind, and significantly alters the vertical distribution of wind speed from the non-saltating case. These ideas, coupled with observational evidence, were used by Bagnold (1941) to calculate an expression for the horizontal mass flux of dust particles during saltation. He found that the vertically integrated horizontal mass flux,  $q$ , can be written

$$q = B \frac{\rho_a}{g} u_*^3, \quad (1.2)$$

where  $B$  is a dimensionless constant. This is a very important result. It indicates that the flux of particles is proportional to the cube of the wind velocity, a relation which is observed to hold in the field (eg Shao *et al.*, 1993).

The entrainment of dust is further affected by the presence of moisture. Moisture increases the inter-particle cohesion forces between particles in the bed, leading to an increase in the threshold friction velocity, or a decrease in the particle flux. Empirical expressions have been formulated which attempt to quantify the effect of moisture on particle entrainment (eg Hotta *et al.*, 1984). A physically-based parameterisation, based on work by Fecan *et al.* (1999), which attempts to quantify these effects, is included in the dust model developed for this thesis, and is described in section 3.3.3. However, there remain many uncertainties in this area, for example, it is possible that a persistent strong wind could dry the uppermost layer of an otherwise moist soil very quickly.

Saltating particles quickly fall back to the bed, and represent primarily a horizontal flux. In order for this horizontal flux to be transferred to a vertical flux, and so for particles to remain in the atmosphere for a significant time, the turbulent motions of the air must be sufficiently large to overcome the particles' vertical settling velocity,  $v_s$ . If this is the case, the particles are said to be in suspension. The settling velocity of a particle,  $v_s$ , is proportional to the square of the particle's radius (see section

3.4.2). The vertical turbulent motions of the atmosphere can be characterised by the quantity  $\sigma = \sqrt{w'^2}$ , where  $w'$  is the deviation of the vertical windspeed,  $w$ , from the mean,  $\bar{w}$ .  $\sigma$  represents the force opposing the particle's tendency to settle, and is proportional to the friction velocity,  $u^*$  (Stull, 1988). Pye (1987) uses the ratio  $v_s/u^*$  as a measure of the degree of suspension of dust particles. He finds that for a significant amount of suspension to take place, it is required that  $v_s/u^* < 0.1$ . This means that for a grain radius of  $20\mu\text{m}$ , for which the settling velocity is  $0.13\text{ms}^{-1}$ , suspension will take place if  $u^* > 1.30\text{ms}^{-1}$ . Assuming a neutral atmosphere, and a roughness length of  $0.02\text{m}$ , this requires a wind speed at 10 metres, of  $20\text{ms}^{-1}$ . This is a relatively strong wind, compared to the annual mean over most desert regions. However, these can occur near regions of convection and strong surface heating, for example in dust devils (eg Sinclair, 1969) or haboobs (eg Lawson, 1971), or during seasonal strong winds, for example the Shamal in Arabia (eg Mambery, 1983), or the Harmattan in north-west Africa, which can transport Saharan dust as far as Brazil (Prospero *et al.*, 1981).

### 1.1.2 Sinks of Dust

Dust particles in suspension can be removed from the atmosphere by a variety of processes.

For large particles, the most efficient of these is dry deposition. This is when entrained particles come to rest at the surface, either due to their settling velocity, or due to turbulent eddies which bring them into contact with the ground. The latter of these occurs often at the boundaries between different surface types, for example when dust passes from a desert region to a more vegetated region. Over periods of thousands of years, regions which are favourable for dust deposition continually grow due to the input of dust particles, and build up into sediments called loess. These loess deposits cover about 5% of the Earth's surface. They are located relatively close to source regions, and are primarily made up of fine-sand and silt-sized particles (Pye, 1987).

Smaller particles are removed primarily by the process of wet deposition. This is when particles are scavenged by falling precipitation from above, or when fine particles act as nuclei around which cloud droplets can develop. The process of scavenging is most efficient for very large and very small particles; particles of radius of order  $1\mu\text{m}$  are not readily removed in this way. The role of dust particles as cloud condensation nuclei is discussed in section 1.2.2.

Dust which is deposited in certain regions can provide a record of deposition over large timescales. Dust particles which are deposited over stable ice sheets provide such a record, which can be obtained by extracting ice-cores from the sheet. Similarly, ocean cores can provide a record of dust deposition over the ocean. These records are described in more detail in section 1.3.3.

## **1.2 The Radiative Effects of Dust**

The radiative effects and optical properties of dust are not considered in this thesis, but are discussed here for completeness. The effects can be divided into two types, direct and indirect.

The direct effects of dust are due to the scattering and absorption of solar and thermal radiation, by the dust particles themselves. The physical principles behind these mechanisms are well understood, but quantifying the net radiative effect of dust is very difficult, due to large uncertainties in the optical properties of the particles, uncertainties in particle size distributions, variations in properties between dust originating from different regions, complications due to the irregular shape of dust particles, and the difficulties in correctly measuring or simulating the global distribution of atmospheric dust.

Indirect effects include the interaction of dust particles with clouds, and the ability of dust to act as a nutrient to terrestrial and marine life. These effects are much less-well understood, and the mechanisms behind them are uncertain. However, these indirect effects have potentially very important effects.

### **1.2.1 Direct radiative effects**

This section briefly discusses the direct radiative effect due to scattering and absorption by aerosol particles, in the short and long-wave, based on the summary given by Seinfeld and Pandis (1998). It goes on to discuss some estimates of the net radiative forcing by mineral dust.

### Short-wave forcing

Particles in the atmosphere can interact with solar radiation in two ways; by absorption and by scattering. The majority of scattering is elastic, that is, the scattered radiation is of the same wavelength as that which is incident.

If monochromatic radiation, of intensity  $F_0$  (in units of  $\text{Wm}^{-2}$ ), and of wavelength  $\lambda$ , impinges on a particle, then the amount of radiation which is scattered is  $F_{scatt} = C_{scatt}F_0$  (in units of Watts), where  $C_{scatt}(\lambda)$  is the single particle scattering cross section (in units of  $\text{m}^2$ ). Similarly, the amount absorbed is  $F_{abs} = C_{abs}(\lambda)F_0$ .

The scattering and absorption cross sections can be scaled by the geometric cross sectional area of the particle,  $A_p = \pi r_p^2$ , to give efficiencies,

$$Q_{scat}(\lambda) = \frac{C_{scat}(\lambda)}{A_p} \quad , \quad Q_{abs}(\lambda) = \frac{C_{abs}(\lambda)}{A_p} \quad (1.3)$$

The sum of these gives the extinction efficiency,  $Q_{ext}$ , which is a measure of the efficiency with which the particle interacts with radiation. The ratio,  $Q_{scat}/Q_{ext}$  is called the single scattering albedo,  $\omega$ , and is a measure of the amount of radiation which is scattered, as oppose to absorbed.  $\omega$  is a very important parameter; non-absorbing particles, for which  $\omega = 1$ , will cool the surface, whereas non-scattering particles, for which  $\omega = 0$ , will have a heating effect.

Another important parameter is the phase function,  $P$ , which describes the angular distribution of scattered light. Particles which are very small compared to the incident radiation scatter equally in the forward and backward directions. Larger particles tend to scatter predominantly in the forwards direction. A related parameter is the upscatter fraction,  $\beta$ . This is the fraction of incident radiation which is scattered vertically upwards.

The theory of absorption and scattering of radiation by spherical particles is called Mie theory, and is described by Hansen and Travis (1974) and Bohren and Huffman (1983). Using this theory, it is possible to relate  $Q_{scatt}$  and  $Q_{abs}$ , and hence  $\omega$ , to the complex refractive index of the particle,  $m = n + ik$ , the radius of the particle,  $r_p$ , and the wavelength of the radiation,  $\lambda$ . Wiscombe and Grams (1976) developed a theory to calculate  $\beta$ , in terms of the properties of the particle, the solar zenith angle, and the wavelength. Another parameter is the extinction coefficient,  $b_{ext}$ , which is equal

to the extinction cross section, multiplied by the number density of optically active aerosols. This gives a measure of the fraction of radiation which interacts with aerosol, per unit length of the path of the impinging radiation. When integrated over the path length, it gives the optical thickness,  $\tau$ . Together, these properties,  $\beta$ ,  $\omega$ , and  $b_{ext}$ , enable the radiative effects of aerosols in the short-wave to be calculated.

By considering multiple reflections of a beam of radiation of intensity  $F_0$ , incident on a layer of dust in a cloud-free atmosphere, Seinfeld and Pandis (1998) show that the total flux out of the top of the atmosphere,  $R$ , is given by

$$R = F_0 T_a^2 \left( r + \frac{t^2 A_s}{1 - A_s r} \right), \quad (1.4)$$

where the reflectance of the dust layer,  $r = (1 - e^{-\tau})\beta\omega$ , the transmittance of the dust layer,  $t = e^{-\tau} + (1 - e^{-\tau})(1 - \beta)\omega$ ,  $T_a$  is the transmittance of the atmosphere in the absence of dust, and  $A_s$  is the albedo of the Earth's surface.

In the absence of an aerosol layer, the total flux at the top of the atmosphere would be  $F_0 T_a^2 A_s$ . Therefore, equation 1.4 shows that the aerosol can have a cooling or warming effect. If the term in brackets is greater than  $A_s$ , there is more radiation leaving the atmosphere than in the aerosol-free case, and there is a cooling. If the term in brackets is less than  $A_s$ , less radiation leaves the atmosphere than in the aerosol-free case, and there is a warming effect. Over high-albedo surfaces, such as ice-sheets or deserts, the aerosol is likely to produce a warming, whereas over low-albedo surfaces, such as oceans or forests, the aerosol will lead to a cooling. For an aerosol which is non-absorbing, there is always a net cooling effect.

The effect of dust in the short-wave is independent of the height of the dust layer, however, it depends on the surface albedo, the concentration of dust, and the optical properties of dust, which can be written in terms of the single-scattering albedo,  $\omega$ , the upscatter fraction,  $\beta$ , and the extinction coefficient,  $b_{ext}$ . In practice, all these parameters are both particle-size and wavelength dependent, which makes the problem of assessing the radiative effects of dust in the short-wave extremely difficult.

## Long-wave forcing

Dust absorbs and scatters radiation in the long-wave part of the electromagnetic spectrum, as well as in the short-wave. In addition to this, it also emits at these wavelengths. This means that it interacts with the radiation which is emitted from the surface of the earth, and the radiation which is emitted throughout the depth of the atmosphere. The effect of dust in the atmosphere in the long-wave is to produce a positive forcing, *i.e.* a warming. The magnitude of the forcing can be estimated using simple models, which divide the atmosphere into several levels, one of which contains dust (eg Liao and Seinfeld, 1998). These models show that the total change in forcing at the top of the atmosphere is greatest when the aerosol layer is high up in the atmosphere, and the greatest forcing at the surface occurs when the aerosol layer is closest to the surface. If the aerosol layer is very high up, the surface forcing is very small.

The great problem is that, as in the short-wave, the optical properties in the long-wave are highly wavelength and particle-size dependent. The global average surface long-wave radiative effect of dust is estimated to be about a third smaller than the short-wave effect (Woodward, 2001).

## Estimates of direct radiative forcing

There have been a few modelling studies which have been carried out with the aim of predicting the direct radiative effect of dust on a global scale, at the present day.

Tegen and Fung (1994) have developed an off-line dust-cycle model, with parameterisations of the sources, transport and sinks of dust. The results have been validated by comparison with satellite and ground-based data, and the interannual variability in the model has been examined (Tegen and Miller, 1998). The dust concentrations predicted by the model have been used to calculate radiative forcings at the top of the atmosphere (TOA) and at the surface (Tegen *et al.*, 1996). The model predicts a global mean TOA forcing of  $+0.09\text{Wm}^{-2}$ , and a surface forcing of  $-0.96\text{Wm}^{-2}$ , due to anthropogenic dust.

Woodward (2001) has developed an on-line dust model, forced by winds output from the Hadley Centre GCM, which has also been tested against satellite and ground-based data. This model predicts a global mean TOA forcing of  $+0.07\text{Wm}^{-2}$ , made up of  $-0.16\text{Wm}^{-2}$  in the shortwave, and  $+0.23\text{Wm}^{-2}$  in the longwave. At the surface, the model predicts a net forcing due to dust of  $-0.82\text{Wm}^{-2}$ , made up

of  $-1.22\text{Wm}^{-2}$  in the shortwave, and  $+0.4\text{Wm}^{-2}$  in the longwave. These values of estimated radiative forcing can be compared to that due to anthropogenic greenhouse gases and sulphates, surface estimates of which, from the IPCC, are  $+2.43\text{Wm}^{-2}$  and  $-0.4\text{Wm}^{-2}$  respectively (Houghton *et al.*, 2001).

It seems that these global forcings due to dust are reasonably significant, but locally, especially over Arabia and the Equatorial East Atlantic, the annual mean forcings in these models can be as high as  $-25\text{Wm}^{-2}$  (Woodward, 2001). Observational studies, carried out by the Met Research Flight, have shown that single dust events can produce huge forcings of the order of  $-60\text{Wm}^{-2}$  at the TOA (Haywood *et al.*, 2001).

Predictions of direct radiative forcings due to dust are still in a preliminary stage, as a number of approximations have to be made concerning the particle size distribution, and the radiative properties of dust. Mineralogy, and hence optical properties, of dust vary across the globe (Claquin *et al.*, 1999); however, the studies mentioned here do not take this into consideration, and in general calculate radiative forcings based on the optical properties of Saharan dust. Claquin (1999) has shown that by including these effects, the magnitude of the surface forcing due to dust increases. Similarly, the effect of non-sphericity is ignored, and this is believed to be an important factor in the determination of the optical properties of dust (Kalshnikova, 2001).

### 1.2.2 Indirect radiative effects

Aerosols can have indirect as well as direct radiative effects. Indirect effects are when the presence of aerosol, or a change in the concentration of aerosol, affects another component of the earth-system, which then has a direct effect on the radiative forcing of climate. There are many indirect effects of aerosols. For dust, two of these which could be important are the effects dust can have on clouds, and the effects dust can have on ecosystems. These two effects are described briefly in this section. Their magnitude is yet to be quantified.

## Cloud-dust interactions

In order for a droplet to form in a cloud, there has to be a nucleation site, or the process is highly inefficient; in the laboratory, air can become up to 500% supersaturated before droplets form (Seinfeld and Pandis, 1998). Cloud Condensation Nucleii (CCN) are particles which allow air which is supersaturated to a degree commonly found in the atmosphere, to form droplets. A CCN can be defined as a particle which allows air to form droplets at a supersaturation of 10% or above (Seinfeld and Pandis, 1998). Particles which can act as CCN tend to be hydrophilic; examples are sulphates, or sea-salt.

To a first approximation, dust particles are not good CCN, as they are not particularly hydrophilic. However, it is found that dust particles can become coated with sulphate, and so become good CCN (Levin *et al.*, 1996). The processes by which this occurs are not well understood, but it has been suggested that cloud drops, originally nucleated on sulfate CCN, could collect dust particles by collision. Once the drops evaporated, a dust particle, coated with sulfate, would be left behind, and would be an extremely good CCN (Levin, 2001).

There are two principal effects that the presence of CCN can have on cloud development and climate. The first of these is that when they are present when a cloud is forming, they increase the number of nucleation sites which are available. This leads to an increase in the number of droplets, and a decrease in the average mass of each droplet. This in turn leads to an increase in the cloud albedo, due to an increase in multiple scattering of incoming solar radiation. This effect will in general lead to a cooling of the surface.

The second effect involves the cloud lifetime, and amount of precipitation. A large number of small droplets will in general lead to less precipitation, than a small number of large droplets. Therefore, it is expected that the presence of CCN will lead to an increase in cloud lifetime. However, Levin (2001) has found that the very large drops produced by a few sulphate-coated dust particles can make the clouds much more effective rain and drizzle producers.

There has been very little work done on quantifying the effects of these processes, and their importance remains unknown. However, it is possible that the presence of atmospheric dust could significantly affect the growth and development of clouds.

## **Ecosystem-dust interactions**

Oceanic phytoplankton are an important sink of atmospheric carbon. Their respiratory cycle takes carbon dioxide which originated in the atmosphere, and incorporates it into their biomass. When they die, they sink to the ocean floor, thereby removing carbon dioxide from the atmosphere. An increase in the productivity of these phytoplankton can therefore lead to a decrease in atmospheric carbon dioxide, and an atmospheric cooling.

In many marine ecosystems, the productivity of phytoplankton is limited by their supply of certain nutrients, in particular iron. Martin (1990) postulated that ferrous aeolian dust deposited on the ocean could be an important source of iron to phytoplankton. He suggested that an increase in dust deposition on the oceans could lead to an increase in productivity in iron-limited regions, resulting in a decrease in atmospheric carbon dioxide, and hence an atmospheric cooling. This process, from changes in dust deposition to changes in temperature, is called the iron hypothesis. Martin (1990) further postulated that this mechanism could be partly responsible for climate change over glacial-interglacial timescales; and also suggested that it could be possible to produce a cooling, offsetting the greenhouse effect, by seeding the oceans with iron.

To test the iron hypothesis, many experiments have been carried out in which iron has been added to oceanic regions, and the productivity of phytoplankton measured (eg Martin *et al.*, 1994, Boyd *et al.*, 1994). These have shown that phytoplankton productivity can indeed increase following addition of iron. Furthermore, a recent modelling study (Watson *et al.*, 2000), has attributed half of the CO<sub>2</sub> reduction during past glacial climates to increased uptake of CO<sub>2</sub> by phytoplankton, due to increased iron fertilisation by wind-blown dust. However, it has also been argued (Maher and Dennis, 2001) that the amount of dust deposited over the Southern Ocean, even during glacial periods, was very small, and that the timing of changes in polar CO<sub>2</sub> compared to the timing of changes in dust flux do not match, casting some doubt on the significance of the iron hypothesis in influencing climate change.

It has also been suggested that a similar mechanism could exist for terrestrial ecosystems (Swap *et al.*, 1992). In winter, dust originating from the Sahara is deposited in the Amazon basin. The soils here are nutrient-poor, partly because the high humidity causes run-off of nutrients. It is possible that this Saharan dust is fertilising the Amazonian soil, and sustaining the rainforest (Swap *et al.*, 1992). The climatic effect of this fertilisation would be a cooling, as plants' respiration draws carbon dioxide

from the atmosphere. Once again, this is a process to which a magnitude is yet to be assigned.

This is a highly controversial area, and the magnitude of any climatic effect, resulting in this way from changes in dust deposition, is unknown. However, it remains a possibility that this indirect effect of dust is an important one, and is a potential feedback mechanism acting on the earth-system.

### **1.3 The Climate and Dust Cycle at the Last Glacial Maximum**

The previous section has discussed the importance of the dust cycle. Now, changes in climate, and in dust, in the past, are considered.

A period of great interest to paleoclimatology occurred 21,000 years ago, when the great ice sheets, covering much of Northern Europe and North America, were at their greatest extent in the last 125,000 years, and the climate was generally cooler than the present day. This time period is called the Last Glacial Maximum, or LGM. Furthermore, analysis of ice cores and ocean cores shows that there was a global increase in dust deposition at this time, of up to 20 times (Mahowald *et al.*, 1999). One of the aims of this thesis is to bring these two facts together, and to explain the changes in dust deposition in terms of changes in climate.

This section explains the reasons for the cooler climate of the LGM, the driving force behind which is changes in radiative forcing due to changes in the orbital parameters of the Earth. It goes on to discuss the major changes in climate between the LGM and present day, and explains the DIRTMAP dataset, which provides a record of dust deposition at the two time periods. Finally, it puts forward several explanations for the observed increase in dust deposition at the LGM.

#### **1.3.1 The role of Milankovitch forcing in climate change**

Throughout the Earth's history, due to the gravitational effects of the sun, moon and other planets, there have been changes to the degree of ellipticity of its orbit (eccentricity), angle of inclination to the plane of the orbit (obliquity) and timing of the seasons with respect to the perihelion of the orbit (precession). This has resulted in changes to the spatial and seasonal distribution of solar energy flux impinging at the top of the atmosphere, even though the globally and annually averaged flux

has remained almost constant (neglecting variations in the amount of energy actually released from the sun, modulated by, for example, the number of sunspots). The fact that these changes could be important for climate was put forward by Milankovitch (1941), whom the theory is named after, and elaborated by Berger (1979).

Variations in the orbital eccentricity have an average period of about 100,000 years, the obliquity a period of 41,000 years, and the precession, periods of 19,000 and 23,000 years. The combination of these effects gives rise to a timeseries of the strength of incoming solar radiation which is very variable. The fact that this timeseries is reflected in the records provided by climate proxies such as corals, which also show significant strength in the frequencies corresponding to the orbital forcings (eg Hays *et al.*, 1976), strongly suggests that changes in the Earth's orbit have played an important role in causing the glacial-interglacial cycle.

However, the actual magnitude of these changes in forcing are relatively small, and, as mentioned before, are almost zero when averaged over the globe and over the year. There clearly must be mechanisms which amplify the changes in insolation, and which lead to the changes observed in the paleo record. In particular, the strongest signal in the paleo record is at a period of 100,000 years, which corresponds to the eccentricity period. However, this is by far the weakest signal in terms of magnitude of the forcing. Possible mechanisms for such amplifications are the ice-albedo feedback, and changes in ocean circulation.

Figure 1.3a shows a timeseries of temperature, as inferred from the Deuterium signal from the Vostok ice-core in Antarctica (Jouzel *et al.*, 1987, Jouzel *et al.*, 1993). It shows clearly the strong 100,000 year cycle in temperature, and the transition between glacial (*e.g.* 110kyrBP - 20kyrBP), and interglacial (*e.g.* 10kyrBP - present day) periods. Also indicated is the time of the Last Glacial Maximum (LGM). It occurred towards the end of the last glaciation, and coincides with the end of a period of reduced solar insolation in summer at northern high latitudes, which can be an indicator of ice-sheet growth. Also shown is the dust record from the same ice-core (Jouzel *et al.*, 1993, Petit *et al.*, 1990). It can be seen that in general, high dust concentrations are approximately coincident with cold climate. In particular, there is a maximum in dust concentration at the LGM. The next section explains in more detail how the climate at the time of the LGM was different to that of the present day. The following sections link these changes in climate to changes in the dust cycle.

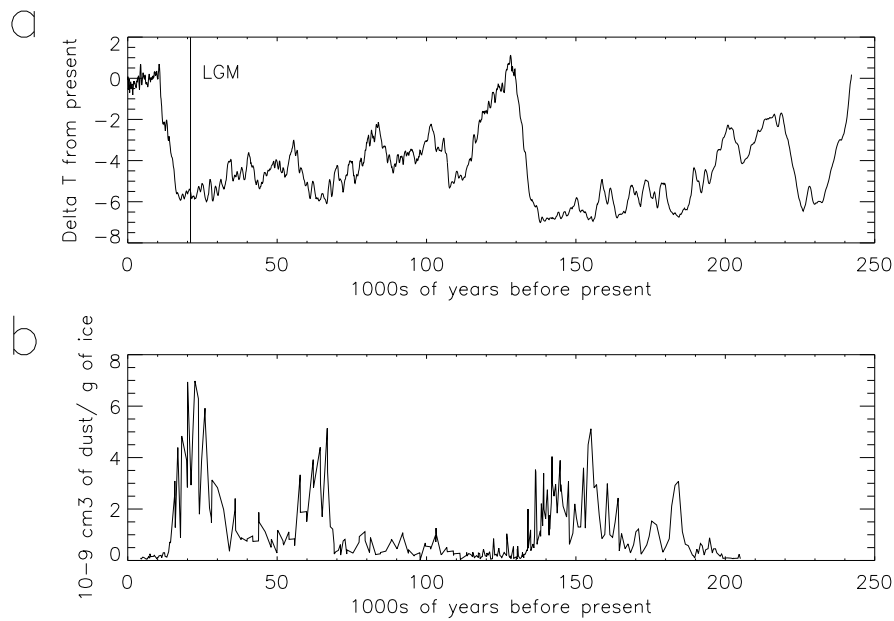


**Figure 1.3:** (a) Timeseries of temperature deviation from the present day, from the Vostok ice-core, as derived from Deuterium measurements (Jouzel *et al.*, 1987, Jouzel *et al.*, 1993). Vertical line shows the time of the Last Glacial Maximum.(b) Timeseries of dust concentration in the same ice-core (Jouzel *et al.*, 1993, Petit *et al.*, 1990).

### 1.3.2 The climate of the LGM

The LGM is a period which has been studied in great detail by paleoclimatologists. It was the focus of the CLIMAP project members (1981) study, which aimed to bring together a great number of paleoclimate proxies from the LGM, to build up datasets of several climate variables, including temperature and sea-ice extent. These datasets can be used as boundary conditions to constrain climate models, which aim to simulate the LGM climate. However, different models can produce very different climatologies, even given the same boundary conditions. PMIP is a project designed to compare several different paleoclimate models, all constrained by the same boundary conditions (Joussaume and Taylor, 1995). One of the models used in PMIP is the Hadley Centre atmosphere-only GCM, HadAM3, which is used in this thesis, and is described in section 2.2.1. Some results from this model, when constrained by boundary conditions as used in PMIP, are shown here. They are thought to be a reasonable representation of the climate of the LGM.

Figure 1.4 shows the surface air temperature at the LGM, expressed as a difference between the LGM and present day, as simulated by HadAM3. The ocean temperatures are constrained by the CLIMAP SSTs. It can be seen that, in general, there was a general cooling of climate at the LGM. In particular, the spatial extent and effect of the northern hemisphere high latitude ice-sheets can be seen. The

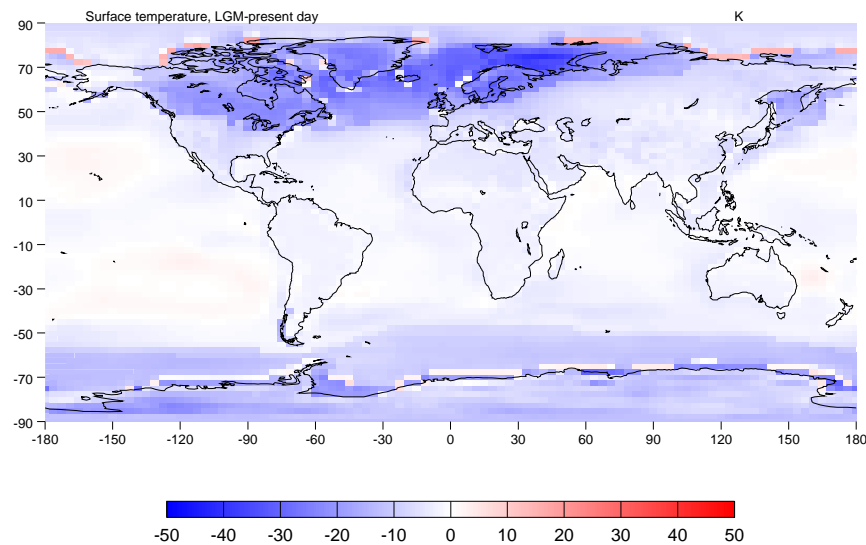


**Figure 1.4:** Annual mean surface air temperature, LGM-present day, from HadAM3 modelled climatologies, using CLIMAP SST changes. Units are degrees Celsius.

slight warmings in the tropical Pacific from the CLIMAP dataset are now believed to be unrealistic (Hostetler and Mix, 1999).

Because of this cooling, there was a general decrease in evaporation from the oceans and land. This is thought to have caused a decrease in the intensity of the hydrological cycle, and therefore a decrease in precipitation. Figure 1.5 shows the HadAM3 simulation of precipitation, again expressed as a difference between the LGM and present day. Precipitation is not particularly well simulated by GCMs, but the general trend, of a decrease in precipitation over land at the LGM, is most likely robust. Those regions which are simulated as having greater rainfall at the LGM than at the present day are in regions where the CLIMAP SSTs are probably too warm, as explained in the previous paragraph.

In addition, the greater cooling at high latitudes compared to the tropics at the LGM causes an increase in the meridional temperature gradient. Due to the thermal wind balance, it is expected that this leads to an increase in the vertical wind shear, an increase in baroclinicity, and stronger storms. This effect is simulated by the GCM, and shows up as an increase in the strength of the westerlies over the Southern Ocean, as shown in the plot of annual mean surface wind strength in figure 1.6.

The above figures are based on prescribed sea surface temperatures. Using a simple slab ocean model would lead to broadly similar conclusions, except that they do not predict any of the warm ocean temperatures included in CLIMAP (Dong and Valdes, 1998). There were many other changes in

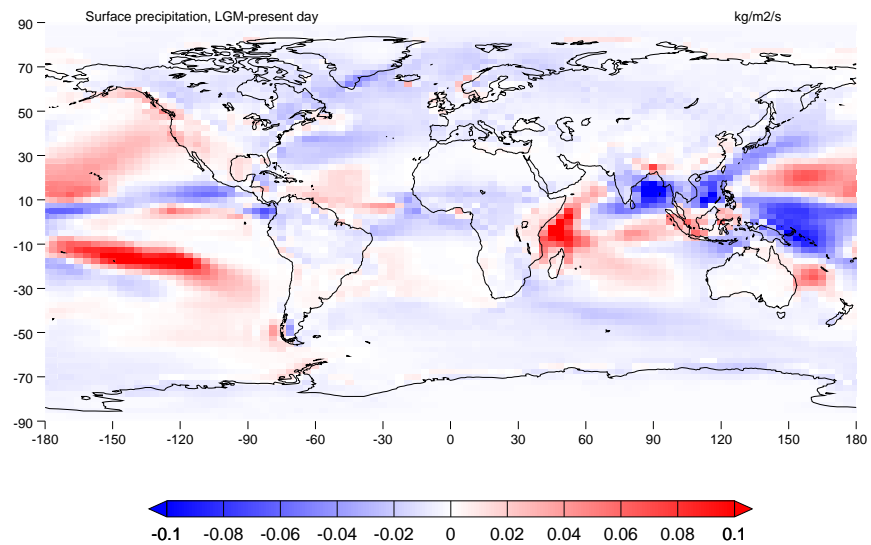


**Figure 1.5:** Annual mean surface precipitation, LGM-present day, from HadAM3 modelled climatologies, using CLIMAP SST changes. Units are  $\text{kg m}^{-2} \text{s}^{-1}$ .

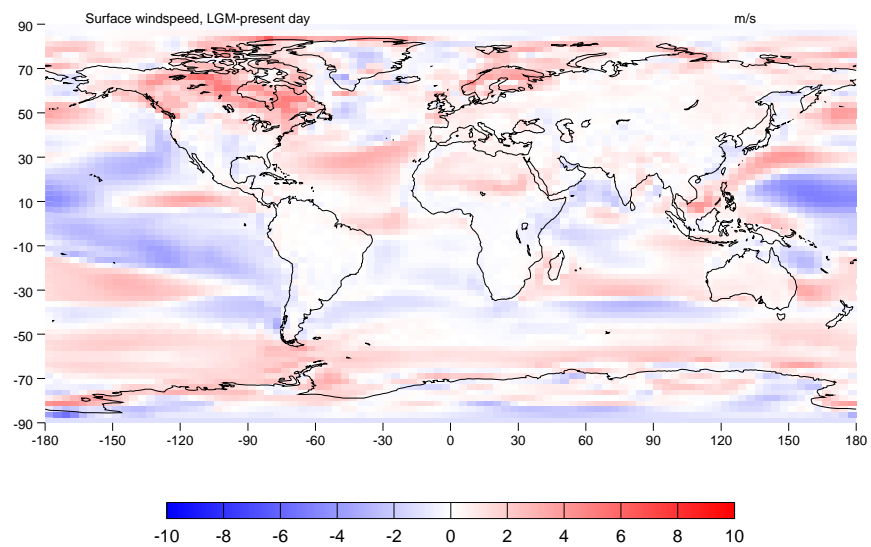


**Figure 1.6:** Annual mean surface wind strength, LGM-present day, from HadAM3 modelled climatologies, using CLIMAP SST changes. Units are  $\text{ms}^{-1}$ .

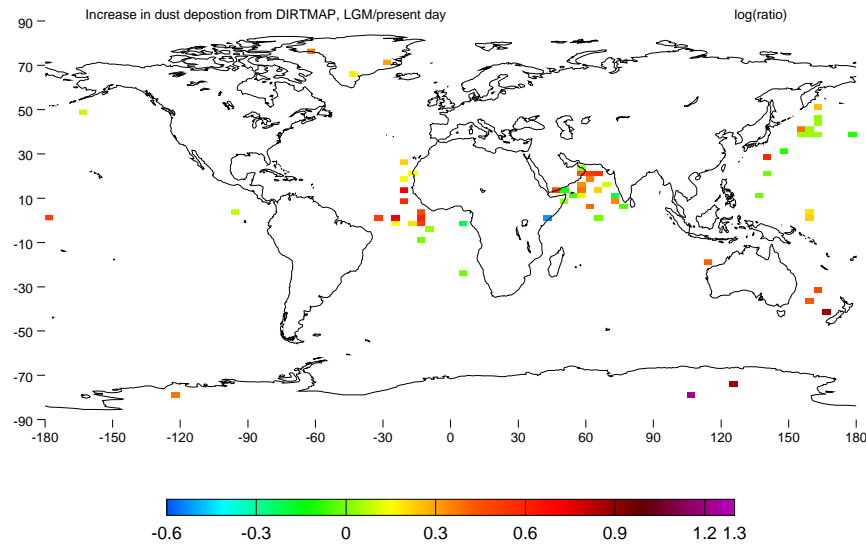


**Figure 1.7:**  $\log_{10}$  of the ratio of LGM to present day dust deposition, from the DIRTMAP dataset.

climate at the LGM, including the aerosol loading of the atmosphere. Of particular interest for this thesis are the changes in dust concentration in the atmosphere. The next section discusses the various data which exist for atmospheric dust at the time of the LGM.

### 1.3.3 Dust Records of the LGM: the DIRTMAP dataset

There are many paleoclimate proxies for atmospheric dust at the LGM, in the form of ice-cores (eg Thompson and Moseley-Thompson, 1981) and ocean cores (eg Sirocko *et al.*, 1991), but until recently they were scattered over the literature, and only a small portion were used in any one dust study (eg Andersen *et al.*, 1998). However, Mahowald *et al.* (1999) collated much of this information into a dataset, Dust Indicators and Records from Terrestrial and MARine Paleoenvironments, DIRTMAP, which can be used as a valuable validation tool for dust models attempting to simulate the dust cycle of the LGM. The dataset has records of dust deposition at the present day and LGM, at various locations. The ratio of LGM to present day global deposition, from the DIRTMAP dataset, is shown in figure 1.7. It shows a general increase in dust deposition, but also illustrates the fact that the signal can vary greatly over relatively short spatial distances. The DIRTMAP dataset was used by Mahowald *et al.* (1999) as a validation tool in their dust cycle simulations (see section 1.4.5). The dataset is used in a similar way in this study, where a comparison is made between modelled dust deposition, and that from DIRTMAP (see section 4.4.3). However, DIRTMAP is a record of dust deposition at very isolated, and local sites, and does not represent the average deposition over a large area. Furthermore,

in order to convert from dust concentrations in ice or sediment, to dust deposition, estimates have to be made of the ice or sediment accumulation, both at the present day and LGM. An additional problem is that the sediment and ice-core records are a very different form of archive, and there may be issues associated with a comparison between them, for example a possible dissolution of dust in the ocean sediment. These problems are highlighted by the case of Dome C ice-core, where 5 analyses have resulted in estimates of the increase in dust deposition at the LGM compared to the present day of  $\times 3$ ,  $\times 6$ ,  $\times 8.5$ ,  $\times 11$  and  $\times 12$ , by Thompson and Moseley-Thompson (1981), Petit *et al.* (1981), and Royer *et al.* (1983).

In addition to the absolute amount of dust deposited at the LGM and present day, several of the sites in the DIRTMAP dataset contain further information. For example, they provide a continuous record of dust deposition in times both intermediate between the LGM and present day, and before the LGM. An example is shown in figure 1.3b, which shows the record of dust deposition at Vostok, Antarctica. The timeseries has been extended back a further 200,000 years by Petit *et al.* (1999), and the general result of an increase in dust deposition at Antarctica during glaciated periods, and in particular at periods preceding a change to an interglacial state, is robust over at least 4 glacial-interglacial cycles. A challenge for dust cycle modellers is to be able to simulate and understand the entire timeseries of dust deposition across the globe; however, for this and previous studies, concentration is focused on the present day and LGM. Section 6.3.4 explains how the work in this study can be extended to other time periods.

As well as total mass of dust, some ice-cores have a record of particle size distributions (Steffensen, 1997). Because the ice-cores are in general far from the source regions, it is expected that only particles small enough to have a very slow sedimentation rate will be found in these ice-cores. This is indeed the case, and the particles in ice-cores tend to be distributed about a mean of about 1 micron in radius. This provides a further constraint on both present day and LGM dust cycle simulations.

At Dome C ice-core in Antarctica, mineralogical analysis has been carried out, where the ratio of several mineralogical isotopes in the dust is measured (Grousset *et al.*, 1992, Basile *et al.*, 1997). The ratios are then compared to that from dust in potential source areas. It is found that these ratios provide a very distinctive signature which is different for dust from different source regions. This points to the fact that the LGM dust in the Dome C core originated from Patagonia in South America, as opposed to the deserts of South Africa or Australia. Similarly, analysis of dust from the GISP II ice core indicates an East Asian origin of dust in Greenland, as opposed to North America or the Sahara

(Biscaye *et al.*, 1997). This analysis can be used as another constraint on dust cycle models. A caveat to this work is that it can only prove that a region is not a source for the dust, not that a region is a source; regions which are yet to be tested are always potential sources. This means, for example, that local dust from the margins of the ice-sheet in Greenland are still a potential source for Greenland ice-core dust, as they are yet to be tested.

In summary, the DIRTMAP dataset, coupled with information on provenance and particle-size, can help to constrain a dust model. However, it must be remembered that the data in DIRTMAP represents dust deposition at very localised regions, which may be affected by local variations, and does not represent an average over a large region.

#### 1.3.4 Possible reasons for changes in dust deposition

There are several reasons why there might be more dust at the LGM, all of which are related to the changes in climate.

Firstly, there may have been changes in the atmospheric circulation, which caused dust to be more efficiently transported to regions where we have records of dust deposition. For example, it is conceivable that an increase in the strength of the westerlies over the Southern Ocean could lead to more efficient transport from Patagonia to Antarctica, due to a shorter journey time (Krinner and Genthon, 2001). The efficiency of transport from potential dust source regions to Antarctica is investigated directly in chapter 2.

An increase in baroclinicity, leading to greater storminess and stronger gust strengths, as explained in section 1.3, could lead to an increase in dust entrainment from the ground. This is a potentially important factor, due to the cubic dependence of dust flux on wind speed. Indeed, it has been proposed that the large increases in dust deposition over Antarctica are due mainly to this effect (Basile *et al.*, 1997).

Decreases in soil moisture at the LGM, associated with changes in the hydrological cycle, could have led to an increase in dust entrainment, due to the dependence of threshold wind strength for entrainment on soil moisture.

A decrease in precipitation could lead to longer lifetimes of dust, and hence an increase in dust de-

posited away from source regions, or it may lead to less deposition locally, directly from the decrease in precipitation.

Finally, vegetation changes at the LGM, due to changes primarily in temperature and precipitation, could have led to more areas of barren land; with more exposed soil there would be more entrainment of particles into the atmosphere. The conclusion of work by Mahowald *et al.* (1999) was that vegetation changes are the single most important reason for the increase in dust deposition at the LGM.

All of the above are possible reasons for the observed changes in dust at the LGM. Discovering their relative importance, is one of the aims of this thesis, and is carried out in chapter 5.

## 1.4 Previous Work on LGM Dust Cycle Modelling

Over the past decade, several dust cycle models have been developed independently. Some of these have been applied to the problem of dust deposition at the Last Glacial Maximum, whereas others have concentrated on the radiative effects of present day global dust distributions. The radiative models are described in section 1.2.1, along with a discussion of their results.

This section describes a selection of the LGM dust models in chronological order, summarising their results, and commenting on their successes and weaknesses. Finally, there is a summary of the main conclusions and avenues for research which arise from a study of the literature.

### 1.4.1 Jousaume

The first global model used to simulate the dust cycle was developed by Jousaume (1990). The Jousaume model is online, and is run within the LMD GCM, running at a  $64 \times 50$  gridpoint resolution, with 11 vertical levels. The lifecycle of particles of radius  $1\mu\text{m}$  is simulated.

An upstream advection scheme (see section 3.2.1) is implemented, as well as transport of dust by convection and diffusion. The potential dust source regions are modelled as being regions where the soil water content, as predicted by the climate model, is less than a threshold; there is no seasonality in

the potential source extent. Entrainment of dust is parameterised as being proportional to the surface wind speed, with no threshold speed. A sedimentation velocity, and surface dry deposition is included. Wet deposition is parameterised by assuming that dust particles and water vapour are removed with the same efficiency, in effect assuming that the dust particles are acting as cloud condensation nuclei. Scavenging by falling precipitation is neglected.

The model is forced with perpetual August and February climate fields, for 60 days for each month, after a 40 day spin-up period. A strong seasonal dependence of dust mobilisation is found, with twice as much atmospheric dust in August as in February. This is attributed to changes in atmospheric circulation, in particular an increase in vertical transport of dust in northern hemisphere summer. The main problems with the simulation of the present day dust cycle in the Joussaume model are an over-simulation of the eastwards transport of Saharan dust in August, and an underestimate of the westwards transport in February. Also, the Asian dust source is underestimated, and the Australian dust source is over-simulated, with respect to sea-haze observations.

These discrepancies with data are attributed by Joussaume in part to the climate of the LMD GCM, in particular, an overestimate of the strength of the Indian summer monsoon. Joussaume also indicates that another source of errors derives from the oversimplified treatment of the dust cycle itself, especially the definition of source areas, the linear dependence of dust flux on wind speed (as opposed to a third-power dependence), and the absence of a threshold wind speed. She also cites the high diffusion of the advection scheme as another source of error, and the fact that only one particle size is simulated.

The modelled change in dust concentrations at the LGM, is described in Joussaume (1993). At the LGM, the source regions change very slightly as a result of the moisture-dependent source region definition. The Saharan and Australian modelled source regions are expanded at the LGM, and there is a decrease in potential source area in the region of the Gobi desert. The model predicts only a weak global change in the concentration of dust at the LGM, and the changes are very inhomogeneous. There is no change in deposition over East Antarctica, compared to an observed change of  $\times 4$ , but there is an increase in dust over Greenland of  $\times 4$  compared to an observed change of about  $\times 3$  (Mahowald *et al.*, 1999). However, at the time this work was published, it was thought that observed increases in dust deposition at Camp Century (Thompson and Moseley-Thompson, 1981), of the order of  $\times 100$ , were typical for the whole of Greenland, so it was thought that the modelled increase of  $\times 4$  was too small. The origin of dust over Antarctica at the LGM is Australian in the Joussaume model,

which is in contradiction with the mineralogical evidence (Grousset *et al.*, 1992, Basile *et al.*, 1997).

Joussaume puts forward several reasons for the failures of this model, most of which are similar to the reasons for discrepancies with observations in the present day integrations. In particular, Joussaume points out that 60 days of integration is very short, and that there may be biases due to particular events which are not reflective of a true climatology of dust.

In summary, the Joussaume model, although state of the art at the time of publication, has a great many deficiencies. The most important of these are probably the definition of the potential source areas, the linear and threshold-less entrainment of dust, and the low resolution of the model. These simplifications manifest themselves in the fact that in general, the increases in dust at the LGM, and certain aspects of the present day dust cycle, do not agree with observations.

However, despite these limitations, more recent dust models can trace their roots back to this model, and the ideas on which it is based.

### 1.4.2 Genthon

Genthon (1992) applied the GISS model II GCM to the problem of Antarctic dust at the present day and LGM. The GCM is run at a  $46 \times 18$  gridbox resolution, and with 9 vertical layers, and forces the dust model online. 3 particle sizes are simulated, in the range 0.2 to  $5 \mu\text{m}$  radius.

The potential source areas in the model are deserts, which do not vary seasonally, and do not change between the present day and LGM integrations. For the first time, a cubic dependence on windspeed of dust entrainment is included, but there is still no threshold windspeed for entrainment. The Genthon model includes transport by advection, convection and diffusion. Removal is by dry and wet (including condensation and collision scavenging) deposition.

The model is run for 27 months, including a 1-month spin-up period, under both present day and LGM boundary conditions. It is found that the model fails to simulate a large increase in dust concentration over Antarctica. The largest increase is in East Antarctica, where the increase is by a factor of 2. This increase is due to modelled increased wind speeds at the source regions, and an increase in transport efficiency to the poles at the LGM. Genthon concludes that the observed increases in dust concentration in Antarctica are therefore due to increases in the potential source regions, which are

not simulated in the model.

In summary, the Genthon model is similar to the Joussaume model, with the main difference being a cubic dependence of dust on windspeed. However, despite this improvement, the model results are very similar to those of Joussaume. The model was run for longer than the Joussaume model, but at a coarser resolution.

### 1.4.3 Andersen

The Andersen *et al.* (1998) model is based on that of Genthon, using similar dust parameterisations. It is more advanced as it is forced by the higher resolution ( $64 \times 48 \times 15$  layers) LMDz GCM; however, only one particle size, of radius  $1\mu\text{m}$ , is simulated. In addition, a soil moisture criterion for dust entrainment is included, with no entrainment if the soil moisture content is greater than 3% of the holding capacity of the ground.

The model is run for 2 years, under both present day and LGM boundary conditions. The source regions do not change between the two time periods. At the present day, the model simulates well the observed dust distribution. However, the Australian and North African sources are over-simulated, and the Asian source is under-simulated.

At the LGM, there are significant increases in dust deposition in northern hemisphere high latitudes, with the increase in Greenland, of a factor of 2-3, mainly originating from small local areas. This is in contradiction to the mineralogical evidence, which indicates an Asian origin of LGM Greenland dust (Biscaye *et al.*, 1997), although local sources are yet to be tested by this method. There is an increase in dust deposition at the LGM over Antarctica of 1.5. This is less than observed, and it is not clear exactly which source regions are responsible for the increase.

In summary, the Andersen model simulates increases in dust in the Northern Hemisphere of a consistent magnitude, but inconsistent origin, as compared with observations. Over Antarctica, the simulated increase in dust is too small. These changes are due to a combination of changes in wind speed, soil moisture and precipitation; however, it is not known which of these processes are most important.

#### 1.4.4 Reader

The Reader *et al.* (1999) dust model is driven by the CCCma GCM, running at a T32 resolution, with 10 vertical levels. The dust model includes a cubic dependence of dust entrainment on wind speed, no threshold speed, a bare soil fraction definition of potential source regions as defined by a global dataset, and removal of dust by sedimentation, turbulent deposition and precipitation scavenging. There is a soil moisture entrainment criterion, with a linear dependence of dust flux on moisture content, and a threshold moisture chosen to match the results with dust concentration observations.

The model is run for a 3 month spin up period, followed by a year, for both LGM and present day integrations. Different geographical source regions are advected separately, and so the origin of dust arriving at a site (for example of an ice-core) can be determined. This information is used to constrain the relative amount of dust which is entrained from the dust sources, given knowledge of the provenance of dust at Antarctic and Greenland ice-cores.

It is found that there is a doubling of the amount of dust in Greenland, and a trebling of the amount in Antarctica. The authors infer that there needs to be a 5-25 fold increase in the strength of the Asian source from the present day to the LGM, in order to match observations of both deposition and provenance of dust, and a 6-7 fold increase in the strength of the Patagonian source, on top of the increases which are simulated in the model. They propose several mechanisms for these non-simulated increases, including an increase in gustiness, and the availability of fine soils.

In conclusion, the Reader model sheds some light on the magnitude of the increases of dust flux which are needed to agree with both the concentration and provenance of dust in ice-cores. However, the model doesn't lead to obvious conclusions as what the processes might be which cause the increases.

#### 1.4.5 Mahowald

The Mahowald *et al.* (1999) model is an offline model, and is driven by the ECHAM3 GCM, for both LGM and present day simulations. The GCM runs at a  $4^\circ \times 5^\circ$  resolution, with 19 vertical layers. A spectral method is used for simulating the aerosol size distribution, in which the evolution of a size mode centred on  $2.5\mu\text{m}$  is simulated.

The source regions are defined using a vegetation model, BIOME3. The vegetation model is forced

by either present day or LGM climate, to produce Leaf Area Index (LAI) global fields for the two time periods. The potential source strength is related to the LAI in a linear fashion. Entrainment of dust is proportional to the cube of the wind velocity, with a threshold of  $5\text{ms}^{-1}$ . Sedimentation, and dry and wet deposition are included. There is a simple threshold criterion for soil moisture effects.

The model was run for 13 months, including a one-month spin-up. The results for the present day and LGM are compared to the DIRTMAP dataset, which provides a record of dust deposition at various points on the globe, based mainly on ice-cores and ocean-cores, for the LGM and present day. The present day total dust emissions rate is chosen to match a mean of the amount which is observed, of 3000Mt/yr.

The present day distribution of dust agrees qualitatively well with satellite observations, although the relative strength of the Asian source is too weak, and that of Australia is too strong. The modelled deposition also agrees reasonably with the DIRTMAP dataset for the present day, although the same errors are present as for concentration. At the LGM, the BIOME3 model predicts an increase in the global potential source regions, especially in Australia and Asia. There is a corresponding increase in atmospheric dust loading, and dust deposition. Compared to the DIRTMAP dataset, the increases at the LGM are well simulated, except that the increase in dust deposition over the North Pacific is over-simulated by a factor of more than 10. In order to gain some insight into the reasons for the modelled increase in dust deposition, the model is re-run with the present day potential source areas, but LGM forcing fields. It is found that only a small increase in dust deposition is simulated in this case, compared to with the LGM vegetation. Therefore, it is concluded that it is the changes in vegetation at the LGM which are primarily responsible for the increases in dust seen at the LGM. However, the model fails to correctly simulate the provenance of Antarctic dust, attributing 50% of the increases seen there to an increase in the strength of the Australian source. Similarly, increases in Greenland are due to increases in dust source strength at high latitudes, as well as the Gobi desert.

In conclusion, the Mahowald model is a big improvement on previous models as it includes significant changes to the potential source areas at the LGM. It is also an improvement on previous work as it uses a much larger validation dataset, and does not rely on just a few high latitude ice-cores for its validation. However, problems with the model are its failure to correctly simulate provenance, resulting from an underestimation of the Asian source, and an overestimation of the Australian source. The model indicates that it is the increase in source regions which is responsible for the increased dust loading of the atmosphere at the LGM. However, it is not known if this result is model specific, and

little is presented in the way of the sensitivity of the results to the model parameters. Moreover, the simulations are relatively short, and only use CLIMAP based SST simulations of the LGM.

### **1.4.6 Summary**

There have been several attempts in the last decade to model the global dust cycle at the LGM and present day.

There have been improvements in model results since the earliest attempts, but the most important reasons for this are not known. There have been improvements in the way dust entrainment is parameterised, and the effect of vegetation, as well as an improvement in model resolution and advection schemes.

Areas where there have been little progress are in the effect of soil moisture, and the removal of dust by wet deposition. Little has been done in the way of quantitatively validating the models for the present day, and models consistently underestimate the strength of the Asian dust source, and overestimate the Australian source. Neither has there been a lot of progress in really understanding the relative importance of different processes in explaining the changes in dust deposition seen at the LGM. No model has yet been able to correctly simulate the provenance of LGM ice-core dust, which indicates that in some cases, good agreement with deposition observations may have been obtained for the wrong reasons.

It seems that there remains a lot of work to be done in the field of modelling the dust cycle at the LGM.

## **1.5 Aims of this study, and plan of the thesis**

The aim of this study is to understand and simulate the dust cycle at the present day, and Last Glacial Maximum, and to test to see if the results are in agreement with observational data. Included in this is the aim of understanding in detail the effects and relative importance of the different aspects of the dust cycle, both for the present day, and the LGM. This work improves on that carried out previously, by using a more sophisticated model, by employing a more comprehensive and quantitative validation

procedure, and by concentrating on gaining understanding of the processes involved.

In particular, chapter 2 addresses the question of whether changes to the transport of dust at the LGM are an important factor in explaining the increase in dust observed at the LGM in the ice core record. This is carried out using a simple trajectory model, which is forced by winds from the present day and LGM, as simulated by the Hadley Centre GCM.

Chapter 3 describes a more advanced model, developed as part of this thesis, which can be used to simulate the entire dust cycle. As well as describing model parameterisations in some detail, a suite of results are presented, which show clearly the relative importance and effect of the different parameterisations included in the model.

Chapter 4 includes a series of sensitivity studies, testing the model parameterisations. It also includes two case studies, where the model is forced by ERA data, and attempts to simulate the observed dust distributions which resulted after severe storms in the Gobi and Sahara deserts. Finally, this chapter contains the results from a 10-year integration of the model. The results are compared to dust concentration, and deposition data from the DIRTMAP dataset.

Chapter 5 concentrates on the dust cycle at the LGM. As in the previous chapter, a 10 year run is also carried out, and the results compared to the DIRTMAP dataset, and measurements of the provenance of ice-core dust. This comparison suggests that the model can be improved, and consequently, a one-year integration is carried out, with improvements based on the sensitivity studies in chapter 4. The results from this experiment agree much better with data.

Finally, chapter 6 summarises all the work of the previous chapters, draws conclusions, and highlights possible avenues for future research.

---

## CHAPTER 2

### Transport of Dust to Ice-Core Sites

#### 2.1 Introduction

As outlined in section 1.3.4, there are many possible causes of the increase in dust deposition at the LGM, as observed in ice-cores and marine sediments. Section 1.4.6 emphasised that although some previous studies have been able to reproduce the increases in dust, the principal mechanisms behind the increases are still not known. One reason for this is the fact that previous studies have investigated the dust cycle in the framework of global dust models, and, on the whole, have not decoupled the individual components of the dust cycle in order to gain an understanding of their relative importance. An exception to this, is the study of Mahowald *et al.* (1999), in which, in addition to the LGM and present day control runs, an experiment was carried out with present day potential source regions, and LGM entrainment, transport and deposition. This resulted in very similar dust concentrations to the present day control, indicating that it is the change in potential source regions, resulting from changes in vegetation, which causes the increases in dust deposition at the LGM, as opposed to changes in transport or entrainment of dust. However, it is not known how dust-model or GCM specific this result is, or how robust to interannual variability. Furthermore, inabilities of this model to correctly simulate the provenance of LGM dust, have cast doubt on their other conclusions. Therefore, it remains a challenge to isolate the principal causes of the increased dust deposition at the LGM.

In this chapter, one single component of the dust cycle is studied in isolation, by decoupling it from the rest of the cycle. This component is the *transport* of dust. Changes in circulation, caused by drastic changes in global temperature structure, due mainly to ice-sheet expansion, have been suggested as a possible reason for the increase in dust at ice-cores sites at the LGM (Kriger and Genthon, 2001).

In this study, a modelling approach is used, in which back trajectories, initialised at various ice-core sites, are calculated. Two experiments are carried out; in the first, the trajectories are forced by modelled present day winds, in the second, by modelled LGM winds. The results from the two

experiments are compared using a variety of diagnostics; understanding is gained of the LGM and present day circulations, and of their influence on the transport of dust. The question of whether changes in transport could have caused the observed increases in dust deposition at high latitudes at the LGM, is answered.

This chapter starts with a model description section, including a comparison of the modelled winds with observations, continues with a results and discussion section, and finishes with conclusions.

## 2.2 Model Description

A trajectory is the path of a parcel of air, as transported by the wind. Given an initial position, the final position a time  $T$  later, and the trajectory of the particle, can be calculated by incrementally solving

$$d\mathbf{x} = \mathbf{u}dt \quad (2.1)$$

$T/dt$  times. This is a Lagrangian process, and requires knowledge of the wind field,  $\mathbf{u}$ , at all times and in all places. Back trajectories are the reverse; given a final position, they calculate an initial position, and the trajectory between them, by solving

$$d\mathbf{x} = -\mathbf{u}dt \quad (2.2)$$

in the same way as for forward trajectories.

For this work, the atmospheric trajectories of parcels of air which arrive at ice-core sites is to be investigated. Therefore, *back* trajectories are calculated, initialised at the sites of ice-cores. The back trajectories are forced by fields of  $\mathbf{u}$ , output from the Hadley Centre GCM, HadAM3. This GCM, and the winds which it produces, are described and discussed in the next section, 2.2.1. The method by which the trajectories are calculated is described in section 2.2.2, and section 2.2.3 describes the experimental setup, and presents some example back trajectories.

### 2.2.1 The General Circulation Model: HadAM3

This section briefly describes the Met Office Unified Model (UM), which is used to force the trajectory model in this experiment. It also summarises results from Pope *et al.* (2000), in which a comparison is made of the modelled winds with those from an observational dataset.

The development of the UM (Cullen, 1993) has been driven by the needs of both climate modelling and forecasting. The version used in the majority of this study is the Hadley Centre climate version, HadAM3, the most recent atmosphere-only version of the Unified Model. HadAM3 is a hydrostatic, grid-point model, with a resolution of  $3.75^\circ \times 2.5^\circ$ , or  $96 \times 73$  gridpoints, on an Arakawa B-grid, and 19 vertical levels. The model uses the convection scheme of Gregory and Rowntree (1990), and the impact of convection on momentum is based on the scheme developed by Gregory *et al.* (1997). The model uses the radiation scheme of Edwards and Slingo (1996), and the MOSES land surface scheme (Cox *et al.*, 1999).

For the study described in this chapter, the output from the model which is used is the wind velocity,  $\mathbf{u}$ , which consists of three components, the zonal wind,  $u$ , the meridional wind,  $v$ , and the vertical coordinate wind strength,  $\dot{\eta}$ . To gain confidence in the output from the model, it is necessary to provide a comparison of the modelled wind strengths with a dataset of observations. This is particularly important because the model is being used for a paleoclimatology study; if there is no confidence in the model's present day wind strengths, there will be even less confidence in the LGM predictions.

Pope *et al.* (2000) have compared the modelled winds from HadAM3 with the ECMWF Re-analysis product, ERA15, which is a hybrid dataset of assimilated observations and model, extending from 1979 to 1993 (Gibson *et al.*, 1997, Kallberg, 1997). The winds are constrained by observational data from radiosondes and ground-based stations, but there is a dearth of observational data over remote regions such as the Southern Ocean, Central Pacific and Antarctica. One conclusion from this work is that HadAM3 does a very good job of simulating the global circulation, and does a much better job than its predecessors at predicting wind velocities. The main reason for the improvement is the introduction of the convective momentum transport scheme. Analysis of blocking index also shows very good agreement with observations. Below a height of 200mbar, the error in the zonally averaged zonal wind is less than  $2\text{ms}^{-1}$  nearly everywhere.

However, there is a large easterly bias near the tropical tropopause, and a westerly bias in the southern

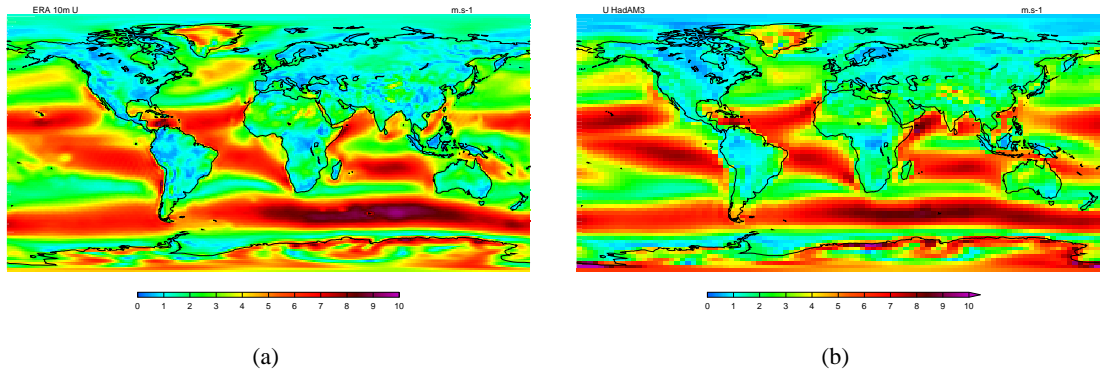


**Figure 2.1:** The annual mean surface wind strength,  $U$ , from the (a) ERA and (b) HadAM3 climatologies.

hemisphere stratosphere at high latitudes. The biggest modelled systematic error in the winds is due to a high pressure bias in the model at high latitudes.

Of particular interest to this trajectory study, Connelley and Cattle (1994) have carried out a study concentrating on the modelled simulation of the Antarctic region by the UM. This shows that the Antarctic climate of the UM is in general realistic, and that the strong katabatic winds are as accurate as can be expected given the resolution of the model.

As a further test of the modelled winds, the modelled surface wind strength can be compared to that of the ERA dataset. The climatologies of annual mean surface wind strength from HadAM3 and ERA are shown in figure 2.1. The annual mean wind speeds,  $U$ , are calculated from monthly mean wind velocities,  $u_i$  and  $v_i$ , such that

$$U = \frac{1}{12} \sum_{i=\text{Dec,Jan,Feb,etc.}} \sqrt{u_i^2 + v_i^2} \quad (2.3)$$

The figure shows that, given the model resolution, HadAM3 is doing a very good job of simulating both the magnitude and spatial distribution of the surface wind strength, particularly over ocean regions. In general, the HadAM3 wind strengths are too strong over the tropical oceans, and too weak over mid-latitude oceans. However, as noted earlier, this is probably mainly illustrating differences between the ERA model winds, and HadAM3 model winds, since the tropical and southern oceans are poorly observed. Over land, HadAM3 is in general over-estimating the wind strength, for example over western Australia and southern Patagonia. However, the errors in the present day winds

are much smaller than the difference between the present day and LGM winds. This is a necessary prerequisite for a study of this kind, where a comparison is being made between the LGM and present day results.

## 2.2.2 The Trajectory Model: OFFLINE

The model which is used to calculate the trajectories is called OFFLINE, and was written by John Methven at the University of Reading. A full description of the model, and a discussion of its accuracy, on which this section is based, can be found in Methven (1997).

### Description

The OFFLINE code consists of two main components, an interpolation scheme and an integrator scheme.

The interpolation scheme is used to calculate the wind velocity at a particle's position in time and space. This is done using a bilinear scheme in the horizontal, and a cubic scheme in the vertical, where linear interpolation is insufficient due to the large curvature of vertical profiles near the tropopause. In the temporal, the interpolation of the wind fields is linear. To avoid problems with advection over the poles, the winds are interpolated onto a Cartesian coordinate system, with the origin at the centre of the Earth.

The integrator scheme, used to calculate a particle's trajectory, is based on the Runge Kutta 4th order scheme, which is considerably more accurate than linear schemes (Press *et al.*, 1992). It involves calculation of the wind velocity at two upstream and two downstream locations at every timestep. Sensitivity studies show that it is the vertical resolution which most strongly influences the accuracy of the trajectories (Methven, 1997). A comparison of the trajectory scheme with a tracer scheme that solves the advection-diffusion equation, which is similar to that used in previous dust-modelling work, shows that the trajectory scheme is less diffusive than the tracer scheme, and preserves strong tracer gradients (Methven, 1997).

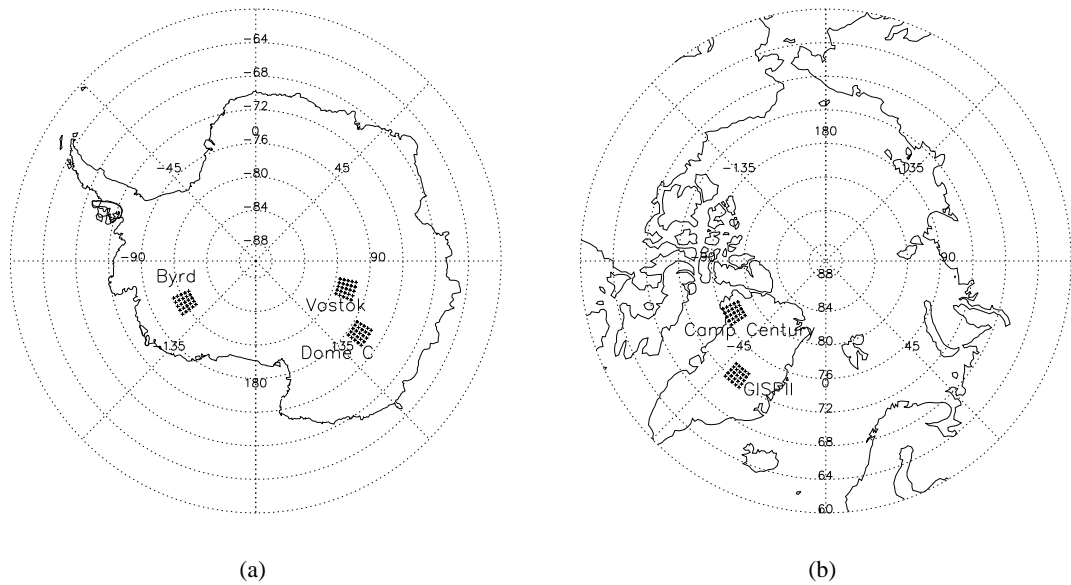


**Figure 2.2:** Points from where the back trajectories are initialised, (a) Antarctic sites, and (b) Greenland sites.

### 2.2.3 Model Setup

Five ice-cores are chosen to be investigated; Dome C, Vostok and Byrd in Antarctica, and GISP II and Camp Century in Greenland.

These particular ice-core sites are chosen because they have published dust records which extend back to the LGM (there are only 12 such cores in total (Kohfeld and Harrison, 2001)), and they represent the major regions in which polar cores have been drilled. Attention is focused on polar cores because dust from tropical cores such as those from the Andes or Himalayas, is thought to have local sources (Thompson *et al.*, 1989, Thompson *et al.*, 1995), transport from which is unlikely to be well simulated by a climate GCM, which has too coarse a resolution. In addition, the mineralogy of dust from the Dome C and GISP II ice-cores has been studied, giving evidence of the likely source regions of dust in these two cores (Basile *et al.*, 1997, Biscaye *et al.*, 1997).

Back trajectories are initialised from each of these five sites, horizontally in squares of 25, covering an area of 50,000km<sup>2</sup>, centred on the ice-core sites. This arrangement is shown in figure 2.2. This horizontal arrangement allows for a greater sampling of trajectories than if only a single trajectory were initialised from each site. The chaotic nature of the atmospheric circulation means that it is expected that trajectories which have been initialised from slightly differing locations will diverge in

a relatively short time.

In the vertical, the trajectories are initialised at 5 levels of the forcing GCM's vertical coordinate,  $\eta$ .  $\eta$  is a hybrid coordinate which is terrain-following near the surface, and pressure-following high up in the atmosphere. The  $\eta$  levels at which the trajectories are initialised are 0.95 (near-surface), 0.8, 0.6, 0.4 (top of the troposphere) and 0.2 (at 200mbar, in the lower stratosphere for high latitude locations). This arrangement in the vertical is chosen to reflect the fact that particles can be removed from the atmosphere by both dry and wet deposition. The particles which arrive at the ice-core site near the surface can be considered to be removed by dry and wet deposition, those which arrive above can be considered to be removed by wet deposition. Particles which arrive at the ice-core site at the level in the stratosphere have no clear method of removal, but are included for completeness.

The trajectories have a lifetime,  $T$ , of 30 days. This is an upper limit for the lifetime of a micron-sized dust particle in the atmosphere. The timestep of the trajectory model is 30 minutes, and forcing wind fields are read in every 6 hours. Trajectories are initialised every 6 hours, for a total of 10 years, for both the LGM and present day. This represents a total of  $3.6 \times 10^6$  trajectories for each of the 5 ice-cores.

For the present day, the GCM, HadAM3, which produces the wind fields, is constrained by observed boundary conditions, which conform to the Atmospheric Model Inter-comparison Project (AMIP) standard (Gates, 1992), a study designed to provide a framework in which different models can be tested under the same boundary conditions.

For the LGM, the GCM boundary conditions are the same as for the present day, except that CLIMAP SSTs and sea-ice extent are used (CLIMAP project members, 1981), a Peltier (1994) land-sea mask, orography and ice-sheet extent, and an atmospheric  $\text{CO}_2$  content of 200ppmv. These LGM boundary conditions conform to the Paleoclimate Model Inter-comparison Project (PMIP) standard. The climatologies shown in section 1.3.2 are from a GCM run, constrained by the boundary conditions described above.

Figure 2.3 shows example back trajectory ensembles, for the Dome C, Antarctica, and GISP II, Greenland, ice-cores. The trajectories are those initialised at midnight on the 10th December, in the 10th year of the present day integration, from a height of  $\eta = 0.6$  (mid-tropopause). There are 25 trajectories for each ice-core site, arranged in a  $5 \times 5$  matrix, as in figure 2.2. For the Dome C ensemble,

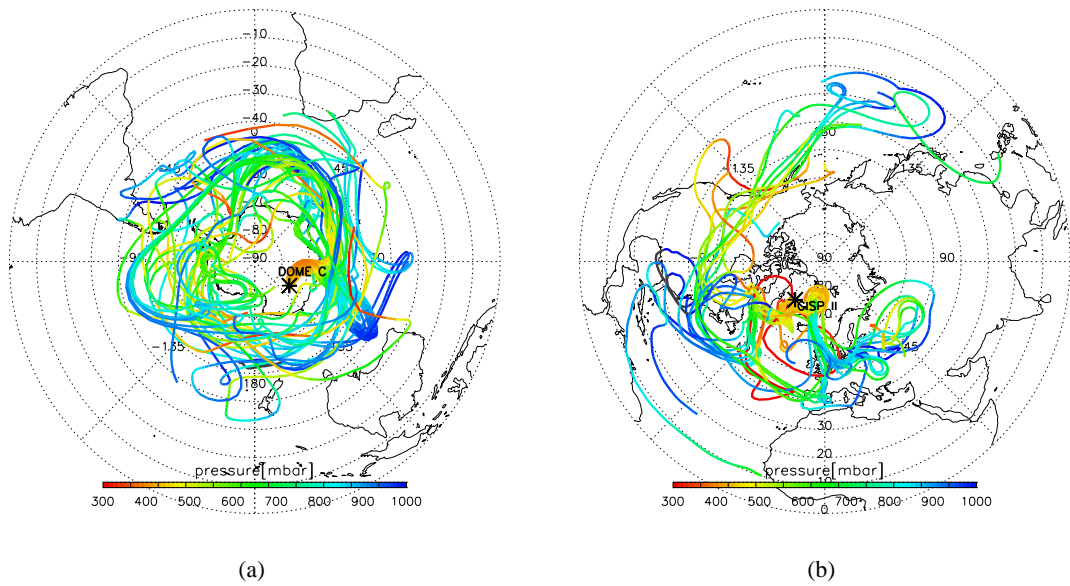


**Figure 2.3:** Example 30-day back trajectories, initialised on the 10th December, in the tenth year of the present day model run, at a height of  $\eta = 0.6$ , from (a) Dome C and (b) GISP II. The colours indicate the altitude of the trajectories, in pressure units.

the flow is predominantly westerly; the back trajectories being advected by the strong winds over the Southern Ocean. Although initialised from a small area, the back trajectories quickly diverge, and after 30 days there is little correlation between them. In general, the back trajectories fall in height as they move away from the pole, and rise as they move towards the pole. In the course of 30 days, very few trajectories reach further equatorwards than  $40^\circ\text{S}$ .

For the GISP II ensemble, the flow is more complicated. There is westerly transport, with back trajectories originating over the Pacific, and being transported over North America. There are a couple of trajectories which are advected from the equatorial Atlantic by Easterlies, and then northwards into the westerly flow of the mid-latitude Atlantic. There is also some easterly transport from Asia, associated with an area of high pressure over the Urals.

These two ensembles represent only a tiny fraction of the total number of back trajectories which are calculated. To examine every trajectory in this way would be impossible; methods are needed by which the information contained in them can be analysed. After some experimentation with a number of methods, two diagnostics are found to be suited to this purpose.

The first of these, discussed in section 2.3.1, involves calculation of the density of trajectories over the globe. The trajectory density at a point on the earth is a measure of the efficiency of the transport,

from that point, to the ice-core site. This is useful for understanding how the atmospheric circulation affects transport to the ice-core sites, and how it varies between season and time period.

The second diagnostic, discussed in section 2.3.2 involves counting the number of back trajectories which pass over potential dust source regions. This method gives direct information about how atmospheric transport might affect both the concentration, and origin, of ice-core dust.

## 2.3 Results

### 2.3.1 Trajectory Densities

Each 30-day back trajectory in the experiment represents the path of a parcel of air, and is defined by a series of 120 latitude, longitude and pressure (height) triplets, representing the precise position of the parcel of air at 6-hourly intervals. The final triplet for each trajectory is the position at which the trajectory is initialised, the site of the ice-core.

To calculate the trajectory density of an ensemble of such back trajectories, the earth is first divided into an array of gridboxes. Then, each position triplet from every trajectory in the ensemble is binned into the appropriate gridbox. Finally, each gridbox is normalised by its area. The resulting trajectory density field is in units of trajectory points per square metre per period over which the analysis is carried out. For this study, the gridboxes are  $1^\circ \times 1^\circ$ , and extend through the depth of the atmosphere. The final trajectory density is normalised, to give a density per year.

The results in this section are presented by examining each ice-core in turn. It turns out that the three Antarctic cores have very similar results, as do the two Greenland cores. Therefore, control sites, Dome C in Antarctica and GISP II in Greenland, are examined in detail, and the other cores are presented as perturbations from the controls.

#### Dome C

Figure 2.4 shows the trajectory density, calculated in the way explained above, for all the trajectories initialised at Dome C ice-core, over the 10 year period, in the present day experiment, for the DJF and

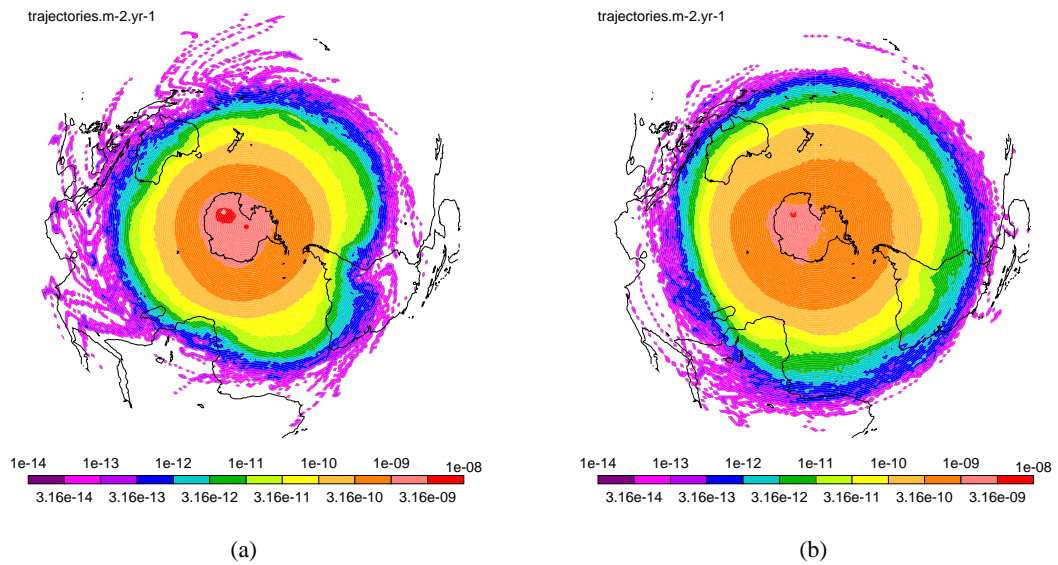


**Figure 2.4:** Present day annual mean trajectory density, for trajectories initialised at Dome C, Antarctica. (a) is for DJF, (b) is for JJA. Units are trajectories  $\text{m}^{-2}\text{yr}^{-1}$ .

JJA seasons. The logarithm of trajectory density is shown due to the fact that the trajectory density decreases exponentially with distance from the the ice-core site. The first point to note is that the trajectory density is highly zonally symmetric. The meridional transport is weak, and the trajectory density decreases rapidly moving away from the pole. The zonal symmetry arises from the strong westerly circulation over the Southern Ocean, which acts to mix trajectories, and average out their asymmetric component over a period of years.

Unsurprisingly, the highest density is at the ice-core site itself. There is also a slight anomaly at the pole, possibly caused by the small gridbox size in this region. There is more meridional transport in JJA (winter), than in DJF (summer). There are some zonal asymmetries in DJF, equatorwards of  $40^{\circ}\text{S}$ , resulting in a relatively high trajectory density in the southern Atlantic, compared to over South America at the same latitude. These asymmetries are possibly related to regions of high pressure over the Southern Hemisphere oceans at about  $50^{\circ}\text{S}$  in DJF; in JJA there is a more zonally symmetric belt of high pressure over both land and sea at this latitude.

The higher trajectory density equatorwards of  $50^{\circ}\text{S}$  in JJA, compared to DJF, is possibly related to the fact that at these latitudes, the majority of the trajectories are close to the surface, and that the modelled surface westerlies in the band  $50^{\circ}\text{S}$  to  $60^{\circ}\text{S}$ , which act to trap trajectories at high latitudes, are stronger in DJF than JJA.

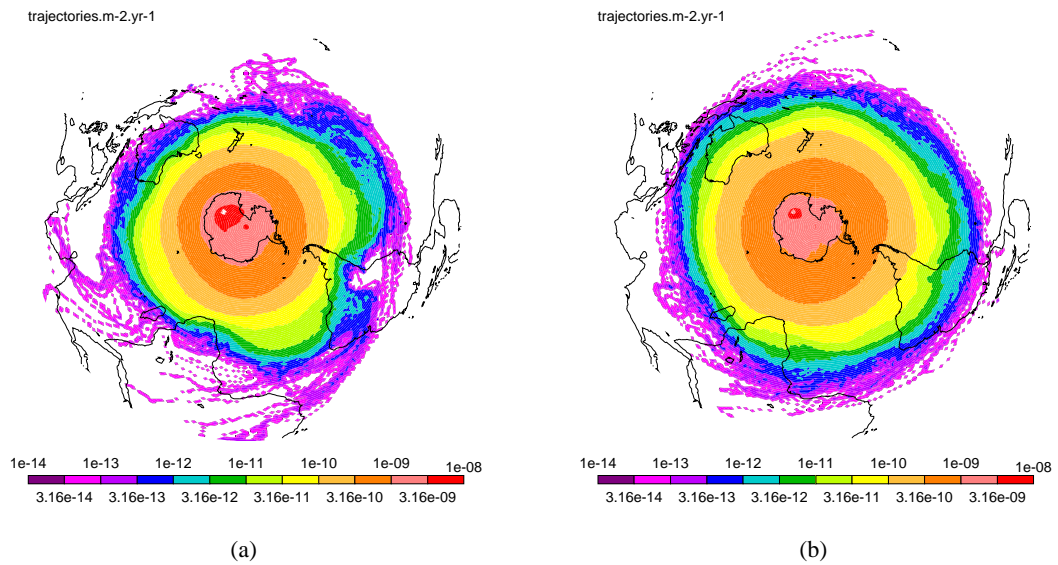


**Figure 2.5:** LGM annual mean trajectory density, for trajectories initialised at Dome C, Antarctica. (a) is for DJF, (b) is for JJA. Units are trajectories  $\text{m}^{-2}\text{yr}^{-1}$ .

Figure 2.5 shows a similar plot, but for the LGM experiment. This is remarkably similar to the density plots obtained in the present day experiment, and all the same comments apply. However, there are subtle differences, which are shown in figure 2.6; figure 2.6(a) is the difference between the annual mean present day and LGM trajectory densities, and figure 2.6(b) is the logarithm<sub>10</sub> of their ratio. A Student T-test (Press *et al.*, 1992) carried out on this data shows the differences to be significant at a 95% confidence level, polewards of 30°S.

The difference shows that at the LGM, the trajectory density is higher over Antarctica, and at the present day, the trajectory density is greater over the Southern Ocean. At the LGM, the predominant transport close to the ice-core site is westwards, whereas at the present day it is eastwards. These same differences are reflected in the ratio of trajectory density, but the differences at lower latitudes are highlighted. These show a higher trajectory density at the present day than at the LGM, in regions equatorwards of 40°S. In particular, there is a higher trajectory density at the present day over the potential dust source regions of Australia, South Africa and Patagonia. This may be related to the modelled 500mbar zonal mean southerly wind velocities between 50°S and 60°S, which are more intense at the LGM than at the present day. These southerly winds would tend to suppress the transport from mid-latitudes to the poles, and cause a decreased trajectory density at the LGM at low latitudes. The higher trajectory density at the present day at low latitudes may also be related to the annual mean surface zonal wind in a latitude band of -60° to -70°, which is stronger at the LGM than at the

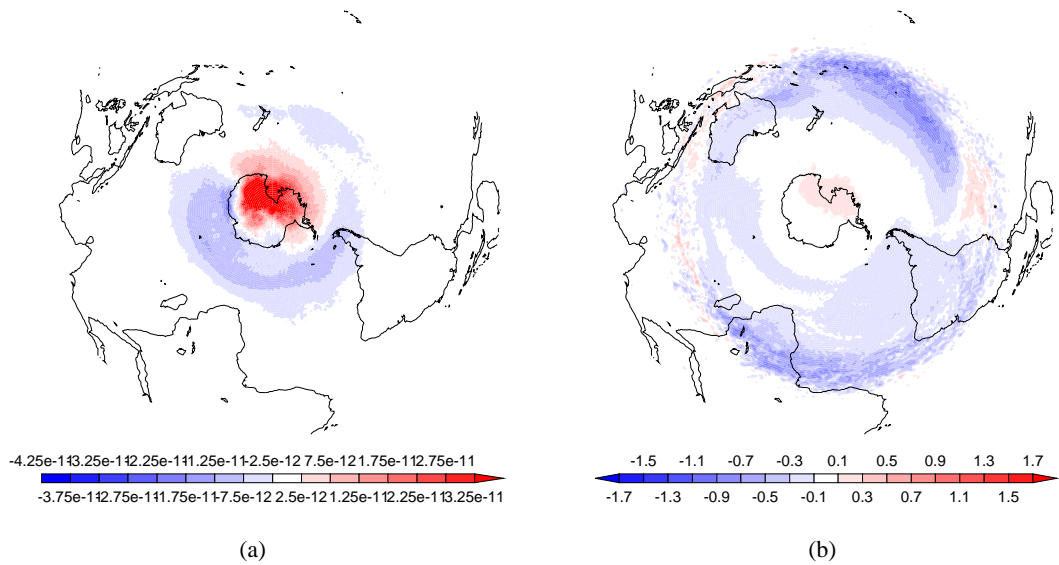


**Figure 2.6:** (a) Difference in Dome C annual mean trajectory density, LGM - present day, in units of trajectories  $\text{m}^{-2}\text{yr}^{-1}$ . (b)  $\text{Logarithm}_{10}$  of the ratio of LGM to present day Dome C annual mean trajectory density.

present day, by about  $2\text{ms}^{-1}$ . In a similar way to the seasonal differences in trajectory density, this greater zonal wind, related to an increase in baroclinicity associated with the stronger equator to pole temperature gradient at the LGM, could act to trap trajectories at high latitudes, and inhibit transport across this band.

### Vostok and Byrd

The Vostok ice-core site is situated close to that of Dome C (see figure 2.2), in Western Antarctica. Figure 2.7 shows the ratio of LGM to present day trajectory density, for the Vostok site, for comparison with figure 2.6(b) (the Dome C site). The ratio is remarkably similar to that of Dome C, and all the comments applied to the Dome C results, including seasonality, are also applicable to Vostok. At Vostok, the difference between the present day and LGM trajectory density is slightly less marked, but is of the same sign.

The Byrd ice-core site is situated on the Eastern side of Antarctica, several thousand kilometres from Dome C and Vostok (see figure 2.2). The density of trajectories which are initialised at Byrd are very similar to those initialised at Dome C and Vostok, at both the present day and LGM. The changes in density between the LGM and present day are also very similar to the other two Antarctic cores, with

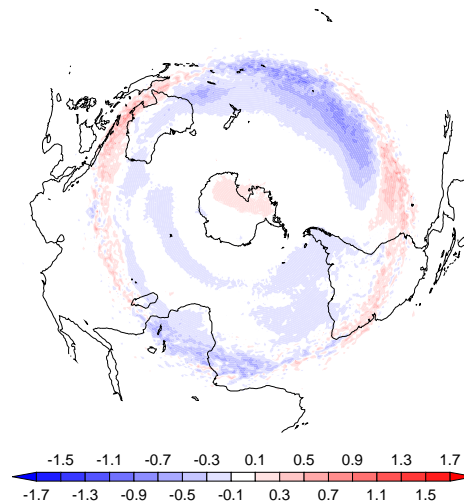


**Figure 2.7:**  $\text{Logarithm}_{10}$  of the ratio of LGM to present day Vostok annual mean trajectory density.

a few minor differences, most notably that the differences over the Southern Ocean and Patagonia are less marked. However, in absolute terms, the differences in trajectory density in these regions is still of the same sign.

### GISP II and Camp Century

The GISP II ice core is located in central Greenland (see figure 2.2). Figure 2.8 shows the trajectory density, from the present day integration, for the DJF and JJA seasons. As for the Antarctic results, the trajectory density decreases exponentially with distance from the pole. In DJF (winter), the trajectory density is very zonally symmetric. In JJA (summer), there is more zonal asymmetry. In particular, there is a local maximum in trajectory density off the east coast of China, and a corresponding minimum over India. It is likely that this asymmetry derives from the Asian monsoon circulation, and the associated strong easterlies over the maritime continent and south-westerlies in south east Asia. This monsoon circulation is present only in JJA, and so its effects are not seen in the DJF trajectory density. The other main zonal asymmetries are local minima over western North America, and the eastern Sahara, and corresponding maxima in the eastern Pacific and western Atlantic. The asymmetry over western North America is likely to be associated with the ridge of high pressure over the Rockies. The jet is strongest in DJF, and so the asymmetry is most marked in JJA.

As for the Dome C experiment, the trajectory densities for the LGM and present day are remarkably similar. If anything, there is slightly more zonal asymmetry at the LGM. Surprisingly, the extensive

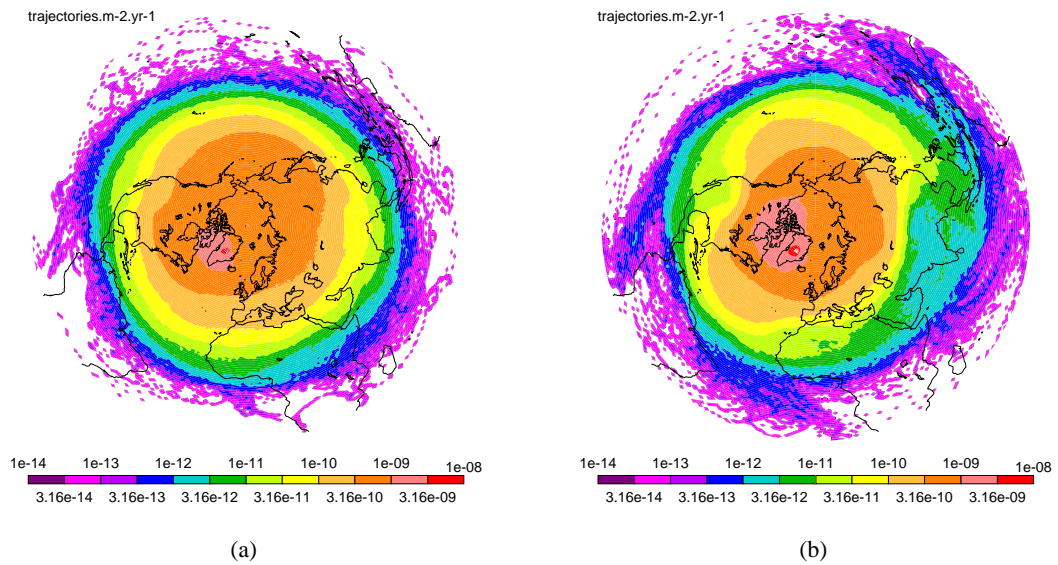


**Figure 2.8:** Present day annual mean trajectory density, for trajectories initialised at GISP II, Greenland. (a) is for DJF, (b) is for JJA. Units are trajectories  $\text{m}^{-2}\text{yr}^{-1}$ .

northern hemisphere ice-sheets do not perturb the transport of dust to the ice-cores in a big way. Figure 2.9 shows the difference between, and ratios of, the trajectory densities at the LGM and the present day, for the trajectories initialised at GISP II. The absolute difference shows that at the LGM, the trajectory density is greater at the pole, and at the present day, it is greater at mid-latitudes; at the LGM, the trajectories are more confined to high latitudes. The ratio of LGM to present day trajectory density shows that over the potential source regions of the Sahara, North America, and Asia, the trajectory density is higher at the present day. In a similar way to the Antarctic cores, these differences may result from the modelled 500mbar zonal mean southerly wind velocities between  $55^{\circ}\text{N}$  and  $75^{\circ}\text{N}$ , which are more intense at the present day.

Camp Century is situated in northwest Greenland (see figure 2.2). Similarly as for the Antarctic results, the trajectory densities of Camp Century are remarkably similar to those of GISP II, at both the present day and LGM.

## Discussion

There are several interesting results to come out from this study of trajectory densities, which have a bearing on the transport of dust to ice-cores, and how it differs at the LGM and present day.

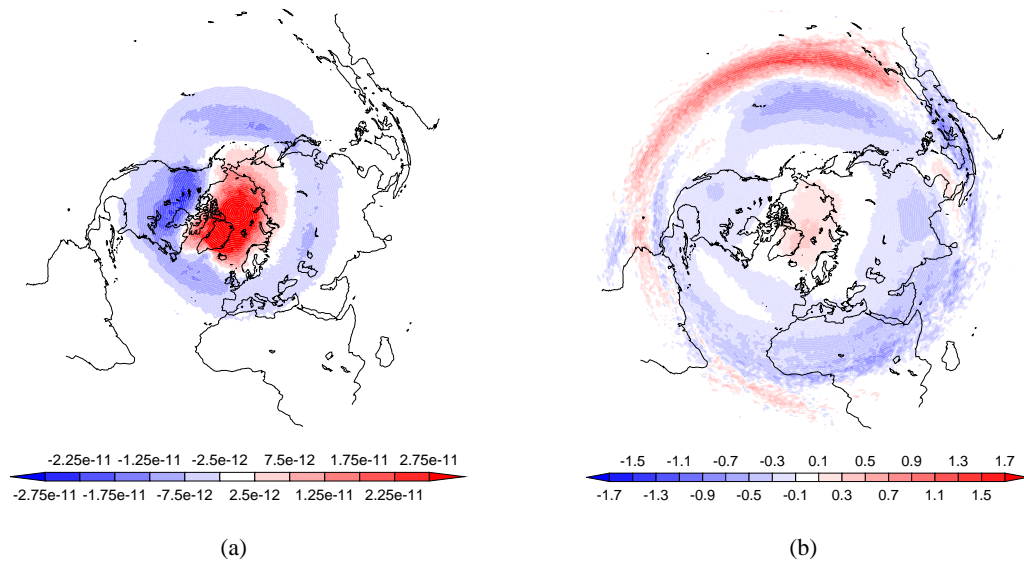


**Figure 2.9:** (a) Difference in GISP II annual mean trajectory density, LGM - present day, in units of trajectories  $\text{m}^{-2}\text{yr}^{-1}$ . (b)  $\log_{10}$  of the ratio of LGM to present day GISP II annual mean trajectory density.

Firstly, there is the general pattern of trajectory density, which in the Southern Hemisphere is very zonally symmetric, at both time periods. There is more zonal asymmetry in the Northern Hemisphere, caused by the presence of the continents, the Asian monsoon, and strong meridional winds over the Eastern Pacific and Eastern Atlantic. The trajectory density is highest over potential source regions in winter in both poles, indicating that winter is the most efficient time for dust transport from these regions to the sites of polar ice-cores.

At the LGM, the trajectories are very similar to the present day, in both poles. The biggest relative changes are seen at the latitudes of potential dust source regions, where the trajectory density is lower at the LGM than at the present day. A likely cause for this difference is the stronger zonal flow at the LGM, which reduces the efficiency of the meridional transport. These results indicate that dust transport from potential source regions to the sites of polar ice-cores is more efficient at the present day than at the LGM.

Another result is the striking similarity between results from different ice-cores. All three Antarctic cores show a high degree of correlation with each other, as do the two Greenland cores. This implies that by studying the results from one ice-core, conclusions can be made about the transport of dust to other cores from the same region. In the next section, attention is focused on results from the Dome C and GISP II results.

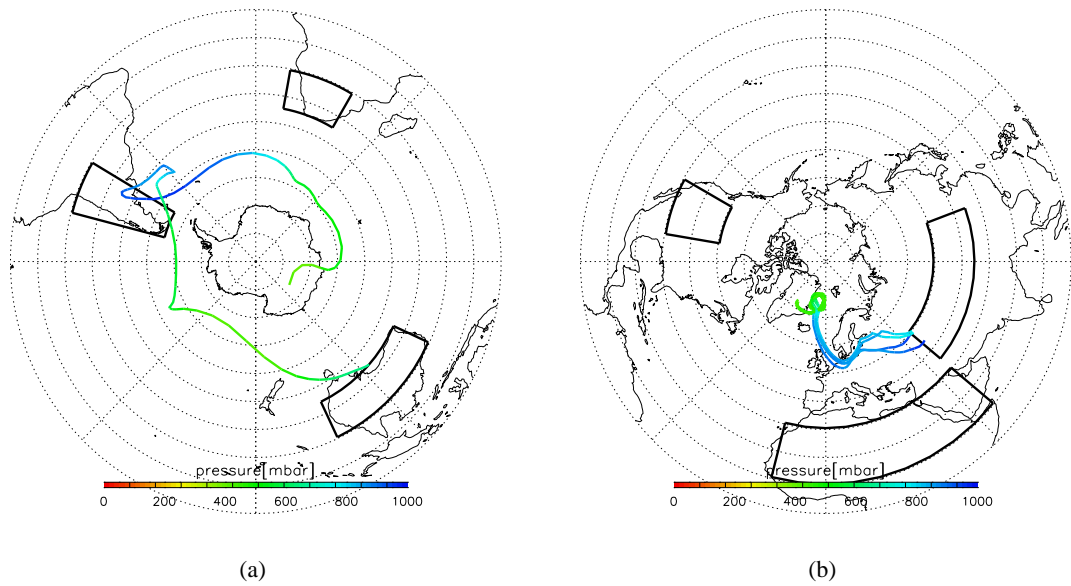


**Figure 2.10:** The potential source regions of (a) Patagonia, Australia and South Africa, and (b) Central Asia, North America and Sahara. Also shown are the trajectories from figure 2.3, which pass over the potential source regions of (a) Australia and (b) Central Asia.

### 2.3.2 Trajectory Counting

The trajectory density analysis in the preceding section gives an understanding of how changes in circulation can affect the transport to ice-core sites. It can also qualitatively address the question of how this is important for the dust cycle.

This section makes a more quantitative analysis of the relevance of this work to dust. The method used, involves counting the number of back trajectories which pass over potential source regions. These regions, chosen so as to encompass the principal desert regions of the Earth, are shown in figure 2.10. Also shown in these figures, are those trajectories which pass over the source regions of Australia and Central Asia respectively, from the same ensemble as in figure 2.3. Of the total of 25 back trajectories initialised at each core, 4% (one trajectory) is traced back to Australia, and 16% (four trajectories) are traced back to Central Asia. These percentages can be regarded as a measure of the transport efficiency from Australia and Central Asia, to Dome C and GISP II; a high percentage represents a high efficiency. This analysis is applied to the trajectories in the 10 year experiment, for both present day and LGM, for Dome C and GISP II. The results are discussed below; those for Dome C have been published in Lunt and Valdes (2001)

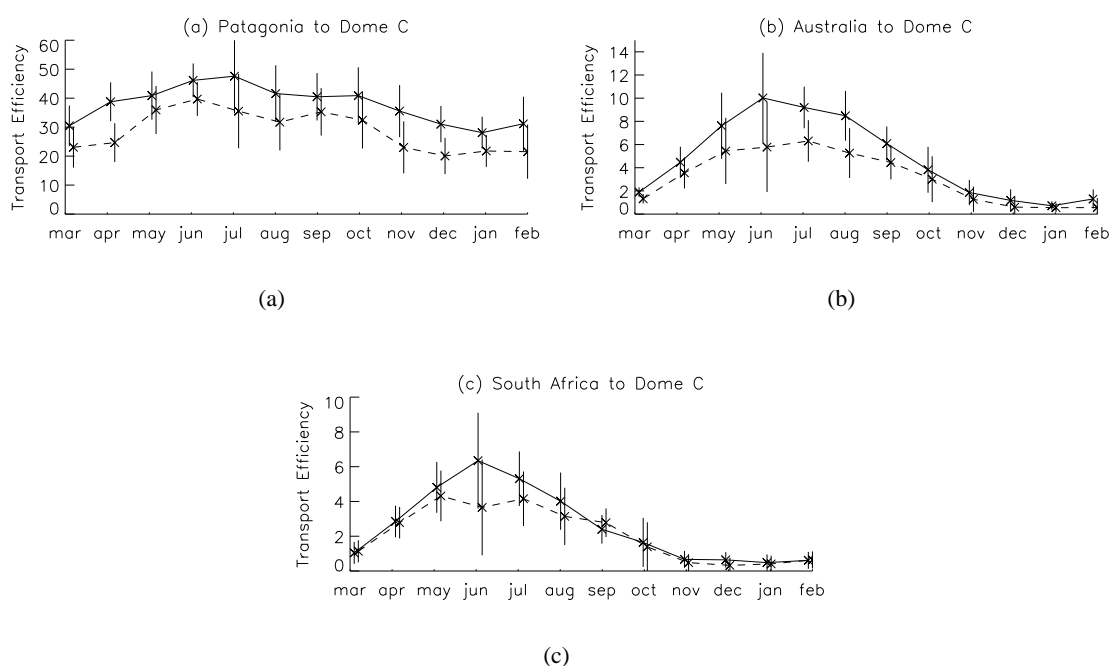


**Figure 2.11:** Transport efficiency to Dome C, from (a) Patagonia, (b) Australia and (c) South Africa, as a function of time of year. Solid line is for the present day, dashed line is for the LGM. The error bars show one standard deviation of interannual variability. Note the change in scale between the plots.

## Dome C

Figure 2.11 shows the transport efficiency (percentage of back trajectories traced back from the ice-core to the source), for the Dome C ice-core, and the potential dust source regions of Patagonia, Australia and South Africa, as a function of month of the year, for the ten years of present day and LGM integration. From all three potential source regions, the transport efficiency is greater at the present day than at the LGM. The ratio of LGM to present day annual mean transport efficiency is 0.76 for Patagonia, 0.67 for Australia and 0.82 for South Africa. This is consistent with the trajectory density plot of figure 2.6(b), which shows negative values over all potential source regions.

There is a strong seasonal cycle in transport efficiency from the Australian and South African sources, with a maximum in JJA (winter), and a minimum in DJF (summer). Transport from Patagonia is more constant throughout the year, although there is still a maximum in winter. This seasonality can be understood by reference to figures 2.4 and 2.5, which shows a higher trajectory density at the latitude of the source regions in JJA than in DJF.

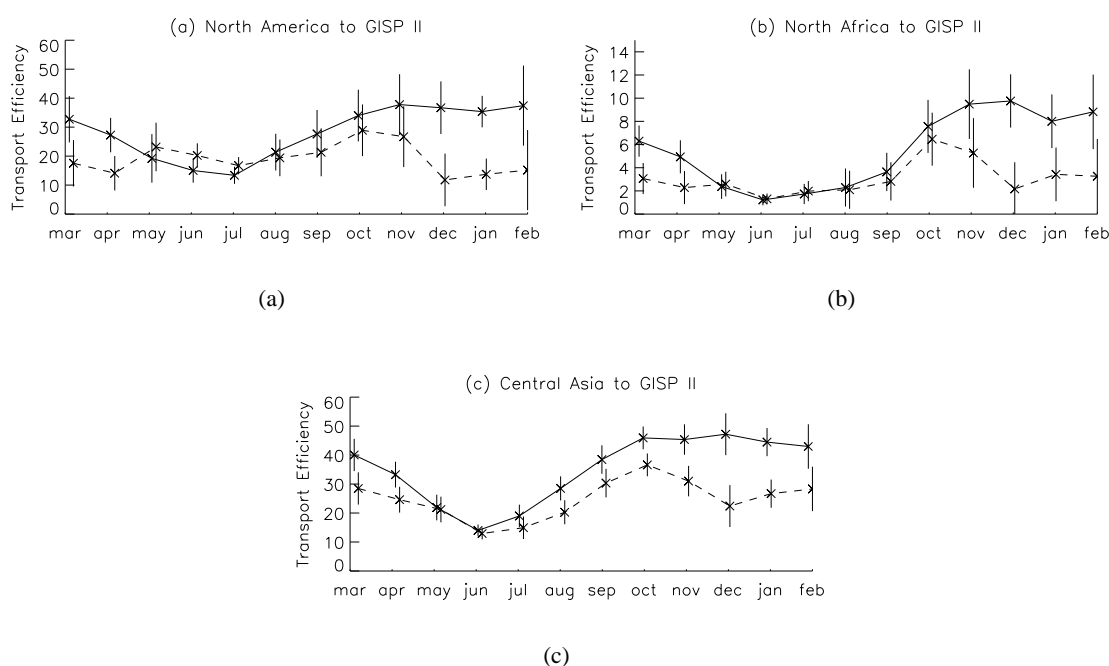


**Figure 2.12:** Transport efficiency to GISP II, from (a) North America, (b) Sahara and (c) Central Asia, as a function of time of year. Solid line is for the present day, dashed line is for the LGM. The error bars show one standard deviation of interannual variability. Note the change in scale between the plots.

The interannual variability in transport efficiency at the LGM and present day is large, one standard deviation being on average 22% of the mean for Patagonia, 34% for Australia and 43% for South Africa.

Transport from Patagonia to Dome C is much more efficient than transport from Australia or South Africa, at both the LGM and present day. Once again, this can be understood from the trajectory densities in figures 2.4 and 2.5. These show a higher trajectory density over the Patagonian source region than over the other two regions. This is due to the fact that the modelled Patagonian source region extends further south than the other two regions; the zonally symmetric nature of the trajectory densities means that the Patagonian region encompasses an area of higher trajectory density.

## GISP II

Figure 2.12 is similar to figure 2.11, except that the ice-core site is GISP II, and the potential source regions are North America, North Africa and Central Asia.

As in the Southern Hemisphere case, the present day transport efficiency is in general greater than that of the LGM, for all three potential source regions. The ratio of LGM to present day annual mean transport efficiency is 0.68 for North America, 0.56 for North Africa and 0.54 for Central Asia. This is unsurprising, given the difference in LGM and present day trajectory density, highlighted in figure 2.9, which shows a greater trajectory density over the potential source regions at the present day.

The LGM seasonal cycle of transport efficiency is different to that of the present day. At the present day, the transport efficiency is at a maximum in winter for all three source regions, and at a minimum in summer. At the LGM, there is a maximum in October, followed by a sudden decrease in efficiency in December.

The interannual variability of the transport efficiency is large for the North American and North African sources, but for the Central Asian source, one standard deviation is only 14% of the mean at the present day, and 26% at the LGM.

The magnitude of transport efficiency for the Central Asian and North American sources is comparable, and much greater than that for the North African source. This is because, as in the southern hemisphere case, it is the source regions at high latitudes which have the greatest transport efficiency, due to the zonal symmetry of the trajectory density.

## 2.4 Conclusions

This back trajectory modelling study shows that changes in the atmospheric circulation, and hence changes in transport, are not sufficient to explain the increases in dust deposition at the LGM, seen in the polar ice-core record. In fact, it shows that the transport of dust from potential source regions to the poles is more efficient at the present day than at the LGM. This implies that the increase in dust deposition at the poles at the LGM is due to changes in other aspects of the dust cycle, the size or strength of the source regions, or the deposition of dust.

Comparison of trajectory densities with the mean modelled wind fields point to the strength of the surface zonal wind, in the latitude bands  $50^{\circ}\text{S}$ - $70^{\circ}\text{S}$  and  $50^{\circ}\text{N}$ - $70^{\circ}\text{N}$ , as being the main factor controlling the efficiency of transport from the source regions to the poles; a strong zonal wind in this region acts as a barrier to dust moving polewards. The modelled zonal wind in this region is stronger

at the LGM than at the present day, associated with an increased meridional temperature gradient, and a greater baroclinicity.

The transport efficiency from southern hemisphere source regions to the Antarctic ice-core sites is in general greatest in the winter, and least in the summer. This can also be related to the strength of the zonal wind at southern hemisphere mid-latitudes, which is strongest in summer. The seasonality is so strong that if the dust at the LGM is produced in winter, and dust at the present day is produced in summer, then the changes in transport, coupled to the time of dust production, could be the cause of the increases in dust at the poles at the LGM. However, sections 4.4.2 and 5.2.3, which investigate the seasonality of the sources, show that this is unlikely, and that the seasonality of dust production in the Southern Hemisphere does not change significantly between the LGM and present day.

The interannual variability of the transport efficiency is large, and in reality it is probably even larger than simulated here, due to the fact that the SSTs used to constrain the GCM represent a climatological mean, and themselves neglect interannual variability. This indicates that models which attempt to simulate the dust cycle need to be run over a number of years, if they are to draw valid conclusions. Previous LGM dust models have failed to do this (eg Andersen *et al.*, 1998, Mahowald *et al.*, 1999), casting a doubt over their principal findings. For this reason, the dust model which is developed in the next chapter, is run for a period of 10 years, under both present day and LGM conditions. The results from these runs are discussed in sections 4.4.2 and 5.2.2 of this thesis.

In the Southern Hemisphere, the modelled transport is consistent with a Patagonian provenance of Antarctic dust at both the LGM and present day. In the Northern Hemisphere, the circulation favours the transport from both North America and Asia to Greenland over that from the Sahara. These results can be understood from the very zonal nature of the transport, and the fact that the transport efficiency decreases sharply away from the poles, leading to the polewards extent of the sources being the determining factor controlling the transport efficiency from them to the ice-core sites. Patagonia is the source region which extends furthest south; North America and Asia extend further north than the Saharan source.

## 2.5 Discussion

There are several points which need addressing when considering the accuracy and validity of the results of this trajectory study.

The accuracy of the trajectory model, and of the present day winds produced by HadAM3, have been discussed in sections 2.2.2 and 2.2.1. The LGM boundary conditions used to force HadAM3 conform to the PMIP standard (Joussaume and Taylor, 1995). It is believed that the CLIMAP SSTs are too warm by a couple of degrees in the tropics (Hostetler and Mix, 1999), and that the sea-ice extends too far northwards in the Southern Hemisphere (Crosta *et al.*, 1998). In the place of prescribed SSTs and sea-ice, the use of a slab-ocean model coupled to the GCM leads to a decrease in the intensity of modelled zonal winds over the Southern Ocean at the LGM (Dong and Valdes, 1998), and may result in more similarity between the LGM and present day trajectories.

Sensitivity studies show that the conclusions drawn from the work in this chapter are not sensitive to the length of the trajectories calculated, so long as they are sufficiently long to reach the source regions, and not so long that all trajectories can eventually be traced to all source regions.

The results presented here are the sum of all 5 vertical distributions of initialised particles, four in the troposphere, and one in the stratosphere. The conclusions are the same for all the tropospheric heights individually. The trajectories tend to fall in height as they move equatorwards, and consequently, over the source regions, the average trajectories are very close to the surface. Therefore the tropospheric trajectories do indeed represent possible paths of dust particles, which are entrained at the surface, and then deposited at the site of the ice-core, throughout the depth of the atmosphere, by both wet and dry deposition. The stratospheric trajectories are less representative of dust transport, and tend to remain in the stratosphere throughout their 30-day lifetime. However, these trajectories are included for completeness, and can only affect the results by at most 20%.

The zonal extent of the potential source regions makes little difference to the analysis in this chapter. This is due to the fact that the trajectories in general move in a zonal direction, and so will pass over a region, whether its zonal extent is large or small. The equatorward extent of the source regions also makes little difference, as extending the regions equatorwards will only catch a few more trajectories, due to their low density at low latitudes. However, the results are sensitive to the polewards extent of the source regions. The fact that the Patagonian source dominates in the Southern Hemisphere, and

the North American and Asian sources dominate in the Northern Hemisphere, is due to the fact that it is these source regions which extend furthest polewards.

In the context of counting trajectories over source regions, the results from Dome C and GISP II have been discussed here. The similarity in trajectory densities, found for the three Antarctic and two Greenland cores, leads to a belief that the conclusions from this study apply to all the Antarctic and Greenland ice-core sites.

In this study, local sources, such as dust from the margins of the Greenland and Antarctic ice-sheets, is ignored. These regions would have a very large transport efficiency. This analysis is best suited to sources which are remote from the ice-core itself.

A comparison could be made between the trajectories calculated using the winds from HadAM3, and those from an observational dataset, such as ERA. However, reanalyses like ERA have scant observations in regions of interest for this study, such as Greenland, Antarctica and the Southern Ocean, and the winds in these regions are essentially derived from a model anyway. Such a comparison would be model-model rather than observations-model.

The effect of precipitation, and removal of dust by sedimentation, is not included in this model, nor is the effect of the surface wind on entrainment. These processes could be accounted for by including an inverse settling velocity, and discounting trajectories which passed through regions of heavy precipitation, or which arrived at the source regions when the surface wind was below some threshold. However, the purpose of this study is to decouple the transport from the rest of the dust cycle. These interactions are best studied in the framework of a complete dust cycle model, simulating the sources, transport and sinks of dust in one model. A dust model such as this is developed in the next chapter, and tested and used throughout the rest of the thesis.

---

## CHAPTER 3

### The Dust Model

The previous chapter describes a trajectory model, which can be used to investigate the transport of dust to ice core sites, under LGM and present day boundary conditions. It also explains that for further progress to be made, it is necessary to study all aspects of the dust cycle, and how they interact. A dust cycle model, simulating the sources, transport and sinks, is a suitable framework in which to study these interactions. Using a model such as this is an ideal way to investigate the dust cycle, and how it varies at different time periods.

This chapter describes the development of a dust-cycle model. The model is tested, and used as a tool, in subsequent chapters.

#### 3.1 Introduction

There are two types of dust model, in-line and off-line. In-line models are formulated as part of a GCM simulation, and are run simultaneously and within the GCM. Off-line models are forced by modelled fields output from a GCM, or by observed meteorological fields, such as those produced by the ECMWF.

Off-line models have the advantage that, when forced by GCM output, they only need the GCM to be run once, and so are in general more computationally efficient than in-line models, allowing a greater number of sensitivity studies to be carried out. They also have the advantage that real meteorological data can easily be used to force them, allowing case studies of real events to be carried out.

In-line models have the advantage that they capture more of the short-timescale variability in atmospheric fields. Variability captured by the off-line approach is limited by the GCM output timestep, which is usually greater than the GCM model timestep itself. In-line models also have the advantage that they are more suitable for studying dust-climate feedbacks, such as the relationship between dust,

radiation balance and atmospheric dynamics.

The dust model described in this chapter is of the off-line variety. It is built around the tracer model, TOMCAT (Chipperfield and Simon, 1996, Stockwell and Chipperfield, 1996), which can be forced by observed fields, or by GCM output. TOMCAT models the transport of dust, by advection, convection and vertical diffusion.

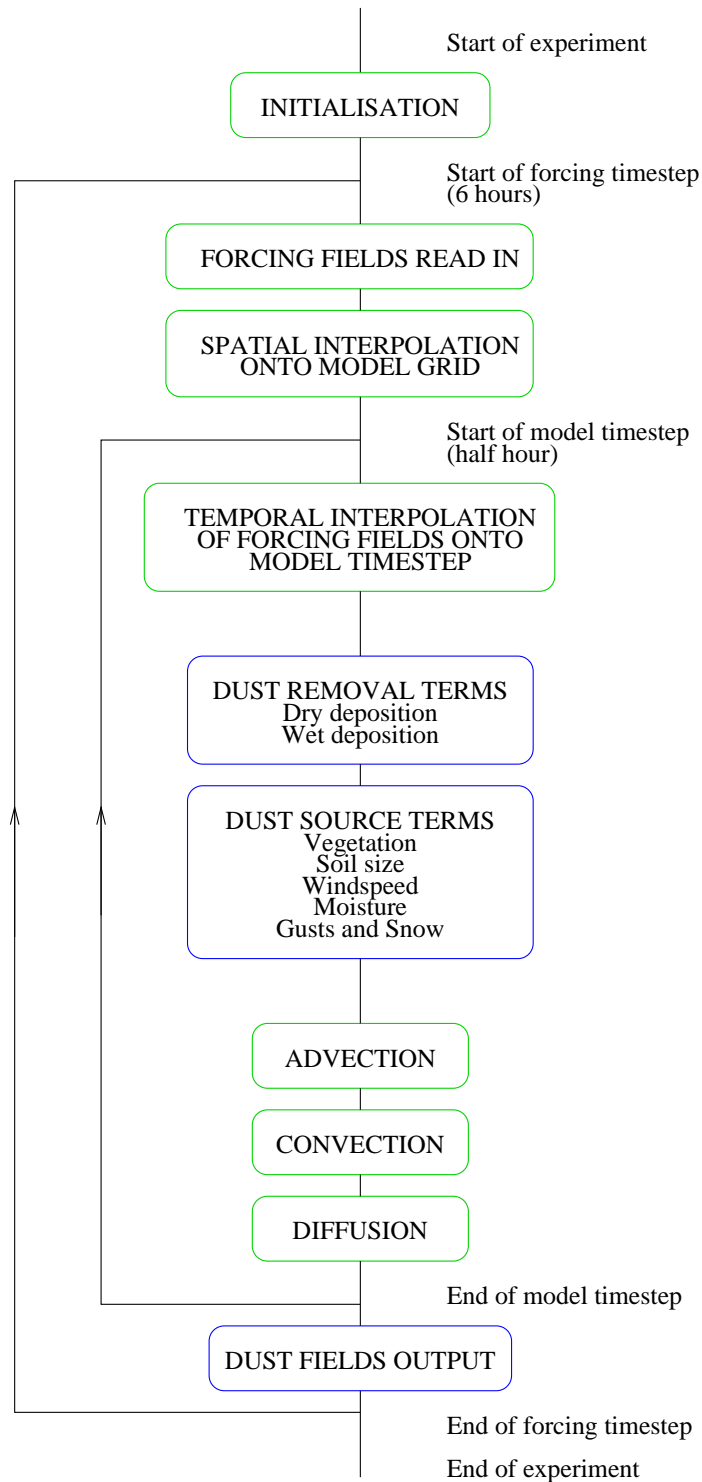
The dust model, which consists of several components, including the sources and sinks of dust, is described in some detail in the following sections. After each component of the model is described, its effect is assessed by the presentation and discussion of a one-year integration of the dust model, including the component.

Figure 3.1 shows a simple flowchart of the final model, results from which are summarised in section 3.6. It illustrates the separate components of the model, and how they fit together.

## 3.2 Modelling the Transport of Dust

Dust in the atmosphere is transported by several mechanisms. The most important of these is advection by large-scale winds. Dust is also transported vertically by convection, by diffusion and, due to the finite mass of dust particles, by sedimentation under the action of gravity. Other mechanisms for transport include orographically-induced motions, and vertical transport in frontal regions. At the core of any dust model is the simulation of these transport mechanisms.

Advection by the large-scale winds can be calculated explicitly, given knowledge of the global wind field, by solving the flux form of the tracer-transport equation (equation 3.1). Other transport mechanisms, which occur on a scale which is in general unresolved by global climate models, are parameterised. These parameterisation schemes often require knowledge of global fields other than the wind velocity; for example, convection schemes often require fields of specific humidity and temperature. The transport of dust in this model is carried out using TOMCAT. TOMCAT simulates transport of tracer by advection, convection and vertical diffusion. It does not include sub-gridscale orographic effects explicitly, nor does it include a special treatment of frontal lifting. The schemes used by TOMCAT to simulate transport by advection, convection and vertical diffusion are described in sections 3.2.1, 3.2.2 and 3.2.3.



**Figure 3.1:** A flowchart, showing the different components of the dust model. The sections labelled in green are the TOMCAT model. The sections in blue are the dust-specific parts of the model, developed for this thesis.

### 3.2.1 TOMCAT simulation of advection: The Prather Scheme

The advection of a trace constituent of the atmosphere, in the absence of sources and sinks, is given by the flux form of the tracer-transport equation:

$$\frac{\partial}{\partial t}(r\rho) + \nabla \cdot (\mathbf{u}r\rho) = 0, \quad (3.1)$$

where  $r$  is the mass mixing ratio of tracer ( $\text{kgkg}^{-1}$ ),  $\rho$  is the local density of air ( $\text{kgm}^{-3}$ ), and  $\mathbf{u}$  is the wind velocity ( $\text{ms}^{-1}$ ).

For the problem of tracer advection, the velocity,  $\mathbf{u}$  is known (from analysis or GCM output), and a numerical scheme is required to solve equation 3.1. TOMCAT uses the Prather (1986) advection scheme of second-order moments. This is an extension of the slopes scheme of Russell and Lerner (1981), which is itself an extension of the upstream scheme. All these schemes are stable up to the Courant limit ( $\frac{\Delta x}{\Delta t} = u_x$  in the x-direction).

The upstream scheme calculates the flux into a gridbox, as the tracer concentration in the ‘up-wind’ gridbox, multiplied by the wind velocity at the interface of the two gridboxes, multiplied by the model timestep. To illustrate this scheme, figure 3.2a shows a one-dimensional distribution of tracer, in a field of uniform speed,  $u$ , to the right. The shaded regions, of width  $u dt$ , show the amount of tracer which leaves each gridbox in a time  $dt$ . Figure 3.2b shows the new distribution after this time  $dt$ , using the upwind scheme. The scheme conserves the total mass of tracer.

The slopes scheme of Russell and Lerner extends this by taking into account the gradient of tracer within the up-wind gridbox. After each timestep, new tracer gradients are calculated at each gridbox, according to the amount and gradient of tracer leaving the upwind gridbox. A schematic of the evolution of the distribution in figure 3.2a, as calculated by the slopes scheme, is illustrated in figure 3.2c. The slopes scheme conserves the total tracer gradient (the first order moment of tracer) as well as the total mass of tracer.

The Prather scheme further extends this by taking into account the ‘curve’ of tracer concentration in the up-wind gridbox, as illustrated in figure 3.2d. The scheme, as implemented in TOMCAT, is described in some detail in Chipperfield and Simon (1996). The scheme conserves total tracer mass, and first and second order moments of tracer.

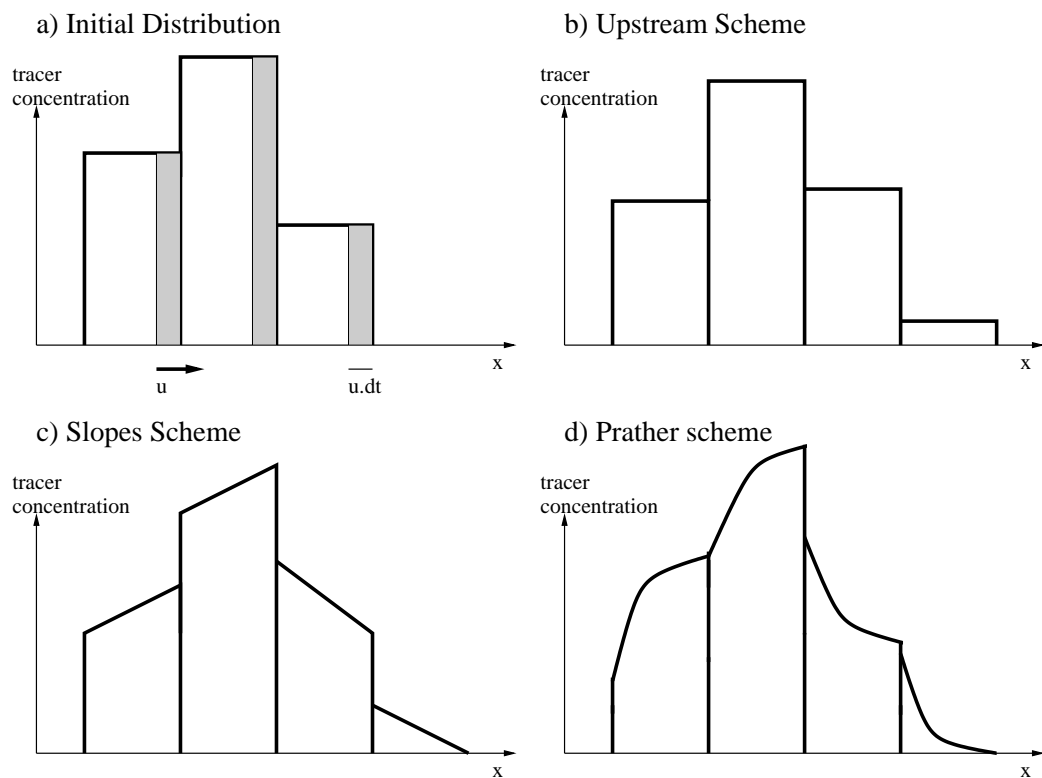


**Figure 3.2:** (a) Initial tracer distribution, in a field of uniform speed,  $u$ . The shaded regions show the amount of tracer which leaves each gridbox in a time  $dt$ . (b),(c) and (d) are schematics of the tracer distribution after time  $dt$ , as calculated by the upstream, slopes and Prather schemes respectively.

Several modifications to the Prather scheme, which are implemented in TOMCAT, have to be made, to enable it to be used in an atmospheric model effectively. Firstly, near the poles, gridboxes become very small in the zonal direction, and so to ensure stability, several gridboxes are joined together and their average properties advected. Also at the poles, the cross-polar flux is calculated explicitly, as in the Prather scheme it would normally be zero, even if the cross-polar wind were non-zero. A spatial leap-frog scheme is employed, so that the timestep for zonal advection is shorter than the timestep for meridional advection. This is because in general the zonal wind is stronger than the meridional wind. Finally, a form of flux limiting may be applied to ensure positivity of tracer concentration (the Prather scheme on its own does not necessarily preserve positive tracer concentrations). This flux limiting adds to the diffusivity of the Prather scheme (Chipperfield and Simon, 1996).

Comparisons have been made between the Prather scheme and other advection schemes. Prather (1986) compares his scheme to the slopes scheme, and finds that it is better at advecting step functions in one dimension. The slopes scheme requires 4 or 5 gridpoints to resolve a step function, whereas the Prather scheme requires only two points to maintain the advecting step. Prather also compares his scheme to several others in a ‘clock’ experiment, in which a cosine function is advected in a rigidly rotating plane. He finds that his scheme has lower diffusion and absolute errors than the other schemes tested. Chipperfield and Nikiforakis (1998) compare the Prather scheme to the weighted-area flux (WAF) scheme (Toro, 1992), which is the scheme used in the Met Office GCM. The WAF scheme can be used with several different flux limiters, the most commonly used in atmosphere models being the Van Leer limiter. They show that the WAF scheme with the Van Leer limiter is more diffusive even than the slopes scheme, and much more diffusive than the Prather scheme.

The downside of using the Prather scheme is that it is relatively expensive in terms of CPU time, and has large memory requirements. Prather finds that his scheme takes 1.5 times longer to run than the slopes scheme, and requires twice as many two-dimensional arrays to be stored. However, it is felt that these problems are outweighed by the increased accuracy of the Prather scheme, as it gives confidence that advection errors in the dust model are at a minimum. The impact on the simulation of the dust cycle, caused by using the slopes scheme as opposed to the default Prather scheme, is investigated in section 4.2.4.

### 3.2.2 TOMCAT simulation of convection: The Tiedke Scheme

Transport of tracer by convection in TOMCAT is described by Stockwell and Chipperfield (1996). The scheme is based on that of Tiedtke (1989). It is a mass-flux scheme which simulates the convective-induced fluxes by explicitly modelling cloud circulations. This makes it a more suitable scheme for use in tracer transport modelling than adjustment schemes, where no fluxes are calculated.

As well as the horizontal wind field,  $\mathbf{u}_H$ , the scheme requires 3-dimensional fields of specific humidity,  $q$  and temperature,  $T$  to be supplied. These may be simulated by a GCM or taken from meteorological analyses.

Initially, the scheme makes a test for convective instability, and the cloud base is found. The scheme then simulates cumulus updraughts and entrainment of environmental air into the cloud and detrainment of cloud air into the environment. The magnitude of these are related to the horizontal convergence of moisture below the cloud, and the difference between cloud and environmental specific humidity at the cloud base. To maintain mass balance, a sub-grid subsidence of environmental air is included.

Stockwell and Chipperfield (1996) have used the convection scheme described above, with ECMWF analysis, to calculate predicted global rainfall, for comparison with observations. They find that the monthly mean fields of predicted precipitation look sensible. Further tests of the convective scheme are described in section 3.2.4.

### 3.2.3 TOMCAT simulation of vertical diffusion: The Louis Scheme

The Louis (1979) vertical diffusion scheme is based on the assumption that the vertical turbulent flux of tracer,  $T_r$ , can be calculated in a similar fashion to the vertical turbulent flux of momentum,  $-\overline{u'w'}$ .  $T_r$  is therefore proportional to the vertical gradient of tracer concentration, the wind shear, and the mixing length. The mixing length is assumed to vary linearly with height, up to a maximum of 500m at the top of the boundary layer.

The Louis scheme has the disadvantage that it does not take into account large eddy transport which can occur even when not all of the boundary layer is statically unstable. Furthermore, the scheme doesn't explicitly model detrainment out of the boundary layer, into the free atmosphere, which occurs

at the top of the boundary layer. Both of these effects lead TOMCAT to under-predict the amount of diffusive mixing in the boundary layer (Stockwell and Chipperfield, 1996).

### 3.2.4 Testing transport in the dust model

In order to investigate the transport of tracer by advection, convection and diffusion, and to test the TOMCAT code, an experiment can be carried out, in which all land points are considered as tracer source regions, and in which the tracer is removed at a rate defined by a characteristic e-folding lifetime, similar to a radioactive gas. This is similar to a simulation of atmospheric Radon, except that in this experiment, ice-covered regions are considered to be sources.

The TOMCAT code is run for a 390 day period, including a 30-day spin-up period, and is forced by wind, humidity, temperature and surface pressure fields, output from the HadAM3 GCM, running under the same present-day boundary conditions as described in section 2.2.1. The resolution of the TOMCAT model is the same as that of the GCM, that is  $3.75^\circ \times 2.5^\circ$ . The land-sea mask which represents the source regions is that of Peltier (1994). This is at a  $1^\circ \times 1^\circ$  resolution, and is used because it is part of a time series of land-sea masks which includes the Last Glacial Maximum, and therefore can be used consistently with the paleo experiments described in chapter 5. This high resolution land sea mask is needed because in later experiments, it is found that using the GCM's land-sea mask, at a  $3.75^\circ \times 2.5^\circ$  resolution, can result in spuriously large dust emissions from certain gridboxes, for example the southern tip of South America, where wind speeds are very strong.

Interpolating the Peltier land-sea mask onto the TOMCAT model grid, results in the land representing a total source area of  $1.46 \times 10^{14} \text{m}^2$ , or 28.7% of the total Earth's surface. At each model timestep (half an hour),  $1 \text{kgm}^{-2}$  of tracer is emitted from land areas into the lowest model level, representing a global emission rate of  $8.14 \times 10^{10} \text{kgs}^{-1}$ . The e-folding lifetime of the tracer is chosen to be 5 days, a possible lifetime of micron-sized atmospheric dust. In steady state, the total atmospheric concentration of tracer,  $M_0$ , is expected to be  $3.52 \times 10^{16} \text{kg}$ . Figure 3.3 shows the resulting timeseries of the total global amount of atmospheric tracer. It shows that the equilibrium mass is as expected, and that the timescale to equilibrate is about a month. It shows that the advection, convection and diffusion schemes are all conserving mass as expected.

Figure 3.4 shows the vertically integrated tracer concentration, for the DJF and JJA seasons. Dust is

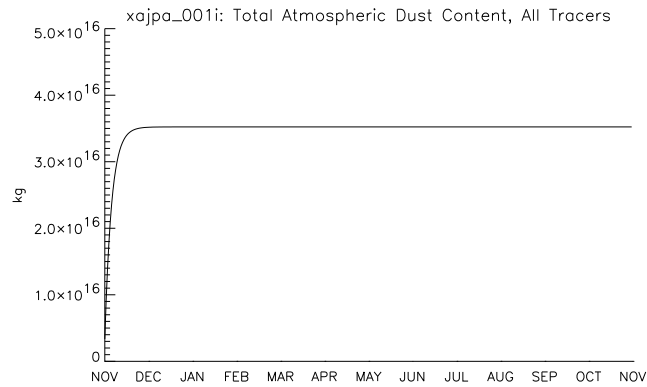


**Figure 3.3:** Timeseries of total atmospheric dust concentration, from the experiment including advection, convection and diffusion, a land-sea mask source, and a 5-day decay.

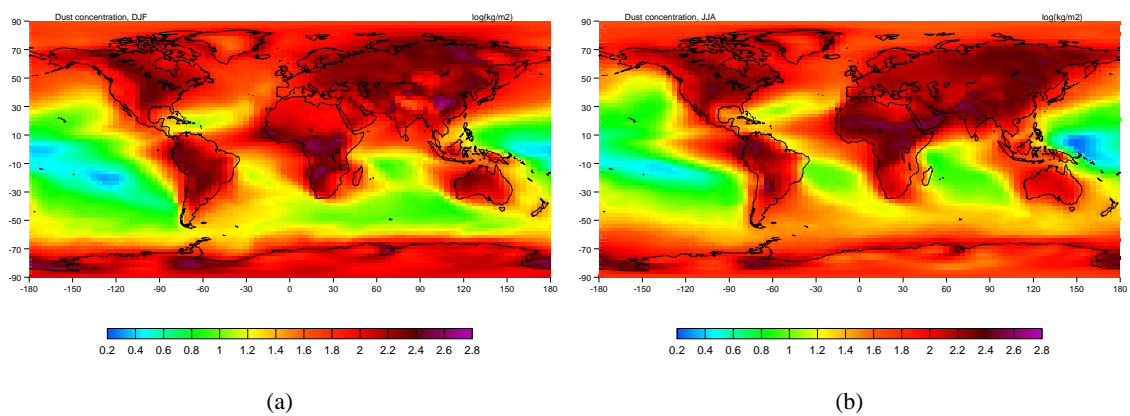


**Figure 3.4:**  $\log_{10}$  of the vertically integrated tracer concentration, in units of  $\text{kgm}^{-2}$ , for the experiment including all land points as sources of tracer, advection, convection and diffusion, and a 5-day e-folding lifetime. (a) is DJF and (b) is JJA.

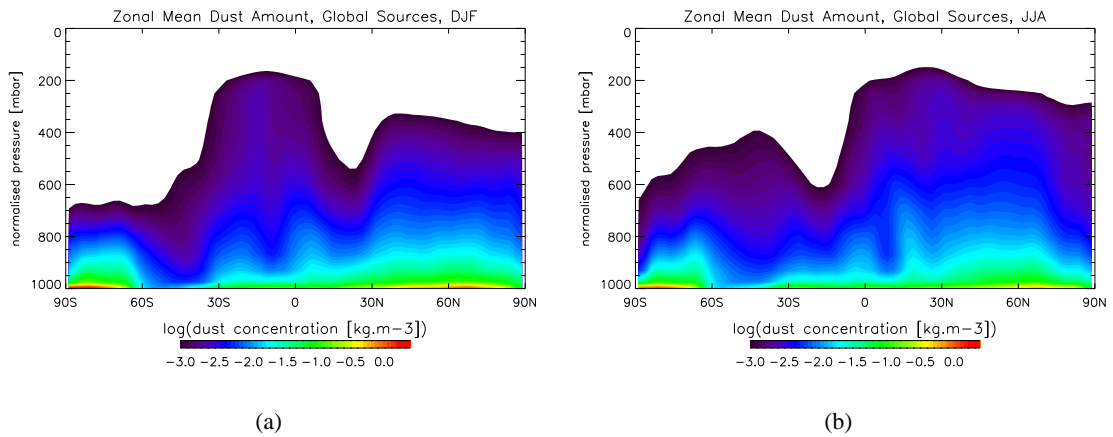


**Figure 3.5:** Logarithm<sub>10</sub> of the zonal mean tracer concentration, in units of  $\text{kgm}^{-3}$ , for the experiment in which all land points are sources of tracer, and advection, convection and diffusion are included. (a) is DJF and (c) is JJA. White areas show a dust concentration less than  $10^{-3}\text{kgm}^{-3}$

seen to be transported from land masses and over oceans. The effects of the tropical easterlies and mid-latitude westerlies are clearly seen, for example transporting tracer westwards from North Africa over the Atlantic, and Eastwards from Patagonia into the Southern Ocean. The tracer is distributed inhomogeneously over the continents, despite the fact that the source is homogeneous; in general, the tracer concentration is a maximum in regions of low level convergence (low pressure), and a minimum in regions of low level divergence (high pressure). Figure 3.5 shows the latitudinal and height distribution of tracer, for the same experiment. The majority of tracer is resident in the lowest model level, but there is significant transport through the lowest kilometre or so of the atmosphere. In the tropics, the maximum in vertical transport occurs when there is a maximum in convective activity, in the summer season. Vertical transport is seen to be a maximum in JJA in the Northern Hemisphere and in DJF in the Southern Hemisphere.

Further to this experiment, in order to investigate the influence of convection and diffusion on the vertical distribution of tracer, three additional experiments are carried out, with the same sources and sinks of tracers, but with different components of the transport in place. In the first of these, only advection is included. In the second, advection and diffusion are included, and in the third, advection and convection.

The factors influencing the vertical distribution of tracer can be seen by examining the differences in vertical distribution between these experiments. The ratio of the zonal mean dust distribution in the advection and diffusion experiment, to that in the advection-only experiment, is shown in figure

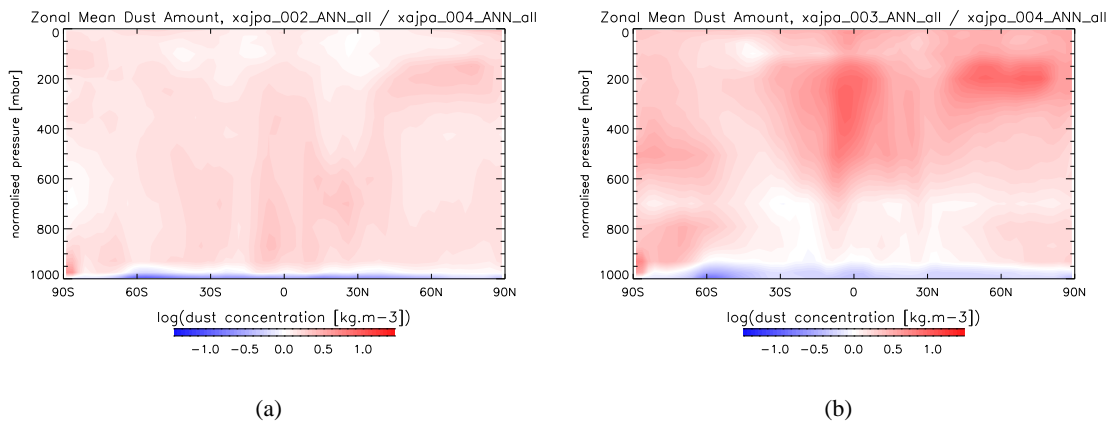


**Figure 3.6:**  $\text{Logarithm}_{10}$  of the ratio of the zonal mean tracer concentration, (a) of the advection and diffusion experiment, to the advection-only experiment, (b) of the advection and convection experiment to the advection-only experiment.

3.6(a). It shows that at the surface, in the lowest model level, there is up to 10 times as much tracer in the run without diffusion compared to the run with diffusion. This tracer is re-distributed throughout the atmosphere, but most of the tracer which is transported from the lowest model level goes to the second model level. Figure 3.6(b) shows a similar plot, of the ratio of the tracer concentration in the advection and convection experiment to the advection-only experiment. The convection is having a larger effect than the diffusion at high altitudes, especially in the tropics. However, comparison of the two figures, shows that in the TOMCAT model, diffusion is much more important than convection for transporting mass in the lower troposphere.

### 3.3 Modelling the Sources of Dust

It is essential when modelling the global dust cycle to correctly simulate the geographical distribution and the relative strengths of dust-source regions. There are several factors which contribute to a region being an effective dust source. There must be little or no vegetation in the region, as the presence of vegetation decreases the wind speed very close to the surface, and acts as a barrier to entrained dust entering the free atmosphere, where it can be advected large distances. The soil must also be relatively dry, as the presence of moisture can suppress entrainment of dust. There must be a plentiful supply of particles of a size which can easily be entrained, which excludes regions which are rocky, as opposed to sandy. Finally, there must be surface winds of a strength sufficient to entrain particles, and to carry them away from the source region.

This source-modelling section describes how these factors have been taken into account in the dust model developed for this thesis.

### 3.3.1 Influences of Vegetation on Source Strength

A representation of global vegetation is a good starting point for a simulation of global dust sources, because areas which are densely vegetated are not strong sources of dust. For this thesis, a method of representing global vegetation is needed which can be applied to both present day and paleo climates consistently.

Datasets have been compiled of present-day global vegetation (eg Wilson and Henderson-Sellers, 1985), but there is no equivalent reliable dataset for paleo vegetation. Therefore, a vegetation *model* is used, which, given various climatic data, predicts a vegetation type, or biome, at each gridbox. The climatic data may be derived from observations, or output from GCMs, constrained by present-day or paleo boundary conditions.

In this section, the vegetation model used in this study, BIOME4, is described. Some results from the model are discussed, and it is shown how they can be used to simulate dust source regions.

#### BIOME4

BIOME4 (Kaplan, 2001) is a global vegetation model developed in the Paleoclimatology and Global Ecology group in the Max Planck Institute, Germany. It supersedes the BIOME3 model (Haxeltine and Prentice, 1996), used to simulate dust sources by Mahowald *et al.* (1999). The main difference between BIOME3 and BIOME4 is a better representation of Arctic ecosystems.

Central to the model are the concepts of Net Primary Productivity and Leaf Area Index. Net Primary Productivity (NPP) is the difference between the total carbon uptake from air through photosynthesis, and carbon loss due to respiration, by living plants. Its units are  $\text{gCm}^{-2}\text{day}^{-1}$ . Leaf Area Index (LAI) is half the total leaf area per  $\text{m}^2$  of ground. Its units are  $\text{m}^2\text{m}^{-2}$ .

The spatially varying inputs to the model are monthly means of surface temperature, precipitation and hours of sunshine, and soil texture and annual minimum surface temperature. A global mean  $\text{CO}_2$

concentration is also input. Output for each gridbox, on a yearly timestep, is one of 27 biome-types (for example desert, or tropical rainforest), LAI and NPP.

On a monthly timestep, the model considers the competition between 7 Plant Functional Types (PFTs), at each gridbox (for example cool grass, or tropical broad-leaved evergreen). The model uses a coupled carbon and water-flux model, forced by climatic data, to calculate a maximum sustainable LAI and NPP for each PFT. The PFT with the highest annual NPP is chosen as representative of the dominant vegetation in the gridbox. A biome is assigned to each gridbox based on the dominant PFT, other PFTs present and other variables such as LAI.

There are several further factors taken into account. For example, some PFTs are eliminated if the absolute minimum temperature is too low, or too high, to simulate their tolerance to extremes in climate. Grasses are eliminated if the soil moisture or precipitation is too high, to simulate the effect of fire and competition for light in determining the dominance of grass-like versus tree-like vegetation. A simple temperature-related algorithm is also used to describe the seasonal growth characteristics (phenologies) of PFTs.

#### **Results from BIOME4**

The primary output from the model is biome-type, however, different vegetation models, and observational datasets of global vegetation, use differing definitions of biomes. This can make a quantitative comparison of model and observations difficult. Haxeltine and Prentice (1996) performed a comparison of a present-day BIOME3 run, at a  $0.5^\circ \times 0.5^\circ$  resolution, with a combination of several vegetation maps. They found a good agreement, and in particular, the BIOME3 model well simulated areas of sparse vegetation and deserts. This gives confidence in the ability of the model to simulate these regions.

In order to simulate present-day vegetation for this study, a control run is carried out. BIOME4 is forced by monthly mean fields of surface temperature, precipitation, hours of sunshine, and absolute minimum temperature, derived from the Leemans and Cramer (1991) dataset, and soil texture from Wilson and Henderson-Sellers (1985). The  $\text{CO}_2$  concentration is set at 340ppmv. The model resolution is  $3.75^\circ \times 2.5^\circ$ .

One way of overcoming the difficulties of validation based on vegetation type is to look at other

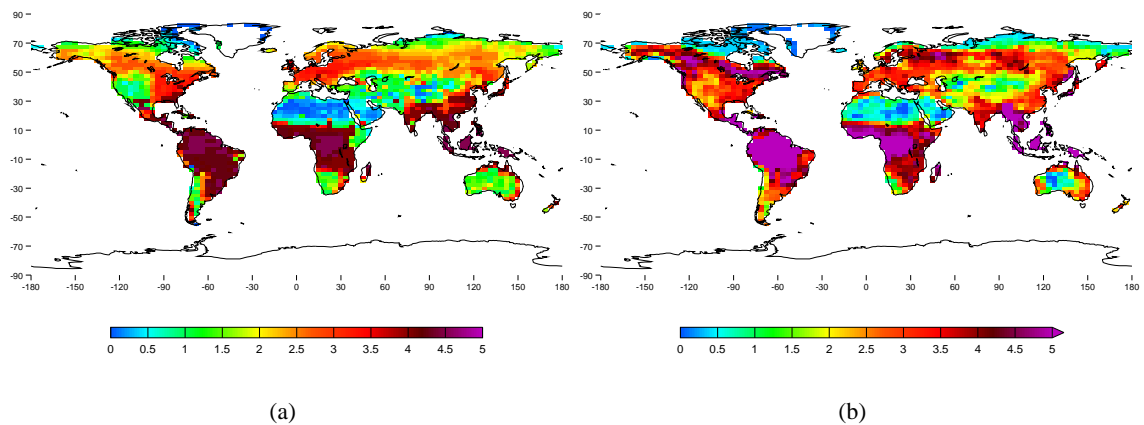


**Figure 3.7:** Leaf Area Index [ $\text{m}^2\text{m}^{-2}$ ]. (a) LAI output from the present-day control BIOME4 run. (b) LAI derived from the Wilson and Henderson-Sellers (1985) land cover dataset.

output from the model. A suitable choice is LAI, because as will be shown, this can be used as an indicator of the potential of a region to be a dust source. The LAI output from the present-day control run of BIOME4 is shown in figure 3.7(a). A comparison can be made between the BIOME4 LAI and the LAI used in the land-surface scheme of the Met Office Unified Model. This is derived from the Wilson and Henderson-Sellers (1985)  $1^\circ \times 1^\circ$  dataset, which is based on data from a large number of atlases, maps and books. The vegetation classes in the Wilson and Henderson-Sellers (WHS) dataset are converted to LAI using a lookup table (Cox *et al.*, 1999), which is then interpolated onto the  $3.75^\circ \times 2.5^\circ$  grid. The resulting LAI is shown in figure 3.7(b). Comparison of actual values of LAI in figure 3.7 is of limited use, as the WHS LAIs depend very strongly on the values in the lookup table used to derive them. However, it is useful to compare the geographical distribution and relative values of LAI, in particular in relation to the areas of low LAI, which are of interest as potential dust-source regions.

In general, the BIOME4 model tends to predict greater LAIs at high latitudes, and lesser LAIs at mid and low latitudes, relative to the WHS-derived LAI. The polar deserts are very similar in WHS and BIOME4. The geographical extent of the Saharan and Arabian areas of low LAI are also very similar in the two datasets. The Australian desert is more expansive, but slightly more vegetated, in the BIOME4 model. The west Asian desert is larger and, relative to north Africa, less vegetated in BIOME4 than in WHS. There is more of a contrast in LAI between the west and east of North America in BIOME4. In South America, there is an area of very low leaf area index in the region of north western Patagonia, which is not seen in WHS.

Despite these differences, there is in general good geographical agreement between the WHS LAI and the BIOME4 LAI. The next section shows how LAI can be used as a measure of the potential a region has to emit dust.

### Using LAI to predict potential dust source regions

It is a reasonable assumption that regions which have a low LAI will be potentially stronger emitters of dust than regions with a large LAI. Potential Dust Source Strength (PDSS),  $S$ , can be defined as the fraction of a gridbox which is able to emit dust, based purely on the vegetation present, and neglecting effects such as soil moisture, wind strength or erodibility of the soil. PDSS can be related to the LAI,  $L$ . A gridbox with a large value of  $L$  is potentially completely covered with leaves, so a definition of PDSS could be simply the fraction of a gridbox which is uncovered, assuming a homogeneous distribution of vegetation throughout the gridbox. However, this neglects the fact that the vegetation is likely to be distributed inhomogeneously over the area of one gridbox. A gridbox with a mid value of  $L$  may consist of a region half the size of the gridbox which is unvegetated, and another region with a large value of  $L$ . To account for this, a maximum LAI,  $L_{max}$ , can be defined as the maximum LAI which will permit a region to be a source. Regions with an LAI less than  $L_{max}$  have a PDSS which varies linearly with LAI. This is in effect parameterising the inhomogeneity of the vegetation. So the PDSS can be written

$$S = \begin{cases} \frac{1}{L_{max}}(L_{max} - L) & \text{if } L < L_{max} \\ 0 & \text{otherwise} \end{cases} \quad (3.2)$$

$L_{max}$  is a tuneable parameter which is expected to be close to 1. After some experimentation, a value of  $L_{max}$  of 1.2 is chosen. Figure 3.8 shows the global PDSS from the present day control run of BIOME4, using this value. It has been interpolated onto the dust model grid, and multiplied by the Peltier land-sea mask from section 3.2.4. It represents the potential of a gridbox to be a dust source, based on the vegetation present alone, and is the first step in the simulation of the global dust cycle. The value of 1.2 for  $L_{max}$  allows for the inhomogeneity of the vegetation, but also ensures that heavily vegetated regions, such as tropical rainforests, are excluded from being sources at all. Furthermore, previous studies have simulated an Australian source comparable in strength to that of the Sahara (eg Tegen and Fung, 1994), which is not in agreement with satellite data. This value of

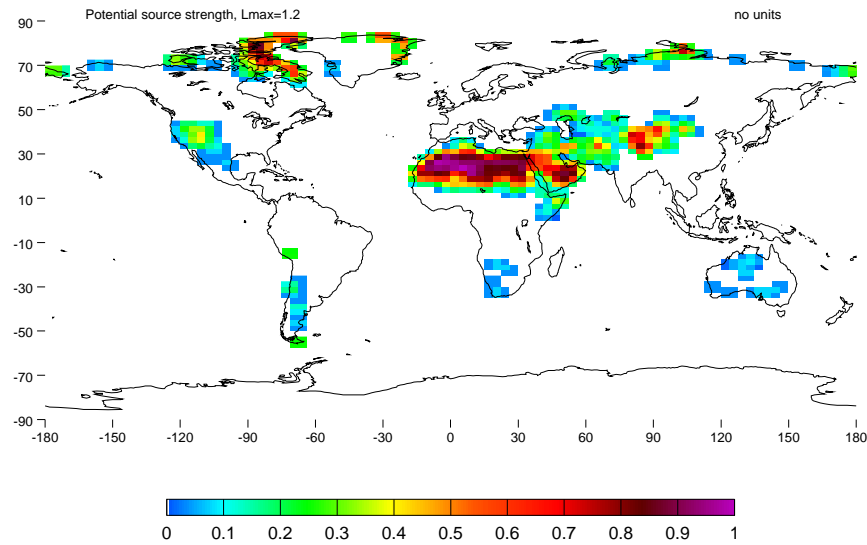


**Figure 3.8:** Potential dust source strength, PDSS, derived from the present-day control BIOME4 run, using equation 3.2, with  $L_{max} = 1.2$

$L_{max}$  results in an Australian source which is significantly less than the Sahara, both in strength and area. The dependence of PDSS on  $L_{max}$  is investigated further in section 4.2.1.

### Testing vegetation effects in the dust model

To illustrate how this definition of potential source strength affects the simulation of the dust cycle, the model is run for a year, with source regions defined as the PDSS shown in figure 3.8. As before, the removal term is a radioactive-type decay, with an e-folding lifetime of 5 days. This experiment is identical to that described in section 3.2.4, except that the source regions are modulated by the presence of vegetation.

The vertically integrated tracer concentration from this experiment is shown in figure 3.9, for the DJF and JJA seasons. This shows that by using PDSS as an indicator of source strength, the distribution of tracer is beginning to look recognisable as a dust distribution. The strongest source is the Sahara, where the PDSS is close to 1. The next strongest sources are those in Arabia and Asia, followed by the North American sources. The Southern Hemisphere sources are relatively weak, and very little dust is transported as far as central Antarctica. There is about 20 times as much dust over the Northern Hemisphere oceans as over the Southern Hemisphere oceans. There is little cross-equatorial transport of dust.

This experiment also sheds light on the seasonality of the transport of dust from source regions. A

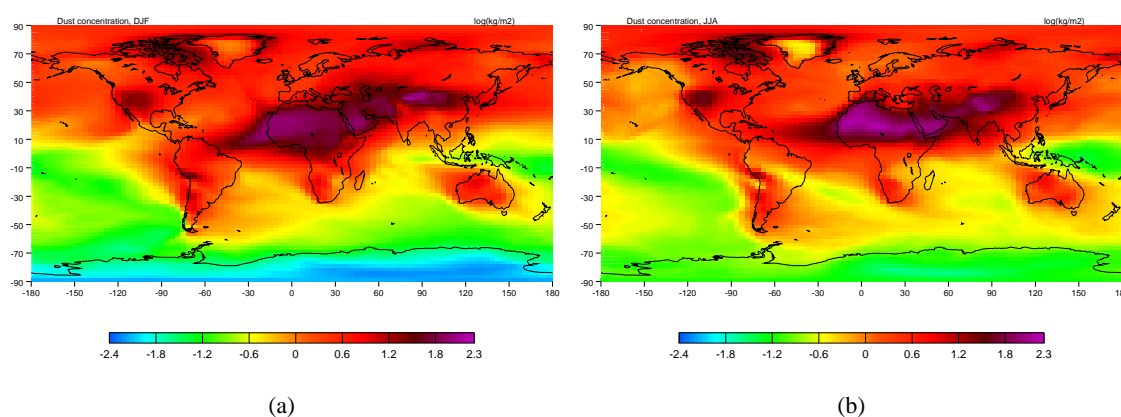


**Figure 3.9:**  $\text{Logarithm}_{10}$  of the vertically integrated tracer concentration, in units of  $\text{kgm}^{-2}$ , for the experiment including vegetation dependent sources, as in figure 3.8, and a 5-day e-folding lifetime. (a) is DJF and (b) is JJA.

particular point to note is that the concentration of dust over Antarctica is at a minimum in DJF (summer) and a maximum in JJA (winter). This seasonality is in agreement with the trajectory analysis carried out in chapter 2, and summarised in figure 2.11. Similarly, the concentration over Greenland is a minimum in summer, and a maximum in winter; also in agreement with the trajectory analysis.

Dust transport from the Sahara, over the Atlantic, displays a strong seasonality, with a shift of the plume from westwards at JJA to south westwards in DJF. This shift of the Saharan dust plume, from the north in summer to further south in winter, is well observed, and results in increased dust concentrations in northern hemisphere summer in the Caribbean (Prospero *et al.*, 1970), and in northern hemisphere winter in South America (Prospero *et al.*, 1981). This experiment shows that this can, at least in part, be explained by the shift in wind regimes, rather than purely a seasonality in the source strength.

Similarly, dust south of Arabia shows a marked seasonality in dust concentration, the maximum being in JJA. Again, this is in agreement with observations (eg Husar *et al.*, 1997).

The region of the North Pacific, where the atmospheric dust is originating mainly from the Asian source, also shows a seasonality, with a minimum in JJA. Observations show a maximum in MAM in this region, implying that this cannot be explained purely by seasonal changes to transport of dust.

Dust concentrations in the Patagonian and Australian regions do not exhibit much seasonality. If there is a seasonality of dust concentration in this region, it would require an experiment running for longer

than a year to observe it.

### 3.3.2 The Particle Size Distribution of Parent Soils

In order to model the sources of atmospheric dust, it is important to have a good representation of the particle size distribution (PSD) of the parent soil from which the dust is derived, of the PSD of the dust entrained into the atmosphere, and of the subsequent evolution of the PSD. This is because the processes by which dust is entrained into the atmosphere are very dependent on particle size, as are the processes which remove dust from the atmosphere, and the radiative properties of dust particles. This section describes how the dust model simulates the particle size distribution of the parent soil.

#### Observations and modelling of particle size distributions

PSDs can be represented by plots of  $\frac{dM}{d(\log r)}$ , equal areas under which represent equal amounts of mass. PSDs can also be represented by frequency plots, where the fraction of the soil within a series of size ranges is shown.

Dust models are able to simulate the size-dependent properties of particles by splitting the continuous PSD into a series of bins, each representing a different particle size-range, and modelling the evolution of each of these bins separately. This is the approach used in this dust model.

Ideally, there would be a large number of bins, each representing a small particle size range. However, due to the high computing cost of simulating many bins, a compromise is made between the accuracy and speed of the model. This model potentially simulates 6 particle sizes, distributed logarithmically, in the range  $3.16 \times 10^{-8} \text{m}$  to  $3.16 \times 10^{-5} \text{m}$ . Figure 3.10 shows a frequency plot of the measured PSD of two soils collected in the United States (Sumner, 1998); overlaid are the ranges of the 6 size bins in the model. The number of bins, and their range, is the same as that used in the Met Office dust model (Woodward, 2001). The figure shows that PSDs can vary a lot over relatively small geographical distances. This highlights the need for high-resolution global information on particle size distributions, for use in this dust model.

It also shows that there can be a significant amount of soil mass which is not captured by the largest bin; however, particles of this size are in general too large to be entrained into the atmosphere by the

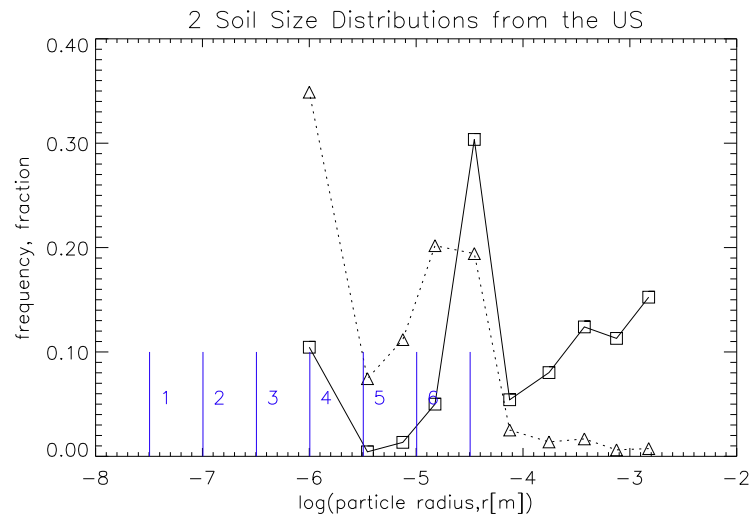


**Figure 3.10:** Frequency plot of the Particle Size Distribution (PSD) from two soils collected in North America (Sumner, 1998). The frequency of particles of radius  $10^{-6}$  m includes the frequency for all particles less than this radius. Overlaid in blue, are the ranges of the 6 size bins in the dust model.

surface wind, and if they are entrained, they soon fall back to earth. The large amount of mass of radius  $10^{-6}$  m is due to the fact that the soil distributions were measured using a series of sieves, and the smallest mesh-size was  $10^{-6}$  m.

Bagnold (1941) found that desert soils often consist of two or more log-normally distributed modes. Since then, there have been attempts to characterise PSDs by assuming a form of the distribution, for example lognormal or skewed-lognormal, and adjusting values for any parameters by comparison with observations (Chatenet *et al.*, 1996). However, these techniques are yet to be applied on a global scale.

There are several global soils datasets available, nearly all of which have been derived from the UNESCO FAO Soil Map of the World (FAO/UNESCO, 1974). This map identifies 106 major soil types, each of which are divided into several horizons - distinct layers of soil with differing properties. In the FAO map, the particle size distribution of each horizon is characterised by the percentage of soil by mass which falls into several size ranges: very coarse sand, coarse sand, medium sand, fine sand, very fine sand, silt and clay. However, the soil datasets derived from the UNESCO map do not retain all this information. For example, the Wilson and Henderson-Sellers (1985) dataset classifies soils as coarse, medium or fine, at a  $1^\circ \times 1^\circ$  resolution. The global dataset which retains most of the soil-size information from the FAO map is that of Webb *et al.* (1991). This gives a percentage of sand, silt and clay at a  $1^\circ \times 1^\circ$  resolution, in up to 15 soil horizons. The size ranges corresponding to the

sand, silt and clay regimes, are shown in figure 3.11. For this dust model, only the uppermost horizon is considered, as this is the one which is directly affected by the wind. This is reasonable because the uppermost level is always at least a couple of centimetres thick, and in general the PSD does not vary greatly with depth.

Clearly, a lot of information about the actual PSD has been lost by characterising soils in this way. In order to estimate the particle size distribution over the complete range of particle sizes, it is necessary to carry out some form of extrapolation from the Webb *et al.* (1991) dataset. In particular, for dust modelling, more information is needed about the size distribution within the clay regime, as it is clay particles which make up the majority of the total mass of dust away from source regions.

Previous dust modelling studies have in general assumed forms of the particle size distribution which vary linearly within the sand, silt and clay regimes (Tegen and Fung, 1994, Woodward, 2001). This can lead to discontinuities in the simulated soil size distribution, or over-prediction of the amount of very fine particles.

In order to get over these problems, a new approach has been devised for use in this dust model. It makes use of the fact that PSDs are generally multi-modal lognormal. It assumes that the distribution is in fact made up of three lognormal modes, relating to the sand, silt and clay soil regimes. The total soil distribution can be therefore be written

$$\frac{dM_{\text{tot}}}{d(\log r)} = \sum_{x=\text{sand,silt,clay}} A_x e^{-\left(\frac{\log\left(\frac{r}{r0_x}\right)}{\sigma_x}\right)^2} \quad (3.3)$$

$r0_x$  are given by the centres of the sand, silt and clay regimes. Small values of the parameters  $\sigma_x$  would lead to three distinct modes which is unrealistic. Large  $\sigma_x$  would lead to a blurring of the three modes, and to an over-simulation of very large and very small particles. Consideration of the above points, and a study of actual PSDs (eg Chatenet *et al.*, 1996), leads to a choice for  $\sigma_x$  of

$$\sigma_{\text{sand}} = \sigma_{\text{silt}} = \sigma_{\text{clay}} = 1.0 \quad (3.4)$$

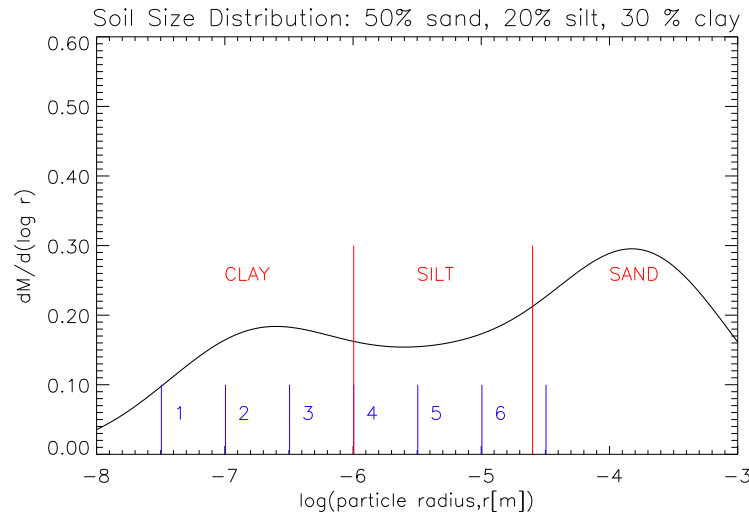


**Figure 3.11:** Assumed Particle Size Distribution (PSD), calculated using equation 3.3, given a soil consisting of 50% sand, 20% silt, and 30% clay. Overlaid in blue, are the ranges of the 6 size bins in the dust model. Overlaid in red, are the ranges of the clay, sand and silt regimes.

$A_x$  can then be calculated such that

$$\int_{r=0}^{r=\infty} \frac{dM_x}{d(\log r)} d(\log r) = \text{fraction of total mass in regime } x. \quad (3.5)$$

Figure 3.11 shows the distribution which is calculated for a soil characterised as consisting of 50% sand, 20% silt and 30% clay. The distribution is continuous, and simulates the decrease in mass of fine-clay sized particles. The disadvantage of this method is that although the relative amount of mass in each of the three modes matches the WRL data, when combined together the relative amounts in the three soil regimes are no longer exactly correct. The distribution in figure 3.11 actually consists of 49% sand, 23% silt and 28% clay. Also, the amount of very large particles is over-simulated compared to observations. However, it is felt that these errors are outweighed by the advantages of having a continuous distribution, and of using a method which is based on observations.

### Testing soil size effects in the dust model

By applying the technique of fitting tri-modal distributions to the WRL dataset, and by integrating the resulting particle size distribution over the ranges corresponding to the separate size bins, the relative amount of mass in each of the 6 size bins in each gridbox is calculated. These distributions, on a  $1^\circ \times 1^\circ$  resolution, are then interpolated onto the model resolution ( $3.75^\circ \times 2.5^\circ$ ). The resulting

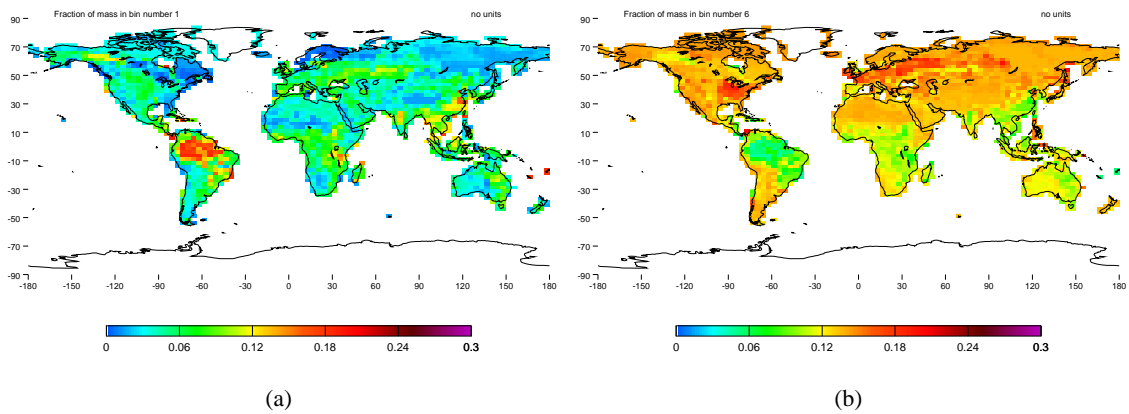


**Figure 3.12:** Fraction of the total mass contributed by (a) the smallest size bin (representing particles of a typical radius of  $5.62 \times 10^{-8}$  m) and (b) the largest size bin (representing particles of a typical radius of  $1.78 \times 10^{-5}$  m).

distributions, for the smallest and largest bins (representing particles of a typical radius of  $5.62 \times 10^{-8}$  m and  $1.78 \times 10^{-5}$  m), are shown in figure 3.12. The bin representing the largest particle size contains the most mass of all the bins, and the figure shows that the amount of mass in this size bin is quite homogeneous. The smallest particle size is distributed more inhomogeneously; the largest amount of the smallest particles occurs in the region of the Amazon. This is due to the high clay content in this region, which probably results from the high soil moisture, which allows a fast rate of chemical weathering of soil particles. Desert regions tend to be dominated by larger particles.

The next in the series of test experiments simulates the evolution of particles in each size bin. The source term for this experiment, is the land-sea mask, multiplied by the vegetation factor (section 3.3.1), multiplied by the fraction of mass in each bin. The same 5-day e-folding lifetime is applied. The results can be summarised by stating that the relative change in dust concentration reflects the relative amounts of mass in each size bin. For example, the concentration of dust in the smallest size bin, is large over Australia, reflecting the relatively fine soils in Eastern Australia. The largest change is a relative decrease in concentration, in all size bins, over north Greenland, due to the fact that the WRL dataset classifies some Greenland land points as ice-covered, which are ice-free in the BIOME4 model.

### 3.3.3 Entrainment of Dust by the Surface Wind

This section explains the theory behind entrainment of dust into the atmosphere, for both wet and dry soils, and goes on to show how this theory is implemented in the dust model.

#### Entrainment of dry soil

Bagnold (1941) made measurements of the wind speed profile during saltation and found that it was significantly altered from the non-saltating case. He assumed that for windspeeds above the threshold, the momentum of the wind is transferred to the saltating particles, which then pass it to the surface. Using these ideas, and dimensional analysis, he suggested that the horizontal flux of particles is proportional to the cube of the wind friction velocity. His results are summarised in section 1.1.1.

This cubic dependence of dust flux on friction velocity has indeed been observed in the field (eg Shao *et al.* (1993)), and more recently, several authors have derived equations relating the horizontal flux of particles to the wind friction velocity, or the wind speed measured at some reference height. Greeley *et al.* (1994) found that of these, the formulation of White (1979) most closely agrees with experimental data.

White suggested that the flux of particles could be calculated by considering an average horizontal pathlength,  $L$ , of saltating particles, and using dimensional analysis. If the vertical speed of the saltating particles is  $W$ , then the pathlength is given by

$$L \simeq \frac{W^2}{g}. \quad (3.6)$$

The total surface shear stress,  $\tau = \rho_a u^{*2}$ , is partitioned between the wind shear stress,  $\tau_{\text{wind}}$  and the stress on the surface due to the saltating particles,  $\tau_{\text{sand}}$ . In order that the particles continue saltating, the wind shear stress must be  $\tau_{\text{wind}} = \rho_a u_t^{*2}$ . Therefore the stress due to the saltating particles is,

$$\tau_{\text{sand}} = \rho(u^{*2} - u_t^{*2}). \quad (3.7)$$

This is also equal to the momentum loss of the saltating particles. If  $U_f$  is their final horizontal

velocity, and  $U_i$  is their initial horizontal velocity, then

$$\tau_{\text{sand}} = M(U_f - U_i) \quad (3.8)$$

where  $M$  is the mass of particles falling per unit area time. Assuming the collisions are inelastic,

$$U_f - U_i = W. \quad (3.9)$$

He also observed experimentally that

$$M \simeq \rho(u^* - u_t^*) \quad (3.10)$$

and derived an estimation for  $W$ :

$$W \simeq u^* + u_t^*. \quad (3.11)$$

This leads to an expression for the mean pathlength:

$$L \simeq \frac{(u^* + u_t^*)^2}{g}. \quad (3.12)$$

The vertically integrated horizontal flux is assumed to be

$$G \simeq ML \quad (3.13)$$

and so this gives for  $G$ ,

$$G = C \frac{\rho}{g} u^{*3} \left(1 + \frac{u_t^*}{u^*}\right) \left(1 - \frac{u_t^{*2}}{u^{*2}}\right). \quad (3.14)$$

The value for the dimensionless constant of proportionality is  $C = 2.61$ , which comes from wind

tunnel experiments.

Many field experiments, and theoretical models, have attempted to predict the dependence of the threshold friction velocity,  $u_t^*$ , on particle size (eg Bagnold, 1941, Chepil, 1945). In general, it is found that there is a particle radius, approximately  $60\mu\text{m}$ , for which the threshold friction velocity is a minimum, in other words, that particles of this size are most easily entrained. Larger particles are attracted strongly to the bed by gravity, and smaller particles by inter-particle cohesion forces. This is illustrated in figure 1.2, which shows a semi-empirical form of  $u_t^*$ , derived by Marticorena and Bergametti (1995).

However, all of these studies have concentrated on beds consisting of monotonic or nearly monotonic particle size distributions. Figure 3.10 shows that real soils cannot necessarily be described in this way. In reality, it may be that collisions with saltating particles in the  $60\mu\text{m}$  range tend to cause smaller clay particles, which would otherwise stay in the bed due to strong cohesion with their neighbours, to be entrained into the air.

In summary, there remains a lot of uncertainties as to the exact nature of the dependence of  $u_t^*$  on the particle size distribution of the parent soil. Therefore, in this dust model, the threshold friction velocity is taken as a constant, and equal to  $0.4\text{ms}^{-1}$ . This value is chosen because it lies close to the minimum threshold in figure 1.2. Using a constant value for the threshold in this way, is saying that there are always some particles in the bed which are in the size range most easily entrained, and that these particles are likely to collide with particles in the bed of all sizes, and to transfer their momentum.

For the purposes of dust modelling, it is the vertical flux of particles which is of interest. This vertical flux is related to the fraction of the horizontal flux which makes the transition from transport by saltation to transport by suspension. Marticorena and Bergametti (1995) suggest that the vertical flux is likely to be proportional to the vertically integrated horizontal flux, for any one particle size. From experimental data, they give values of the constant of proportionality in terms of the clay content of the soil. Soils with a relatively large clay content make the transition from saltation to suspension more easily, and so the constant of proportionality is greater for high clay-content soils. However, they also note that soils with a very high clay content do not fit into this pattern, as these soils are often crusted.

Because of the uncertainties in this area, due to a lack of experimental data, a constant ratio of vertical to horizontal flux is taken for this experiment. The sensitivity of the model results to this approach is discussed in section 4.2.2. The value taken for the ratio of vertically integrated horizontal to vertical flux is a typical value taken from Marticorena and Bergametti (1995), of  $1 \times 10^{-3} \text{m}^{-1}$ . Therefore, the expression for the vertical dust flux is

$$G = 2.61 \times 10^{-3} \text{m}^{-1} \times \frac{\rho}{g} u^{*3} \left(1 + \frac{u_t^*}{u^*}\right) \left(1 - \frac{u_t^{*2}}{u^{*2}}\right). \quad (3.15)$$

### Entrainment of wet soil

The presence of moisture in the soil tends to decrease the rate of entrainment of dust, relative to a dry soil. This is due to the fact that the water increases the interparticle cohesion forces due to its strong surface tension. Early work studying the effects of moisture on entrainment (eg Chepil, 1956) was mainly empirical, and was applicable to only a limited range of particle sizes.

Fecan *et al.* (1999) describe a parameterisation of the effects of moisture which is based on physical principles, and which can be applied to a wide range of particle sizes. It is this parameterisation which is used in this dust model, and which is described in this section. Based on work by McKenna-Neumann and Nickling (1989), which considered the interparticle capillary forces between two grains of realistic shape, it is assumed that the ratio of the wet-soil threshold friction velocity,  $u_{tw}^*$ , to the dry-soil threshold friction velocity,  $u_{td}^*$ , can be written

$$\frac{u_{tw}^*}{u_{td}^*} = \left[1 + \frac{f(\text{soil properties})}{P}\right]^{0.5} \quad (3.16)$$

Where  $P$  is the moisture tension in the soil. By further assuming that the moisture in the soil,  $w$ , is partitioned between moisture which is responsible for the capillary forces,  $w_{\text{capillary}}$ , and moisture which is adsorbed onto the surfaces of particles in the bed,  $w_{\text{adsorbed}}$ , which does not significantly affect entrainment, and using an empirical equation for  $P$ , based on observations, an expression for the ratio of threshold friction velocities is arrived at:

$$\frac{u_{tw}^*}{u_{td}^*} = [1 + A(w - w')^{b'}]^{0.5} \quad (3.17)$$

where  $A$  and  $b'$  are constants to be determined by observations.  $w'$  is representative of the amount of water adsorbed onto the particles in the bed, and decreases with increasing particle size. Comparison with data from the literature, over particle sizes ranging from clay to sand, leads to the semi-empirical expression for the ratio of threshold friction velocities,

$$\frac{u_{tw}^*}{u_{td}^*} = \begin{cases} 1 & \text{for } w < w' \\ [1 + 1.21(w - w')^{0.68}]^{0.5} & \text{for } w > w', \end{cases} \quad (3.18)$$

where

$$w' = 0.0014(\% \text{clay})^2 + 0.17(\% \text{clay}). \quad (3.19)$$

This expression agrees very well with observations of the effect of moisture on entrainment; Fecan *et al.* (1999) find that the relative mean error in using this expression is just 6.8%, and that 83% of observations agree with the expression to within 10%.

This formulation of the effect of moisture on entrainment is a good one for this dust model as the information it requires, that of soil size distribution and volumetric moisture content of the soil, can be obtained from GCMs or global datasets. It is also based on both physical principles and observations. However, it completely neglects the possible effects that a persistent wind may have in drying out the uppermost layer of soil.

In this dust model, even if the moisture is frozen, then equation 3.18 is still used to calculate the effect of moisture, even though it is probably no longer valid. There has been no work on the effect of frozen moisture on the entrainment of dust. It is probable that the presence of ice will cause a decrease in entrainment relative to dry soil, as the ice may form some sort of lattice, binding the particles together.

### **Entrainment in the dust model**

In the dust model, entrainment is calculated at a half hour timestep. Equation 3.15 is used to calculate the entrainment, with  $u_t^*$  replaced by  $u_{tw}^*$  as given by equation 3.18. The friction velocity,  $u^*$ , is calculated from the wind speed at the lowest model level,  $u_1$ . Assuming hydrostatic balance, and

a constant temperature throughout the lowest model layer, the height of the lowest model level in metres,  $z_1$ , is given by

$$z_1 = -\frac{RT_1}{g} \ln \left( \frac{p_1}{p_0} \right), \quad (3.20)$$

where the temperature and pressure at the lowest model level,  $T_1$  and  $p_1$ , and the surface pressure,  $p_0$  are all read in from the GCM or analyses. The friction velocity is then

$$u^* = \frac{\kappa u_1}{\ln \left( \frac{z}{z_0} \right)}, \quad (3.21)$$

where  $\kappa$  is Von Karman's constant, and  $z_0$  is the roughness length. The roughness length is taken as a constant, and equal to 1.68cm. This value is chosen because it is found that when it is applied to the BIOME4 vegetation, it results in a global field of roughness length which is in good agreement with that used by HadAM3, which produces the winds used to force the dust model. Using a constant value for roughness length is consistent with the assumption outlined in section 3.3.1, that all the dust entrainment in a gridbox is taking place in the unvegetated regions of that gridbox. The volumetric soil moisture content,  $w$ , is calculated from the soil moisture content as given by the GCM or analyses, assuming a soil density of  $2650\text{kgm}^{-3}$ .

### Testing entrainment of dry soil in the dust model

In order to illustrate the model's simulation of entrainment of dust, an experiment is carried out, in which entrainment of dust assuming dry soil is included in the model, in the form of equations 3.15 and 3.21. The transport and deposition of dust is the same as in the experiment described in section 3.3.2. Figure 3.13 shows a timeseries of the total atmospheric mass of dust as simulated, for all size bins, over the period of the experiment. A clear seasonality is seen, with the maximum in dust peaking in MAM and JJA. The seasonality arises principally from the wind strength over source regions. By far the strongest source is the Sahara, and the peaks in dust content in figure 3.13 arise from strong wind events which occur in this region.

Figure 3.14(a) shows the vertically integrated dust concentration from this experiment, for the third

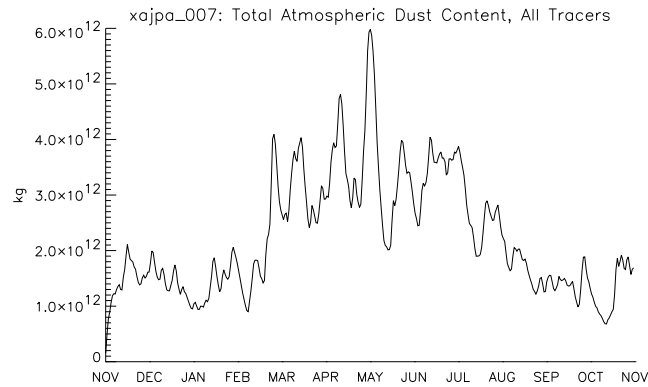


**Figure 3.13:** Timeseries of total atmospheric dust concentration, from the experiment including transport by advection, convection and diffusion, a land-sea mask, vegetation and soil-size source areas, entrainment from equation 3.15, and 5-day decay removal.

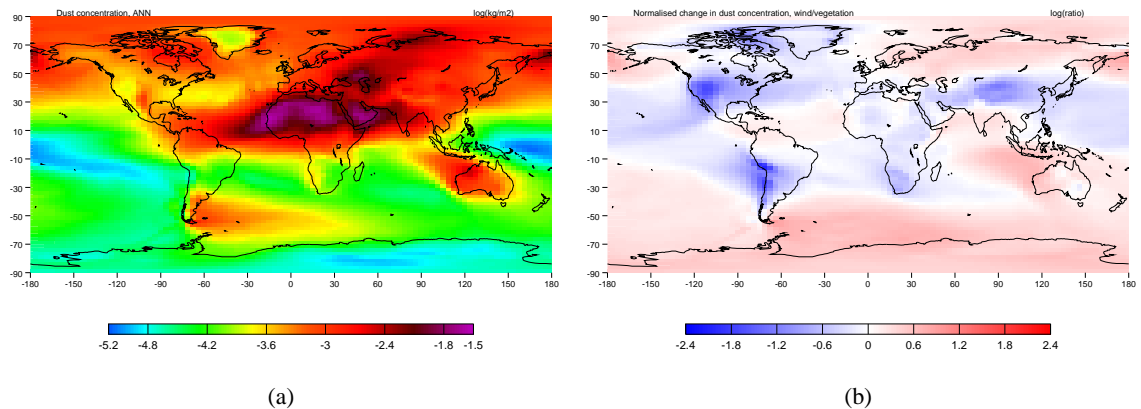


**Figure 3.14:** (a)  $\text{Logarithm}_{10}$  of the annual mean vertically integrated tracer concentration, in units of  $\text{kgm}^{-2}$ , for the experiment including entrainment of dust by the wind, as in equation 3.14, and a 5-day e-folding lifetime. (b)  $\text{Logarithm}_{10}$  of the ratio of the annual mean dust concentration in this experiment, to the previous, with no windspeed dependence. The ratio is normalised so that the mean appears as zero.

size bin, representing particles of a typical radius of  $0.56\mu\text{m}$ , and 3.14(b) shows the ratio between this experiment and the previous one, which did not include the wind-dependent entrainment, normalised so that the mean change appears as zero. The absolute concentration shows that the main Northern Hemisphere sources are the Sahara, Arabia and the desert around the Caspian Sea, and the main Southern Hemisphere sources are Patagonia and Australia. The low winds over southern Africa mean that this region is no longer a strong source of dust.

In HadAM3, the wind strengths over land are greatest over the southernmost tip of Patagonia, and the ratio of concentrations in figure 3.14(b) reflects this fact, with the smallest relative decrease in dust concentration in this region. Western Australia also experiences strong winds in the model. The desert regions of east Asia, North America and Chile are emitting a relatively small amount of dust compared to the previous experiments, because of the low modelled winds in these regions. Section 2.2.1 discusses how accurate the winds in the model are, compared with observational datasets.

The  $u^3$  entrainment parameterisation changes the seasonality of the source regions. The Saharan source has remained similar to that in the previous experiment, apart from a relative decrease in dust production in SON. The southern Saharan plume, which did peak in DJF when only transport was included, now peaks in MAM. However, there still remains a significant amount of dust in DJF, and the seasonality may be clearer in a longer integration. Off the south coast of Arabia, the maximum in dust concentration in JJA is preserved, and enhanced by the inclusion of surface wind effects. In the north Pacific, dust from east Asia is at a maximum in MAM, with a strong peak in December. The Patagonian source is still not displaying any clear seasonality, whereas the Australian source now peaks in SON.

### **Testing entrainment of wet soil in the dust model**

To illustrate the effect of the moisture parameterisation, a further experiment is carried out. The effect of moisture is to raise the threshold friction velocity, as in equation 3.18. The transport and deposition of dust is the same as in the previous experiment described in section 3.3.3. Figure 3.15 shows the vertically integrated dust concentration in this experiment, and the ratio to that in the previous, with no moisture effects.

The largest effect is in Patagonia, where the presence of moisture greatly reduces the dust entrain-

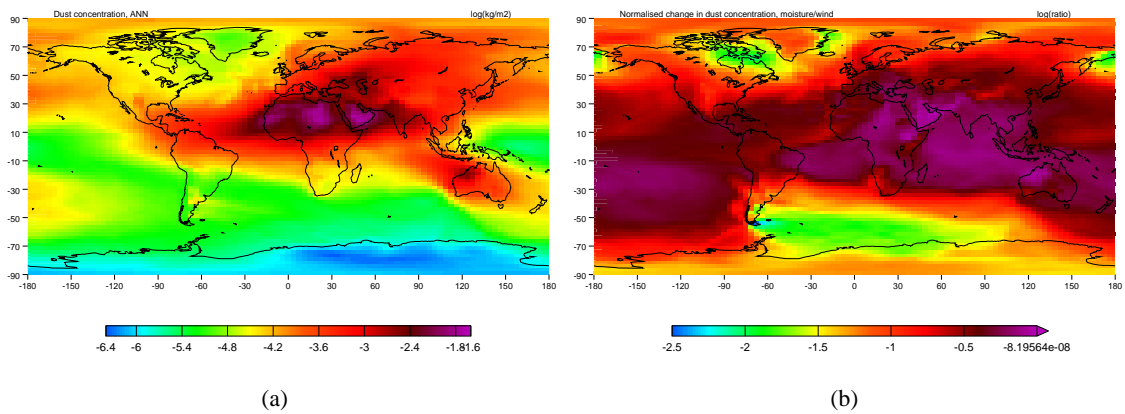


**Figure 3.15:** (a)  $\text{Logarithm}_{10}$  of the annual mean vertically integrated dust concentration, in units of  $\text{kgm}^{-2}$ , for the experiment including moisture effects, as in equation 3.18, and a 5-day e-folding lifetime. (b)  $\text{Logarithm}_{10}$  of the ratio of annual mean dust concentration in this experiment, to the previous, with no moisture effects.

ment. This is particularly true for the southernmost tip of Patagonia, where the presence of moisture decreases the dust concentration by a factor of up to 320. Similarly, in the Northern Hemisphere, sources at high latitudes emit less dust due to the high moisture content of the soil. The Saharan, Arabian and Australian sources aren't greatly effected by the presence of soil moisture.

The moisture is acting to decrease the dust entrainment in Asia in DJF, making the source clearly peak in MAM. There is more variability in the Patagonian and Australian sources, but there seems to be a peak in dust concentration from Patagonia in summer and autumn, and an Australian peak in spring. However, once again, these sites would benefit from further investigation with longer model runs. The other sites are mainly unaffected in their seasonality by the moisture parameterisation, due to their low soil moisture.

The effects of soil moisture in this model are quite significant. However, soil moisture is one of the poorer aspects of GCM simulations, and furthermore, is not well constrained by observations; there are no fully reliable global observed datasets, against which the modelled soil moistures can be validated. In chapter 5, the scheme described and tested above, based on Fecan *et al.* (1999), is replaced by a simpler parameterisation, in which no entrainment occurs if the soil moisture is greater than a threshold value. It is found that this results in a better agreement with observations.

## 3.4 Modelling the Sinks of Dust

Dust in the atmosphere is removed by several processes.

Particles can be scavenged by falling precipitation from above, and can also form nuclei around which condensation develops, eventually causing the dust particle to fall to the surface. These processes are known as wet deposition.

Turbulent motions in the surface layer cause dust particles to come into contact with the surface, where they come to rest. Dust particles also have a downwards component of velocity due to their mass, and if the particle is close to the surface, this will cause the particle to come into contact with the ground, and stick. These processes together are known as dry deposition.

This section describes how wet and dry deposition are parameterised in this dust model.

### 3.4.1 Wet Deposition of Dust

#### Scavenging coefficients

Wet deposition is a term which encompasses many processes, including scavenging by falling rain or snow, and in-cloud scavenging, a process in which a particle forms a cloud-condensation nuclei which grows to form a cloud drop.

In this dust model, in-cloud scavenging is neglected. This is justified because dust particles are not in general hydrophilic, and so are unlikely to be good cloud-condensation nuclei (CCN). Dust particles may become good CCN if they are coated with sulphates (Levin *et al.*, 1996), however the importance of this process is unknown.

The process of scavenging of particles by falling drops is a complicated problem in fluid-dynamics, involving many different parameters. The simplified approach described below is based on a discussion by Seinfeld and Pandis (1998).

The problem can be made clearer by defining a scavenging coefficient,  $\Lambda$ , such that

$$\frac{\partial C}{\partial t} = -\Lambda C \quad (3.22)$$

where  $C$  is the mass concentration of the species being scavenged. In general,  $\Lambda$  is a function of, among other factors, the type and rate of precipitation, and the size distribution of the particles being scavenged. If  $\Lambda$  is assumed to be proportional to the rainfall rate,  $p$ , then another scavenging coefficient can be defined,  $\lambda$ , such that  $\Lambda = p\lambda$ .  $\Lambda$  has units of  $s^{-1}$ , whereas  $\lambda$  has units of  $m^{-1}$  (if precipitation is measured in  $ms^{-1}$ ). In this model, all precipitation is assumed to be rain, due to the lack of data or models available for defining  $\lambda$  for solid precipitation.

To gain an understanding of how one would expect  $\lambda$  to vary with the size of the particles being scavenged, and the size of the scavenging droplets, it is useful to consider a droplet of radius  $R_d$ , falling at a speed  $U_d$ . The droplet sweeps out a volume,  $V$ , equal to  $\pi R_d^2 U_d$ , in unit time. A collision efficiency,  $E$ , can be defined, which is the ratio of the number of actual collisions which take place between the droplet and particles, to the number of particles in the volume  $V$ . By assuming a monotonic raindrop size, the scavenging coefficient can be related to the collision efficiency by

$$\lambda = \frac{3 E}{4 r_p} \quad (3.23)$$

where  $r_p$  is the radius of the raindrop (Seinfeld and Pandis, 1998).

The droplet perturbs the air around it, and modifies the local streamfunction in a way shown in figure 3.16. Particles experience a force which modifies their trajectories and takes them away from the drop. This process decreases the collision efficiency. There are three processes which tend to increase the collision efficiency: Brownian diffusivity, interception and inertial impaction.

The Brownian motion of the particles will bring some of them in contact with the drop. This effect is largest for small particles, which have greater Brownian diffusivity than large particles. Interception occurs when particles whose centre of mass lie outside the volume,  $V$ , come into contact with the droplet anyway, because they have a large enough radius. This process is greatest for large particles. Inertial impaction occurs when particles, due to their inertia, cannot follow the streamlines created by the falling drop. This process is greatest for particles of high mass.

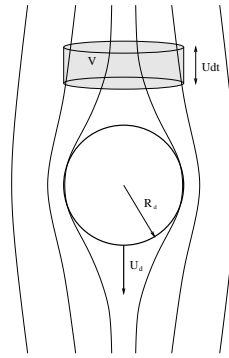


**Figure 3.16:** Schematic showing the modification of streamlines caused by the presence of a droplet of radius  $R_d$ , falling at a speed  $U$ , and the volume,  $V$ , swept out by such a droplet in a time  $dt$ .

There are several empirical expressions for  $E$  and  $\lambda$  in the literature (eg Slinn, 1983), and some observations (eg Volken and Schumann, 1993). In this model, an empirical expression for  $E$  is used, given in appendix A, from Slinn (1983). This empirical expression consists of three terms which are summed to give the collision efficiency. The three terms represent the processes of Brownian diffusion, interception, and inertial impaction. Figure 3.17 shows how they combine to form the collision efficiency. The dotted lines are the diffusion terms, the dashed lines the interception terms, the dot-dash lines the inertial impaction terms, and the solid line the total. It also shows the strong dependence of  $E$  on the droplet radius; the red lines are for a collector droplet of radius 0.1mm, the green lines are for a radius of 0.045mm.

In this dust model, it is assumed that the precipitating drops are monotonic in size. This is because, although in practice, raindrop size varies greatly from location to location, and even within one storm, it would be very difficult to simulate these variations effectively. The dependence of  $\lambda$  on particle size, assuming droplet sizes of 0.1mm(red) and 0.045mm(green), and using the model of Slinn (1983), is shown in figure 3.18 Also shown on this graph are values for scavenging coefficient,  $\lambda$ , as taken from the observational study of Volken and Schumann (1993). It can be seen that the assumption of a small collector droplet size is needed to achieve a good correlation with observations. The small collector droplet also leads to scavenging coefficients which are in good agreement with those used in the Met Office dust model (Woodward, 2001).

It is desirable to use modelled rather than observed values so that scavenging coefficients for particle sizes outside the range of the observations can be calculated sensibly. For each particle size bin, an average value of  $\lambda$  is taken, assuming the small collector droplet radius. This results in values for  $\lambda$  shown in table 3.1. These values are those which are used in the model, and which are used in

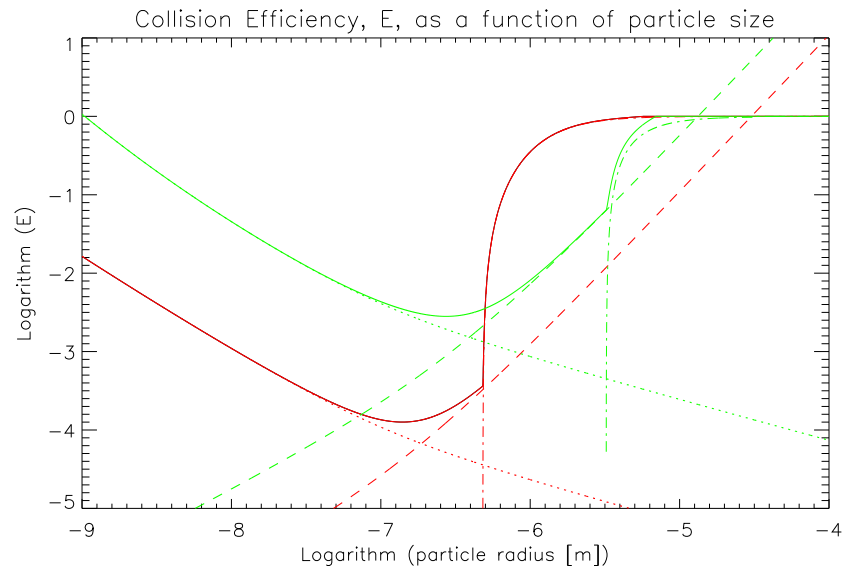


**Figure 3.17:** Solid line is the collision efficiency,  $E$ , as a function of particle size, made up of impaction, diffusion and inertial terms. Dotted line shows the diffusion term, dashed line the interception term and dot-dash line the inertial impaction term. The red lines are for a collector droplet of radius 0.1mm, the green lines are for a radius of 0.045mm. Data calculated using the model of Slinn (1983).

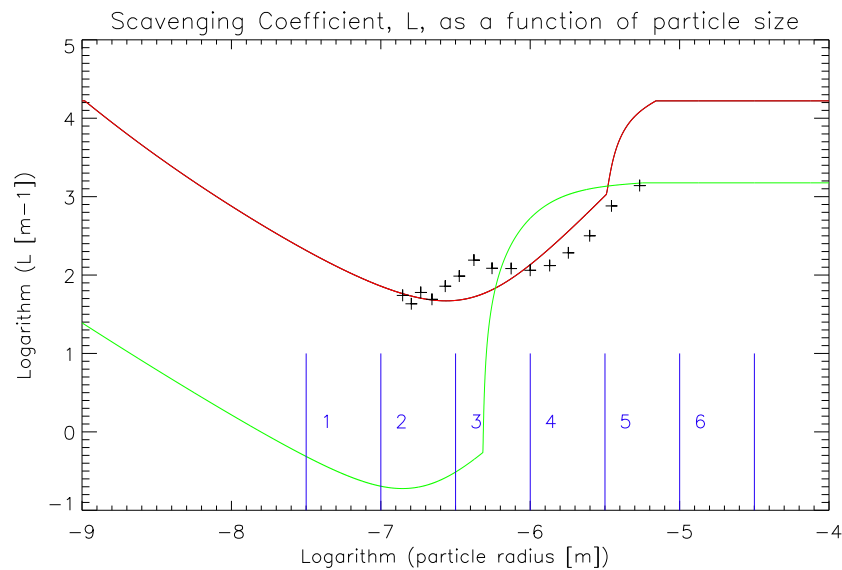


**Figure 3.18:** The scavenging coefficient,  $\lambda$ , as a function of particle size. The green line is for a droplet size of 0.045mm, the red line is for a droplet size of 0.1mm. The crosses show experimental observations of  $\lambda$ , from Volken and Schumann (1993). Overlaid in blue are the ranges of the 6 model size bins.

Size Bin number	1	2	3	4	5	6
representative particle radius ( $\mu\text{m}$ )	0.0562	0.178	0.562	1.78	5.62	17.8
Scavenging Coefficient, $\lambda$ ( $\text{m}^{-1}$ )	120	54	81	580	12000	17000

**Table 3.1:** The scavenging coefficients,  $\lambda$ , used for the 6 model size bins.

the next section, to illustrate the effect of wet deposition. It is clear that the wet deposition will be most efficient for the very large particles, which have enough inertia that they are not affected by the disturbed streamlines caused by the falling droplet, and smallest particles, which can diffuse across the streamlines. Wet deposition will be least efficient for particles in size bin 2, of a typical radius of  $0.18\mu\text{m}$ .

### Vertical structure of precipitation

To complete the parameterisation of wet deposition, an estimation of the rainfall rate,  $p$  is needed. Ideally, a time-varying, three dimensional precipitation field is needed; however, both GCM and ECMWF precipitation data is only of *surface* convective and large-scale precipitation,  $p_0$ . In order to convert these two-dimensional fields into a three dimensional dataset for use in the model, several approximations are made. Use is made of additional data, available from both GCMs and the ECMWF, of the amount of large-scale medium-level cloud,  $A_{med}$ , and large-scale, low-level cloud,  $A_{low}$ . Both these parameters are in units of relative cover, with total cloud cover having a value of 1.

If the precipitation is large scale, then the cloud is divided into an upper and a lower part. The cloud base is at 90% of surface pressure, cloud middle is at about 80% and cloud top is at about 50%. The precipitation varies linearly in the upper part of the cloud, from zero at cloud top, to a value,  $x$ , at cloud middle. The value of  $x$  depends on the medium and low cloud amounts, and is given by

$$x = p_0 \frac{A_{med}}{A_{med} + A_{low}} \quad (3.24)$$

In the bottom part of the cloud, the precipitation varies linearly from the cloud middle value,  $x$  to  $p_0$  at cloud base. This is illustrated in figure 3.19a.

If the precipitation is convective, then cloud base is assumed to be at a pressure which is 90% of surface pressure, and cloud top is assumed to be at the tropopause. The amount of precipitation is assumed to vary linearly from zero at cloud top to the surface value,  $p_0$ , at cloud base. This is illustrated in figure 3.19b.

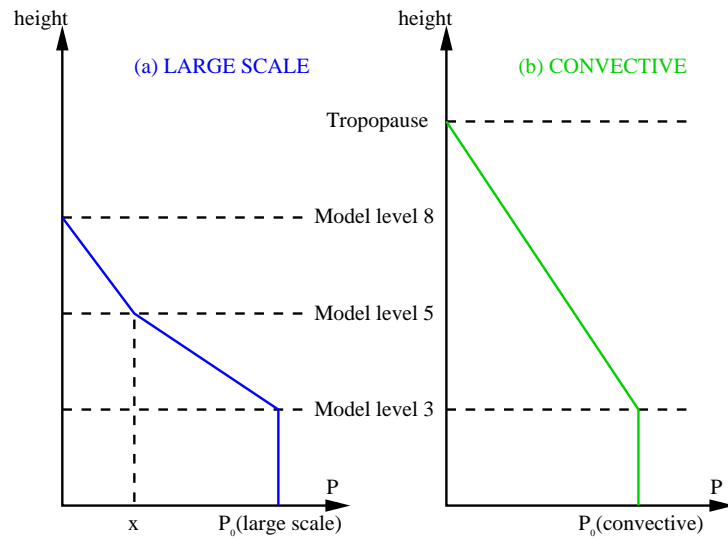


**Figure 3.19:** The assumed profile of precipitation, for (a) large scale and (b) convective precipitation. Model level 3 is at 90% of surface pressure, model level 5 is at about 80% of surface pressure, and model level 8 is at about 50% of surface pressure.

### Testing wet deposition in the dust model

The rate of wet deposition is calculated in this model using a simple forward time scheme, independently for each particle size bin,  $i$ .

$$C_i^{t+\Delta t} = C_i^t e^{-\lambda_i p \Delta t} \quad (3.25)$$

$\lambda_i$  are from table 3.1 and  $p$  is calculated using the assumed vertical distributions of precipitation illustrated in figure 3.19, along with fields of  $p_0$ ,  $A_{med}$  and  $A_{low}$  output from HadAM3 or ECMWF analyses.

To test the model's simulation of wet deposition, a similar run to that described in section 3.3.3, and illustrated in figure 3.15, is carried out; the only difference being that the wet deposition scheme is included, in place of the radioactive decay-type removal. The total amount of tracer for the largest size bin, and the 3rd size bin, and the difference between the concentration of dust in the 3rd bin size in this experiment and that of the previous experiment, is shown in figure 3.20. There are several points to be noted from this experiment. Firstly, there is more dust in this experiment than in the experiment with a 5 day lifetime of dust. This experiment has identical sources to the previous one, and so the differences are due to an increase in the effective lifetime of the dust. The only region where

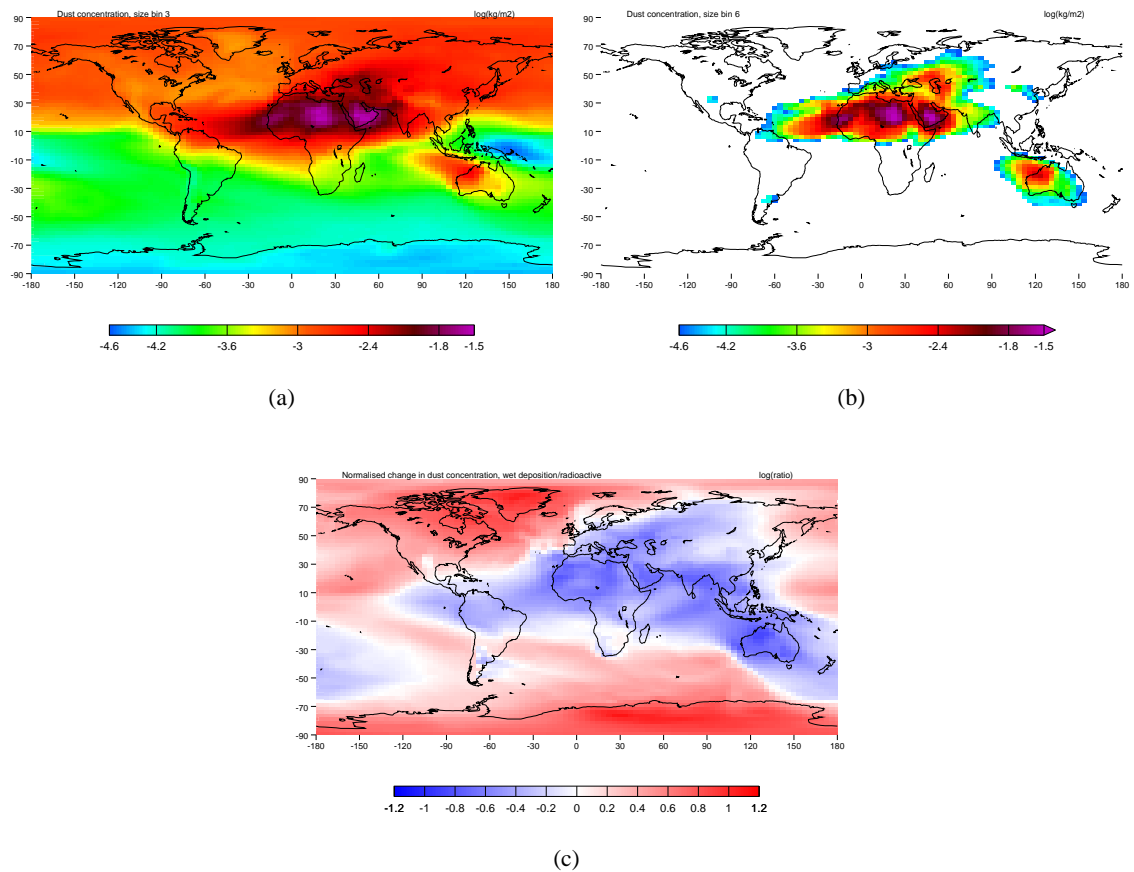


**Figure 3.20:** (a)  $\text{Logarithm}_{10}$  of the annual mean vertically integrated tracer concentration, in units of  $\text{kgm}^{-2}$ , for the experiment including wet deposition, for size bin 3, (b) for size bin 6. (c)  $\text{Logarithm}_{10}$  of the ratio of the annual mean dust concentration of size bin 3 in this experiment, to the previous, with a 5-day e-folding lifetime. The ratio is normalised so that the mean appears as zero.

there is less dust in this experiment is in South East Asia, in JJA. This is due to the intense monsoon rainfall in this region at this time. The largest increases in dust concentration occur over regions with very little precipitation, and in regions remote from the dust sources, in particular Antarctica and the Arctic. There is not a large relative increase in dust over desert regions, which also receive little precipitation, but in terms of absolute amount, these regions have the greatest increase in dust. The seasonality of dust concentration is mostly unchanged, except that the Patagonian source now shows a clear maximum in SON.

There is much less dust in the largest three size bins than in the smallest size bins, and the large dust particles do not travel as far as the smaller ones. This is a marked change from the previous experiment, where the largest bin size accounted for the majority of the dust. This change is due to the fact that the scavenging coefficient is very dependent on particle size (see table 3.1).

In the vertical, the largest relative increase is in the stratosphere, where there is no simulated precipitation, but has very little dust anyway. The largest absolute increase in dust is at the surface.

The timeseries of total atmospheric dust in this experiment displays peaks which are not as sharp as those in the previous experiment. This is again a manifestation of the larger effective lifetime of dust. It is no longer obvious that the total dust amount has reached equilibrium by the end of the first month of integration. However, annual and seasonal means are still calculated by neglecting only the first month.

### 3.4.2 Dry Deposition of Dust

#### Sedimentation

A dust particle, in the absence of any other force, will be accelerated towards the ground under the action of gravity. The atmosphere, however, is a viscous medium and so applies a retarding force to the falling particle. This force, called the Stokes force, is proportional to the speed of the falling particle. A balance between the force of gravity and the Stokes force leads to an expression for the terminal sedimentation velocity of a dust particle,  $v_s$ , of

$$v_s = \frac{2 r_p^2 \rho_p g C_s}{9 \mu_a}, \quad (3.26)$$

where  $\mu_a$  is the air viscosity, and  $C_s$  is the Cunningham slip correction factor, which accounts for the relatively large mean free path of air at high altitudes and for small particles (Seinfeld and Pandis, 1998). The sedimentation velocity scales with the square of the particle radius, so larger particles fall out of the atmosphere more quickly than smaller ones.

The sedimentation velocity is implemented in this dust model, in all levels except for the lowest level (where it is combined with the turbulent deposition velocity, as described in the next section). This process can be quite diffusive, especially when used on the HadAM3 grid, with only 19 vertical model levels. However, the velocities considered are relatively small, especially for the smallest particle sizes, and vertical transport by convection and diffusion is a more important process for determining the vertical structure of all but the largest particle size bins.

### Dry deposition

Dry deposition at the surface can be characterised by considering a deposition velocity,  $v_d(z)$ , which relates the downwards flux of particles towards the surface,  $F(z)$ , to the particle concentration,  $C(z)$ . At a reference height,  $z_0$ ,

$$F(z_0) = v_d(z_0)C(z_0). \quad (3.27)$$

The deposition velocity is equal to the sum of the Stokes settling velocity,  $v_s$ , and a turbulent deposition velocity,  $v_t$

The dry deposition parameterisation scheme used in this dust model calculates  $v_t$  and  $v_s$  in terms of meteorological variables, such as  $\mathbf{u}$  and the roughness length,  $r_0$ . The calculation of  $v_s$  is described in the previous section. The calculation of  $v_t$  and  $v_d$  is based on the resistance analogue model of Seinfeld and Pandis (1998), in which turbulent deposition is viewed as two separate processes; the transport of particles by diffusion through the surface layer, and transport by Brownian motion through the quasi-laminar sub-layer, very close to the surface. The fact that both these processes are driven by the gradient in particle concentration throughout the layers, leads to an analogue with electricity, in which potential differences are replaced by concentration gradients, currents by particle fluxes and conductances by deposition velocities. The details of the parameterisation are given in

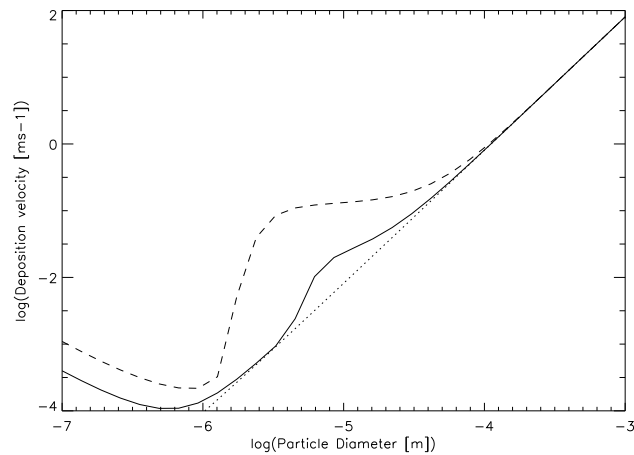


**Figure 3.21:** The deposition velocity,  $v_d$ , as a function of particle diameter, assuming a windspeed at 10m of  $5\text{ms}^{-1}$ , and roughness lengths of 0.0187m (solid line) and 0.1m (dashed line), from the model of Seinfeld and Pandis (1998). Also shown is the Stokes sedimentation velocity (dotted line).

appendix B.

The resistance of the surface-layer is the vertically integrated reciprocal of the eddy diffusivity of the atmosphere, and is particle size independent. It scales with the inverse of the friction velocity, and so is largest over smooth surfaces, or for low windspeeds.

The resistance of the sub-layer is dependent on particle size. For particles smaller than about  $1\mu\text{m}$ , it scales with the Schmidt number, which is the ratio of the kinematic viscosity of the air to the molecular diffusivity of the particle (a measure of its Brownian motion). Particles of radius less than  $0.01\mu\text{m}$ , experience very little resistance due to their large Brownian motion. For particles larger than about  $1\mu\text{m}$ , the resistance is also very small, as these particles have an inertia large enough that they are not affected by abrupt changes in air motion near the surface.

Combining the resistances, and the sedimentation velocity, leads to an expression for the deposition velocity, which is implemented in the dust model in the lowest model level, in the same way as the sedimentation velocity is implemented in other levels. The deposition velocity,  $v_d$ , is illustrated in figure 3.21, as a function of particle size, and for two different roughness lengths. This shows that for dry deposition, as for wet deposition, there is a minimum deposition velocity for particles of diameter  $\sim 1\mu\text{m}$ . The deposition of larger particles is dominated by their sedimentation velocity, due to their large radius. Smaller particles are transported efficiently through the quasi-laminar sub-layer, by their Brownian motion. It also shows the dependence of the deposition velocity on roughness length,  $z_0$ ,

indicating that deposition increases over regions of high roughness length.

### **Testing dry deposition in the dust model**

In an experiment including the source terms, and dry deposition as the only removal term, it is found that for all but the largest particle size, the dust content has not reached equilibrium over the course of the 13 month integration. This is due to the extremely long lifetime of small particles with respect to dry deposition.

Therefore, the dust model is run for a year, with both wet and dry deposition included. Other than this, the same parameters as those described in section 3.4.1 are used. The results show that dry deposition is having a much larger effect on large particles than small ones. This is unsurprising, as large particles have a greater settling velocity. The total effect of dry deposition on the smallest three size bins is very small. For the large particle sizes, the effect can reduce the dust concentration by many orders of magnitude, especially away from the source regions, but these particle sizes already represent a small fraction of the total mass of dust. It is expected that the relative importance of dry and wet removal of the largest particles will be dependent on the order in which the removal terms in the dust model are calculated; at present, the dry deposition is calculated before the wet deposition.

## **3.5 Further Improvements to the Dust Model**

In addition to the components of the dust model which have been described in the previous sections of this chapter, there are some additional parameterisations which can be added. These account for the effect of gusts, and snow cover, on the dust cycle. The following sections describe how these have been included in the model, and the effects which they have.

### **3.5.1 Gusts**

The effect of surface gusts can be important for the entrainment of dust. Gusts are strong wind events which cannot be resolved by a GCM model, because of their short duration, or small spatial extent. Surface gusts are normally associated either with strong convection and precipitation, or with an

unstable boundary layer. Downdraughts, associated with convection, spread out when they approach the surface, converting their vertical velocity into horizontal velocity, leading to gusts. Similarly, an unstable boundary layer leads to the generation of eddies, which bring fast moving air at high levels down to the surface. The next sections describe a parameterisation of gustiness, and the effect this has on the entrainment of dust in the model.

### A gust parameterisation

As described above, the gusts in this model are divided into two types; convective gusts and eddy gusts, which lead to gust speeds,  $u_{conv}$ , and  $u_{eddy}$ , respectively. The total wind speed,  $u$ , is then (Jabouille *et al.*, 1996)

$$u^2 = \bar{u}^2 + u_{conv}^2 + u_{eddy}^2, \quad (3.28)$$

where  $\bar{u}$  is the wind speed as simulated by the GCM.

Redelsperger *et al.* (2000) used observations of gustiness and convective precipitation, over two 1-week periods, to obtain a relationship between surface precipitation,  $p_0$ , and  $u_{conv}$ ;

$$u_{conv} = \ln(1.0 + 6.69p_0 - 0.476p_0^2) \quad (3.29)$$

$p_0$  is in units of  $\text{cmday}^{-1}$ , and  $u_{conv}$  is in  $\text{ms}^{-1}$ . This approach is similar to that of Slingo *et al.* (1994), who found that adding a wind speed of  $3\text{ms}^{-1}$  to gridpoints with precipitating convection improved the tropical circulation in the UGAMP climate model.

Heating of the surface in the day results in a strong heat flux between the surface and the atmosphere above, which is associated with a buoyancy. A buoyancy flux,  $F_{\theta_v}$ , can be defined at the surface as

$$F_{\theta_v} = \overline{w'\theta'_v} \quad (3.30)$$

where  $\theta_v$  is the virtual temperature. Dimensional analysis (Stull, 1988) leads to a vertical velocity

scale,  $w_*$ , associated with the surface heat flux, of

$$w_* = \left[ \frac{g}{\theta_v} Z (\overline{w'\theta'_v}) \right]^{\frac{1}{3}} \quad (3.31)$$

where  $Z$  is the depth of the boundary layer. It is found that this length scale works well, with the magnitude of the vertical velocity fluctuations in thermals being of the same order as  $w_*$  (Stull, 1988).

In a numerical model study, Deardorff (1970), found  $u_{eddy}$  to be proportional to  $w_*$ , via a constant of proportionality,  $\beta$ ;

$$u_{eddy} = \beta w_* \quad (3.32)$$

There have been many studies carried out with the aim of estimating  $\beta$ ; recently, based on an observational case study, Redelsperger *et al.* (2000) estimated  $\beta$  to be 0.65.

### Testing gusts in the dust model

In this dust model, the above parameterisations for the effect of gusts are used. Equation 3.29 is used to calculate  $u_{conv}$ , with  $p_0$  being read in from the GCM or observational analyses.  $u_{eddy}$  is only calculated (from equations 3.31 and 3.32) when the dust model is forced by the GCM, as only then are there values for the height of the boundary layer and the heat fluxes at a short enough timestep. The two components of the gusts are combined with the mean wind in quadrature, as in equation 3.28.

This parameterisation is added to the dust model, and the model run for a year as before. The changes due to gusts are very small in this case. This is due to the fact that the gust speeds,  $u_{gust}$  and  $u_{conv}$  are small compared to the magnitude of the GCM wind speed. The fact that the gusts are added in quadrature to the mean wind speed, means that they have a smaller effect than if they were added linearly. Over source regions,  $u_{eddy}$  is in general greater in magnitude than  $u_{conv}$ , due to the fact that the modelled convective precipitation in these regions is very small.

Despite its relatively small effect, the gust parameterisation is included in future runs, due to its potentially larger effect with different thresholds, and at different time periods. No other dust model

in the literature includes any parameterisation of gusts; the approach used here is a first step towards a more complete treatment of sub-gridscale and sub-timescale processes.

### 3.5.2 Effect of snow cover

#### A snow cover parameterisation

The presence of snow on the ground will clearly reduce the amount of dust which can be entrained into the atmosphere. This effect is also likely to be highly seasonal. This effect is therefore included in the dust model. It seems reasonable that the ability of a region to emit dust should be inversely proportional to the amount of snow which is present, below some threshold value. This can be expressed in a similar way to the dependence of source strength on leaf area index, as follows;

$$f_{snow} = \begin{cases} \frac{S_{thresh}-S}{S_{thresh}} & \text{if } S < S_{thresh} \\ 0 & \text{otherwise,} \end{cases} \quad (3.33)$$

where  $f_{snow}$  is a factor by which the source strength should be multiplied,  $S$  is the snow amount (in  $\text{kgm}^{-2}$ ), and  $S_{thresh}$  is the threshold snow amount.

#### Testing snow cover in the dust model

The snow amount,  $S$ , as predicted by HadAM3, is extremely large over ice sheets, with (somewhat arbitrary) typical values of  $50,000\text{kgm}^{-2}$  over central Antarctica. These regions are already excluded from being source regions due the ice sheet underneath the snow. However, there is snow cover over non ice-sheet regions in winter, for example Alaska has a typical snow cover of about  $50\text{kgm}^{-2}$  in winter. In the absence of any literature on the subject,  $S_{thresh}$  in equation 3.33 is chosen to be  $20\text{kgm}^{-2}$ , equating to a water equivalent thickness of 20mm. This is in the middle of the range of snow thicknesses simulated in the model, outside of ice-sheet regions.

Including this effect in the model results in only a small change to the annual mean dust concentration. The effect is largest in northern hemisphere high latitudes in winter. The seasonal mean DJF concentration change due to the effect of snow cover, is shown in figure 3.22.

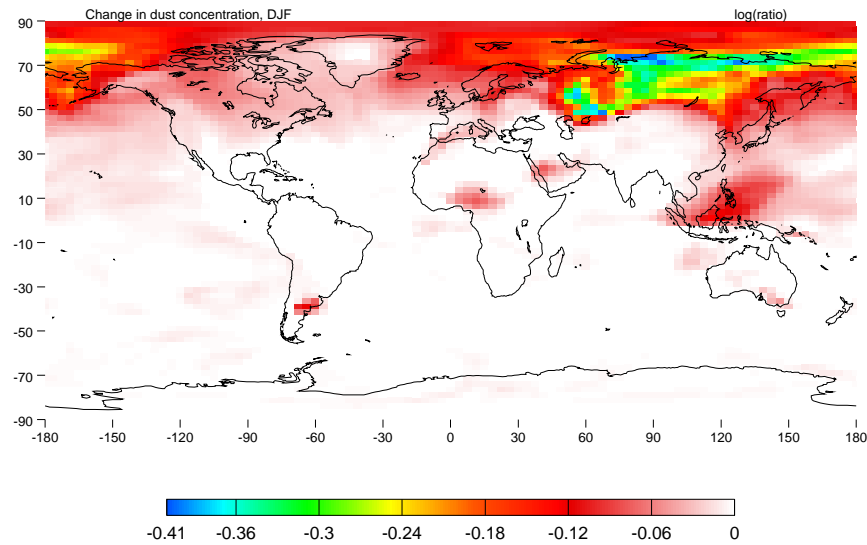


**Figure 3.22:**  $\log_{10}$  of the ratio of annual mean vertically integrated dust concentration in the snow cover experiment, to the previous, without snow effects.

This shows a decrease in dust concentration in the region of Siberia in northern hemisphere winter. There is not a large effect in Canada, another region in which there is substantial snow cover. The overall effect is very small on a global scale, however, it is likely that it could be more significant at the LGM, and so is included in subsequent model integrations.

### 3.6 Summary of results from one-year integration

Sections 3.2 to 3.5.2 describe the evolution of the dust model, from an initial form in which all land surfaces are considered sources, up to the final form, which includes complex parameterisations of the sources and sinks of dust. The final model, as described in section 3.5.2, is the control against which subsequent sensitivity experiments are tested.

The sensitivity of the model results to various parameters, the results from two case studies of dust storm events, and the results from a 10 year integration of the dust model for the present day, are discussed more thoroughly in chapter 4. However, due to the expensive nature of the model runs, these experiments are all carried out with simplified versions of the model, which either simulate one size bin, or combine bins together, as an approximation to the total dust amount.

Here, the results from a one year integration of the model, including all size bins, are summarised. There is only brief discussion of the results; a more complete discussion, and comparison with de-

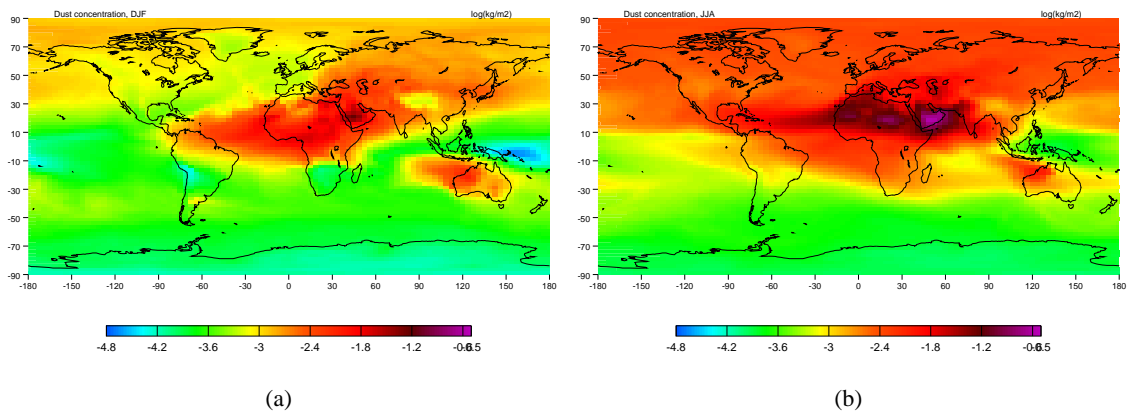


**Figure 3.23:**  $\text{Logarithm}_{10}$  of the vertically integrated tracer concentration, in units of  $\text{kgm}^{-2}$ , for the experiment including all particle size bins, and all parameterisations. (a) is for DJF, (b) is for JJA.

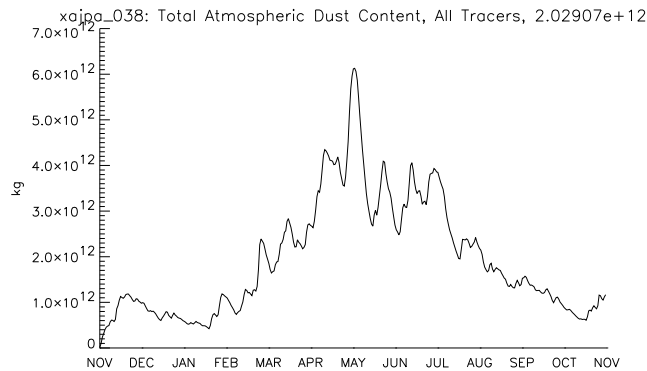


**Figure 3.24:** Timeseries of total atmospheric dust concentration, for the experiment including all size bins, and all parameterisations.

position data and ground-based concentration observations, is applied to the ten-year integration, in section 4.4.2.

The vertically integrated dust concentration, for the DJF and JJA seasons, are shown in figure 3.23. The region in which there is the highest concentration of dust in the atmosphere is Arabia in JJA. The central Saharan region also has a high concentration. More minor sources are the western Sahara, the Aral region, Australia and Central Asia. The regions of lowest concentration are over Antarctica, Greenland, and the tropical Pacific. Dust concentration peaks in the summer in both hemispheres, however, the Asian source emits most dust in MAM. The timeseries of total dust content is shown in figure 3.24. It is similar to the timeseries shown in figure 3.13, which included wind effects only, showing that wind processes are dominating the temporal variability of the atmospheric dust loading. The main differences are that some of the maxima in March and April have been reduced, due to soil

Size Bin number	1	2	3	4	5	6
representative particle radius ( $\mu\text{m}$ )	0.0562	0.178	0.562	1.78	5.62	17.8
Mean atmospheric mass ( $\times 10^{11}\text{kg}$ )	3.2	8.4	7.3	1.3	0.19	0.070

**Table 3.2:** The mean amount of mass in each of the 6 model size bins, during a one-year integration of the model, including all parameterisations.

moisture effects. The timeseries is also slightly smoother, due to the longer lifetime of dust than in the 5-day removal experiment.

The mean relative amount of dust in each size bin is shown in table 3.2. This shows that the size bin which accounts for the majority of the mass is the second, which represents particles of a typical radius of about  $0.2\mu\text{m}$ . The third size bin,  $0.6\mu\text{m}$ , also contributes a similar amount of mass. Compared to most other dust models (eg Woodward, 2001), the modal radius is quite small; typically, models tend to predict mass distributions centred on  $1\mu\text{m}$ . This discrepancy is almost certainly due to the fact that the threshold friction velocity in this dust model is independent of particle size. This was done to take account for the ejection of very small particles by larger, saltating particles. Other models have used threshold velocities which depend on particle size, usually using data from wind tunnel experiments using monotonic sand beds.

### 3.7 Conclusions

This chapter has charted the development of a dust cycle model, including a series of experiments, displaying the effects of the numerous parameterisations which come together to form the dust model. The model has been developed in such a way that it can be applied consistently to a number of different scenarios, including past, present and future climates, as well as real dust events. Emphasis has been, where possible, on founding the parameterisations on physically based schemes, or on observations. However, in many cases, model parameters have been very ill-constrained by data, and values have been chosen based on scant observations. Therefore, it is essential that the sensitivities of the model be tested. This is carried out in the first part of the next chapter. Another essential part of testing a model, is comparing the results to observations, and this is carried out in the second part of the next chapter. In the final work chapter, the model is applied to the problem of dust at the Last Glacial Maximum.

---

## CHAPTER 4

### Modelling the Present Day Dust Cycle

#### 4.1 Introduction

In the previous chapter, the development of a dust model was described, and results from the model were discussed at all stages of the development. Results from the final model were also presented; this final version was tuned to a small extent to agree with some observations, but included many variables which were very poorly constrained by observations.

In this chapter, the model is tested in a variety of ways, and is also used as a tool for understanding the dust cycle at the present day. The testing of the model falls into three parts.

Firstly, the sensitivity of the model to a wide range of variables and parameterisations is tested. This is carried out in the framework of four studies, which examine variables related to vegetation, entrainment, deposition, and advection and resolution.

Secondly, the model is used to recreate two major dust storms from the last ten years, and the results are compared to observations, in the form of satellite data.

Thirdly, the model is run for an extended period of ten years, plus a one year spin-up period, all runs up to this point being for 13 months only. This is to examine interannual variability in the model, as satellite data indicates this to be high (Herman *et al.*, 1997, Husar *et al.*, 1997). The results from this ten year run are compared to observational data of surface dust concentration and deposition. An understanding of the results is gained from an analysis of the strength of the various source regions in the model.

## 4.2 Sensitivity Studies

It is an important part of the development of any model, that its sensitivity to a variety of variables is tested. This is especially important for a dust cycle model, in which many variables are ill-constrained by observations.

Therefore, this section presents a suite of four sensitivity studies, testing the model's response to changes in parameterisations and resolution. The four studies focus on the effects of changing vegetation, entrainment, deposition, and advection and resolution. Each study examines the effects of changing several variables, chosen because they are those likely to have the largest effect on the dust cycle.

The control experiment for all the studies, is the third size bin, representing particles of a typical radius of  $0.6\mu\text{m}$ , from the 6-bin experiment discussed in section 3.6. Results are in general presented as differences from, or ratios of, the control. At the end of each study, there is a brief summary of the results from that study.

### 4.2.1 Vegetation Sensitivity Study

The potential source regions in the control experiment are related to the leaf area index (LAI), output from the vegetation model, BIOME4, forced by observed present day climate. As described in section 3.3.1, this LAI is translated into a potential source strength by defining a maximum LAI,  $L_{max}$ , which can be considered a source region.

The sensitivity of the model results to the definition of the potential source regions is tested. As well as changing the value of  $L_{max}$ , a different climate is used to force BIOME4, a different vegetation model, TRIFFID, is used to calculate the field of LAI, and the LAI is derived from the observational dataset of Wilson and Henderson-Sellers (1985). The vegetation study concludes with a summary of the results.

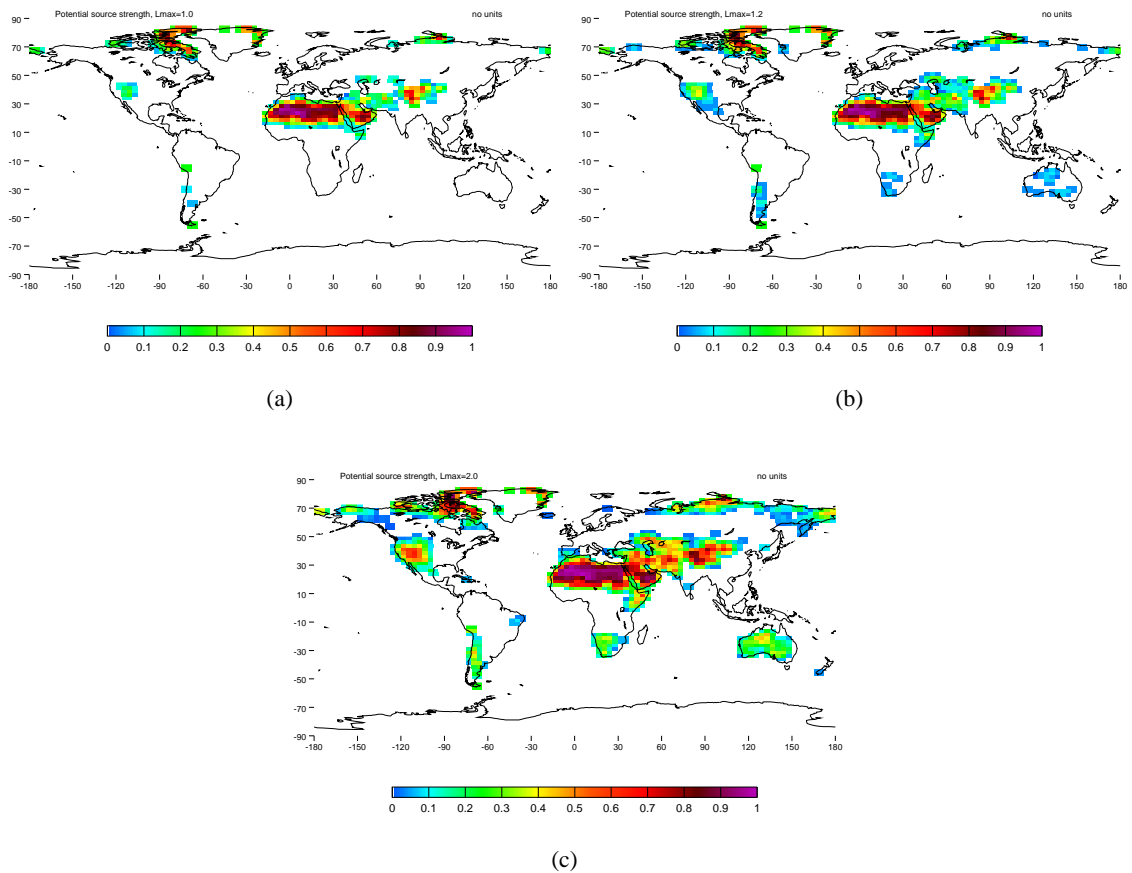


**Figure 4.1:** Potential Source Strengths, derived from BIOME4 Leaf Area Indices, using values of  $L_{max}$  of (a) 1.0, (b) 1.2 (the control) and (c) 2.0.

### Value of $L_{max}$

As described in section 3.3.1, the control experiment has a value for  $L_{max}$  of 1.2, because it is found that this gives a similar looking field of Potential Source Strength (PSS) compared to previous modelling studies, and predicts an Australian source which is not too strong compared to the Saharan source. This section investigates the dependency of PSS on different values of  $L_{max}$ , and the resulting changes in global dust concentration. Figure 4.1 shows the PSS as derived using values for  $L_{max}$  of 1.0 (figure 4.1(a)), 1.2 (the control, figure 4.1(b)) and 2.0 (figure 4.1(c)).

In all regions, PSS increases as the value of  $L_{max}$  increases. There are increases in the value of PSS in gridboxes, as well as an increase in the total area of non-zero PSS. The greatest sensitivity of PSS to  $L_{max}$  occurs in regions where the leaf area index is close to the original threshold. These areas include North America, Patagonia, South Africa, Australia, South-West Asia and Siberia. In particular, note that the Australian and South African sources are completely removed when  $L_{max} =$

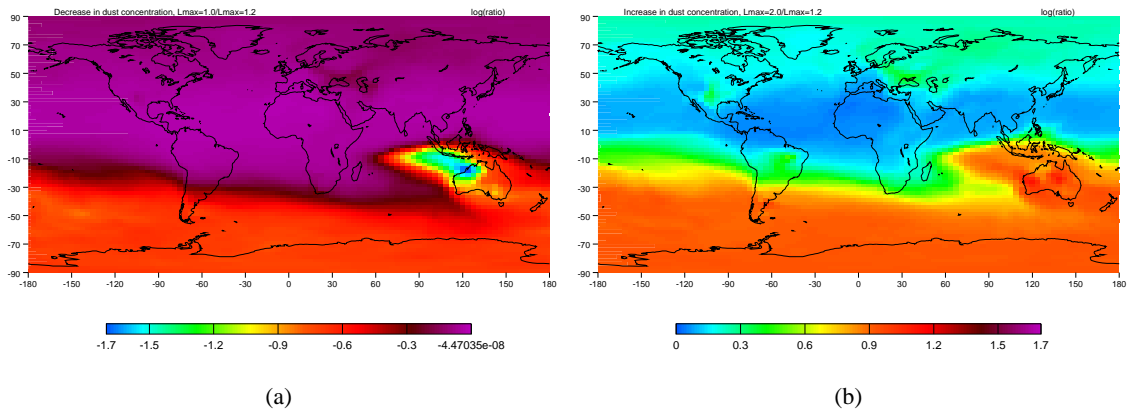


**Figure 4.2:** (a)  $\text{Logarithm}_{10}$  of the ratio of the annual mean vertically integrated dust concentration in the experiment with  $L_{max} = 1.0$ , to the control, with  $L_{max} = 1.2$ . (b) for the experiment with  $L_{max} = 2.0$ .

1.0. However, the regions of the Sahara, Arabia, northern Canada and Greenland, and central Asia, are very insensitive to changes in  $L_{max}$ .

The dust concentrations which result from using these differing fields of PSS, are shown in figure 4.2. The concentrations of dust resulting from using  $L_{max} = 1.0$  (figure 4.2(a)) and  $L_{max} = 2.0$  (figure 4.2(b)) are shown expressed as a ratio of the dust concentration using  $L_{max} = 1.2$  (the control experiment).

Decreasing  $L_{max}$  to 1.0 decreases the global dust content by 13%. Increasing  $L_{max}$  to 2.0 increases the global dust content by 58%. The largest relative effect of changing the value of  $L_{max}$  is in the region of Australia, with associated changes over the Southern Ocean and Antarctica, both for an increase and decrease in  $L_{max}$  from the control. The dust concentration over Antarctica increases by up to a factor of 10 when  $L_{max} = 2.0$ , and decreases by up to a factor of 10 when  $L_{max} = 1.0$ . In terms of absolute value, the largest change is in Australia for both cases, and there are also significant changes in the region of Arabia and around the Caspian and Aral Sea.

### Forcing of BIOME4

In the control experiment, BIOME4 is forced by observed climate from Leemans and Cramer (1991); but there are many other legitimate climatologies which could be used. In order to understand the sensitivity of the dust model to the climate used to force BIOME4, an experiment is carried out in

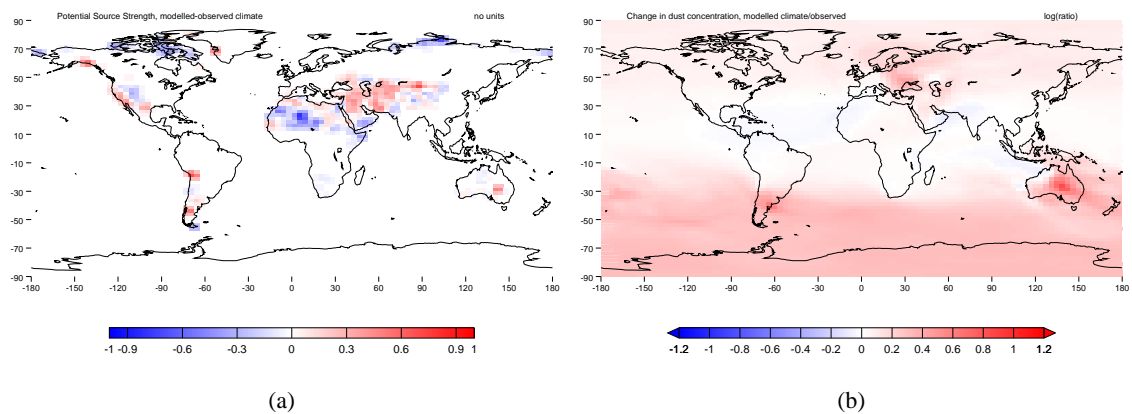


**Figure 4.3:** (a) Potential source strength, modelled-climate forcing of BIOME4 - observed-climate forcing of BIOME4 (the control). (b)  $\log_{10}$  of the ratio of the vertically integrated annual mean dust concentration, in the modelled-climate forcing of BIOME4, to that of the control, with observed-climate.

which BIOME4 is forced by *modelled* climate fields, as predicted by HadAM3, the same model used to force the dust model. The difference in PSS between this perturbed run and the control run, is shown in figure 4.3(a), and the resulting differences in annual mean dust concentration are shown in figure 4.3(b)

Forcing BIOME4 with modelled rather than observed climate, causes an increase in the global dust concentration of 11%. The biggest changes in PSS in the perturbed run are a large increase in south-eastern Australia, Patagonia, western Asia, Arabia and North America. There are decreases in PSS in the central Sahara and northern hemisphere high latitudes. These changes can be related to discrepancies between the observed climatology, and that produced by HadAM3. For example, the Sahel and southern Saharan regions are too wet in HadAM3 compared to observations (P. J. Valdes, University of Reading, *pers. comm.*, 2001).

In terms of fractional changes in dust concentration, figure 4.3(b) shows that the largest increases in dust concentration come from Australia and Patagonia. These increases occur primarily in DJF and MAM, and cause an increase in dust loading over Antarctica in this season. In the Northern Hemisphere, the largest fractional change occurs north of the Black Sea, in JJA and SON. This region is not a source at all in the control run. In terms of absolute changes in dust concentration, the northern Arabian region shows the largest global increase in dust concentration; there are also large increases in the central Sahara. The largest absolute decrease in dust concentration is in southern Arabia, showing that there can be very different effects over relatively short spatial scales. Despite

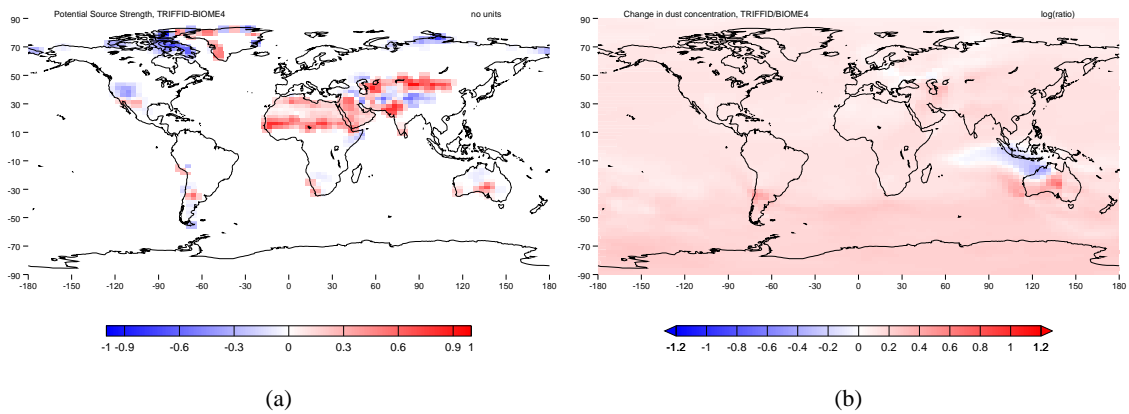


**Figure 4.4:** (a) Potential source strength; predicted by TRIFFID - predicted by BIOME4 (the control). (b)  $\text{Logarithm}_{10}$  of the ratio of the vertically integrated dust concentration in the TRIFFID experiment, to that of the control.

the decrease in source region in the central Sahara, there is an increase in dust in this region, resulting from the increased source region upwind in the eastern Sahara and northern Arabia.

### LAI from TRIFFID

There are many vegetation models which exist and which could be used in a study such as this. It is important to test the dust model's sensitivity to PSSs which have been derived from vegetation models other than BIOME4. One such model is TRIFFID, which is the Met Office's vegetation model (Cox *et al.*, 2000). It is fundamentally different from BIOME4 in that it runs interactively within a GCM, feeding back on the climate, so that the vegetation changes seasonally and interannually, in response to, and causing, short and long-term fluctuations in climate. In this study, for comparison with BIOME4, the annual mean of a 50 year integration is used, in which the climate model is constrained by SSTs from present day observations. All boundary conditions are identical to that used in the control. TRIFFID has been extensively tested, and, like BIOME4, produces an acceptable simulation of natural vegetation, albeit within the large uncertainties in observed biomes and LAI.

TRIFFID, like BIOME4, has LAI as one of its prognostic variables. This field of LAI is used to predict source areas in the same way as the BIOME4 field of LAI is used, with the same threshold of  $L_{max} = 1.2$ . The field of Potential Source Strength, as predicted by TRIFFID, is shown in figure 4.4(a). The resulting change in dust concentration is shown in figure 4.4(b)

The source regions have in general increased in magnitude, but decreased in area. TRIFFID tends to produce fields of LAI which are more intensive, but less extensive than BIOME4. Therefore, the source regions have increased in the centre, but decreased on the margins. For example, the Central Asian source has increased in intensity, but just south of this, in the Himalayas, there has been a decrease in source strength. An exception to this is the Sahara, which has the same extent in both TRIFFID and BIOME4.

The biggest signal in dust concentration is a global increase in dust concentration of 33%. This is due mainly to the increase in PSS in Arabia, and also due to smaller increases in Central Sahara and around the Caspian Sea. In terms of relative dust production, the biggest change is an increase in concentration over Southern Australia which occurs in DJF, and the largest decrease is over Northern Australia in JJA, which again emphasises how local these vegetation change effects can be. The small decreases in Eastern Europe originate from the decrease in source area around the Caspian Sea. However, all the changes are relatively small, compared to those in the experiment carried out by varying  $L_{max}$ .

### **LAI from WHS**

Another change to the vegetation which can be made is to use a field of LAI which is based on observations, rather than model output. A sensible dataset of LAI to use is that used in the forcing GCM itself, HadAM3. This is derived from the Wilson and Henderson-Sellers (1985) (WHS) vegetation dataset, via a lookup table (Cox *et al.*, 1999). This is the most consistent approach to modelling the dust cycle for the present day, but cannot be applied to other time periods, due to the lack of observational data. Moreover, the WHS represents present day vegetation, including any anthropogenic land-use changes. The vegetation models do not simulate any such changes, and hence simulate natural vegetation. In addition, it must be noted that the values in the lookup table to convert biomes to LAI are not fully objective, and so the differences between WHS LAI and the previous models are difficult to interpret. The Potential Source Strength, derived from LAI from the WHS dataset, compared to that of the control, is shown in figure 4.5(a), and figure 4.5(b) shows the resulting change in dust concentration.

The WHS dataset results in lower strength source areas in the Sahara, Asia, Arabia, Patagonia and North America, and higher strengths in Australia and Northern Hemisphere high latitudes. The total

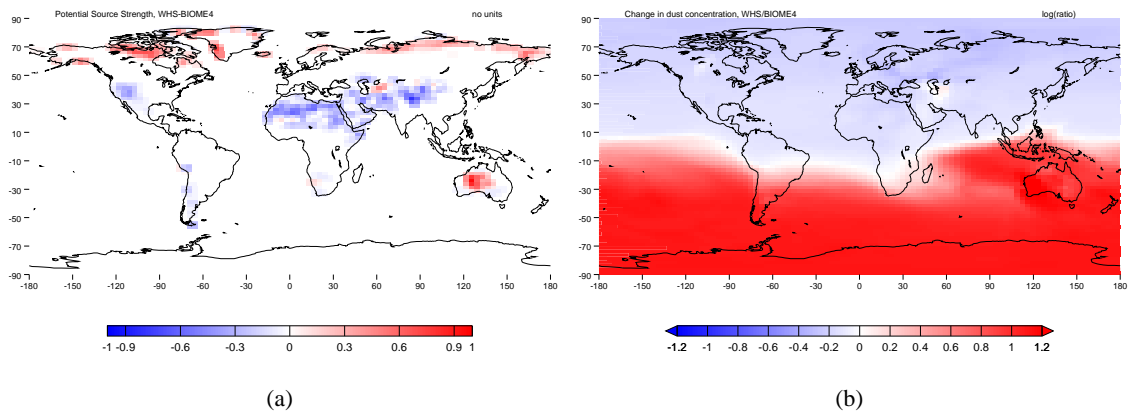


**Figure 4.5:** (a) Potential source strength, WHS - BIOME4 (the control). (b)  $\log_{10}$  of the ratio of the dust concentration in the WHS experiment, to that of the control.

atmospheric dust content is increased by 17%, which is due to the increase in source strength in Western Australia, especially in DJF. In the Northern Hemisphere, the changes are much smaller, the largest decrease in dust concentration being in Central Sahara in MAM. The increase in source strength over Australia causes an increase in dust concentration over Antarctica and the Southern Ocean of at least a factor of 10.

### Conclusions from vegetation study

This vegetation study shows that the global patterns of dust concentration are very sensitive to the way in which potential source strength is defined, and to the vegetation fields used to predict LAI. The Australian region is particularly sensitive to these changes, due to the large spatial variability in vegetation type in this region, and the fact that typical LAIs in this region are close to the control value of  $L_{max} = 1.2$ .

However, the total global dust amount varies relatively little in these studies, the largest change being an increase of 33% when using the TRIFFID model. This is because the Saharan and Arabian regions, which produce the majority of the global dust, are quite insensitive to these vegetation changes; all models and observations agree that the Sahara and Arabia are strong dust sources. There is a greater uncertainty for the Patagonian and Australian source regions; this is potentially an important issue for modelling the correct provenance of Antarctic ice-core dust data.

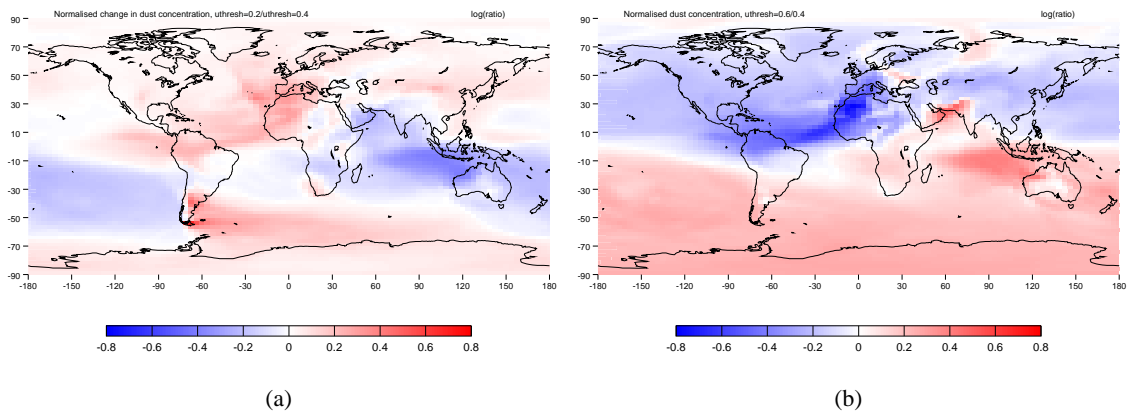


**Figure 4.6:**  $\log_{10}$  of the ratio of the vertically integrated annual mean dust concentration, in the experiment with (a)  $u_t^* = 0.2\text{ms}^{-1}$  to that with  $u_t^* = 0.4\text{ms}^{-1}$  (the control), and (b)  $u_t^* = 0.6\text{ms}^{-1}$  to the control. The ratios are normalised so that the mean change is represented by zero.

## 4.2.2 Entrainment Study

This study of entrainment investigates the sensitivity of the model results to the way in which dust flux is parameterised in the dust model. The variables investigated are the threshold friction velocity, the roughness length, the precise dependence of dust flux on windspeed, the ratio of vertical to horizontal flux, the definition of gustiness, and the way in which snow cover affects entrainment. As in the last section, results are presented in the form of perturbations from the control experiment, described in section 3.6.

### Threshold friction velocity

The threshold friction velocity for particle entrainment,  $u_t^*$ , which appears in equation 3.14 for the horizontal dust flux, represents a windspeed below which there can be no entrainment of dust. In the control experiment,  $u_t^* = 0.4\text{ms}^{-1}$ , a value chosen, as explained in section 3.3.3, to represent the fact that easily entrained large particles can transfer their momentum to smaller particles, which otherwise would be harder to entrain. In this study,  $u_t^*$  is varied from its control value to values of  $0.2\text{ms}^{-1}$  and  $0.6\text{ms}^{-1}$ . The resulting dust concentrations, expressed as ratios between the perturbation runs and the control runs, are shown in figure 4.6.

As expected, the run with a lower threshold results in more atmospheric dust, and the run with a higher

threshold results in less atmospheric dust. The changes are a factor of 7 increase, and 19 decrease, respectively. In the case of a lower threshold, the greatest relative increases are in the western Sahara and Patagonia, with a smaller increase in Asia. The largest relative decreases in dust concentration are over Australia. In terms of absolute increases, by far the biggest change is in the Sahara and Arabia. The spatial pattern of dust changes results from an interaction between the decrease in threshold, and the moisture parameterisation. Without moisture, the biggest relative changes would be in regions where the surface windspeed is of the order of the dry threshold, for example in the north east Saharan region. With moisture effects included, those regions affected most are where the surface windspeed is of the order of the wet threshold, an example being Patagonia.

In the case of a higher threshold, the largest decreases occur in the Northern Hemisphere, with the biggest change in the western Sahara in DJF. The increase in threshold greatly reduces the wintertime dust entrainment associated with the Harmattan. In absolute terms, the biggest decrease in dust concentration is in the central Sahara. The spatial distribution is again related to both the windspeed and soil moisture content.

### **Roughness length**

Section 3.3.3 describes how the friction velocity,  $u^*$ , is calculated from the wind strength at a reference height, and the roughness length,  $z_0$ , which depends on vegetation. That section also explains that a lookup table is used to determine the value of the roughness length at each gridbox, depending on the biome type predicted by BIOME4. For deserts, this value is  $1.7 \times 10^{-2}$ m. However, in HadAM3, the roughness length over bare soil is in fact  $3.0 \times 10^{-3}$ m. This means that in the dust model control run, the friction velocity is being over-simulated in these regions. Therefore, in this experiment, a new constant value for the roughness length of  $3.0 \times 10^{-3}$ m is chosen, to give consistency with HadAM3 over desert regions.

The difference in annual mean dust concentration, between this perturbation integration and the control, is shown in figure 4.7. As expected, the decrease in roughness length causes a decrease in dust production. The global dust content is 15% of the control integration. The spatial pattern of change is remarkably similar to that caused by increasing the threshold wind speed, as shown in figure 4.6(b), including the diminished Harmattan-associated dust entrainment, and consequent decreased transport towards South America. There is also a large decrease in dust concentration over the North Pacific

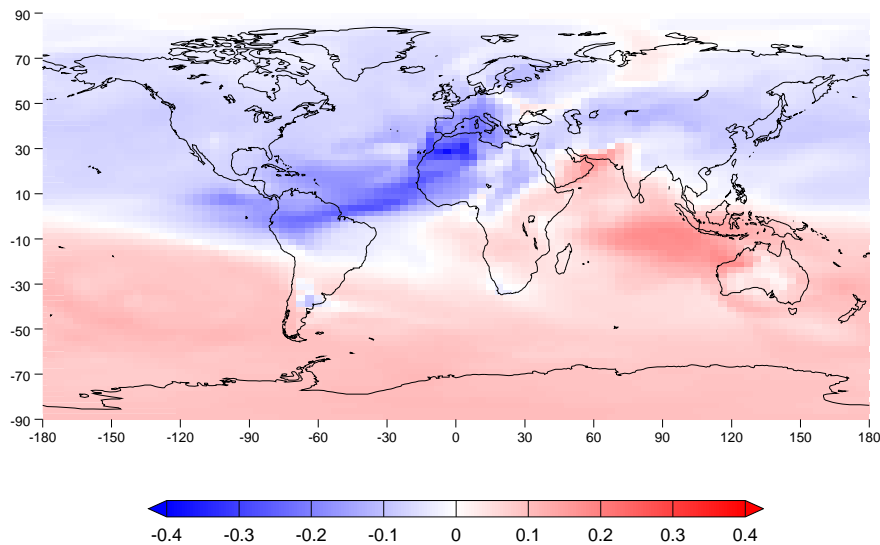


**Figure 4.7:**  $\text{Logarithm}_{10}$  of the ratio of the annual mean dust concentration in the experiment in which  $z_0 = 3.0 \times 10^{-3}$ , to that in the control, with  $z_0 = 1.7 \times 10^{-2}$  m. The ratio is normalised, so that the mean change appears as zero.

in SON, caused by a decrease in dust production in South Asia at this time. The similarity is unsurprising, as equation 3.14, for dust entrainment, includes the ratio  $u_t^*/u^*$ ; increasing  $u_t^*$  will have the same effect as decreasing  $u^*$ .

### Vertical:Horizontal flux ratio

In this experiment, a test is made of the model's sensitivity to the ratio of vertical to horizontal dust flux. In the control experiment, this ratio is a constant value of  $1.0 \times 10^{-3} \text{m}^{-1}$ , but it has been shown that this value can depend heavily on the clay content of the soil (Marticorena and Bergametti, 1995); soils with a high clay content have more fine particles which can make the transition between saltation (horizontal transport) and suspension (vertical transport). Following the work of Marticorena and Bergametti, a log-linear relation between clay content and the ratio of vertical to horizontal flux is assumed for clay contents in the range 0% to 20%, with high clay contents resulting in a larger ratio. However, it is also observed that soils with a very high clay content become crusted and so are not strong emitters of dust, and so these soils can be thought of as having a relatively low ratio of vertical to horizontal flux. These two ideas are combined to produce a dependence of the ratio on clay content shown in figure 4.8. This is the distribution which is used in this sensitivity study.

The amount of clay as a percentage of the total soil mass, which is derived from the WRL dataset, as described in section 3.3.2, is shown in figure 4.9, along with the resulting annual mean atmospheric

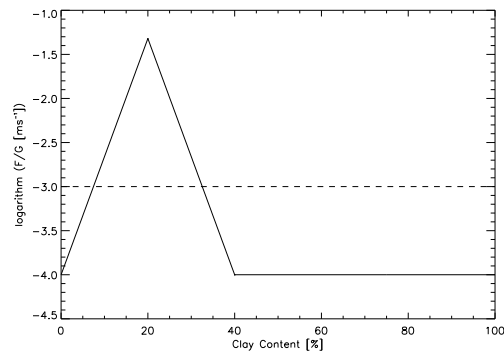


**Figure 4.8:** Solid line is the ratio of vertical to horizontal flux, as a function of clay content of the soil, based on Marticorena and Bergametti (1995). Dashed line is the value used in the control simulation.

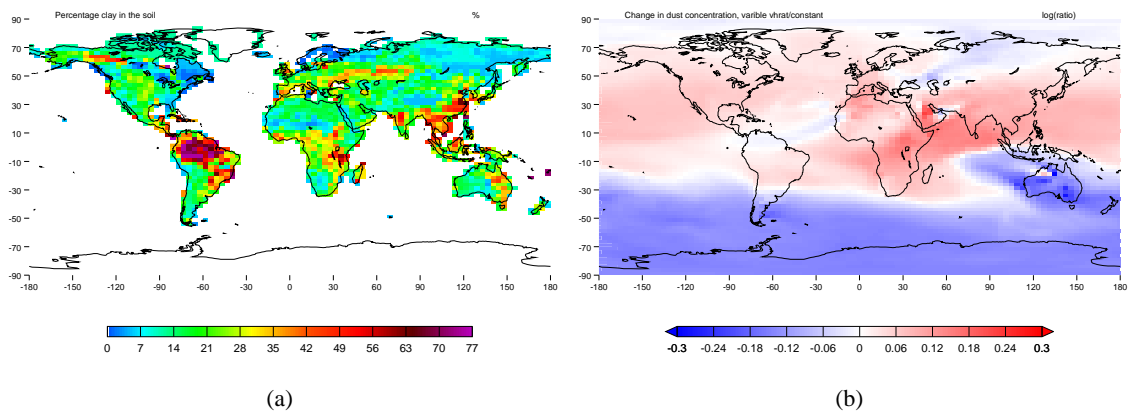


**Figure 4.9:** (a) The percentage of clay in soil, from the WRL dataset. (b) The  $\log_{10}$  of the ratio of the vertically integrated dust concentration from a run using a variable ratio of vertical to horizontal flux, derived from the WRL clay dataset and figure 4.8, to the control run, using a constant ratio of vertical to horizontal flux. The ratio is normalised, so that the mean change appears as zero.

dust distribution, expressed as a fraction of the control experiment, for the third size bin. The smallest size bin has a very similar sensitivity to this change in parameterisation. The main effect of this change in parameterisation is an increase in global dust amount. The total increase is a factor of 615. This is not surprising, as the ratio of vertical to horizontal flux is greater for all particle sizes. The smallest increase in dust production is from Australia. Eastern Australia is a region of high clay content, and for this reason, has a low modelled ratio of vertical to horizontal flux, due to the crusted nature of the soil. The largest increase in dust production are in regions with a clay content of order 20%, especially Arabia. These regions have the greatest modelled ratio of vertical to horizontal flux. In terms of seasonality, the greatest magnitude of relative change is in DJF, when the Australian source is producing a comparatively small amount of dust. This may be due to the fact that this large

dust content run is taking longer to spin up, and DJF is the first season of the integration. In terms of absolute values, the greatest increases in dust production are from Arabia and central Sahara.

### Soil Moisture

Section 3.3.3 shows that introducing the moisture parameterisation, following Fecan *et al.* (1999), can have large effects in the dust model. This is investigated further in this experiment. In most of the preceding sensitivity studies, a single parameter has been changed in the model, and the effect investigated. In the case of moisture, this is difficult as there is not one single parameter which is easily changed in the parameterisation. Therefore, a simpler parameterisation of moisture is introduced, and tested. Instead of a function of moisture and clay content of the soil, acting to increase the threshold friction velocity, a simple moisture threshold is used, as in the model of Mahowald *et al.* (1999). If the soil moisture is greater than a threshold value, then there is no entrainment. In the first integration carried out, a value chosen for the threshold is a gravimetric soil moisture content of 4% (that is, 0.04kg of water in 1kg of soil). This value is chosen to give an atmospheric dust content similar in magnitude to that of the control. After running the model with this value, the mean atmospheric dust content is  $9.3 \times 10^{11}$ kg, compared with  $7.3 \times 10^{11}$ kg in the control, the main increase in dust concentration being in the north eastern Sahara.

This experiment is taken as the new control for the next two experiments, in which the value of the moisture threshold is taken as 2% and 10% respectively. The annual mean dust concentration, expressed as a ratio of the new control, for these two experiments, is shown in figure 4.10.

Decreasing the moisture threshold from 4% to 2% decreases the dust content of the atmosphere by 88%. The largest change is in the north west Sahara and west Asia. The decrease in source strength in these regions causes a relatively large decrease in atmospheric dust at high latitudes. The strongest relative changes are in DJF and SON. The southern hemisphere is much less affected by the change; the dust source of Patagonia is moisture limited anyway, and so decreasing the soil threshold makes little difference, and the dust source region of Australia is dry enough not to be affected even by the lowering of the moisture threshold.

Increasing the moisture threshold to 10% causes an increase in dust loading of 41%. The most affected region in this case is Patagonia. The increase in the strength of the Patagonian dust source caused by

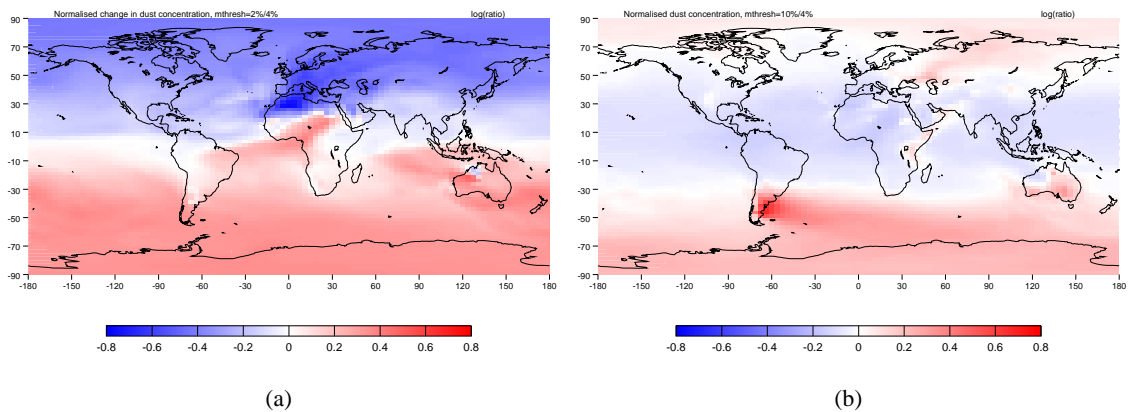


**Figure 4.10:**  $\text{Logarithm}_{10}$  of the ratio of dust concentration in the experiment with a soil moisture threshold of (a) 2% and (b) 10%, to that in the experiment with a soil moisture threshold of 4%. Both ratios are normalised, so that the mean change appears as zero.

raising the threshold, increases the dust loading over Antarctica by a factor of 2.5 in the annual mean, and up to 4 in DJF. In the south west Pacific, off the coast of Argentina, the increases are closer to 10.

### Conclusions from entrainment study

In this entrainment study, it has been shown that the model exhibits a high degree of sensitivity to several variables which are not particularly well constrained by observations. The model shows a similar sensitivity to an increase in threshold friction velocity as to a decrease in roughness length. The spatial patterns of these changes depends as much on the moisture content of the soil as on the surface wind speed. In general, it is shown that decreasing the entrainment threshold increases the relative strength of the Patagonian source, whereas increasing the threshold decreases the relative strength of the north west African source. Using a ratio of vertical to horizontal flux which depends on soil moisture, results in a massive increase in global dust, but a relative decrease in the Australian and Patagonian sources. The Patagonian region is also particularly sensitive to the parameterisation of soil moisture, and raising the moisture threshold can greatly increase the strength of this source region. Further studies have been carried out, on changing the snow cover threshold, the way in which gustiness is parameterised, and the precise form of the flux in equation 3.15, but in all these studies, the model exhibited a very low sensitivity, either not affecting the total dust loading, or affecting it in a linear fashion, with little or no spatial variability. In summary, as in the vegetation study, it is in general the southern hemisphere sources which are most sensitive to changes in the way in which the entrainment of dust is parameterised.

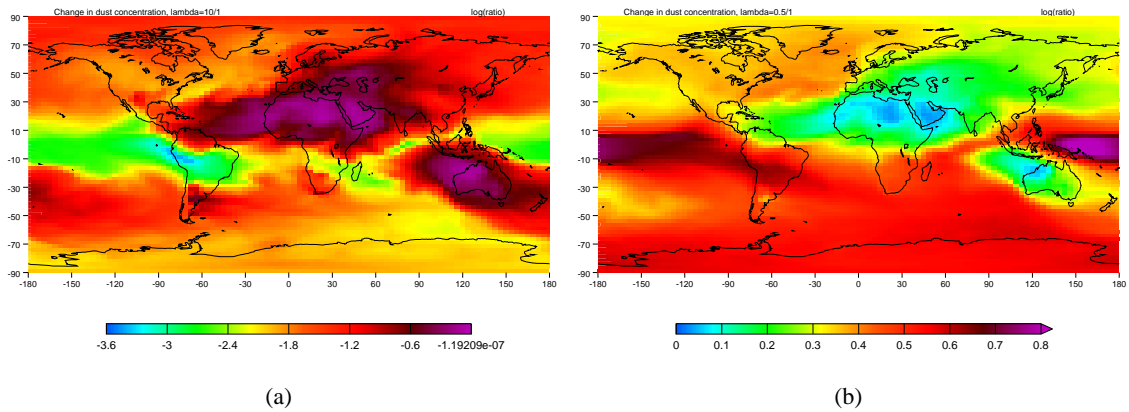


**Figure 4.11:**  $\text{Logarithm}_{10}$  of the ratio of annual mean vertically integrated dust concentration, in the experiment with (a)  $\lambda = 814\text{m}^{-1}$ , and (b)  $\lambda = 40.7\text{m}^{-1}$ , to the control ( $\lambda = 81.4\text{m}^{-1}$ ).

### 4.2.3 Deposition Study

As shown in section 3.6, it is the particles in the sub-micron range which dominate the modelled total atmospheric dust loading, particularly in regions remote from source regions. Particles of this size are removed almost entirely by wet deposition, as their settling velocities are so small. In testing the sensitivity of the model to deposition, therefore, it is sufficient to examine wet deposition alone. There are two factors which influence the wet deposition; the scavenging coefficient and the assumed vertical distribution of precipitation. Because most of the atmospheric dust is in the lowest few model layers, the precise form of the vertical distribution makes little difference to the vertically integrated concentration of dust, although it may affect the vertical dust distribution. Therefore, this study investigates the effect of changing the scavenging coefficient alone.

The scavenging coefficient in the control experiment, derived from the model of Slinn (1983), and normalised to fit the observational data of Volken and Schumann (1993), for particles in the range  $0.3\text{-}1\mu\text{m}$ , is  $81.4\text{m}^{-1}$ . In this experiment, the effect of multiplying the scavenging coefficient by a factor of 10, and of halving it, is investigated. The resulting annual mean, vertically integrated, dust concentrations, expressed as a ratio of that from the control experiment, are shown in figure 4.11.

A scavenging coefficient 10 times greater than the control causes a decrease in global mean dust content of 66%. A scavenging coefficient which is half of the control results in an increase in the global mean dust content of 59%.

Figure 4.11 shows that in regions close to the source, the dust concentration is not greatly affected by

an increase or decrease in scavenging coefficient. This is unsurprising, as there is in general very low precipitation in these regions, and also the precipitation has had less time to rain out the dust. In the case of the increased scavenging coefficient, there is a very clear large decrease in dust concentration over South East Asia in JJA, corresponding to monsoon rains. There is also a relatively large decrease in dust concentration over Antarctica, particularly in JJA. These comments all apply in reverse to the case of decreased scavenging coefficient.

In general, the largest changes in dust concentration are far from the source regions, and in regions of high precipitation. This can be understood by considering that the dust concentration,  $C$ , in the control run, will scale as  $C = C_0 \exp(-\lambda RT)$ , where  $\lambda$  is the scavenging coefficient,  $R$  is the rainfall rate and  $T$  is the distance (in time) from the source. The concentration in the perturbation run will scale as  $C' = C_0 \exp(-\lambda' RT)$ , giving a ratio,  $C'/C = \exp(-RT(\lambda' - \lambda))$ . In the case of increased scavenging coefficient,  $\lambda > \lambda'$ , and the ratio is smallest, and therefore dust decreases are largest, when  $T$  or  $R$  is large, *i.e.* in regions of high precipitation or regions far from the source.

#### 4.2.4 Advection and Resolution Study

In this study, a first, as opposed to second, order moments scheme, and the effect of neglecting the flux limiter in the advection scheme, are tested. By examining ERA wind data at T42 and T106 resolutions, likely effects of changing the horizontal model resolution are also investigated.

##### 1st order vs. 2nd order moments

In section 3.2.1, the Prather advection scheme is described. This scheme conserves second order moments of mass, which gives it an advantage over schemes which conserve only first order moments (Prather, 1986). This sensitivity study investigates the errors introduced by using the first order conserving scheme of Russell and Lerner (1981). Previous dust modelling studies have used advection schemes with a comparable level of accuracy to a first order moments scheme (Prather, 1986).

The ratio of dust concentration between an experiment carried out using conservation of first order moments, and the control, which conserves second order moments, is shown in figure 4.12. It can be seen that the less accurate advection scheme is over-simulating the amount of dust in regions of

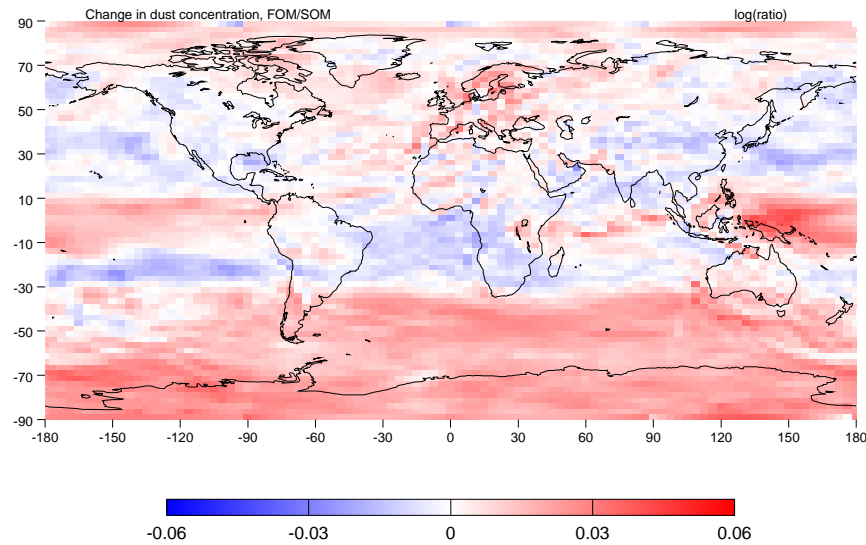


**Figure 4.12:**  $\text{Logarithm}_{10}$  of the ratio of annual mean dust concentration in the experiment conserving first order moments, to the control, conserving second order moments.

very low dust concentration. Over Antarctica, the over-simulation of dust content is of order 8%. This is likely to derive from the fact that the first order moments scheme is more diffusive than the second order moments scheme (Prather, 1986). The over-simulation is of greatest magnitude in DJF, and there is actually less transport to Antarctica in JJA in the first order scheme. In terms of absolute magnitude, the biggest differences are over the Sahara, but the differences here are very inhomogeneous. There is a very small increase in annual mean dust loading of the atmosphere of 0.2%. The first order moments scheme results in a computer time saving of about 60%.

### Flux limiter

In section 3.2.1, it was discussed that the Prather advection scheme in TOMCAT allows the use of a form of flux limiter to preserve positivity at all timesteps. The use of the flux limiter is needed for the accurate simulation of large particles, which have a high settling velocity. The flux limiter is used in the control, and in all other simulations. However, for the size of particle used in the control integration, the settling velocity is so small that vertical motions are not important over one timestep, so use of the flux limiter is optional. This experiment quantifies the loss of accuracy incurred by using the flux limiter.

Figure 4.13, in the same way as figure 4.12, shows the percentage change in dust concentration from the control, for an integration carried out without the flux limiter.

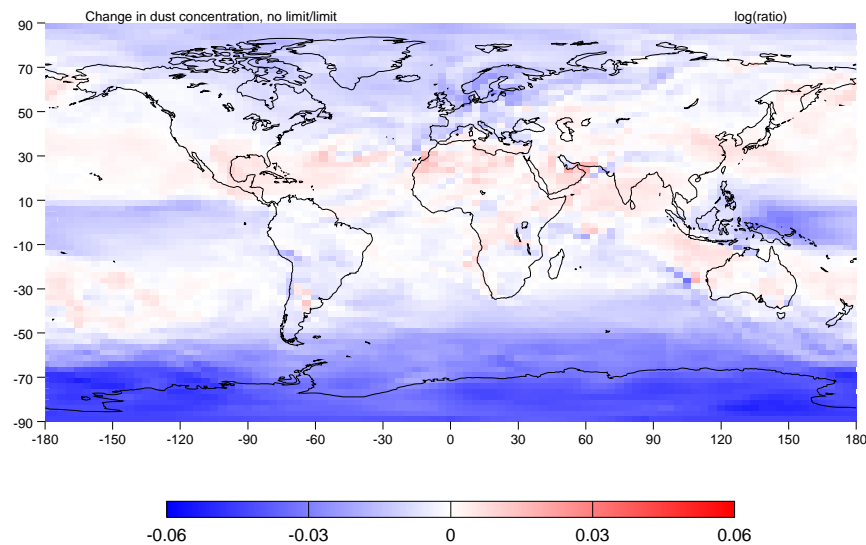


**Figure 4.13:**  $\text{Logarithm}_{10}$  of the ratio of the annual mean dust concentration in an experiment using no flux limiter, to the control, with a flux limiter.

This shows remarkably similar features to those in the previous experiment, with an annual mean decrease in dust concentration over Antarctica, and in other regions of low dust concentration. The magnitude of the changes is also similar to the previous experiment. This shows that it is likely that the flux limiter is introducing some spurious diffusion into the transport of dust.

### Spatial resolution

The control run, and all the sensitivity studies which have been described so far in this chapter, are run at the HadAM3 standard climate resolution of  $3.75^\circ \times 2.5^\circ$ , that is 96 longitudes by 72 latitudes. It is necessary to gain an understanding of the sensitivity of the model to the resolution. It is likely that the most resolution-sensitive component of the model is the surface wind speed, due to the cubic dependence of dust production on wind speed. It is expected that low resolution fields of windspeed will result in less total dust being entrained than high resolution fields.

In order to produce high resolution wind-speeds, for comparison with the control, one possibility would be to run the Unified Model at a higher resolution than the control. However, this would be a very time consuming task. Also, the higher resolution run would soon diverge from the control, and differences in the two runs would be due mainly to the chaotic nature of the atmosphere.

Instead, a different approach is taken, whereby observations of surface wind strength, in the form of European Centre Re-Analysis (ERA) data, at differing resolutions, are compared. The ERA dataset

is introduced in section 2.2.1. Wind speed in the ERA dataset is by default in a spectral format, in the form of vorticity and divergence fields, at a T106 resolution. When converted to grid-point data, the resolution is 320 longitudes by 160 latitudes, on a Gaussian grid. The spectral data can also be truncated to a T42 resolution, resulting in a grid point resolution of 128 longitudes by 64 latitudes. This, lower resolution, is similar to the standard resolution of HadAM3.

In this study, three datasets, of the cube of the surface wind speed, are produced for comparison. The output resolution of all three fields is  $128 \times 64$ . The first of these is produced by taking the spectral T106 data, converting it to gridpoint format at  $320 \times 160$  resolution, taking the cube of the windspeed, and finally interpolating by box-averaging to a resolution of  $128 \times 64$ . The second of these takes the T106 spectral data, truncates it in spectral space to T42, converts to a gridpoint resolution of  $128 \times 64$ , and finally takes the cube. The last takes the T106 spectral data, converts it to gridpoint format at  $320 \times 160$  resolution, interpolates by box-averaging in grid point space to  $128 \times 64$ , and finally takes the cube.

If an interpolation of a field  $x$  to a lower resolution in spectral space can be denoted by  $\tilde{x}$ , and an interpolation in gridpoint space by  $\bar{x}$ , then the above three fields can be written  $\overline{\tilde{u}^3}$ ,  $\tilde{u}^3$  and  $\bar{u}^3$ , respectively.  $\bar{u}^3$  can be thought of as the control field, which retains most of the information from the higher resolution.

The fields are calculated from the ERA data for July 1998, at a temporal resolution of 6 hours. Figure 4.14 shows the monthly mean fields of  $(\tilde{u}^3 - \overline{\tilde{u}^3})/\overline{\tilde{u}^3}$  and  $(\bar{u}^3 - \overline{\bar{u}^3})/\overline{\bar{u}^3}$ . The land-sea mask is applied because it is the dust entrainment, which occurs over land, which scales with the cube of the windspeed.

The plot of  $(\tilde{u}^3 - \overline{\tilde{u}^3})/\overline{\tilde{u}^3}$  (figure 4.14(a)) shows a very noisy field, reflecting the spectral interpolation which has been carried out to obtain it. The mean is a value of -0.2, showing that using the flux interpolated in this way would result in a decrease in dust entrainment of about 20%, assuming that this average applies equally well over source areas as over all land areas. There is not any clear spatial pattern in the increases and decreases.

The plot of  $(\bar{u}^3 - \overline{\bar{u}^3})/\overline{\bar{u}^3}$  (figure 4.14(b)) is a much cleaner signal, and indicates a global decrease in dust production with this decrease in resolution. The average value of this field is also -0.2, and so again would result in a decrease in dust production by 20%. The biggest absolute decreases in dust

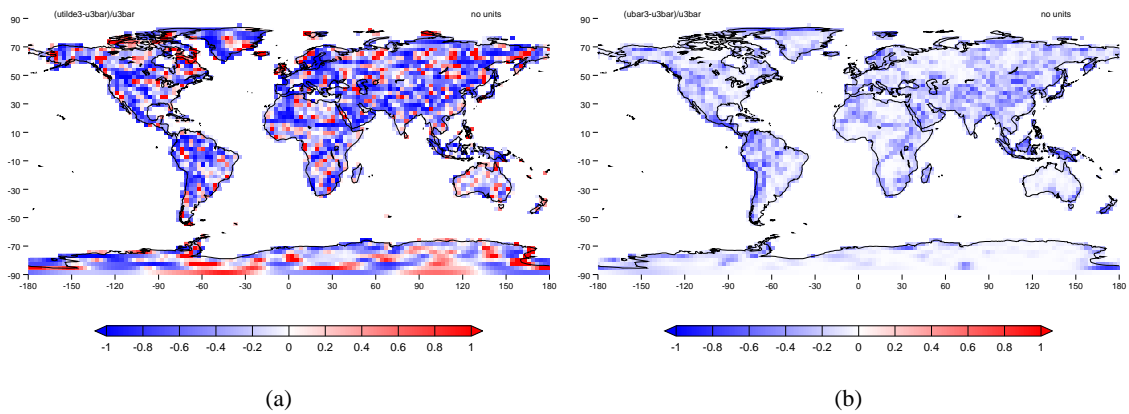


**Figure 4.14:** (a)  $(\tilde{u}^3 - \bar{u}^3)/\bar{u}^3$ , as calculated from 6-hourly ERA data, for July 1998. Only values over land regions are shown. (b)  $(\bar{u}^3 - u^3)/u^3$ , from the same source.

flux would occur where the wind strength is strongest.

It is likely that the HadAM3 model, when used in the dust model, has averaging characteristics most akin to  $\bar{u}^3$ , as the cubing is carried out after the windspeeds have been calculated, and there is no high-resolution information which is used in the running of the HadAM3 GCM. Therefore, we can conclude that in the dust model, there is a possible underestimation of the dust flux, of about 20%, compared to a model running at a  $320 \times 160$  resolution. The biggest underestimates are expected to occur in regions of high windspeed in the HadAM3 model, namely, western Sahara, Patagonia and western Australia.

It is difficult to say how much the windspeeds are underestimated compared to reality, purely from a resolution point of view. It is very likely, however, that the 20% quoted above is an underestimate of the true uncertainty due to small scale variability. Capturing the smallest scale fluctuations would require a model running at a very fine resolution indeed. Furthermore, temporal variability, on time scales shorter than the 6 hourly data, will also lead to uncertainty, although the parameterisation of gustiness is an attempt to represent this process.

### Conclusions from advection and resolution study

The advection study has shown that using a less accurate advection scheme, either in the form of a first order moments scheme, or through using a flux limiter, can result in dust concentrations which are too high, in regions of otherwise low dust concentration. The errors are of the order of 10%.

The resolution study has shown that an increase in resolution from T42, to T106, would result in an increase in dust flux of about 20%. An even higher resolution than T106 would probably increase the dust flux even further. The spatial distribution of this error is hard to predict. It is likely to be most significant in regions of high velocity gradient.

### 4.3 Case Studies

Satellite data can be used as a valuable tool for validating the dust model. This can be limited, however, due to the fact that satellites measure the net radiative effect of dust, rather than the concentration of dust. This means that the satellite data is useful only as a qualitative tool, because of the difficulty of converting between radiative effects and dust concentration, due to uncertainties in the radiative properties of dust, and the effects, among other things, of the altitude of atmospheric dust layers, and the presence of clouds.

However, satellite data has an advantage over many other types of data in that it is produced daily, and can provide nearly global coverage. Satellite data, therefore, is ideally suited to a qualitative study of dust-storm events. In this section, two such events are studied, and output from the dust model compared to data from the TOMS satellite.

#### 4.3.1 Model setup

For each case study, the model is forced by 6 hourly ERA data. The fields available are wind velocities, temperature, humidity, soil moisture, precipitation and cloud amount. This means that the dust model can be run exactly as in the control described in section 3.6, except that the effects of gustiness and snow cover are not included. Section 3.5.1 explains that this is unlikely to effect the results significantly.

The resolution of the ERA data is T42, that is 128 longitudes by 64 latitudes, on a Gaussian grid, with 31 vertical levels. This is similar to the  $96 \times 72$  horizontal resolution of HadAM3; in the vertical, the resolution is greater than the 19 levels of HadAM3, which is likely to lead to an improvement in the simulation of the vertical structure of dust. The ancillary fields used by the model, such as the potential source strength derived from BIOME4 LAI, are interpolated onto the new resolution. The

timestep is 30 minutes, as in the control experiment.

### 4.3.2 Asia; April 1998

On 15th and 19th April, 1998, extremely strong surface winds over Central China, caused huge amounts of dust from the Gobi desert to be entrained into the atmosphere (Husar *et al.*, 2001). The dust cloud resulting from the second of these storms was transported over the Pacific Ocean, and by the 25th April, high dust concentrations were recorded on the west coast of North America (McKendry *et al.*, 2001, Tratt *et al.*, 2001).

Husar *et al.* (2001) explain that the first of these storms was triggered by a dipole of high and low pressure systems over Western Mongolia and Eastern Mongolia respectively, causing strong north-westerly winds. This caused dust to be entrained off the dunes of the Gobi desert in long streaks, which mixed upstream of the winds to form a dust cloud. This cloud moved in a southerly direction, and then turned northwards towards Korea. During this time, the dust cloud was in a region of a precipitating low-pressure system, and so was dissipated relatively quickly by rain; by the 19th April, it was no longer visible on the TOMS satellite data.

The second storm was caused by high winds over Mongolia and north central China, associated with an eastwards moving low-pressure cold front, which caused mean winds of over  $20\text{ms}^{-1}$  over the Gobi desert and loess plateau in the Gansu province of China. This resulted in a towering dust front which moved eastwards to the east coast of China, and over the Pacific. During its transport towards North America, the dust cloud was stretched, and large segments peeled off and were advected towards the Arctic.

Figure 4.15 shows the modelled (left column) and TOMS observed (right column) timeseries for the 16th, 18th, 22nd and 24th April, 1998. There are several points to be noted from a comparison of the two series.

The timing of the initialisation of the dust storms is very good. Both the first and second storm start on the correct day. This is unsurprising, given that the ERA data shows very high wind speeds in the region of the Gobi desert on these two days. Also, the dust cloud is advected at the correct speed, and arrives at the west coast of North America on the 25th, in accordance with the observations. The modelled dust cloud seems to lag the observations by about 6 hours. This is very likely due to the

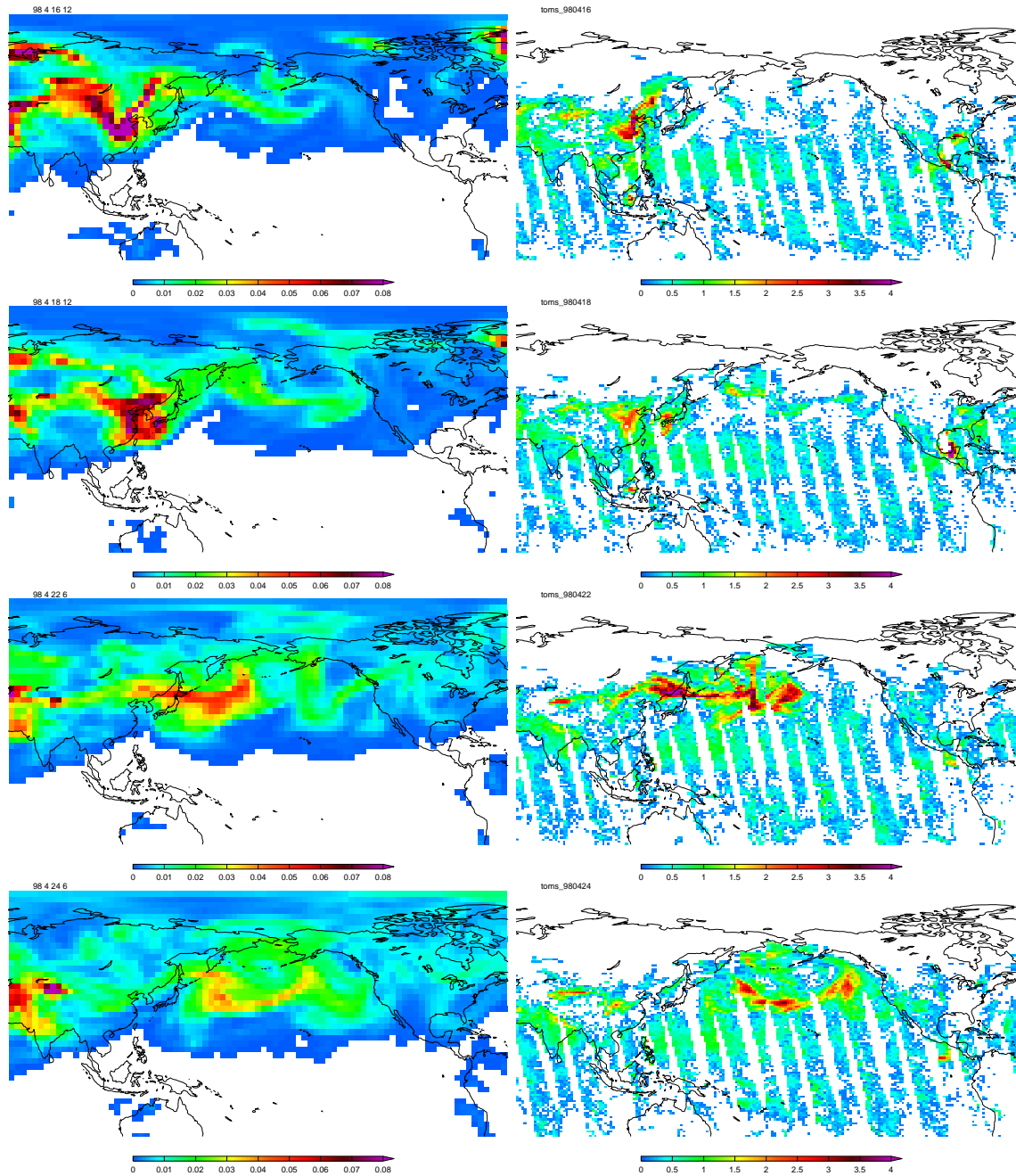


**Figure 4.15:** Modelled vertically integrated dust concentrations, in  $\text{kgm}^{-2}$  (left column), and TOMS satellite aerosol index (right column), for the 16th, 18th, 22nd and 24th April, 1998, in the region of the dust storm. White regions in the TOMS plots are where there is no satellite coverage, or where there is significant cloud cover.

fact that the model output is that of 12:00 GMT every day, whereas the time which the satellite passes overhead of the dust cloud is variable. The general shape of the dust cloud is also well reproduced.

The modelled dust cloud diffuses, and decreases in intensity, more quickly than the satellite data seems to suggest. This could be due to an over-simulation of wet deposition, due to a scavenging coefficient which is too large, to over-diffusion in the advection scheme, or to the non-linear nature of the TOMS aerosol index. The modelled relative strength of global dust concentrations is not in agreement with the satellite data; the modelled dust concentration over the Sahara is much larger than over Asia during the dust storm, whereas in the satellite data, the aerosol index over the Sahara is similar to that over Asia. As well as modelling errors, this could be due to differing optical properties of dust from the two regions, or differing altitudes of the dust layer. The region around the Aral Sea is also producing much more dust in the model than is expected from the TOMS data.

Nickovic *et al.* (2001) have carried out a similar comparison with the same dust storm, as part of the validation of their dust model, which is used to provide forecasts of dust concentration in the Mediterranean region. They find that they, too, are able to simulate well the observed dust cloud shapes, and speed of transport.

### 4.3.3 North Africa; September 1998

TOMS aerosol index data shows that in late September, 1998, an intense dust storm occurred in north-west Africa, causing entrainment of a large quantity of dust, which was subsequently transported across the Atlantic, by tropical easterlies. This dust storm has not been studied in nearly as much detail as the Asian dust storm in the previous section, but is chosen for this work because of the fact that it shows up clearly in the TOMS aerosol archive, and that it occurs within the timeframe of the ERA data which is available in a format which can be used easily with the dust model.

Figure 4.16 shows the modelled (left column) and TOMS observed (right column) timeseries for the 26th, 28th, 30th September and the 2nd October, 1998.

The TOMS data shows the initiation of the dust storm on 26th September, in the north west African region. By the 28th, the dust storm is over the Atlantic, and by 2nd October, it has reached the islands of the Caribbean. The dust model does a reasonable job of simulating the dust storm, in particular, the time of initiation of the dust storm is well reproduced, as is the shape and advection of the dust

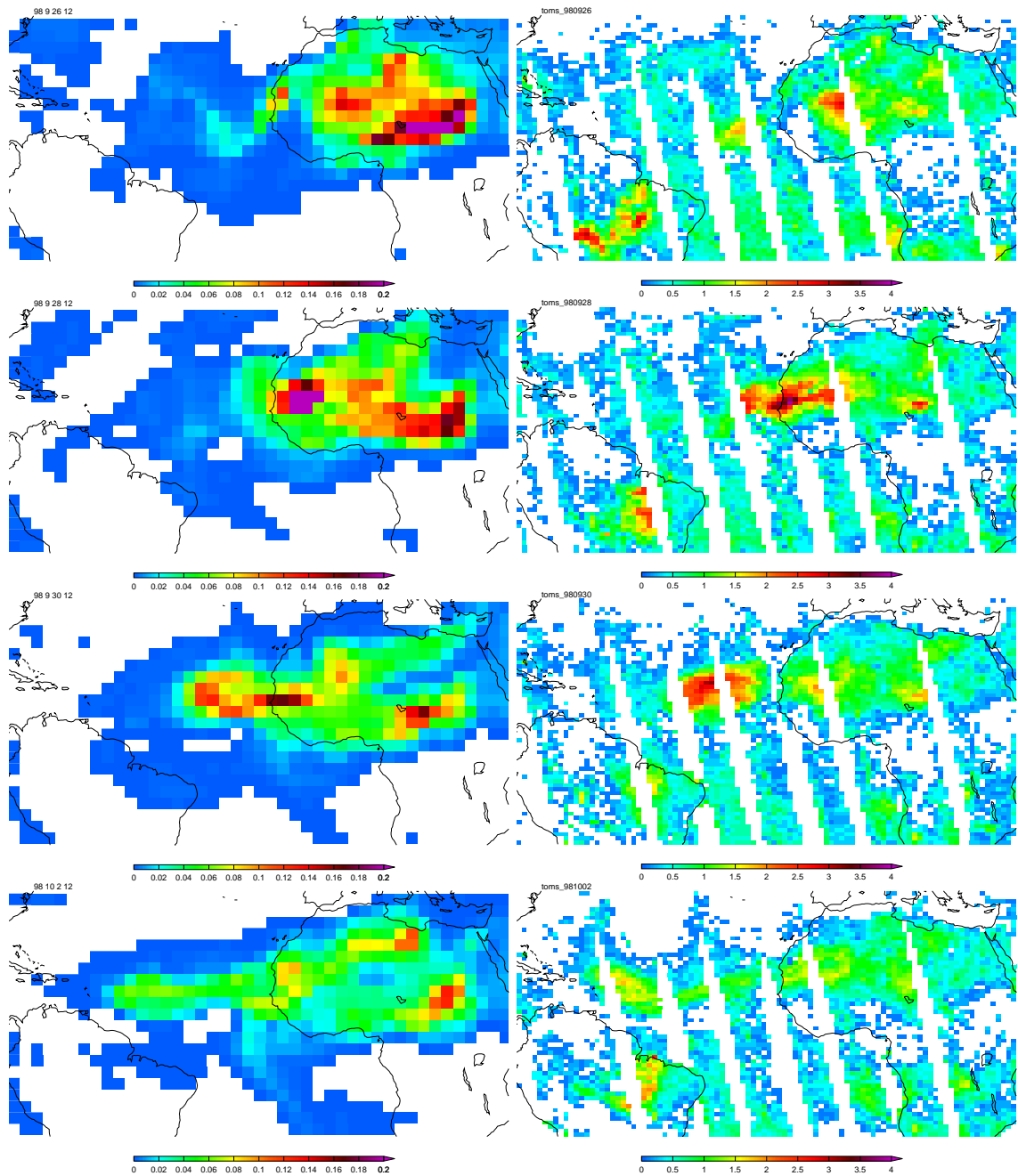


**Figure 4.16:** Modelled vertically integrated dust concentrations, in  $\text{kgm}^{-2}$  (left column), and TOMS satellite aerosol index (right column), for the 26th, 28th, 30th September, and 2nd October, 1998, in the region of the dust storm. White regions in the TOMS plots are where there is no satellite coverage, or where there is significant cloud cover.

cloud which is transported over the Atlantic.

However, there are several discrepancies between the model and observations. The model is predicting high dust concentrations in the southern Sahara, which are not as intense or as widespread in the satellite data. This dust storm is not advected very far and is removed by heavy precipitation in the Sahel region in the model. It is possible that it is not seen by the TOMS satellite because it is too close to the surface; the TOMS satellite cannot see dust which is below a level of about 1km. As in the Asian case, the dust cloud diffuses too quickly in the model, and does not retain its distinctness.

#### 4.3.4 Summary of case studies

In both case studies, the transport and shape of the dust cloud seemed to be well represented by the model. However, the model has difficulty in representing the exact geographic location of the dust storms, and the relative intensities of dust concentrations. For example, the model consistently over-simulates the strength of the Eastern Sahara as a dust source, and seems to underestimate the Asian source.

It is possible that these shortcomings are partly related to problems with the satellite retrievals. The TOMS aerosol index is calculated using assumed optical properties of dust, which, as explained in section 1.2.1, are not well known. The values used are most relevant to Saharan dust, and may not be representative of dust from, for example, the Gobi desert. Also, the TOMS aerosol index is very sensitive to the height of the dust layer, and in particular, has difficulty detecting dust which is close to the surface.

The difficulties that the model has in simulating the relative strengths of different source regions can also suggest ways in which the model could be tuned, to give better agreement. The sensitivity studies in section 4.2 point to numerous ways in which this could be achieved, for example, figure 4.6(b) shows that raising the threshold friction velocity from  $0.4\text{ms}^{-1}$  to  $0.6\text{ms}^{-1}$ , a change which is well within the bounds of the spread in observations, leads to a decrease in dust concentration over the Sahara, relative to over Asia.

These case studies highlight the importance of simulating correctly the geographical location of source areas, but also point to the fact that the shape of dust clouds is not particularly related to the shape of the source location, but to the structure of the advecting winds. This suggests the re-

quirement of an accurate climate model wind simulation.

The case studies give confidence that the model is behaving in a sensible way, and that the way in which the source regions are defined is at least qualitatively good.

## 4.4 10 year integration

Up until this point in the thesis, the experiments have been carried out for a period of 13 months, or, in the case of the case studies, for one month. Due to the chaotic nature of the climate system, and the non-linearity of many components of the dust cycle, it is very likely that the interannual variability of the modelled dust concentrations is large.

In order to test this hypothesis, and to provide results which can be compared with observations which represent the mean of many years, the model is run for a period of 10 years, plus a one year spin-up. The interannual variability is measured, and the dust fields compared with quantitative observations of dust concentration from the University of Miami Aerosol Network, and of dust deposition from the DIRTMAP dataset (Mahowald *et al.*, 1999). Previous modelling studies (eg Woodward, 2001, Mahowald *et al.*, 1999) have compared results to either the Miami or DIRTMAP datasets, but this is the first study to use both.

### 4.4.1 The experimental setup

The Miami and DIRTMAP datasets represent measurements of dust of all particle sizes. Therefore, for a good comparison, it is necessary to simulate the entire range of particle sizes in the model, rather than just one particle size bin, as has been done so far in the sensitivity studies in this chapter. One possibility would be to simulate all 6 particle size bins, as in section 3.6. However, this would be expensive in terms of computer time. An alternative approach suggests itself from the results of this 6-particle size bin experiment, summarised in table 3.2, which shows that 92.4% of the total mass is included in the smallest three size bins, representing dust of sub-micron radius. This means that a good representation of the total global dust amount can be obtained by simulating these three size bins. Furthermore, the majority of the sites in the Miami and DIRTMAP datasets are remote from source regions, meaning that the dust which arrives there is very likely to be in this size range. The

only difference in the modelled evolution of these particles results from their differing sedimentation velocities, which in turn comes from their differing radii, and their scavenging coefficients. In this size range, by far the most important of these is the scavenging coefficient. Table 3.1 shows that the scavenging coefficient does not vary greatly between these three particle sizes, being 120, 54 and  $81\text{m}^{-1}$  respectively. Therefore, the three smallest size bins can be combined together, and representative values of the radii and scavenging coefficients used. These representative values are the average of the values in table 3.1, scaled by the masses in table 3.2; the resulting typical radius is  $2.92 \times 10^{-7}\text{m}$ , and the typical scavenging coefficient is  $82.1\text{m}^{-1}$ . The source terms for the three particle size bins are added linearly. This experimental setup therefore approximates the simulation of the three smallest particle size bins, representing more than 90% of the total mass of atmospheric dust. This approximation is likely to be closest to the simulation including all size bins in regions remote from the source regions. Because only sub-micron particles are being simulated in this experiment, it makes sense to use a ratio of vertical to horizontal flux which is suited to soils of a high clay content. Based on work by Iversen and White (1982), this is taken as  $2.6 \times 10^{-5}\text{m}^{-1}$ , compared to the value used in the one year experiments, of  $1.0 \times 10^{-3}\text{m}^{-1}$ .

In the next chapter, another 10 year integration is carried out, but forced by LGM climate conditions. The two experiments are compared and contrasted, and so need to be as consistent as possible. In the experiments carried out so far, the HadAM3 GCM is run with observed SSTs and vegetation for the present day to produce the climate fields, and the source regions are defined from a BIOME4 integration, forced by the HadAM3 climate, normalised by the observed climate, as described in section 3.3.1.

It is not possible to carry out an LGM integration which is consistent with this, due to the lack of observational vegetation datasets for the LGM. Furthermore, the present day runs carried out so far have not been entirely self-consistent as the vegetation which acts to force the GCM (the Wilson and Henderson-Sellers (1985) vegetation dataset) is different from the vegetation which is used to define the source regions (vegetation fields output from BIOME4). Because of these reasons, a new experimental setup is used for the 10-year present day integration, which is designed to be both self-consistent, and consistent with the LGM integration in the next chapter.

Because of the errors in the CLIMAP SSTs, discussed in section 1.3.2, and so that the present day and LGM integrations can be as consistent as possible, the Met Office GCM is run in slab-ocean mode, rather than in atmosphere-only mode. This GCM is called HadSM3, and uses a prescribed oceanic

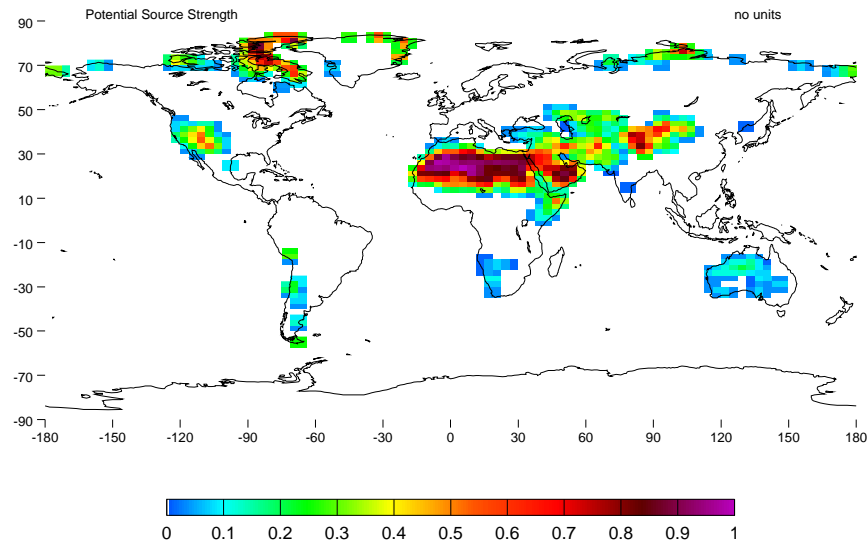


**Figure 4.17:** The field of Potential Source Strength, as used in the present day 10 year experiment, in which BIOME4 is forced by climate anomalies from HadSM3.

horizontal transport of heat, which is calibrated to give good agreement with observations of present day SSTs. Initially, the HadSM3 GCM is run for 10 years, under standard present day boundary conditions.

The resulting climate is then used to drive the BIOME4 vegetation model. It is found that small errors in the model climate result in large changes to the simulated vegetation. Hence, it is decided to couple the vegetation-climate models using anomalies only. This procedure is common in such simulations (eg de Noblet *et al.*, 1996). The resulting biome field is then used as the input into a new run of HadSM3, as well as being used to calculate the source terms for the dust model. Wind and other fields output from the new run are used to force the dust model. This ensures that the BIOME4 and climate model use a self-consistent set of boundary conditions. It also ensures that the field of potential source strength, as used by the dust model, is consistent with the vegetation in the climate model.

The same value of  $L_{max}$  of 1.2 is used to define potential source regions, and all other model parameters are the same as in previous experiments. There was an improvement in the method of coupling the climate to the vegetation in the course of the thesis, so that the present day field of Leaf Area Index used in the ten year experiment is slightly different from that used as the control for previous work. The previous work used BIOME4 and Leemans and Cramer (1991). This new study uses HadSM3 climate anomalies; the differences are due to the fact that the anomaly method is not a perfect system. The new potential source strength field, used in the ten year experiment, is shown in figure 4.17. This

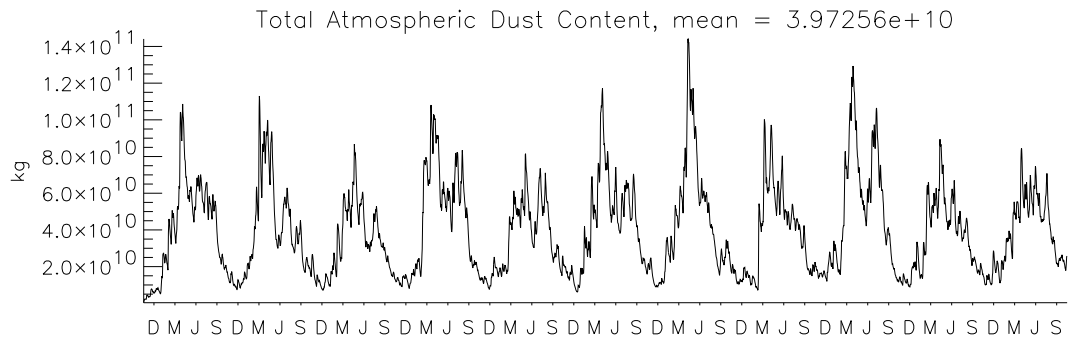


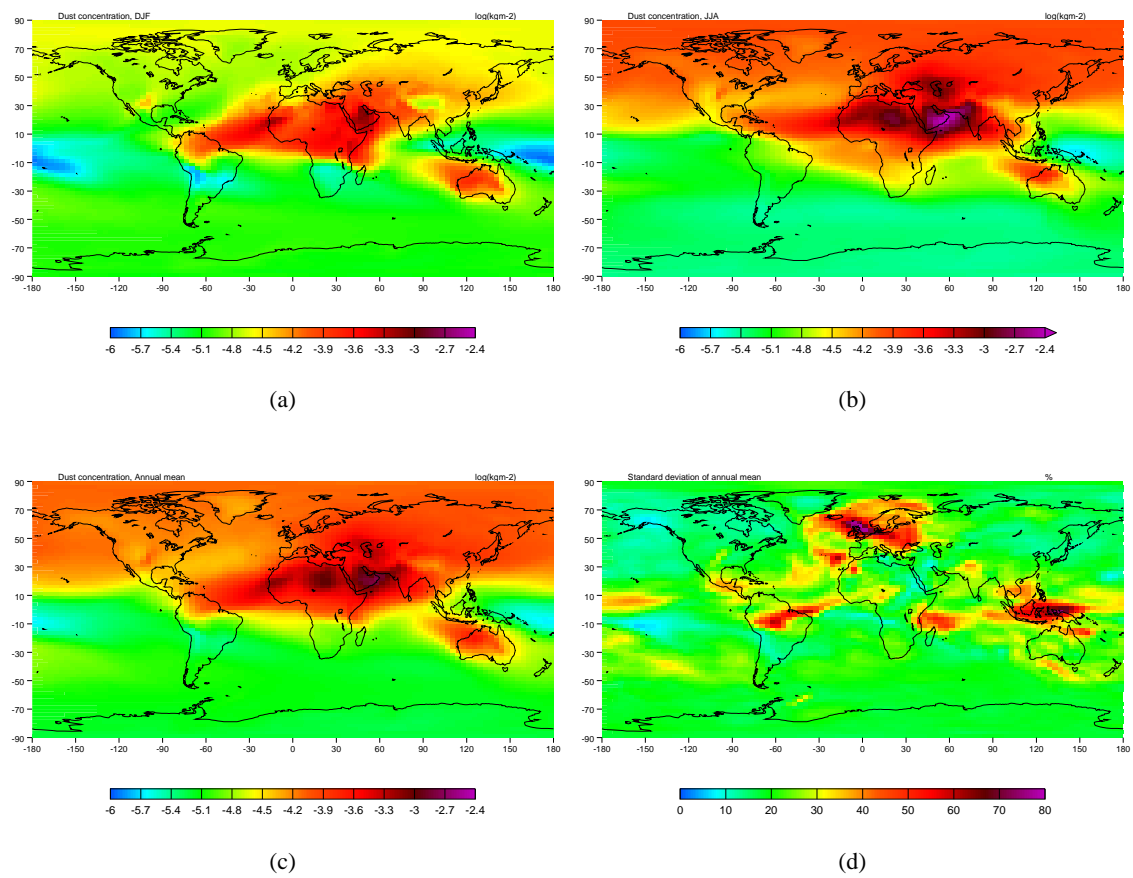
**Figure 4.18:** Timeseries of total atmospheric dust content, from the ten year present day experiment, plus one spinup year. Ticks on the x-axis mark the 15th day of the months of December, March, June and September.

field is for comparison with the original field, in figure 3.8. The biggest differences are in the regions of Australia and North America; the potential source strength in these regions is higher in the new field than in the control. The value of  $L_{max} = 1.2$  was chosen originally so that the Australian source was minimised in comparison to other regions. With this new field, this is no longer the case, and so it can be said there is less tuning which goes into this new study.

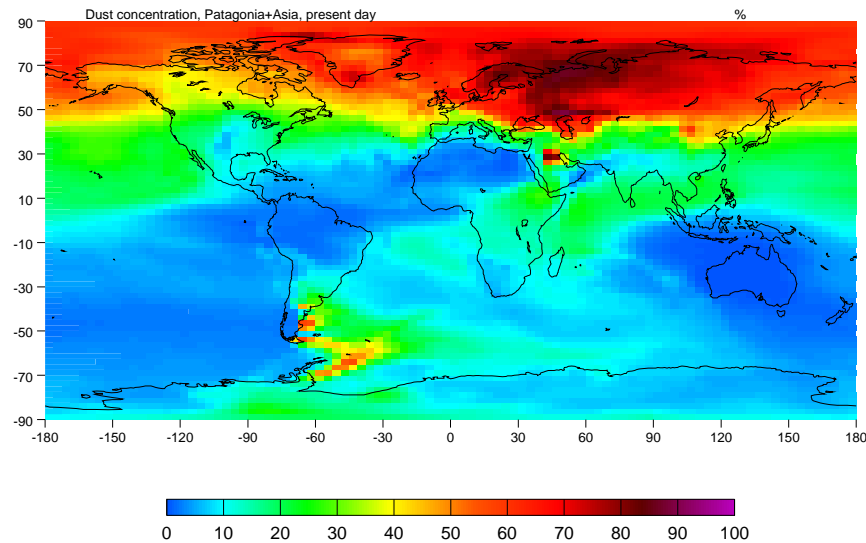
#### 4.4.2 The model results

Figure 4.18 shows a timeseries of the total global dust amount, over the 11 year period of the experiment. The timeseries clearly shows the annual cycle of dust content in the atmosphere. The maxima are in Northern Hemisphere summer, and the minima in Northern Hemisphere winter. In JJA, the dust content is very variable, and consists of several sharp maxima, whereas in DJF it is smoother. The timeseries also highlights the interannual variability in the model; the year of maximum dust content is the ninth year, with a mean of  $4.9 \times 10^{10}$  kg, and the least dusty year is the third year, with a mean of  $3.3 \times 10^{10}$  kg. The standard deviation of the ten annual means is 13%.

Figure 4.19 shows the DJF, JJA, and annual mean, vertically integrated dust concentration, and the standard deviation, expressed as a percentage of the annual mean. The general features of the seasonal variation of dust concentration are very similar to those observed in the one year experiment with six tracers, the results from which are shown in figure 3.23. Differences include the fact that in DJF, the dust at Northern Hemisphere polar latitudes is decreased in the new experiment, dust from Patagonia is decreased, and dust production from Somalia is increased. In JJA, the largest differences are a decrease in dust concentrations off the west coast of north Africa in the new experiment, and an



**Figure 4.19:** (a)  $\log_{10}$  of the vertically integrated dust concentration, in  $\text{kgm}^{-2}$ , in the 10 year present day experiment, for DJF, (b) for JJA and (c) for the annual mean. (d) Standard deviation of the annual mean dust concentration, expressed as a percentage of the annual mean.



**Figure 4.20:** Fraction of dust in the 10 year present day experiment, which derives from the source regions of Asia and South America.

increase in dust over Antarctica. Some of these differences may be due to the fact that the previous, 6-bin experiment was carried out for only a year, others may be attributable to the changed climate of the slab model, compared to the fixed SSTs. In agreement with satellite data (eg Husar *et al.*, 1997, Herman *et al.*, 1997), the Saharan plume shifts from westwards at JJA, transporting dust towards the Caribbean, to further south in DJF, transporting dust to South America. The dust concentration over the Sahara and North Pacific peaks in MAM, over Arabia in JJA, and over Australia in SON. The standard deviation of dust concentration is very spatially variable. There are maxima north and south of the Saharan dust plume, presumably caused by large variability in the magnitude of the oscillation of the plume. There is also a large variability over north and eastern Europe. This may be connected with Saharan dust, which, during some years, is transported northwards, and becomes entrained into the mid-latitude westerlies. Other regions of high variability, for example over the maritime continent, seem to be associated with low dust concentrations.

In addition to the experiment described above, another ten year experiment is carried out, simultaneously with the first, in which all source regions are set to zero, except for the west and east Asian and South American Sources. At the present day, this allows the seasonality of dust production from different source regions to be related to the seasonality of the dust concentration. At the LGM, this technique also provides a way of checking to what extent the model agrees with mineralogical evidence on the origin of dust in certain regions. Figure 4.20 shows the fraction of dust in the annual mean of the ten year experiment, which originates from the source regions of Asia and South America. It shows that in the Asian region, the dust predominantly originates from this region, whereas

in the rest of the Northern Hemisphere, the atmospheric dust originates from other sources. In the Southern Hemisphere, the South American source contributes only a small fraction of the total atmospheric dust loading. This information is used in the next section, comparing the modelled seasonality of dust concentrations with observations from the University of Miami dataset.

In order to gain more insight into what is driving the dust concentrations, it is necessary to look at the model results in more detail. The dust concentrations shown above are related to the sources, transport and sinks of dust, which interact together in a non-linear fashion. However, it is possible to disentangle them to some extent, and to gain a deeper understanding of what processes are going on. The next section examines the sources of dust in the ten year experiment in more detail.

### **Sources of Dust in the 10 year experiment**

As well as atmospheric dust concentration, in the ten year experiment, the model also outputs information on the amount of dust which is emitted into the atmosphere, from each gridbox, at each timestep. There are five pieces of information which are output; the first is the potential source strength at each gridbox, calculated from the leaf area index, which is linked solely to the vegetation, the second includes the effect of snow cover, the third is the particle flux, assuming dry soil and zero gustiness, the fourth is the flux including gust effects, and the fifth is the final flux, including gust and soil moisture effects, which is the flux which is injected into the lowest model level. Together, these give an understanding not only of the total amount of dust which is emitted, but how this varies geographically, seasonally, interannually, and crucially, how this amount depends on wind strength, moisture and other effects.

To analyse these new diagnostics, the globe is divided into several regions, shown in figure 4.21, over which the source information is summed. The wind-influenced timeseries of dust production are very noisy, due to the cubic dependence of dust entrainment on wind speed, and so means are taken over each month, and over each of the ten years. An example of the snow, wind, gust and final moisture data is shown in figure 4.22, for the region of North America. It shows that the dust flux is affected by the presence of snow in the winter months, with the largest effect being in January. The wind in this region means that the greatest entrainment, assuming dry soil and no gusts, is in March and April, with a secondary peak in October. The gusts do not have a large effect, but the inclusion of moisture greatly decreases the entrainment all year round, but most notably in MAM, leading to a single peak

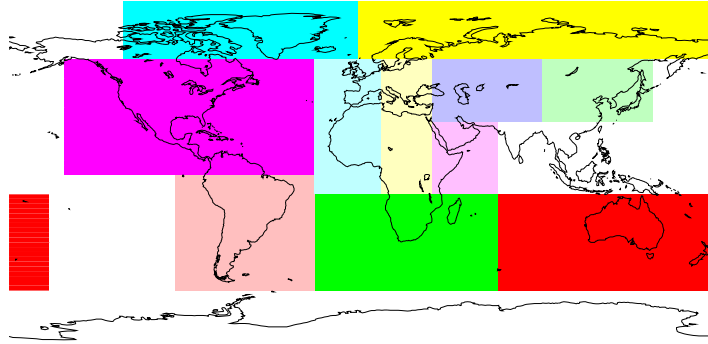


**Figure 4.21:** The source regions, as used in section 4.4.2. From the top, left to right, they are Greenland, Siberia, North America, West Sahara, East Sahara, West Asia, East Asia, Arabia, South America, South Africa and Australia.

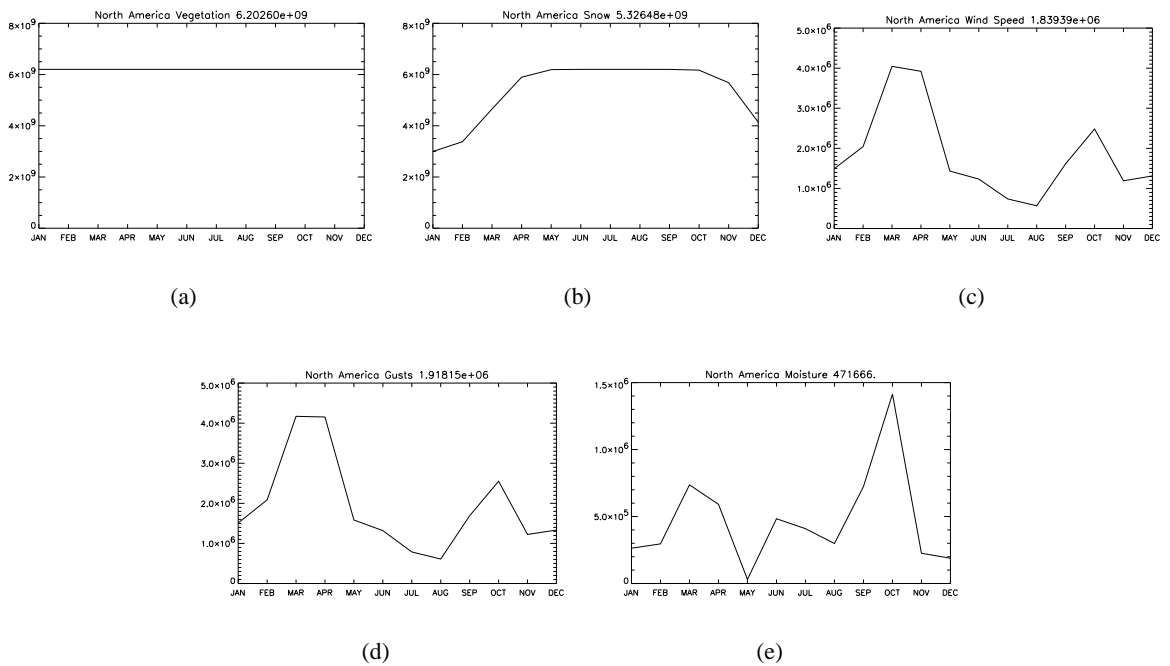


**Figure 4.22:** The surface flux of dust, in units of kg per half hour, emitted from the source regions of North America, in the ten year present day run. (a) Shows the flux calculated from vegetation effects alone, (b) shows the flux calculated from the vegetation and snow cover, (c) shows the wind-affected flux, assuming dry soil and no gusts, (d) shows the flux including gusts, and (e) shows the final flux including gusts and moisture, which is the flux which is injected into the lowest model level. Note the change of axis between the five plots. The numbers in the titles show the annual mean dust flux, in kg per half hour.

in dust entrainment in October. The presence of moisture decreases the total dust entrainment by 75%.

The final source strengths for the other source regions are shown in figure 4.23, in order of total source strength, greatest first. The sources not covered by any of the regions account for less than 0.2% of the total global input of dust. The strongest source region is that of Arabia. The seasonality in this region is determined by the strong shamal winds in JJA. The presence of soil moisture decreases the overall dust production by 33%, but this does not affect the seasonality.

The next strongest sources are that of Eastern Sahara, followed by the Western Sahara. The strongest winds in these regions are in northern hemisphere spring, and this is not affected by the presence of soil moisture. The Western Sahara also shows a smaller secondary maximum in August, also related to the wind speed.

The fourth strongest source region is that of West Asia. Here the seasonality is determined by a combination of the windspeed, which gives a primary production maxima in April, and a secondary maximum in July, and the presence of soil moisture, which inhibits the production of dust in April, leading to a primary maximum in dust production in July, and a less important maximum in April. The moisture decreases the total source strength by 46%.

The fifth strongest source region is Australia. Here, the winds lead to maxima in dust production in February and October. However, high soil moisture in February leads to a decrease in production at this time. Overall, the soil moisture decreases the dust production by 47%.

The rest of the source regions are weak in comparison, and together account for only 1.3% of the total dust source into the atmosphere. It is worth noting that the soil moisture in East Asia decreases the dust emissions, by 83%, and results in a source which has its maximum output in April and May. The source regions of Siberia and Greenland are entirely modulated by the presence of snow, and are reduced greatly by soil moisture. In South America, the presence of soil moisture leads to a very large decrease in source strength of 98.7%, and allows significant entrainment only in the month of May.

This analysis aids understanding of the important processes which control the dust cycle. It has been shown that in general, in the tropics, the seasonality of the windspeed controls the seasonality of dust production, in mid-latitudes it is the soil moisture which is more important, and at high latitudes, it is the snow cover and moisture which control the production of dust. In the next section, the seasonality

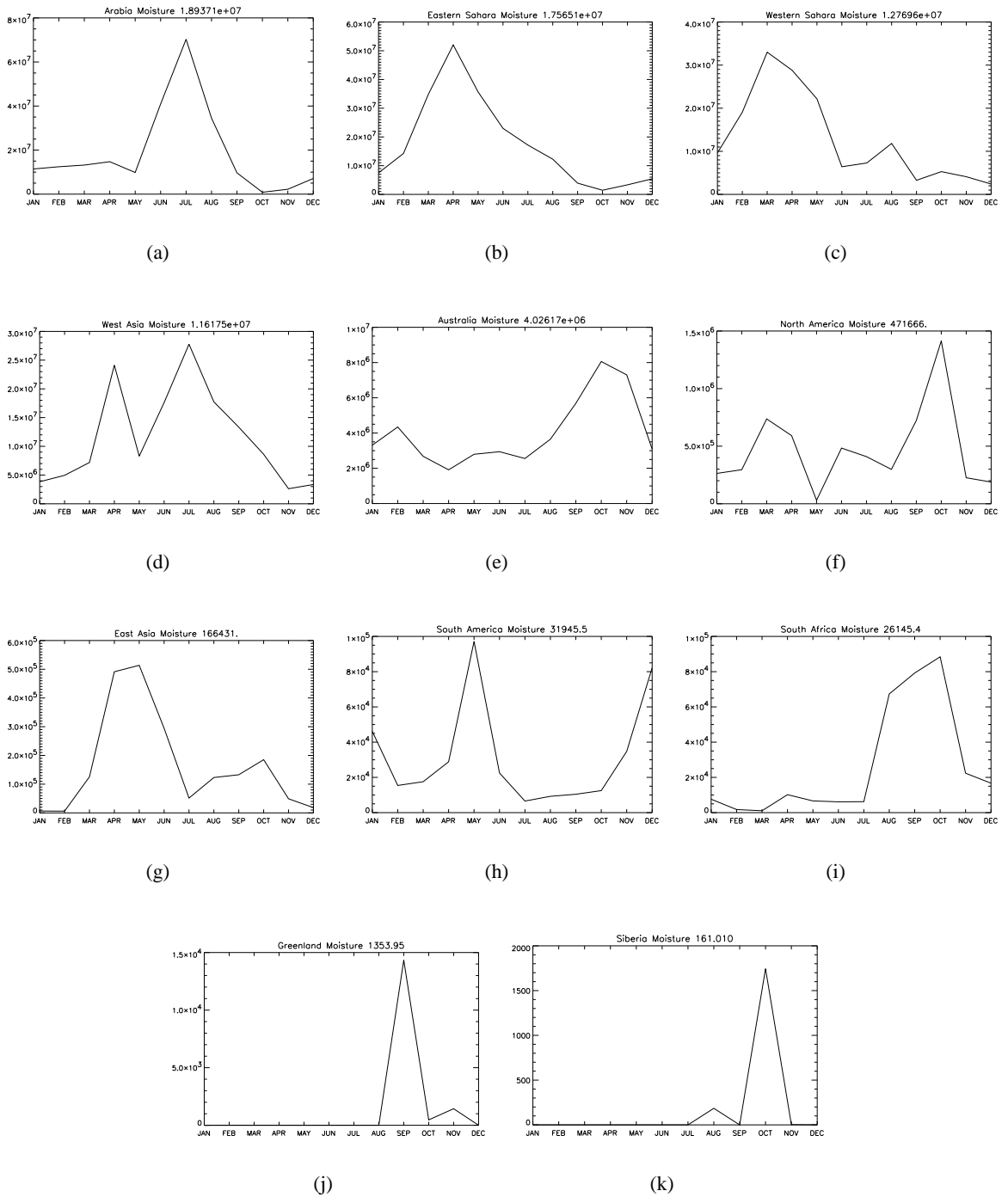


**Figure 4.23:** Modelled dust flux emitted into the atmosphere, in units of kg per half hour, in the ten year present day experiment, for the source regions of (a) Arabia, (b) east Sahara, (c) west Sahara, (d) west Asia, (e) Australia, (f) North America, (g) east Asia, (h) South America, (i) South Africa, (j) Greenland, and (k) Siberia. Note the differences in scale between the plots. The numbers in the titles show the annual mean dust flux, in kg per half hour.

of dust concentrations is compared to data, and it is helpful to be able to relate this to the seasonality of the dust sources themselves.

### 4.4.3 Comparison with observations

It is essential for any model to be subjected to rigorous validation. In the context of dust modelling, this can be difficult, as there are no global datasets of observations which can easily be compared with data from a dust cycle model. The observations which do exist, can be divided into two types.

Firstly, there are those which measure some function of the optical properties of dust, for example the optical depth of the atmosphere. When dust is the most important aerosol in the spectral region which is examined, this gives an indication of the amount of dust which is present. Examples of this first type of observations are the TOMS and AVHRR satellite aerosol products, with nearly global coverage, and the Aeronet network, which consists of ground-based photometers at 192 sites over the Earth.

Secondly, there are direct measurements of either dust concentration or dust deposition. Examples of these are the DIRTMAP dust deposition dataset, and the University of Miami aerosol network, which measures dust concentrations close to the surface. This second type of observations is always local in character.

For this study, direct validation is only possible through the second type of observation. It is beyond the scope of this study to attempt to convert dust concentrations, as predicted by the dust model, into the units of optical depth, or TOMS aerosol index. This is notoriously difficult, due to uncertainties both in the optical properties of dust, and in defining exactly what the satellites are measuring, and the effects of, for example, varying vertical distributions of dust, and cloud cover.

This section is divided into two parts. Firstly there is a quantitative comparison of modelled surface concentrations with data from the Miami aerosol network, and secondly, there is a quantitative comparison of the modelled dust deposition with the DIRTMAP dataset.

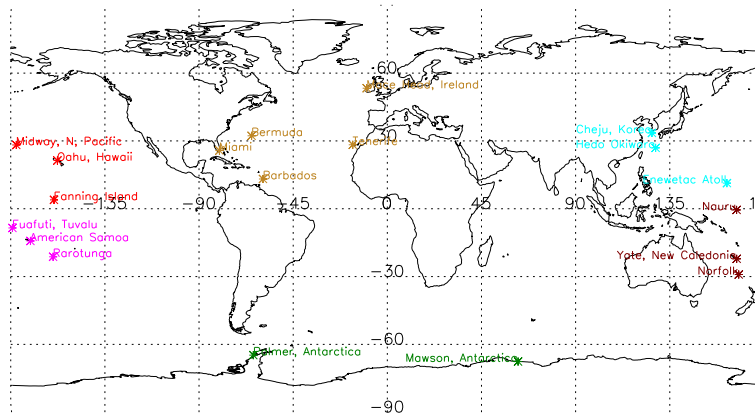


**Figure 4.24:** The sites of the stations in the Miami Aerosol Network which provide a complete set of dust concentration measurements. The colours group the data points into the regions of the north-east Pacific (red), north Atlantic (orange), north-west Pacific (light blue), south-east Pacific (magenta), south-west Pacific (maroon) and Antarctica (dark green)

### University of Miami Aerosol Network

The University of Miami Aerosol Network consists of a network of aerosol counters, which provide data on the concentration of various chemicals and aerosols in the atmosphere, close to the surface. Those sites which provide measurements of dust concentration are shown in figure 4.24. Measurements are not taken very regularly, approximately once every two days, although this varies between the sites, as does the total length of the record.

Figure 4.25 shows a plot of the annual mean modelled dust concentration at the various sites, and the annual mean measurements of dust concentration. The error bars on both the modelled and observed dust concentrations show one standard deviation of interannual variability. In general, the model is doing a good job of simulating the concentrations at the different sites. The difference between the mean of the logarithms of the modelled concentrations, and that of the observed concentrations, is 0.43. This shows that the model is on average over-simulating the dust concentration by a factor of  $10^{0.43} = 2.7$ . The solid line in figure 4.25 is the locus of perfect results. The dotted line is the locus of perfect results, after correcting for the systematic over-simulation.

About the line of perfect fit, there is relatively little scatter, and the log correlation coefficient is 0.84. This gives confidence that the model is simulating well the relative dust concentrations at the Miami Network sites. There is not a systematic bias in any one region, except that the concentrations in the East Pacific region are all relatively over-predicted. This may be due to an over-simulation of the North American dust source.

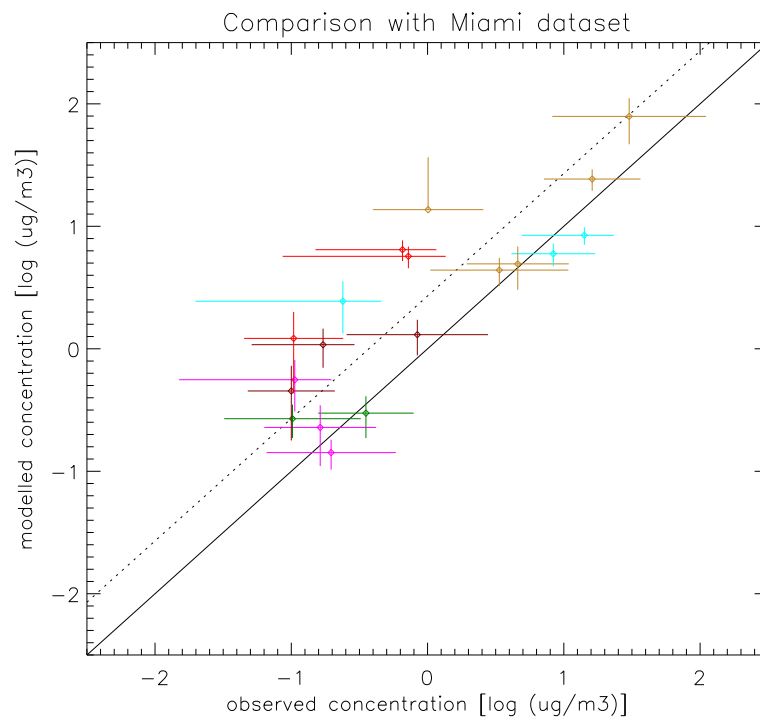


**Figure 4.25:** Plot of modelled versus observed surface concentrations at the sites of the University of Miami Aerosol Network. The error bars show one standard deviation of interannual variability, in both the observed and modelled concentrations. The solid diagonal line shows the line of perfect fit. The dotted diagonal line shows the average fraction by which the modelled results disagree with the data. The colours relate the data points to the regions in figure 4.24.

As well as the annual mean dust concentration, the Miami Aerosol Network contains information on the seasonality of the dust concentrations. Figure 4.26 shows the seasonal cycle of dust concentration, as measured at the sites in the network (the solid lines). Also shown (dashed lines) are the modelled seasonal cycles of dust concentration at the sites, which have been scaled so that their means are the same as the observations. The sites are examined in turn, and comparisons made between the observed and modelled concentrations. The modelled results can be understood in terms of the seasonalities of the source strengths in figure 4.23, and the provenance information provided by figure 4.20, derived from the Patagonia and Asia only integration. The numbers next to each site, show the total number of observations which were made to produce each monthly value of dust concentration, on average.

(a) Mawson - 22 days per month

The agreement between the modelled and observed concentrations is good. The modelled dust in this region is predominantly of Australian origin, and the modelled seasonality reflects that of the Australian source, which peaks in October.

(b) Palmer - 5 days per month

At the Palmer station, there are two peaks in the modelled concentrations, that in May is likely to come from South America, and that in southern hemisphere spring from Australia. There is poor agreement with the observations, but this is possibly related to the small number of observations taken at this site.

(c) Yate - 8 days per month, and (f) Norfolk - 13 days per month

At the stations of Yate and Norfolk, the modelled dust comes from Australia, and because of this, peaks in southern hemisphere spring. In Yate, this agrees with the observations, but at Norfolk Island the agreement is poorer, probably due to one very dusty September; the site at Norfolk has only two years of data.

(d) Funafuti - 13 days per month

In Funafuti, the modelled dust concentrations are extremely small, due mainly to the fact that transport of dust to the site from potential source regions is very low, as shown in figure 4.19(c). Although the observed peak in August and September is reproduced, there is a further modelled peak in March and April, which is not observed. The origin of this is possibly North America.

(e) Nauru - 12 days per month

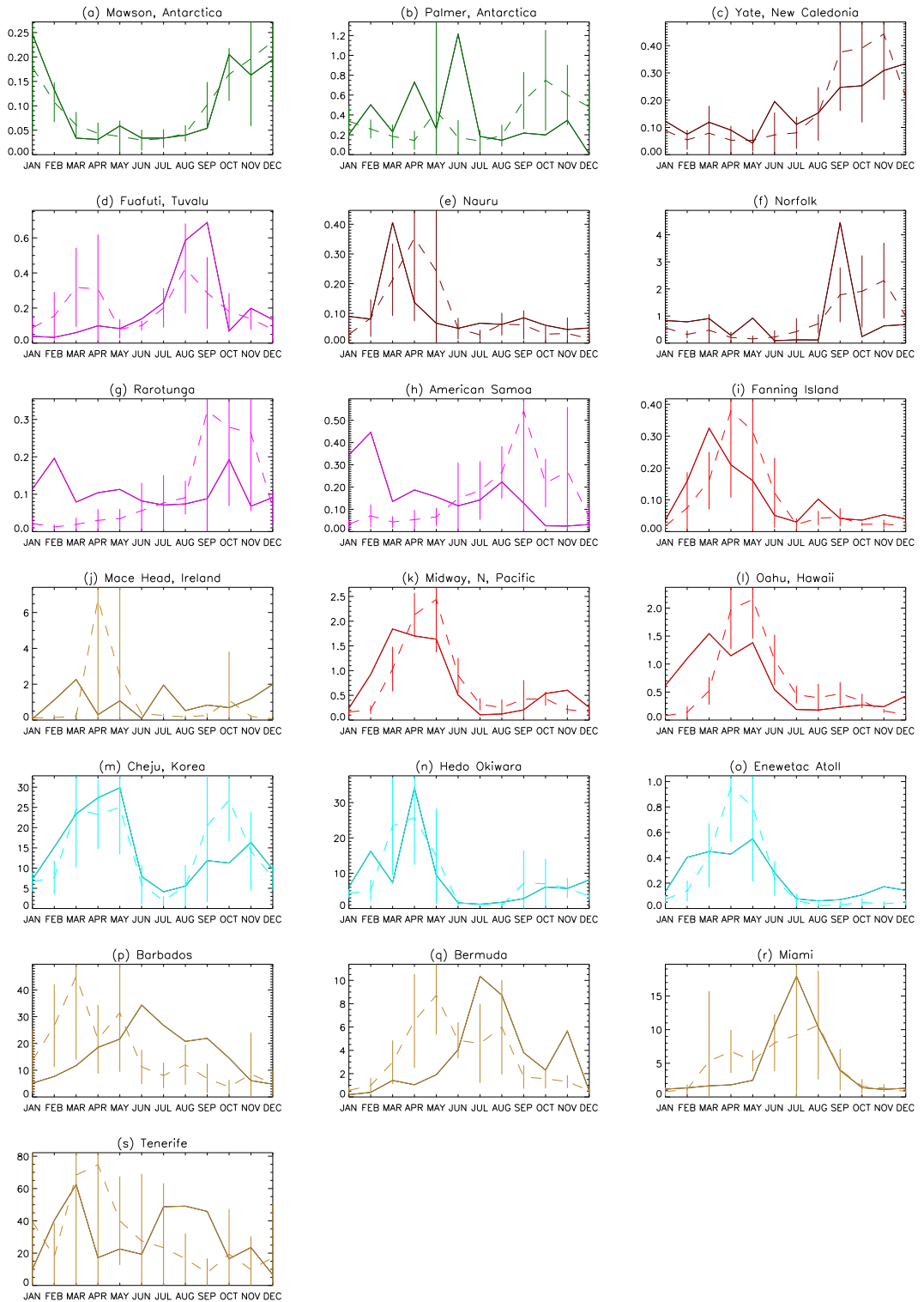


**Figure 4.26:** The seasonal variation of dust concentration at the sites of the University of Miami Aerosol Network. Solid lines are observations, dotted lines are modelled results, which have been scaled to give the same annual mean as the observations. The vertical lines show the interannual variability of the modelled results. The colours relate the data points to the regions in figure 4.24.

In Nauru, there is good agreement between modelled and observed seasonality. Nauru is on the equator, and it is possible that the dust here is of northern hemisphere origin, possibly Arabian or North American, and this is the reason for the peak in northern hemisphere spring. However, the dust concentration here is very low.

(g) American Samoa - 17 days per month, and (h) Rarotunga - 14 days per month

In American Samoa and Rarotunga, the modelled dust has its origin in Australia, and this is reflected in the modelled concentration which peaks in southern hemisphere spring. However, the observations are not in good agreement with the observational data, which shows a peak in February in American Samoa. Once again, the dust concentrations in these regions are very low.

(i) Fanning Island - 14 days per month, (k) Midway - 25 days per month, (l) Oahu - 17 days per month, (m) Cheju - 7 days per month, (n) Hedo Okiwara - 6 days per month, and (o) Enewatac Atoll - 12 days per month

In these northern hemisphere Pacific and Asian east-coast sites, there is very good agreement between the modelled and observed seasonality, which both in general show a primary peak in northern hemisphere spring, and a secondary peak in northern hemisphere autumn. The modelled dust at Cheju and Hedo Okiwara is of east Asian origin; that at the other sites is probably a mixture of Asian and North American.

(j) Mace Head - 16 days per month

At Mace Head, there is no clear seasonality in the observations. The model shows two peaks, in April and October, probably corresponding to the peaks in the west Saharan source.

(p) Barbados - 410 days per month

In Barbados, the observations show a clear peak in June. This is not reproduced in the model, where the concentration peaks in February, probably due to a combination of the east and west Saharan sources, and transport effects.

(q) Bermuda - 91 days per month, and (r) Miami - 154 days per month

In Bermuda and Miami, the observed dust concentration peaks in July. It is thought that atmospheric dust in this region is primarily of Saharan origin (Prospero *et al.*, 1970). However, the model cannot recreate this, and instead shows peaks in May in Bermuda, and in August in Miami. This is possibly related to a poor representation of transport in the model, an underestimation of the summer Saharan

source, or an overestimate of the strength of the North American source.

(s) Tenerife - 161 days per month

Tenerife is situated very close to the Sahara, and the dust originates from there. The seasonality of the modelled concentration follows very closely that of the modelled Saharan source, peaking in spring, but the observations show two peaks, in March and autumn. This again points to an underestimation of the summer Saharan source.

### Summary

In general, in the North Pacific, the model is doing a remarkably good job of recreating the observed seasonality at the sites of the Miami Network, with a major peak in northern hemisphere spring, and a secondary peak in northern hemisphere autumn. In the Atlantic, the model is not performing as well, and fails to recreate the maximum in dust concentration in summer, instead, simulating maxima in spring. This error may be due to an oversimulation of the North American source, or a mis-representation of the seasonality of the Saharan source. At many other sites, for example in the Palmer station in Antarctica, the number of observations is very small, and disagreements between model and data are not necessarily due to errors in the model.

### Comparison with the DIRTMAP dataset

The DIRTMAP dataset, which includes records of present day dust deposition rates to ice-cores, ocean cores and sediment traps, has been introduced in section 1.3.3. It is very different from the Miami Network for several reasons. Among these are that the data from the sediment cores and ice cores represent average values over a period of many decades, rather than being true present day values. In this way, the DIRTMAP dataset is better for comparing with the dust model, which does not include any anthropogenic land-use changes. The Miami Network data is likely to be influenced by local effects, such as topography, whereas the sediment data in the DIRTMAP dataset may be influenced by oceanic currents, and fluvial inputs. Figure 4.27 shows the locations of the sites in the DIRTMAP dataset.

Figure 4.28 shows a comparison of modelled with observed dust deposition. In general, the deposition of dust in the model is in good agreement with the DIRTMAP dataset. The difference between the mean of the logarithms of the observations, and the mean of the logarithms of the modelled

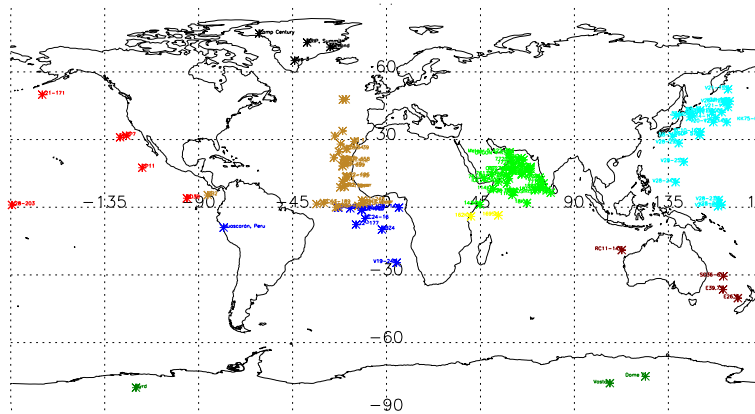


**Figure 4.27:** The sites of the ice-cores, ocean cores and sediment traps in the DIRTMAP database. The colours group the data points into the regions of the Arctic (black), the north-east Pacific (red), the north Atlantic (orange), the north Indian (green), the north-west Pacific (light blue), the south Atlantic (dark blue), the south Indian (yellow), the south-west Pacific (maroon), and Antarctica (dark green).

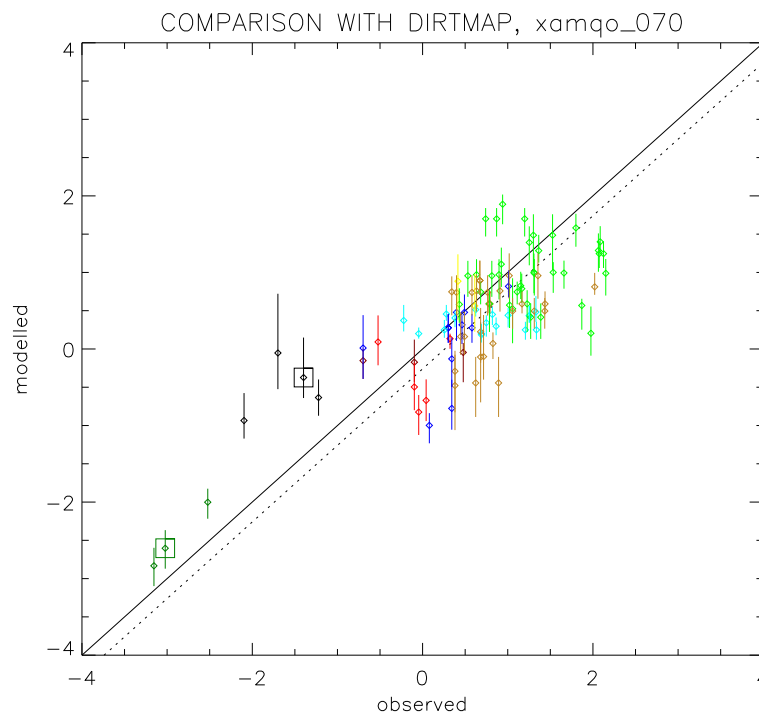


**Figure 4.28:** Modelled versus observed deposition at the sites of the DIRTMAP dataset. The error bars on the modelled results show one standard deviation of interannual variability. The solid diagonal line shows the line of perfect fit. The dotted diagonal line shows the average fraction by which the modelled results disagree with the data. The colours relate the different data sites to the regions in figure 4.27. The boxed points are the sites of Dome C, Antarctica (dark green) and Camp Century, Greenland (black). The units on both axis are  $\log_{10}(\text{g/m}^2/\text{year})$ .

results, is 0.26, which means that on average, the model is under-simulating deposition by a factor of  $10^{0.26} = 1.8$ ; this value is represented by the dotted line in figure 4.28. As with the University of Miami comparison, the scatter about this line is relatively small. The log correlation coefficient is 0.78, which is similar to the value obtained by Mahowald *et al.* (1999) with their model, and the same observational data, of 0.76. The deposition at the high latitude ice core sites of Antarctica, and Greenland in particular (shown by the dark green and black data points respectively), is relatively over-simulated compared to other regions in the model. This could be due to a variety of errors, including the basic state climate of the HadSM3 GCM, over-estimating precipitation in these regions. Figure 4.11(a) also implies that it could be related to an underestimation of the scavenging coefficient of dust in the model; a higher value decreases the dust concentration over Antarctica and Greenland relatively more than in other regions. A contributing factor over Antarctica may also be the spuriously high concentration of dust in this area, introduced by the use of the flux limiter in the advection scheme, as demonstrated in section 4.2.4. There is no strong systematic bias in any of the other regions.

The high level of agreement between model and data gives confidence that the dust model is performing well under present day conditions. Considering that no real tuning has been carried out, except for the value of the ratio of vertical to horizontal flux, and to a lesser extent, the value of  $L_{max}$ , this is very encouraging.

A cause for concern is that the DIRTMAP data and the Miami data appear to be mutually incompatible in the model, in that whereas the DIRTMAP data is under-simulated by a factor of 1.8, the Miami data is over-simulated by a factor of 2.7. This inconsistency reflects the very different nature of the two datasets, and is probably not serious.

## 4.5 Discussion and Conclusions

There are many conclusions which can be drawn from the work carried out in this chapter, and several areas which require a further discussion.

The vegetation sensitivity study shows that there are certain regions which are very sensitive to the way in which source regions are defined. In particular, the Australian source region is very sensitive to these definitions. By an appropriate choice of  $L_{max}$ , the Australian source can be made to either

completely disappear, or to become comparable in strength with major sources such as the Sahara, with little change in these other major source regions. This then affects the dust concentration in other regions, in particular the Southern Ocean and Antarctica. The problems which previous dust models have had, in over-simulating the strength of the Australian source (eg Mahowald *et al.*, 1999, Woodward, 2001), could in theory be reduced, by a judicious choice of  $L_{max}$ . The TRIFFID vegetation model actually gives similar results to the BIOME4 control, in terms of spatial resolution, neglecting a fairly homogeneous general increase in dust concentration. This is despite the fact that the Potential Source Strengths predicted by the two models look quite different. This is very encouraging, as it implies that results in this thesis, at least for the present day, may be largely independent of the vegetation model used. However, it may be that the two vegetation models give very different results for the Last Glacial Maximum, and other time periods.

The entrainment sensitivity study also shows a strong sensitivity to various parameters. Once again, a choice of a value of threshold friction velocity could be used to control the relative strength of specific source regions, for example, lowering the threshold increases the relative strength of the Patagonian source, and hence the dust concentration over the Southern Ocean and Antarctica. Decreasing the roughness length is found to have a similar effect to raising the entrainment threshold velocity. The ratio of vertical to horizontal flux can be modified, and made to depend on the clay content of the soil. This results in an increase in dust emissions, but a relative decrease in dust emissions from Australia and Patagonia. The parameterisation of soil moisture also displays differing sensitivities in different regions. Raising the moisture threshold greatly increases the strength of the Patagonian source compared to other regions. Lowering the threshold has greatest effect in the Northern Hemisphere. It is found that the model is largely insensitive to the way in which gusts are parameterised, the precise form of the flux of dust, and the snow cover.

The wet deposition study shows that the model results are very sensitive to the scavenging coefficient used in the model. An increase in scavenging coefficient causes largest changes in regions remote from source regions, for example the polar regions, and in regions of high precipitation, for example over India in the monsoon period.

The model is found to be reasonably sensitive to the way in which the advection is calculated, particularly over regions of low dust concentration. Using a first order advection scheme increases the dust concentration by about 10% over Antarctica; using a flux limiter results in a similar increase. The relatively low resolution of the model means that the dust emissions are being under-simulated.

An increase in resolution from T42 to T106 causes an increase in dust emissions of about 20%. An even higher resolution would be likely to lead to an even larger increase. However, compared to other uncertainties in the model, this is probably not too important.

The case studies are only a qualitative test of the model, but the way in which the model simulates the shape and advection of dust clouds is very encouraging. The precise position and relative intensity of dust storms is not well represented though. The model seems to be at least as good as that of Nickovic *et al.* (2001), who also tested their model with the Asian dust storm of April 1998. The case studies indicate that it should be possible to use the model in a predictive way; forecast wind fields could be used to force the dust model, enabling a dust forecast to be carried out. This could be useful for research organisations such as the Met Office, when planning flights into dust clouds (Haywood *et al.*, 2001). It could also be used to provide warnings of large dust clouds which could pass over urban areas, causing reduction in visibility.

The ten year integration presented in this chapter, shows that the interannual variability of dust production, and atmospheric dust concentration, is large. The standard deviation of ten years' annual mean concentration is 13%, but locally, there is much more variation, with standard deviations up to 80%. The model integration is with a slab ocean, which in general predicts lower interannual variability than a more complex ocean model, and the real world. It is likely that the use of a fully coupled ocean and atmosphere would result in an even higher interannual variability.

An analysis of the source regions in the model is carried out, and it is found that in general, in the tropical deserts, where the soil moisture is very low, it is the windspeed alone which controls the production of dust. At higher latitudes, the soil moisture becomes important, modulating the seasonal cycle of dust production. In the polar deserts, the soil moisture and the snow cover control the seasonal cycle. It is found that Arabia is the region which emits the most dust, followed by the west Sahara, east Sahara, and west Asia.

The model results are compared with data from the University of Miami Aerosol Network. This comparison shows that the model is doing a good job of simulating the seasonal cycle, as well as the magnitude of the dust concentration at the sites of the network. In general, the model is over-simulating dust concentration by a factor of 2.7. The log correlation coefficient of the model and observations is 0.84. The seasonality over the Pacific Ocean is particularly well simulated. Over the Atlantic, agreement is not so good. It is possible that this is due to an over-simulation of North

American dust in these regions, or a mis-representation of the springtime Saharan source.

The results are also compared to the DIRTMAP dataset. Again, agreement is good. On average, there is an under-simulation of deposition by a factor of 1.8. The log correlation coefficient of model and observations is 0.78. In general, there is an over-simulation of deposition in the Arctic, by a factor of about 10. Over Antarctica, the over-simulation is by a factor of about 2.5.

This chapter investigates the characteristics of the dust model, in its almost completely untuned form, and provides an understanding of the processes in the model. The comparison with data highlights the good aspects of the model, as well as pointing to several areas in which the model could be improved. The sensitivity studies suggest ways in which this improvement could be achieved. For example, the primary disagreement between the modelled deposition, and that in the DIRTMAP dataset, is that the model is over-simulating deposition at the poles compared to mid and low latitudes. The deposition study shows that this over-simulation could be decreased by increasing the scavenging coefficient. The undesired effect of dramatically decreasing the absolute deposition could in turn be offset by increasing the ratio of vertical to horizontal flux. In this chapter, a certain, very limited, portion of the parameter space which contains all the combinations of different possible variables in the model, is explored. A vast region is left unexplored. It is almost certain that there exist several combinations of the variables and parameterisations which would give results which agreed very well indeed with all the data. The aim of this chapter has been to catalogue the primary sensitivities of the model, and to carry out a comparison with observations, of the control model, in order to highlight its strengths and weaknesses. Emphasis has been on understanding the main processes which influence the dust cycle, and quantifying their effects.

This chapter is the foundation on which the next chapter is written. The next chapter attempts to simulate, and understand, the dust cycle at the Last Glacial Maximum, and how it is different from that of today, in the framework of a ten year model integration. As in this chapter, a comparison is made of modelled results with observations. The reasons for the increase in dust deposition, as indicated from ocean cores and ice cores, are investigated.

---

## CHAPTER 5

### Modelling the LGM dust cycle

#### 5.1 Introduction

The previous chapter investigated the dust cycle at the present day, using the model developed in chapter 3 as a tool. Sensitivity studies, case studies and a ten year integration, were carried out and analysed. In this chapter, the model is applied to the dust cycle at the Last Glacial Maximum (LGM), 21,000 years ago. As discussed in section 1.3, the LGM was a generally cooler climate than the present day, drier, and less vegetated. Ice-cores, and other paleo data, show that the LGM was also dustier than the present day. There are several reasons why the LGM is studied in this thesis. Among these are that if a model can correctly simulate the observed dust deposition at the LGM, as well as the present day, then one can have more confidence in its general validity, and in particular, in its ability to correctly predict possible future changes to the dust cycle, resulting from climate change. Also, it is of scientific interest to understand *why* there was a greater rate of dust deposition at the LGM. The increase in deposition implies an increase in atmospheric dust loading, and this has implications for the radiative balance at the LGM, and also the importance of indirect effects of dust, mentioned in section 1.2.2. In section 1.4, it is discussed that although previous studies have been able to simulate the observed increase in dust at the poles (Andersen *et al.*, 1998, Mahowald *et al.*, 1999), and have made a start at explaining why the LGM climate should be more dusty than the present day, many questions still remain. Failure to correctly simulate the provenance of LGM polar dust, the relatively short duration of the integrations, and a lack of sensitivity studies and model validation, have cast their conclusions into doubt. Therefore, in this chapter, the dust cycle at the LGM is simulated in a ten year experiment, and the results are analysed using diagnostics introduced in the previous chapter. Emphasis is on understanding the processes involved, and the differences between the two time periods and their causes.

The chapter starts with a description of the model setup for the LGM experiment, and discusses briefly the resulting dust concentrations. An analysis is carried out of the modelled source regions, as

in section 4.4.2, with emphasis on how and why the results are different from those of the present day. The modelled lifetime of atmospheric dust in the LGM and present day experiments is investigated, and this leads on to a comparison, with the DIRTMAP dataset, of the modelled deposition, and ratio of LGM to present day deposition. The deposition is investigated in some detail, particularly at the sites of two polar ice-cores. It is found that an increase in atmospheric dust loading at the LGM is simulated by the model, but that the increase in deposition at high latitudes is not large enough compared to observations. Furthermore, a study of the modelled dust provenance shows that the model fails to simulate the observed Patagonian origin of Antarctic dust. The sensitivity studies, carried out in section 4.2, suggest ways in which the model can be made to better agree with the data. These changes are included in the model, and the resulting simulation is a great improvement. Finally, all the results are summarised, and conclusions drawn.

## 5.2 The ten year experiment

### 5.2.1 Model Setup

To simulate the entire dust cycle at the LGM, the dust model is forced by 6-hourly fields output from the Met Office HadSM3 slab-ocean GCM, running under LGM boundary conditions. These include Peltier (1994) ice sheets, changed orbital parameters, vegetation from the BIOME4 model, a decrease in atmospheric CO<sub>2</sub> concentration from 280ppmv to 200ppmv, and in CH<sub>4</sub> from 690ppbv to 300ppbv. For the slab ocean, the same oceanic fluxes as were calculated for the present day, are assumed to hold, which is in accordance with the standard PMIP experiment for LGM slab ocean models (Joussaume and Taylor, 1995). A comparison made between the LGM slab climate, and that produced with fixed CLIMAP SSTs, carried out with the UGAMP GCM (Dong and Valdes, 1998), indicates that the slab model surface temperatures over land are very similar to the fixed SST temperatures, and that over tropical oceans, the slab SSTs are colder than those in CLIMAP. This may be due to errors in the CLIMAP SSTs (eg Hostetler and Mix, 1999), which are thought to be too warm in the tropics.

The GCM is run at the same resolution as the present day, that is  $3.75^\circ \times 2.5^\circ$  and 19 vertical levels. The dust model is run at the same resolution as the climate GCM which forces it. All other dust-specific parameters, for example the scavenging coefficient, are the same in the two experiments. This model setup is entirely consistent with the setup used in the ten year present day experiment in

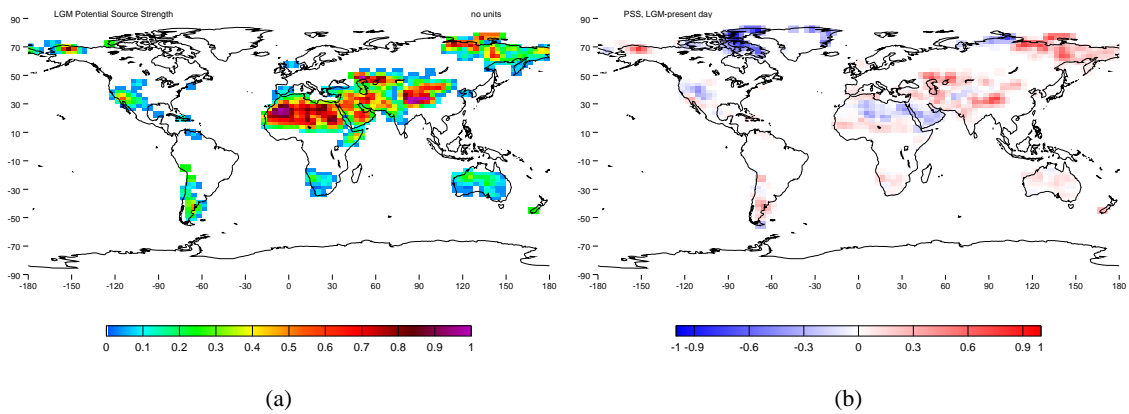


**Figure 5.1:** (a) The Potential Source Strength (PSS) at the LGM, as predicted by BIOME4, using a value of  $L_{max} = 1.2$ . (b) The difference between the modelled LGM and present day PSS.

the previous chapter. The same process could be applied to any other time period, past or future, so long as there existed sensible boundary conditions for the GCM.

To produce a field of LGM potential source strength (PSS), for the ten year integration, the vegetation model BIOME4 is run, forced by modelled LGM climate, output from the standard PMIP run of HadSM3. This climate is corrected by an amount which brings the present day modelled climate into agreement with present day observations. The predicted LGM Leaf Area Index is converted to PSS using equation 3.2, with a value of  $L_{max} = 1.2$ . This field of PSS is shown in figure 5.1, along with the difference between the LGM and present day PSS. In north-east Greenland and northern Canada, there is a large decrease in PSS at the LGM. This is due to the fact that these regions are under the massive Laurentide ice-sheet at the LGM, whereas at the present day, they are ice-free. Similarly, the decrease in LGM PSS at the southern tip of South America is due to the fact that there is a modelled ice-sheet in this region at the LGM. In Alaska and eastern Siberia, there is an increase in PSS. This region is not under ice sheet at the LGM, and there is less precipitation here at the LGM than at the present day, resulting in a decrease in vegetation, and hence an increase in PSS. In general, the increases in potential source strength at the LGM are all in regions of modelled decreases in precipitation, and the decreases in PSS are in regions of increased precipitation. This explains the decreases in PSS over North America, Arabia and the Central Sahara, all of which experience a modelled increase in precipitation at the LGM. Over most other regions, there is a decrease in precipitation, and an increase in PSS, at the LGM.

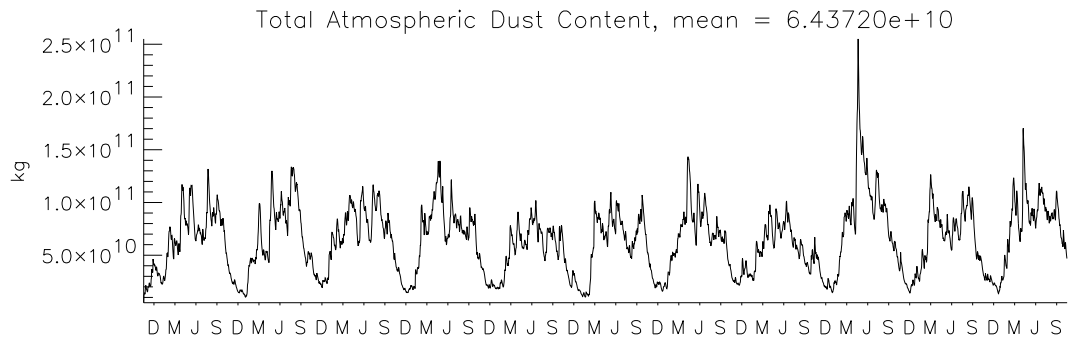


**Figure 5.2:** Timeseries of total atmospheric dust content, from the ten year LGM experiment, plus one spinup year. Ticks on the x-axis mark the 15th day of the months of December, March, June and September.

## 5.2.2 The modelled dust concentration

The field of PSS in figure 5.1(a), along with the wind, temperature, moisture and other fields output from the GCM, are used to force the dust model for a period of ten years, plus a one-year spinup. The resulting timeseries of total atmospheric dust content, is shown in figure 5.2. This is for comparison with the equivalent series for the present day, shown in figure 4.18. After the one year spin-up period, the mean atmospheric dust content is  $6.4 \times 10^{10}$  kg. This is an increase of 62% from the present day value of  $4.0 \times 10^{10}$  kg. The standard deviation of the ten years of annual mean is  $7.8 \times 10^9$  kg, or 12%. The month of minimum atmospheric dust content is December, the maximum is May.

Figures 5.3(a), 5.3(b), and 5.3(c), show the mean dust concentration in DJF, JJA, and the annual mean, respectively. Figure 5.3(d) shows the standard deviation of the annual mean dust concentration, expressed as a percentage of the annual mean. These are for comparison with the present day equivalents, in figure 4.19. In general, the broad seasonality, with a dust concentration maximum in the late spring of each hemisphere, still applies at the LGM, as does the maximum in dust concentration over Arabia and the eastern Sahara in JJA, and the shift in the Saharn plume from southwestwards in DJF and MAM to westwards in JJA. As in the present day case, the interannual variability is large in certain regions, up to 90% of the annual mean over the maritime continent. The spatial distribution of the interannual variability is also similar to that of the present day experiment, with regions of high variability seemingly associated with variability in the transport of dust.

The ratio of LGM to present day dust concentration is shown in figure 5.3(e). This shows that the biggest regional differences in concentration occur over Patagonia and West Asia, where the dust concentration at the LGM is greater than the present day by up to a factor of 5. Associated with the

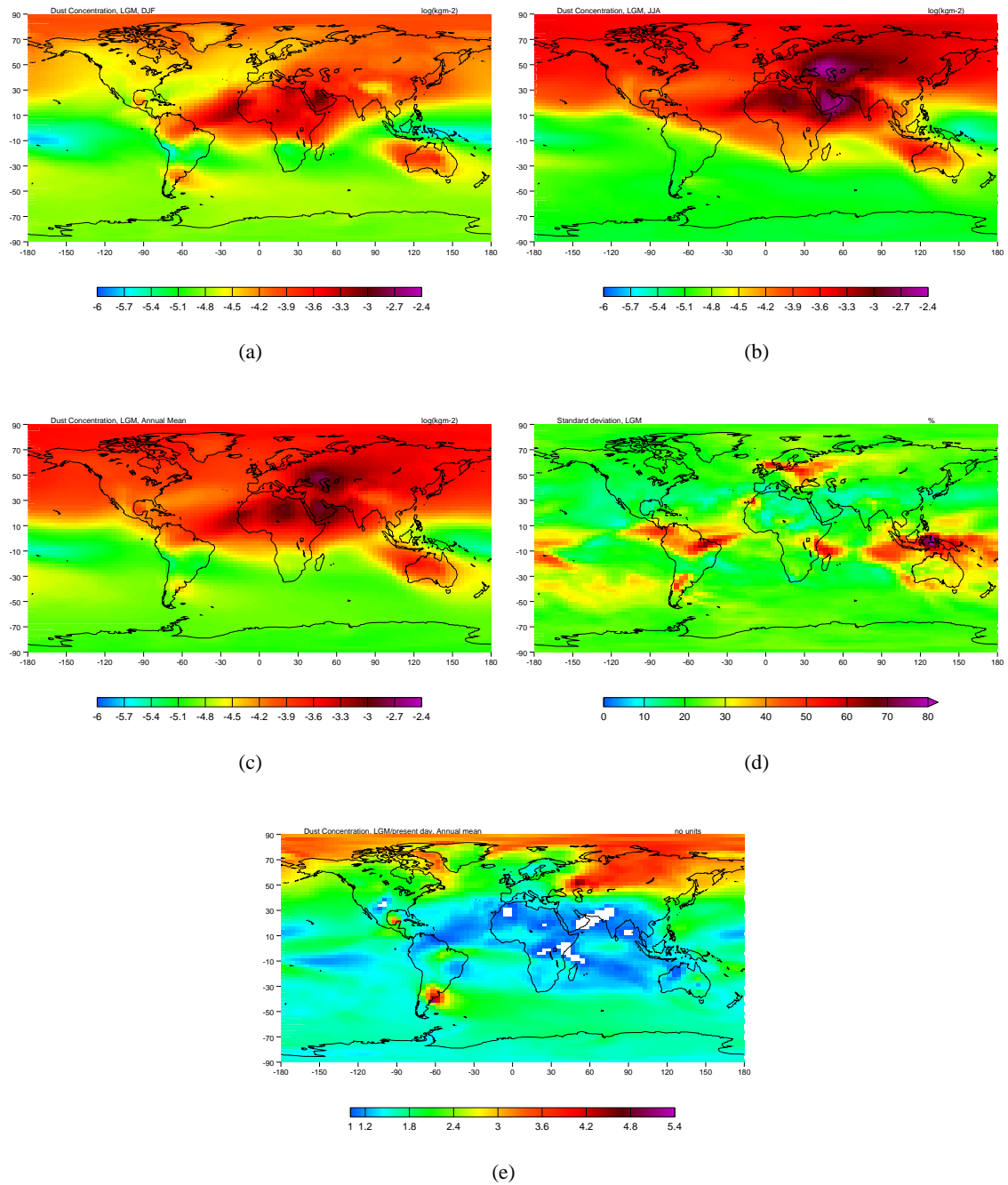


**Figure 5.3:** (a)  $\text{Logarithm}_{10}$  of the mean vertically integrated dust concentration, in units of  $\text{kgm}^{-2}$ , from the LGM 10 year experiment, for DJF, (b) for JJA, and (c) for the annual mean. (d) The standard deviation of the ten years' annual mean dust concentration, expressed as a percentage of the annual mean. (e) The ratio of LGM to present day dust concentrations, from the two ten year experiments. White regions are where there is a decrease in dust concentration.

increase over West Asia, are increases in dust concentration over northern hemisphere high latitudes, of a factor of about 3. In the Southern Hemisphere, increases are less marked, and in particular, over Antarctica, the dust concentration is increased by only 1.5. There is a decrease in dust concentration over south-east Arabia, parts of Africa, and a small decrease in part of North America; however, globally, there is in general an increase in dust concentration.

In the next section, an attempt is made to understand how the dust concentrations shown here, come about, by analysing the source regions separately. In particular, the differences between the LGM and the present day are highlighted.

### 5.2.3 Analysis of source regions

In section 4.4.2, an analysis of the present day source regions was carried out. This analysis is repeated here, for the LGM experiment. Figure 5.4 shows the modelled monthly mean input of dust into the atmosphere, for the regions shown in figure 4.21, in the ten year LGM experiment. The regions are in order of their mean strength at the present day, as in figure 4.23. This final source includes vegetation, snow, wind, gusts and moisture effects. In this section, comments are made on each of the source regions in turn, with emphasis on how the different effects interact to produce the final source which is input into the lowest level of the model, and on how the LGM differs from the present day.

Including vegetation effects alone, the Arabian source at the LGM is decreased by 19% from its present day strength. The modelled wind strength in this region is very similar at the LGM and present day, but the soil is more moist at the LGM, resulting in a decrease in total source of 24%. This means that the Arabian source at the LGM is only the 4th strongest globally. The seasonality of the Arabian source is the same at the LGM as at the present day, with a maximum in July, and minimum in October.

The East Saharan source shows no great change due to vegetation effects alone, but due to an increase in wind speed at the LGM, there is an increase in source strength of 18%. The soil here is more moist at the LGM than the present day, and so the final increase in source strength is 12%. Once again, the seasonality is unchanged from the present day.

In the Western Sahara, there is a slight increase in the vegetative source of 4.5%. With wind effects

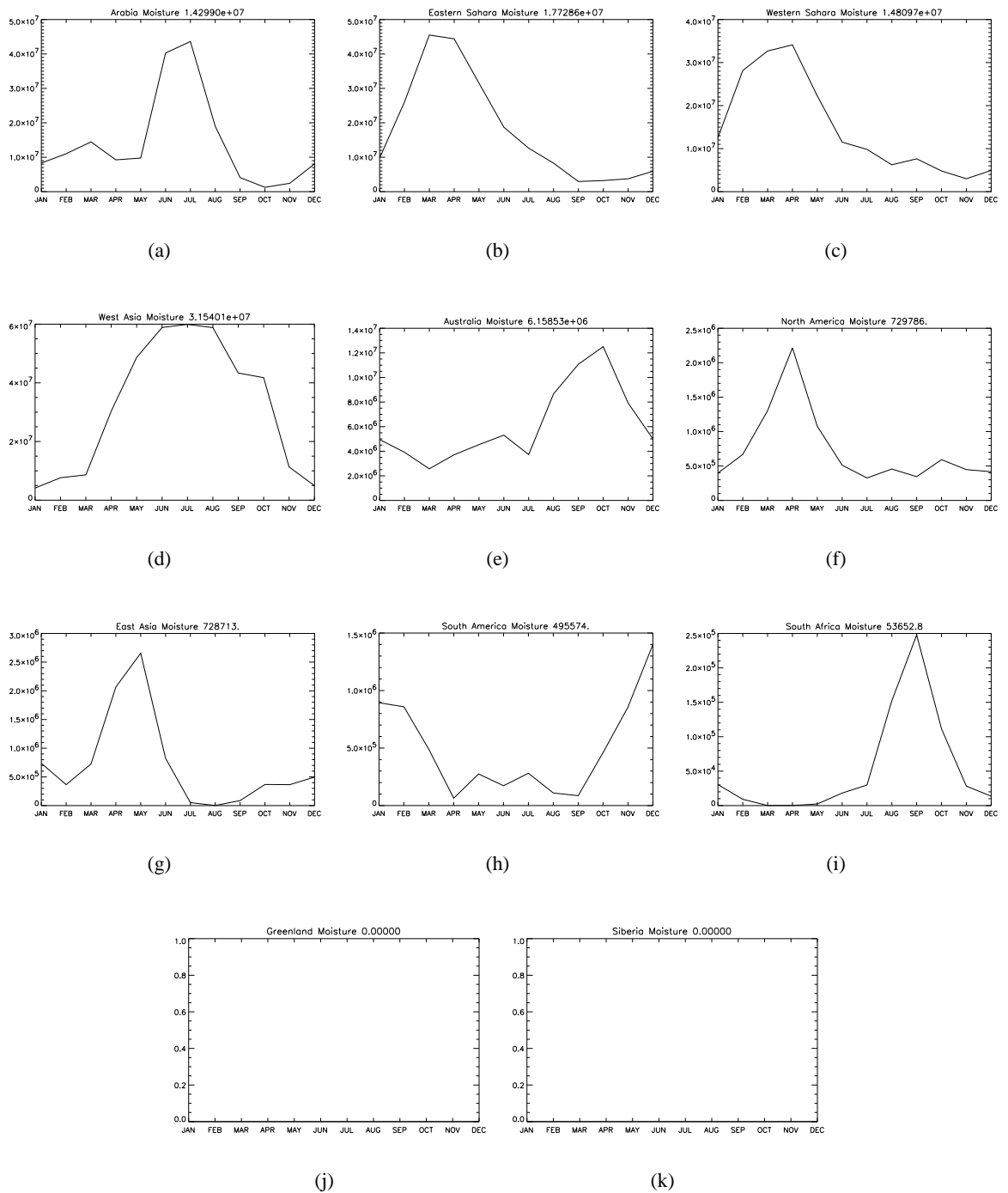


**Figure 5.4:** Modelled dust flux emitted into the atmosphere, in units of kg per half hour, in the ten year LGM experiment, for the source regions of (a) Arabia, (b) east Sahara, (c) west Sahara, (d) west Asia, (e) Australia, (f) North America, (g) east Asia, (h) South America, (i) South Africa, (j) Greenland, and (k) Siberia. Note the differences in scale between the plots. The numbers in the titles show the annual mean dust flux, in kg per half hour.

included, the increase is 13.6%. The drier soil at the LGM increases this further to 16%, but it is the higher LGM wind speed which is primarily causing the increase. The seasonality is mainly unchanged, with a maximum in April, but the secondary maximum in dust production in the present day experiment in August is not present at the LGM.

The West Asian source is greatly increased at the LGM, and becomes the region which emits the most dust globally. This is due to a decrease in vegetation, which causes a 71% increase in source strength, and wind speed effects, which raise this to a 163% increase. The LGM soil moisture is also slightly drier, meaning that the final amount of dust emitted from West Asia at the LGM has increased by 172% of the present day emissions.

The Australian vegetative source strength is almost double that of the present day due to a decrease in vegetation at the LGM. However, the windspeeds are lower at the LGM, resulting in an increase in source of only 72%. Also, the soil is more moist at the LGM, resulting in a final source which is increased by 53%. The seasonality of the Australian source is the same at the LGM as the present day, with a maximum in emissions in October.

In North America, there is a decrease in source due to vegetation effects, of 26%. The wind speed is greater at the LGM, reducing the decrease to 15%. However, the soil is much drier at the LGM, which results in an overall increase of source strength of 55%. At the present day, the soil moisture strongly influences the seasonality of the North American source, but at the LGM, it is the wind speed which is most important, and causes the source to peak in April as opposed to October.

The South African source is dramatically increased due to a decrease in vegetation at the LGM, by 230%. The wind speeds are lower at the LGM though, and so the increase becomes only 13%. Low LGM soil moistures restore the increase up to a final value of 105%. The seasonality of the South African source is unchanged at the LGM, with a maximum in dust production in southern hemisphere spring.

The present day Patagonian source is very weak, in fact the weakest of all the non-polar sources. However, at the LGM, its strength is greatly increased, by a factor of 15.5. There is a vegetative increase in source of 162%. With wind speed effects included, this falls slightly to an increase of 117%. However, it is the decrease in soil moisture at the LGM which is the principal cause of the increase in source; the moisture results in an overall source increase of 1451% of the present day

emissions.

At the LGM, there is no modelled dust emitted from the regions of Greenland and Siberia. The former is covered in the Laurentide ice-sheet, and the latter has a soil which is so moist, that no dust is entrained in the entire ten years of the experiment.

It is found that the effects of gusts, and perhaps more surprisingly, snow cover, are not important factors in changing the seasonality of dust emissions at the LGM. However, the snow cover does have an important effect in decreasing the total amount of dust emissions at the LGM. It is found that different regions have very particular reasons for the increases or decreases in source strength, which can either be due mainly to vegetation, as in the case of Australia, or wind strength, as in the case of the Western Sahara, or moisture, as in Patagonia, or a combination of all three, as in West Asia.

Overall, there is an increase in the total global source strength of 36% at the LGM. This section has shown that this is made up of a complex pattern of increases and decreases, caused by a wide variety of different processes.

#### **5.2.4 The modelled lifetime of dust**

In section 3.2.4, it was shown that the global source strength, atmospheric dust loading, and lifetime of dust, are all linked, and that given two of them, it is possible to calculate the third. For the ten-year experiment, due to the sporadic nature of the modelled dust emissions, a monthly mean dust lifetime is calculated, from the ratio of the monthly mean dust loading to the monthly mean dust emissions. This is plotted in figure 5.5, for the LGM (dashed line), and present day (solid line). The error bars show one standard deviation of interannual variability. The annual mean modelled dust lifetime in the LGM experiment is 15.4 days, which is greater than the present day value of 12.9 days. The increase in lifetime most likely arises from the general decrease in precipitation at the LGM, illustrated in figure 1.5. The standard deviation of the modelled lifetime is large, but the seasonality of the lifetime is clear. At the present day, the minimum lifetimes occur in JJA and DJF. It is probable that the JJA minimum is related to strong modelled precipitation events in the tropics in the Northern Hemisphere, and the DJF minimum is the equivalent for the Southern Hemisphere. In JJA the majority of modelled dust is in the Northern hemisphere, but in DJF there is a significant contribution from Australia. At the LGM, the maximum lifetime is in SON.

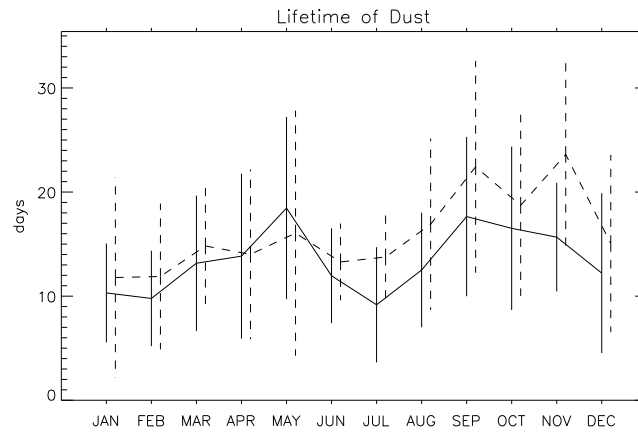


**Figure 5.5:** Annual mean lifetime of dust, in days, in the 10 year LGM experiment (dashed line), and present day experiment (solid line). The error bars show plus and minus one standard deviation of interannual variability. The LGM results are staggered to aid clarity.

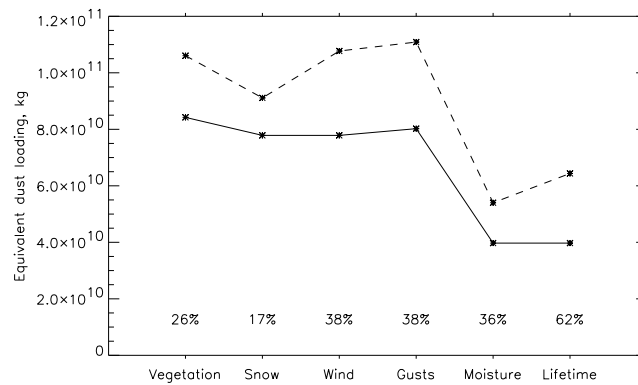


**Figure 5.6:** Annual mean equivalent dust loadings in the present day (solid line) and LGM (dashed line) ten year experiments, given sources calculated from the vegetation, snow, wind, gusts, and moisture effects. Also shown is the actual dust loading (the 'lifetime' loading). The equivalent dust loading is the dust loading, which would result, given the source strength, if the lifetime were that of the present day.

This analysis shows that as well as the increase in source strength, the larger lifetime of dust at the LGM must also contribute to the increase in dust loading. The relative importance of the various effects which combine to cause an increase in atmospheric dust at the LGM, is shown in figure 5.6. The figure shows the total global annual mean source strengths, due to the effects of vegetation, snow, wind, gusts and moisture, for the present day (solid line) and LGM (dashed line). Also shown is the annual mean dust loading, which is the 'lifetime' effect. So that all the effects can be included in one graph, the source effects have been normalised by a factor which converts them from emission rates into 'equivalent dust loadings'. The factor is chosen such that the present day equivalent loading, due to moisture effects, is the same as the lifetime loading. This means that the equivalent loading is the loading which would result, if the lifetime of dust were that of the present day (*i.e.* 12.9 days). The

vegetation and snow values have a further normalisation such that the present day, wind, equivalent loading, is the same as the present day, snow, equivalent loading. The numbers above the x axis show the percentage by which the LGM equivalent loading is greater than that of the present day.

The graph shows that vegetation changes alone, cause an increase in dust loading of 26% at the LGM, the LGM being in general less vegetated than the present day. With snow effects, this increase is reduced to 17%, because there is more snow cover at the LGM. With wind effects included, the increase is of 38%; in general, winds over source regions are stronger at the LGM than at the present day. Gusts have a negligible effect, and moisture acts to reduce the increase slightly to 36%. The lifetime of dust at the LGM is longer than at the present day, and so the final increase in atmospheric dust loading is 62%.

This shows that the decreased vegetation, increased winds, and increased lifetime of dust are all important in producing the increase in global atmospheric dust loading at the LGM. If anything, then the vegetation effect is slightly more important than the wind and lifetime effects, but this is not clear. Neither is it clear how sensitive the results are to the order in which the source terms are calculated, as they interact with each other in a non-linear fashion. However, it is likely that the conclusion of roughly equal importance on vegetation, winds and lifetime, is robust.

### 5.2.5 Comparison with DIRTMAP

It is essential, as with the present day experiment, to validate the LGM experiment with data. There are clearly no satellite comparisons which can be carried out, nor is there any equivalent of the Miami network concentration data. However, there are records of dust deposition, in the DIRTMAP dataset. A similar comparison to that in section 4.4.3 is carried out here, comparing modelled deposition rates to those from observations.

Not all of the present day deposition sites in figure 4.27 have deposition data for the LGM. Figure 5.7 shows the sites which have deposition records at both the LGM and present day, or a record of the change in dust deposition from the present day to the LGM. The sites of Dome C in Antarctica and Camp Century in Greenland have been highlighted with a square, as they are studied in more detail in the next section. Figure 5.8 shows a plot of modelled against observed LGM deposition at the DIRTMAP sites. The comparison at the LGM looks good. The log correlation coefficient is 0.81,

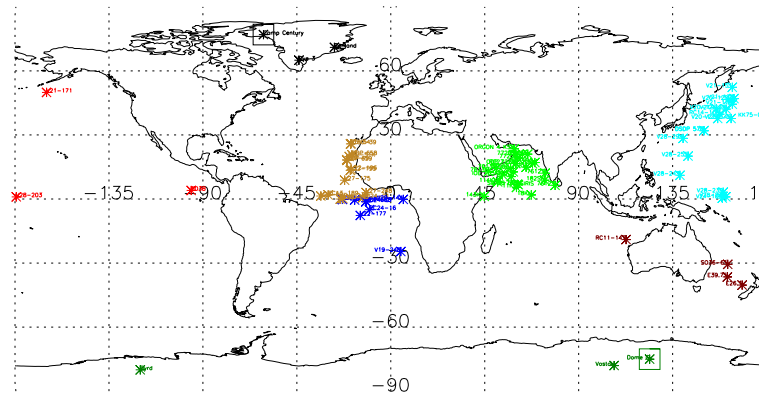


**Figure 5.7:** The sites of the ice-cores and ocean cores in the DIRTMAP database, which have both present day and LGM deposition data, or a record of the increase from LGM to present day. The colours group the data points into the regions of the Arctic (black), the north-east Pacific (red), the North Atlantic (orange), the north Indian (green), the north-west Pacific (light blue), the south Atlantic (dark blue), the south Indian (yellow), the south-west Pacific (maroon), and Antarctica (dark green). The sites of Dome C in Antarctica and Camp Century in Greenland are highlighted with a square.

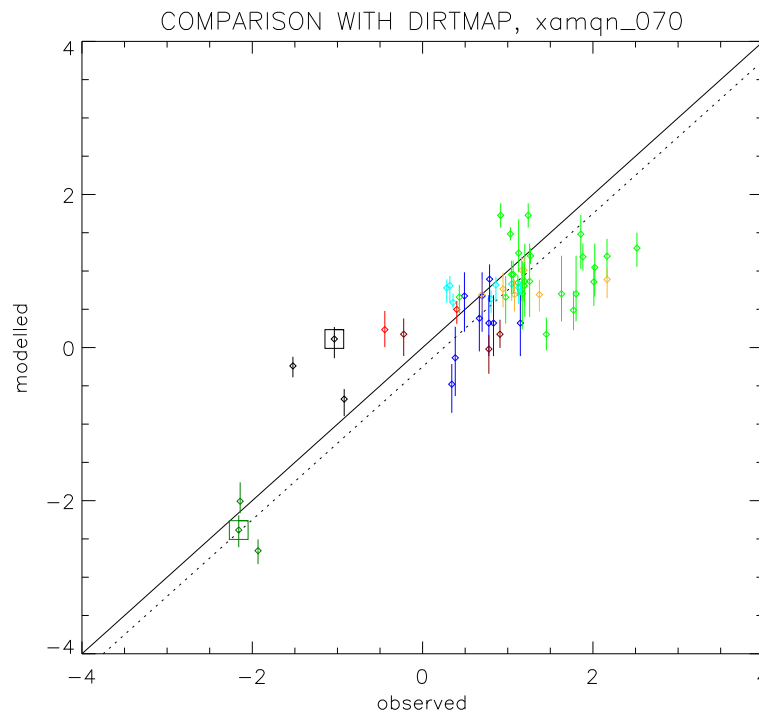


**Figure 5.8:** Modelled versus observed deposition at the LGM at the sites of the DIRTMAP dataset. The units are the logarithm<sub>10</sub> of kg/m<sup>2</sup>/year. The error bars on the modelled results show the maximum and minimum annual deposition from the ten years. The solid diagonal line shows the line of perfect fit. The dotted diagonal line shows the average fraction by which the modelled results disagree with the data. The colours of the points correspond to the colours of the regions in figure 5.7. The boxed points are the sites of Dome C, Antarctica (dark green) and Camp Century, Greenland (black).

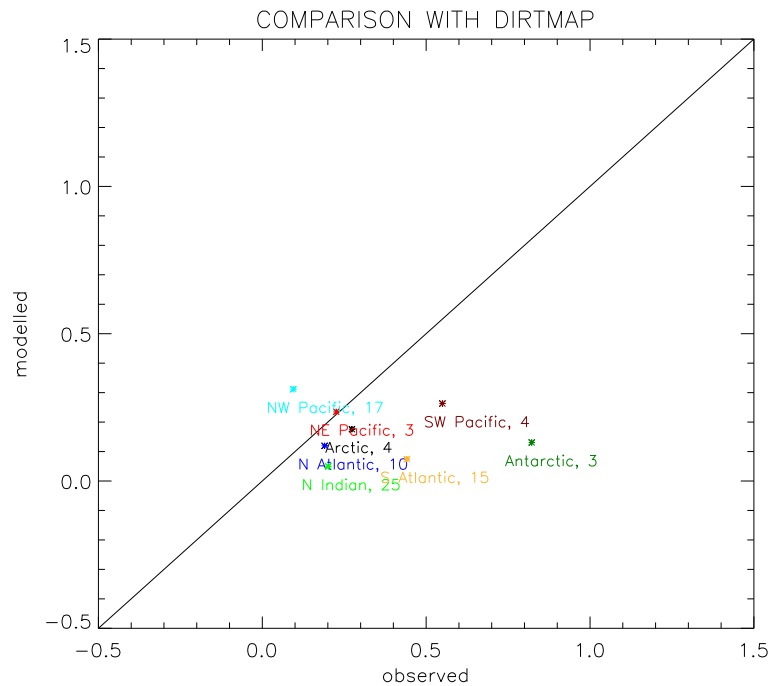


**Figure 5.9:** A comparison of the modelled against observed increases in dust deposition, from the present day to the LGM, in the regions highlighted in figure 5.7. The numbers by each point show the number of data points in that region. Units are the logarithm<sub>10</sub> of the ratio of LGM to present day deposition.

compared to 0.78 at the present day. The modelled deposition is on average less than the observed by a factor of 1.8, which is the same factor as the present day; this error is shown by the dotted line in figure 5.8. The largest systematic regional errors are an over-simulation of deposition over Greenland (black), an under-simulation over the north Indian Ocean (light green), and an under-simulation over the Atlantic (orange and dark blue).

The way in which models have traditionally been tested (eg Andersen *et al.*, 1998, Mahowald *et al.*, 1999), is by how well they simulate observed *changes* in deposition, that is, the ratio of LGM to present day dust deposition. For this analysis, the data points are grouped together into their regions, shown by the different colours in figure 5.7. The average increase or decrease in dust deposition is calculated for each region, and then compared to the equivalent increase or decrease from the model. This comparison is shown in figure 5.9. It shows that although the model is showing an increase in dust deposition in all regions, it is not in general large enough compared to the observations at the DIRTMAP data sites. In particular, the model fails to simulate the large increase in dust deposition observed at the Antarctic cores. This is due to an over-simulation of deposition at the present day; figure 5.8 shows that at the LGM, the agreement with data over Antarctica is good. The observed increases over the North and south Atlantic, and north Indian Ocean are all under-simulated, due

mainly to an under-simulation of deposition at the LGM. Over the north-west Pacific, the increase is over-simulated, due to an underestimate of deposition at the present day.

In summary, the model's biggest weaknesses appear to be that the increase in dust deposition over Antarctica is not large enough compared to observations, and that the deposition over Greenland is over-simulated at both the LGM and present day. The next section investigates possible reasons for this in more detail.

### 5.2.6 Deposition in the ten year experiment

In this section, the deposition in the model is investigated further, and in particular the deposition at the sites of Dome C in Antarctica, and Camp Century in Greenland. These two sites are highlighted with boxes in figure 5.7, and the deposition at the present day and LGM at the sites is highlighted in figures 4.28 and 5.8.

The total deposition at each timestep, can be split into that which comes from dry deposition, that which comes from large scale wet deposition, and that which comes from convective wet deposition. Figure 5.10 shows the relative importance of these different processes, at the present day, and LGM. This shows that the partitioning between the different processes is broadly similar at the LGM and present day. Close to the source regions, and in regions of very low precipitation, dry deposition is a significant process. This is despite the fact that the deposition velocity for particles of this size is small. The model may be sensitive to the order in which the deposition processes are calculated, at present, the dry deposition is calculated first, and so may be relatively over-simulated. The dry deposition process is effective in the source regions, because a large percentage of the total dust loading in these regions is in the lowest model level. Also, in these regions, there is usually very little precipitation. Convective precipitation is the principal remover of dust from the atmosphere in the tropics, and large scale precipitation in mid-latitudes. Unsurprisingly, the partition of convective and large scale removal follows almost exactly the modelled partition of precipitation.

The LGM and present day patterns look very similar, however, there are some differences. At the LGM, dry deposition is the most important mechanism for removal over Antarctica, and in north Greenland, whereas at the present day it is large scale removal which dominates. This is due to a large decrease in the amount of large scale precipitation in these regions at the LGM. At the LGM,

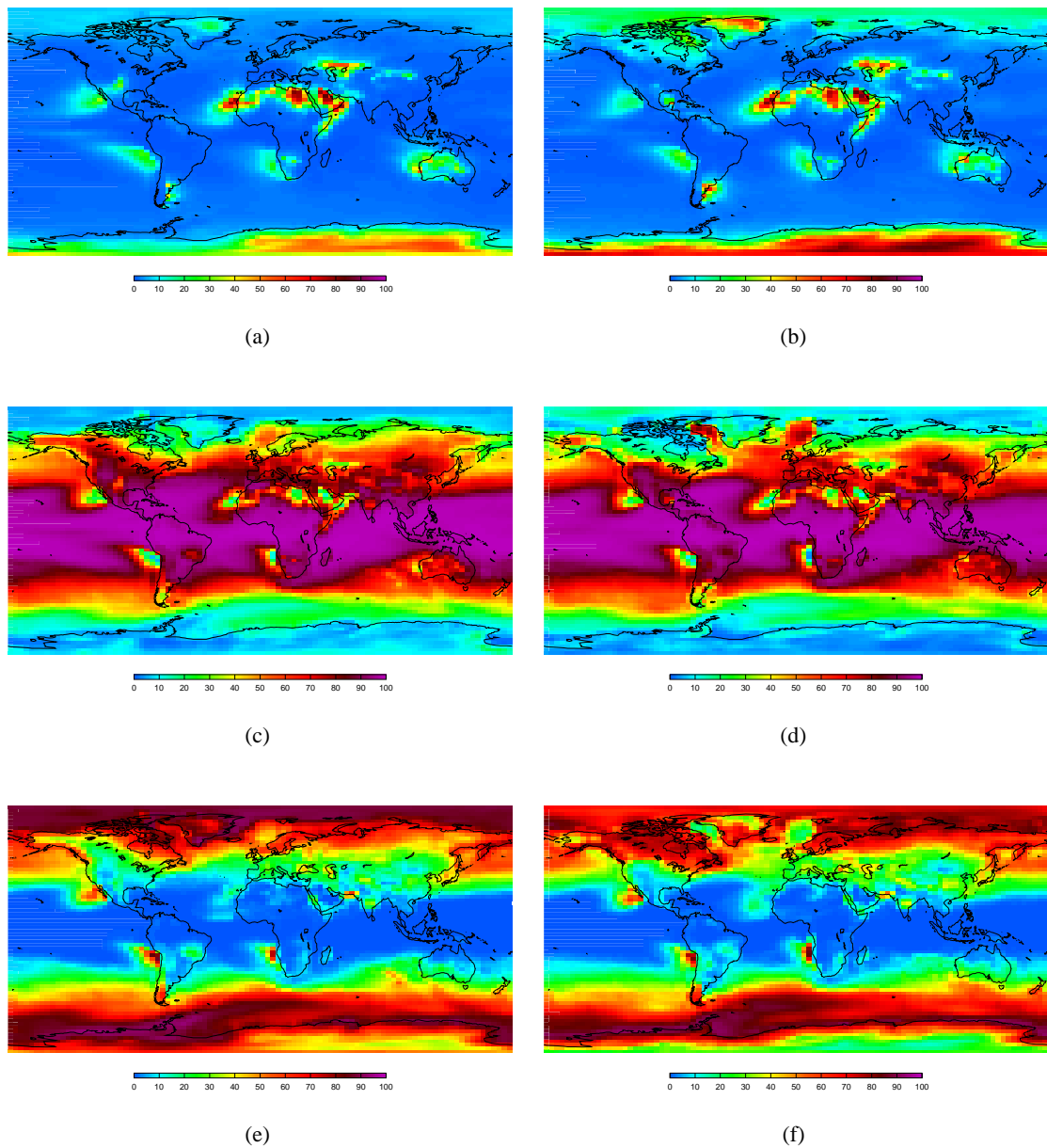


**Figure 5.10:** The percentage deposition which can be attributed to dry deposition (top row), convective deposition (middle row) and large scale deposition (bottom row). The left hand column is for the present day 10 year integration, the right hand column is for the LGM 10 year integration.

	Dry deposition mg/year	Convective deposition mg/year	Large scale deposition mg/year	Total deposition mg/year	Concentration kgm <sup>-2</sup>
present day	0.66 (26%)	0.17 (7.0%)	1.7 (67%)	2.5	0.0021
LGM	1.9 (47%)	0.21 (5.1%)	2.0 (48%)	4.1	0.0035
increase	190%	21%	20%	65%	63%

**Table 5.1:** Modelled dust deposition and atmospheric concentration at Dome C, Antarctica, at the present day and LGM, and the percentage increase from present day to LGM. The numbers in brackets are the percentage of the total deposition which is due to each deposition process.

	Dry deposition mg/year	Convective deposition mg/year	Large scale deposition mg/year	Total deposition mg/year	Concentration kgm <sup>-2</sup>
present day	23 (5.4%)	60 (14%)	340 (80%)	420	0.026
LGM	150 (11%)	730 (57%)	420 (32%)	1300	0.0035
increase	540%	1100%	22%	210%	210%

**Table 5.2:** Modelled dust deposition and atmospheric concentration at Camp Century, Greenland, at the present day and LGM, and the percentage increase from present day to LGM. The numbers in brackets are the percentage of the total deposition which is due to each deposition process.

the convective deposition is very small over the extensive northern hemisphere ice sheets over North America, and large scale removal dominates in these regions, whereas convection is the principal remover at the present day. This is probably due to the very cold LGM surface temperatures suppressing convection. West of Greenland, there is a tongue of convectively-dominated removal of dust at the LGM. This region is not covered by ice sheet, and it could be that the relatively warm temperatures at the sea surface, and very cold air aloft blowing off the nearby ice-sheets, may be triggering convection.

The switch in mechanism, from the present day to the LGM, for dust removal over Antarctica, is highlighted in table 5.1, which shows the modelled dust deposition rate at the site of Dome C ice core, at the LGM and present day, due to the three removal processes. Also shown is the total dust deposition, and the vertically integrated dust concentration at the Dome C site. This shows that the increase in dust deposition at the LGM is of a similar order to the increase in atmospheric dust concentration over Antarctica (65% compared to 63%). At the present day, the deposition at Dome C is primarily due to large scale precipitation processes, with some dry deposition. However, at the LGM, the deposition is equally partitioned between the two processes. The fraction of deposition due to large scale precipitation has gone down, due to a decrease in large scale precipitation in the region. However, why the dry deposition has increased more than the dust concentration itself is not clear. It may be due to the dust being at a relatively lower altitude at the LGM.

An equivalent table, but for Camp Century in Greenland, is shown in table 5.2. As in the Dome C case, the concentration increase and total deposition increase are very similar. However, the reasons for the increase are different. At the present day, it is large scale deposition which is dominating the removal, whereas at the LGM, convective deposition is the most important mechanism. This is due to the tongue of convective precipitation west of Greenland.

In summary, the increase in deposition at these two sites is of very similar magnitude to the increase in concentration. This is true over most of the globe, and in particular in regions of high dust concentration. However, in other regions this relation does not hold, especially at northern hemisphere high latitudes, and the fact that the relation holds at the site of Camp Century is not representative of the region as a whole. This analysis has also shown that dry deposition, large scale and convective deposition, all have important roles in determining the total deposition. This points to the fact that the model results may be very sensitive to the way in which these processes are calculated, both in the GCM, and in the dust model itself. Errors in the calculated deposition at Greenland and Antarctica at the present day may be attributable to errors in the modelled precipitation in this region.

### 5.2.7 Provenance of dust in the ten year experiment

As well as the rate of dust deposition at the sites of ice-cores, in some cases, the mineralogy of the dust has been studied. The ratio of certain isotopes provides a signature of the ice-core dust, which can be compared to the same ratio of soils from potential source regions. As explained in section 1.3.3, this analysis points to a South American provenance of Antarctic dust (Grousset *et al.*, 1992, Basile *et al.*, 1997) at the LGM, and an Asian origin of Greenland dust at the LGM (Biscaye *et al.*, 1997). Section 4.4.2 mentions that, in order to test the modelled provenance of Greenland and Antarctic dust, the model is run for the same ten years as the main experiment, but with only Asian and South American sources. The modelled ratio of Asian and Patagonian dust deposition, to total dust deposition, is shown in figure 5.11, for the LGM ten year experiment. The equivalent for the present day is in figure 4.20.

Because there is relatively little cross-hemispheric transport of dust, it can be assumed that north of about 30°N, all the dust in the provenance run is Asian, and south of 30°S, all the dust in the provenance run is South American. Study of daily animations of the transport of dust, and the study of the relative strengths of the different source regions in section 5.2.3, implies that the majority of

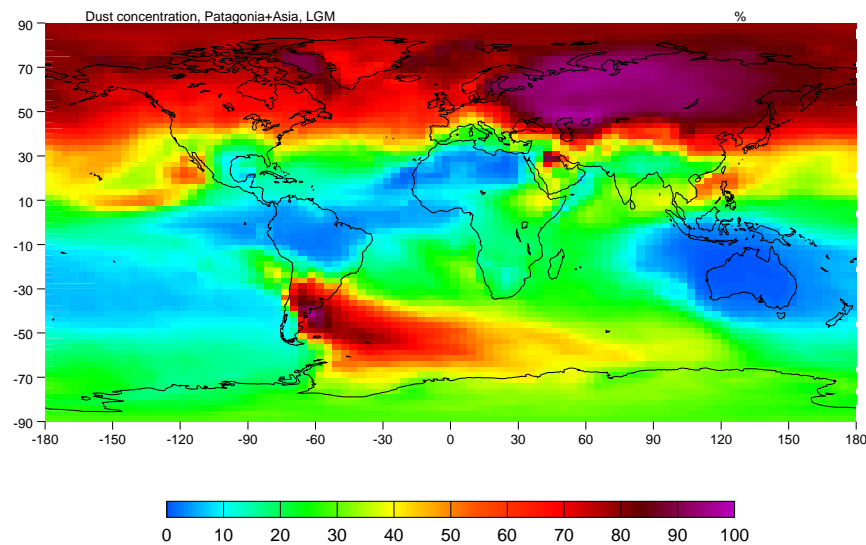


**Figure 5.11:** Ratio of the LGM modelled dust deposition in the South American and Asia-only run, to that in the run including all source regions, expressed as a percentage.

southern hemisphere dust which is not South American, is Australian, and the majority of Northern Hemisphere dust which is not Asian, is from Arabia and the Sahara. However, this analysis can only categorically state that dust either originates from South America and Asia, or does not. The figure shows that although a significant amount of South American dust is deposited close to the source region, elsewhere, and in particular over Antarctica, the modelled contribution of South American dust to the total dust deposition is small. The model is clearly failing to correctly reproduce the observed provenance of Antarctic dust. However, it can be seen that there is a big increase between the present day and LGM; at Dome C, Antarctica, where the mineralogical analysis was carried out, the modelled ratio of South American dust to other dust is 5.2% at the present day, and 30% at the LGM. In the Northern Hemisphere, the Asian source is most important, especially at the LGM. At GISP II, Greenland, the other site with provenance information, the modelled ratio of Asian dust to dust from other regions is 75% at the LGM. This is in better agreement with the provenance information. A further point to be made is that the simulated provenance in these experiments exhibits a reasonably large degree of interannual variability. In one of the ten years of model integration, Patagonian dust at Dome C represented 40% of the total dust deposition, compared to the mean of 30%.

### 5.2.8 Summary of results from the ten year LGM experiment

In summary, the ten year LGM experiment is entirely consistent with the present day experiment, in terms of the way in which the source regions are defined, and the GCM and dust model parameters.

The LGM modelled dust concentration is increased from the present day concentration by 62%, with the largest relative increases being over Patagonia and West Asia. The increase in concentration can be attributed to an increase in source strength, and an increase in the modelled lifetime of dust. The increase in source strength is by 36% of the present day strength, and results from a combination of decreased LGM vegetation and increased LGM winds, although a decrease in soil moisture is important for the Patagonian source. The increase in dust lifetime is due to a decrease in precipitation at the LGM. Overall, the decrease in vegetation, increase in winds, and decrease in precipitation are equally important in determining the magnitude of the resulting increase in atmospheric dust loading.

The modelled LGM deposition shows a good agreement with DIRTMAP deposition data. However, as at the present day, deposition over Greenland is in general over-simulated. In terms of the modelled against observed changes in dust deposition, agreement is not so good. In particular, the modelled increase over Antarctica is not as significant as in the observations, due to an over-simulation of the present day deposition. Furthermore, the provenance of dust in the LGM experiment is not very well simulated compared to mineralogical analysis of ice-core dust. Instead of a Patagonian origin of Antarctic dust, the model has an Australian origin. Over Greenland, agreement with observations is better, with a predominantly Asian origin of dust. A closer investigation of the deposition of dust in the model shows that dry deposition is the predominant mechanism for dust removal close to source regions, that convective precipitation is removing most dust in the rest of the tropics, and that large scale processes dominate at mid and high latitudes. An exception is over Antarctica, and northern Greenland at the LGM, where dry deposition dominates.

### **5.3 Experiments with an increased scavenging coefficient, and a new moisture parameterisation**

The biggest problems with the model results, are an over-simulation of dust deposition over Greenland at both the present day and LGM, an over-simulation of dust deposition over Antarctica at the LGM, and the failure of the model to correctly simulate the provenance of both present day and LGM high latitude dust.

A possible solution to the former two problems, suggests itself from the sensitivity study of wet deposition, presented in section 4.2.3. Figure 4.11(a) shows that an increase in scavenging coefficient

by a factor of 10, results in a modelled dust concentration over both Antarctica and Greenland, which is decreased more significantly than over other regions, in particular, than regions close to the dust sources. Therefore, it is likely that the modelled deposition at the present day, will be in better accordance with data, with a higher value for the scavenging coefficient. A higher value for the scavenging coefficient can also be justified physically. At present, the model completely neglects in-cloud scavenging. This is the process of dust particles acting as CCN, as explained in section 1.2.2. This could be an important process, especially if dust particles become coated with hydrophilic species, such as sulphates. Joussaume (1990) had in-cloud scavenging of dust as the only removal process in her model. An increased scavenging coefficient could be viewed as a way of indirectly parameterising this process. This is sensible, as both in-cloud scavenging and removal by precipitation are likely to occur under the same sort of circumstances. Furthermore, the scavenging coefficients which are presently used in the model, are based on only one field study (Volken and Schumann, 1993), which is very limited. Removal could have been underestimated in this study for a variety of reasons, for example, the raindrops may have been particularly large, or the dust particles which were studied may not have been representative of dust particles in general.

A possible solution to the problem of the provenance of dust, suggests itself from the moisture sensitivity study of section 4.2.2. This shows that by using a threshold moisture parameterisation, in which the threshold is set to be reasonably high, as opposed to using the scheme of Fecan *et al.* (1999), the entrainment of dust from South America is increased more than from other regions. This can also be justified physically. It is possible that during persistent strong wind events, which are likely to entrain dust, any moisture which is in the uppermost layer of soil will evaporate quickly, leaving a dry top layer of soil, which can be entrained more easily. Furthermore, the soil moisture in the model represents an average over a relatively large gridbox, and there are likely to be inhomogeneities within each gridbox. It is possible that those regions within a gridbox which are good sources of dust, are also relatively dry.

Therefore, in this section, the results are presented from an experiment which includes the proposed changes, to both the wet deposition, and moisture parameterisations. The model is run for one year, plus a 3 month spin-up, with all parameters the same as in the 10 year experiment, except for a scavenging coefficient which is 5 times larger, and a threshold parameterisation of moisture effects, as in section 4.2.2, with a threshold value of 10%. As in the 10 year case, this modified experiment is run at the LGM and present day, and with one case of all sources, and one with South American

and Asian sources only. Comparisons are made between results from the one-year experiment, and the equivalent year from the ten-year integration.

The change in moisture parameterisation results in a mean source which is greater than in the control. At the present day, there is an increase of a factor of 2.0, and at the LGM, of a factor of 1.9. The change in source is very spatially inhomogeneous, but the largest absolute increases in dust emissions occur in the West Sahara and Somalia at the present day, and also West Asia and Patagonia at the LGM. The increased scavenging coefficient means that there is more dust removed in the modified experiment. The two effects combine to produce a decrease in total atmospheric dust loading. At the present day, the mean dust loading is  $3.6 \times 10^{10}$  kg compared to  $4.1 \times 10^{10}$  kg in the present day control, and at the LGM, the mean dust loading is  $4.7 \times 10^{10}$  kg compared to  $6.6 \times 10^{10}$  kg in the LGM control. The increase in dust loading in this experiment, from the present day to the LGM, is 29%, which is less than the control increase of 63%. The lifetime of dust in this experiment is 5.9 days at the present day, and 5.8 days at the LGM, compared to the control lifetimes of 14 days and 16 days.

The comparison with the Miami aerosol network is just as good in this experiment as in the control; both having a log correlation coefficient of the modelled against observed concentrations of 0.90. However, the agreement with the DIRTMAP data is improved, with correlation coefficients of 0.81 and 0.87 at the present day and LGM respectively, compared to 0.74 and 0.81 in the control. The main improvement however, is in the change in dust deposition from present day to LGM. For comparison with figure 5.9 from the control, figure 5.12 shows the modelled against observed increases in the regions in figure 5.7. This shows that the new model is simulating the observed increases in dust deposition much better, especially at the high latitude sites of Antarctica. A sensitivity study shows that it is the increase in scavenging coefficient, rather than the change in moisture parameterisation, which is primarily responsible for this improvement. Therefore, it can be said that the large modelled increases in dust deposition over Antarctica at the LGM, are due to the reduced LGM precipitation over the Southern Ocean.

However, the comparison of the modelled changes over the Atlantic has not improved; the increase in deposition is still under-simulated, due to an over-estimate of deposition at the present day in the south Atlantic, and an under-estimate of deposition at the LGM in the north Atlantic. The deposition over Greenland is still over-simulated at both the present day and LGM, and the increases over Greenland are not as great as in the data. Sensitivity studies show that increasing the scavenging coefficient still further, results in a larger modelled increase over both Antarctica and Greenland. Section 4.2.2

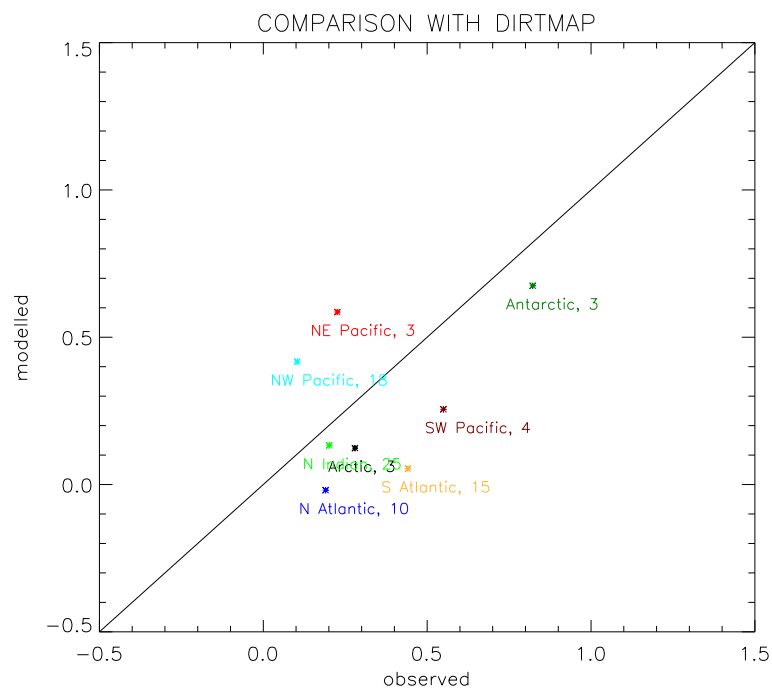


**Figure 5.12:** A comparison of the modelled against observed increases in dust deposition, from the present day to the LGM, in the regions highlighted in figure 5.7. The numbers by each point show the number of data points in that region. The modelled results are from the experiment with an increased scavenging coefficient compared to the control, and a threshold moisture parameterisation, compared to the scheme of Fecan *et al.* (1999) in the control. Units are the logarithm<sub>10</sub> of the ratio of LGM to present day deposition.

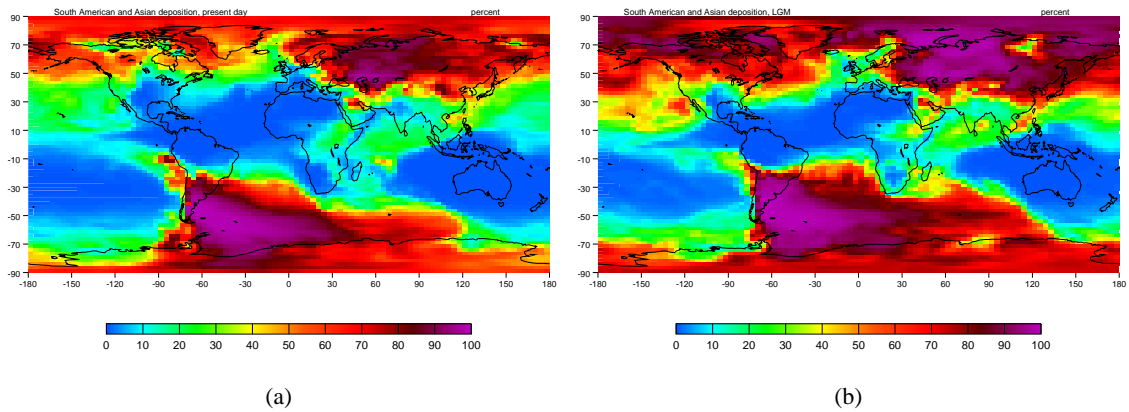


**Figure 5.13:** Ratio of modelled dust deposition from the South American and Asia-only experiment, to that in the experiment including all source regions, expressed as a percentage. (a) is for the present day, and (b) is for the LGM. These experiments are with the increased scavenging coefficient, and threshold moisture parameterisation.

shows that the relative concentration of dust over the Atlantic at the present day can be decreased by raising the threshold friction velocity. If the changes were smaller at the LGM, then raising the threshold friction velocity would result in a larger increase in dust deposition in this region at the LGM, bringing the modelled results closer to the data.

The change in moisture parameterisation means that there are changes to the seasonality of the dust sources in some regions. At the LGM, this effect is small, due to the relatively low LGM soil moisture. However, at the present day, there are changes to the North American source, which peaks in March and April instead of October, to the Patagonian source, which no longer peaks in May and December, but in December alone, and to the West Asian source, which has a large maximum in April, and a secondary maximum in July, as opposed to the other way around.

Figure 5.13 shows percentage of the dust deposition which originates from South America and Asia, at the present day and LGM, in this increased scavenging coefficient experiment. This is for comparison with the results from the control experiment in figure 5.11. At Dome C, where the mineralogical evidence points to a Patagonian provenance at the LGM (Basile *et al.*, 1997), the modified model is predicting that 29% of the dust is Patagonian at the present day, and 72% is Patagonian at the LGM, compared to 4.6% and 20% in the control. Although the strength of the Patagonian source in this modified experiment is increased greatly by the change in moisture parameterisation, it is still less than that of Australia. The fact that despite this, Patagonian dust dominates over Antarctica, shows that there must be a higher transport efficiency from Patagonia to Antarctica, than from Australia to

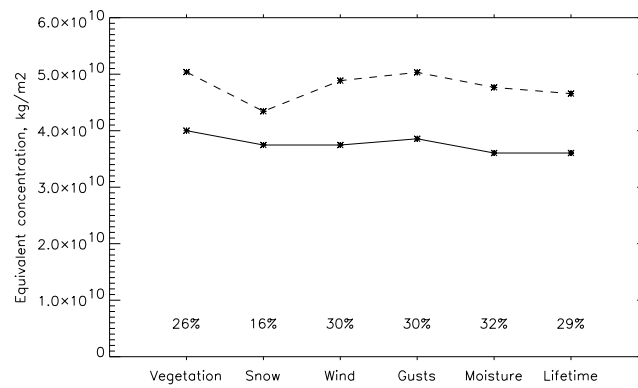


**Figure 5.14:** Annual mean equivalent dust loadings in the present day (solid line) and LGM (dashed line) one year experiments, with increased scavenging coefficient, and modified moisture parameterisation. For sources calculated from the vegetation, snow, wind, gusts, and moisture effects. Also shown is the actual dust loading (the 'lifetime' loading). The equivalent dust loading is the dust loading, which would result, given the source strength, if the lifetime were that of the present day.

Antarctica. This is in agreement with conclusions from the trajectory analysis, carried out in chapter 2.

The change in scavenging coefficient leads to a greater percentage of dust of Asian origin over Greenland. At GISP II, the mineralogical evidence points to an Asian origin of the dust. The modified model is predicting that 80% of the dust is of Asian origin at the LGM, compared to 76% in the control.

The change in moisture parameterisation means that the source regions are no longer strongly influenced by soil moisture. The increase in scavenging coefficient means that dust has a similar lifetime at the LGM and present day. This means that the relative importance of the different processes, which contribute to the global increase in dust loading, has changed. Figure 5.14 shows the equivalent dust loadings for each stage in the source calculation, and the final global dust loading, for this modified experiment. This is for comparison with results from the control experiment, in figure 5.6. This shows that the lifetime effect is no longer contributing to the increase in dust loading at the LGM. As a result, the overall increase in atmospheric dust loading is not as large as in the control. However, the winds and vegetation effects are still as important as each other in producing the increase in atmospheric dust loading at the LGM.

## 5.4 Conclusions

In this chapter, the dust cycle model, as developed in chapter 3, and tested under present day conditions in chapter 4, is applied to the problem of simulating the dust cycle at the Last Glacial Maximum. Firstly, the dust model, in its largely untuned form, is run for ten years, and the modelled deposition compared to that from the DIRTMAP dataset. It is found that the model predicts an increase in atmospheric dust loading of 62% of the present day loading, which can be attributed to a decrease in vegetation, an increase in surface wind strength, and an increase in the lifetime of atmospheric dust. Different processes are responsible for the increase in different regions, and this is highlighted by the source analysis carried out in section 5.2.3. This analysis involves recording the computed dust emission during various stages of its calculation, and can pinpoint the reasons for increases or decreases in regional source strength. However, the model fails to capture the large increases in dust deposition at polar latitudes, and does not reproduce the observed provenance of Antarctic dust.

Many of the variables and parameterisations, which combine together to form the dust model, are not well constrained by observations. Therefore, the failures of the model could be attributed to choices made for certain variables, during the development of the dust model, which were from within a wide range of possible and justifiable choices. Therefore, several studies are carried out, very similar to those in section 4.2, in which the sensitivity of the LGM dust deposition to changes in model variables, is tested. These indicate that an increase of the scavenging coefficient, and a weakening of the influence of soil moisture on dust entrainment, could give better results than the untuned model. It is found that including both of these changes, results in a comparison with the Miami aerosol network which is largely unchanged from the control, and a comparison with DIRTMAP which is improved. In particular, the modified model results in a larger increase in dust deposition over Antarctica than in the control, and also results in a principally Patagonian provenance of LGM Antarctic dust, in accordance with observations.

The lifetime of dust in the modified experiment is very similar at the LGM and present day. This means that the global increase in atmospheric dust loading can be attributed to a combination of vegetation decreases, and wind strength increases. The fact that moisture effects are less significant in the modified experiment means that the increase in Patagonian source strength is due solely to a decrease in vegetation, and the increase in Asian source strength is due to a combination of decreased vegetation, and increased winds. The increase in dust deposition over Antarctica is due partly to the

increase in Patagonian source strength, and but mainly to the decreased precipitation at the LGM over the Southern Ocean and Antarctica, which results in a larger fraction of present day dust being rained out, than LGM dust. The Patagonian origin of Antarctic dust can be ascribed to a higher transport efficiency from Patagonia to Antarctica than from Australia to Antarctica. This supports the trajectory work carried out in chapter 2, which suggests that the reason for the higher transport efficiency, is the more poleward extent of the Patagonian source.

The work presented in this chapter has demonstrated that, within the uncertainties of the dust model, it is possible to reproduce very well both the observed changes in dust deposition, and the implied provenance of polar dust. A set of model parameters has been found which gives results which agree well with the data; it is very likely that this agreement could be improved by changing other variables slightly. It is also possible that there is a completely different set of variables which would reproduce equally well the limited observations of both LGM and present day dust. Therefore, the model results do not necessarily agree well with the data for the right reasons. However, because the model was developed by starting with best-guess estimates of each model parameter, it is likely that the broad conclusions of this chapter are robust.

---

## **CHAPTER 6**

### **Conclusions**

#### **6.1 Principal Findings**

The main result which comes from this thesis, is that a dust model has been developed, which, within the uncertainties in the parameterisations, can simulate well, dust concentrations and deposition at the present day, individual dust events, global changes in dust deposition between the LGM and present day, and the provenance of Antarctic and Greenland LGM dust.

The reasons for the greater atmospheric dust loading at the LGM is found to be a combination of decreased vegetation, and increased winds. Over Antarctica, the relatively large increases in dust deposition are also due to decreased rainfall over the Southern Ocean. A trajectory study shows that changes to the transport of dust, due to changes in the atmospheric circulation, are unlikely to play a role in causing the increases in deposition over Antarctica and Greenland. The Patagonian provenance of Antarctic dust at the LGM is due primarily to the higher transport efficiency from Patagonia to Antarctica, a result coming from both the trajectory and dust modelling work.

#### **6.2 Summary of Results**

There are two main areas of research in this thesis. Firstly, there is an analysis of the transport of dust, from source regions, to the sites of high latitude ice-cores. Secondly, a dust cycle model is developed, and used as a tool to investigate the dust cycle at the present day, and at the Last Glacial Maximum.

### 6.2.1 Analysis of transport

An off-line trajectory model, using LGM and present day wind fields from the Met Office GCM, are used to calculate back trajectories, initialised from the sites of Antarctic and Greenland ice cores. Trajectory densities show that the transport is remarkably similar at the LGM and present day. However, differences are shown up when the number of trajectories which pass over potential source regions are counted. This analysis shows that the transport efficiency from the potential source regions to the polar cores, is more efficient at the present day than at the LGM. This implies that the observed increases in dust deposition over Antarctica at the LGM, are not due to changes in the transport of dust alone. It also shows that the transport is more efficient from Patagonia to Antarctica, than from Australia and South Africa. This is due to the fact that the trajectory density is very zonally symmetric, and Patagonia is further south than the other two sources. This shows that if the Patagonian and Australian sources were of similar strength, and the removal of dust did not favour one source over the other, then Patagonian dust would dominate at the sites of the Antarctic ice cores.

### 6.2.2 Dust cycle modelling

The dust model is built around the chemical tracer model, TOMCAT, and can be forced by output from the Met Office GCM, or ERA data. The dust-specific parameterisations are based largely on previous modelling and observational work. The final model is probably one of the most sophisticated off-line models yet developed.

Unvegetated regions are defined by Leaf Area Indices, output from the BIOME4 vegetation model. This is similar to the approach used by Mahowald *et al.* (1999). Potential source regions are defined using a threshold of Leaf Area Index,  $L_{max}$ . The model results are very sensitive to the value chosen for  $L_{max}$ , particularly over Australia, but they do not change as significantly when a different vegetation model, TRIFFID, is used, at least for the present day simulation. The exact value of  $L_{max}$  is not well constrained by observations. It is a variable which could be used to tune the model results towards observations.

The entrainment of dust depends primarily on the surface friction velocity,  $u^*$ , and a threshold velocity,  $u_t^*$ . The dependence of horizontal dust flux on  $u^*$  and  $u_t^*$  is taken from Marticorena and Bergametti (1995). The results are not sensitive to the exact form of this dependence, but are sensitive to the value

of  $u_t^*$ , particularly in the regions of the north-west Sahara, and Australia. In cases of monotonic particle sizes,  $u_t^*$  is reasonably well constrained by observations. However, it is not known how different sized particles interact to determine  $u_t^*$  in the case of a range of particle sizes. Therefore, the value of  $u_t^*$  is taken to be a constant with particle size. This results in an over-estimate of the fraction of mass in the sub-micron particle size range.

The ratio of the vertical to horizontal flux is another variable which is not well constrained by observations. Initially, a mean value is chosen from the work of Marticorena and Bergametti (1995), but in the ten year and LGM experiments, a lower value is taken to represent the fact that the model is simulating sub-micron particles, which are likely to derive from soils with a high clay content, which may become crusted and resistant to erosion.

The presence of moisture has a large effect on dust emissions in the scheme of Fecan *et al.* (1999), reducing global dust emissions by a half. Moisture has a particularly large effect in reducing emissions from Patagonia. It is found that in order to correctly simulate the provenance of LGM dust, it is necessary to reduce the effect that moisture has on entrainment, by moving over to a threshold scheme, akin to that used by Woodward (2001) and Tegen and Fung (1994). With this scheme in place, LGM emissions from Patagonia are increased from the control by a factor of 9.4, whereas emissions from Australia increase by only 2.3. As a result, LGM dust deposited at the site of Dome C is 72% Patagonian, in accordance with observations of provenance.

The removal of dust in the particle size range simulated in the sub-micron range, by dry deposition, is significant only in regions very close to the source, or in regions of low precipitation, such as Antarctica, and Greenland at the LGM. The scavenging coefficient for wet deposition is determined over the range of particle sizes of interest, by using the model of Slinn (1983), and normalising the results to agree with observations from Volken and Schumann (1993). It is found that by using the resulting scavenging coefficients, it is not possible to reproduce the large increases in dust deposition over Antarctica at the LGM. Sensitivity studies indicate that at the present day, the dust deposition over Antarctica can be reduced greatly by increasing the scavenging coefficient. Therefore, in the final version of the model, the scavenging coefficient is increased by a factor of 5. This results in an increase in dust deposition at the LGM over Antarctica which is in better agreement with observations from the DIRTMAP dataset.

The model is used to simulate two real dust storm events, and performs well, especially in its repre-

sensation of the shape of dust clouds, and their speed and direction of advection. However, the exact location of the origin of dust storms is not well simulated, nor is the relative strength of different events over the globe. A quantitative analysis is not possible, due to the highly non-linear dependence of the satellite retrievals on the optical properties, and altitude, of the dust. The model agrees well at the present day with annual mean dust concentration and dust deposition data from the Miami and DIRTMAP datasets. A comparison is made of the seasonality of dust concentration in the Miami Aerosol Network, and the seasonality of the modelled concentrations. The model simulates seasonality reasonably well, especially over the Pacific. However, it struggles to reproduce the summer maximum in concentration over the Caribbean. Some of the inconsistencies between model and data can be attributed to the sparsity of the observations, both in time and space.

## 6.3 Future Work

The field of dust cycle modelling is relatively new. With advancing technology, progress has been rapid, but there remains a lot of work to be done, and many unanswered questions. This section describes how the work in this thesis can be improved, built upon, and applied to a number of these questions. This includes, extending the trajectory work from chapter 2, improving the dust cycle model, and applying the dust cycle model to a range of new problems. Also included, are suggestions to the dust-observing community, of areas in which improved observations could be of a great help to the modelling community.

### 6.3.1 Extending the trajectory work

In the near future, it is hoped that the trajectory counting analysis can be applied to the remaining three of the five ice-core sites studied in chapter 2. The trajectory densities, such as those in figure 2.4, have been integrated over the potential source regions, for all of the five cores. The results from this analysis are in close agreement with the trajectory counting technique, and are a lot quicker to carry out, but are more sensitive to the precise definition of the potential source regions. The integrating technique indicates that the conclusions described for Dome C and GISP II, that is decreased transport efficiency at the LGM, and a transport favouring Patagonian provenance of Dome C dust, and Asian and North American provenance of GISP II dust, will carry over to the other Atlantic and Greenland

cores.

Work is currently underway, in collaboration with the British Antarctic Survey, on analysing a further 5 Antarctic ice-core sites. The aim of this work is to investigate whether dust from these sites is all likely to have the same dust source, so that large spikes in dust signals can be used to synchronise the timing of the records in each core.

Back trajectories, initialised at two tropical ice core sites, have already been calculated. The transport of dust to these tropical cores is of shorter range than to the Antarctic and Greenland cores, due to the close proximity of their likely sources. It is therefore likely that the transport is highly dependent on local topography and weather systems, which are unresolved by the GCM, and so these cores do not lend themselves to this type of analysis. However, the trajectories do shed light on some interesting differences between the present day and LGM circulation, in particular the weaker LGM monsoon circulation.

An extension of this trajectory work is to record the modelled precipitation along each trajectory. Those trajectories which experienced high levels of precipitation could be discounted, thereby parameterising the effect of wet deposition of dust. However, it may be found that these effects are best examined in the framework of the dust cycle model; the real purpose of the trajectory work being to isolate transport processes alone.

A further extension of the trajectory work is in the field of water isotope analysis. The fraction of isotopes of oxygen and hydrogen are used as a proxy for temperature in ice-cores. One of the fundamental assumptions of interpreting the isotopic record, is that the sources of these isotopes has not changed dramatically over the climate record. The northern Pacific has a different  $\delta^{18}\text{O}$  than the northern Atlantic, and so if the circulation changed to favour transport from one source, to another source, then the calculated change in isotopic fraction would also change, leading to an anomalous inferred temperature change. This analysis has been carried out, using back trajectories initialised at GISP II in Greenland, and potential source regions of the north Atlantic and north Pacific, at the LGM and present day (Lunt and Valdes, 2000). It indicates that such a shift in source region does not occur, and that the ratio of Atlantic and Pacific water isotopes stays the same at the LGM and present day.

To tie in the back trajectory analysis with the forward dust cycle modelling, a test could be made of the reproducibility of the trajectory work by the dust model. In section 3.3.1, the dust model is run

with regional source strengths based purely on the vegetation, and a simple radioactive type decay of dust. This same source could be applied to the dust model, but with the LGM circulation. If the dust model and trajectory model were in agreement, then the concentration of dust at the Antarctic and Greenland sites should be less at the LGM than at the present day. Any disagreement would probably be due to weaknesses in the Prather advection scheme in the dust model, and would point to a possible reason for the difficulties which the model has in reproducing the DIRTMAP data over Antarctica.

### 6.3.2 Improvements to the dust model

There are several ways in which the dust model parameterisations, or the diagnostics which are used to analyse it, could be improved. The list below is by no means exhaustive, but gives an indication of those which are likely to have the largest effect.

#### Parameterisations

Satellite data, such as that from TOMS, and observations of dust storm activity, point to the fact that there are several ‘hot-spots’ of dust emissions, which are on a smaller spatial scale than implied from the modelled fields of potential source strength. Section 1.1.1 highlights the Bodele depression in Chad, and Lake Eyre in Australia, as two such regions, and mentions that it has been noted that these regions have a high silt content, and are in general of lower altitude than their surroundings. At present, the dust model does not include any treatment of these regions. Recently, other modellers have attempted to include parameterisations of these hot-spots (eg Tegen, 2001) into their models. In order to achieve better agreement with satellite data for the present day, it is probably necessary to include a similar parameterisation in this dust model. An approach which could be used is that of Tegen (2001), in which global topography, along with a hydrology model, which estimates the extent of lakes at different time periods, is used to predict the extent of the hot-spots. This method is good because it can be applied to a variety of time periods, and is not limited to the present day. The effect of such a parameterisation would be to increase the dust emissions from these hot-spots; emissions from other regions may have to be reduced to compensate.

Another effect which is neglected in this dust model, is the seasonal variability of vegetation; at present, an annual mean leaf area index is used to define the potential source regions. This could

potentially be a large effect, particularly at high latitudes (Pye, 1987). This effect could be included in the model relatively easily, by using monthly mean output from the BIOME4 model. An alternative approach would be to move over to the TRIFFID vegetation model, which can run interactively with the HadSM3 GCM, responding to, and influencing, climate variability. The transition over to the TRIFFID model should be reasonably easy; section 4.2.1 shows that at the present day, in the annual mean, the results do not vary much from those of BIOME4, so the model should not require any major tuning. However, there may be more significant differences at the LGM. It may also be worth considering alternative parameterisations of Potential Source Strength, not necessarily solely based on leaf area index

At present, the model includes a parameterisation of the effects of gustiness, which attempts to capture the effect of sub-gridscale winds. However, the modelled gusts are not particularly strong. This may be due to the fact that the parameterisation was developed mainly for use over oceans, and in regions of high precipitation. In this dust model, the entrainment is occurring over deserts, and so the gustiness is small. It is probable that a new approach is needed if small scale effects such as haboobs are to be included in the model. This could be based on an indicator of convective activity other than precipitation, for example the vertical profile of  $\theta$ . This would increase the modelled wind speed, even in desert regions.

Yet another effect which has been neglected in this model is that of roughness elements. These non-erodible elements both cover up part of the soil beneath, and take up part of the momentum of the wind, which would otherwise be available for particle entrainment (Marticorena and Bergametti, 1995). The effect of these elements is therefore to reduce dust entrainment. Marticorena *et al.* (1997) have applied this to the western Sahara, using observations of roughness, and found that it gives a much better comparison with satellite data than using a single value, as is used in this model. The problem with an approach such as this, is that as yet, the information required on roughness is not available on a global scale. However, when this becomes available, it should be included in the dust model. It is not clear how different the LGM roughness would be compared to the present day. The work by Marticorena *et al.* (1997) shows that the effect is likely to be to reduce dust emissions more from the north of the Sahara than the south. Similarly, work by Shao and Leslie (1997) points to a way in which the effects of bombardment could be parameterised, rather than by a constant threshold velocity as in this case. This parameterisation could be applied along with a threshold friction velocity which varied with particle size, and with a vertical to horizontal flux ratio which depends on soil clay

content.

## Diagnostics

In conjunction with the present day and LGM ten year runs, parallel experiments were run, in which only the source regions of South America and Asia emitted dust. This enabled a provenance field to be generated, which showed the fraction of atmospheric dust which was of South American or Asian origin. This could easily be extended by carrying out further experiments including other source regions. Ideally, many experiments would be carried out, each representing dust from one of the source regions in figure 4.21. This would result in a much better understanding of the dust cycle, providing the ability to relate the global dust concentration to the global source regions. This information could also be used to test the model against measurements of provenance. So far, these have only been used in the Antarctic and Greenland cases, where measurements of provenance suggest a Patagonian and Asian source respectively, but recently, similar provenance measurements have been made on dust from various ocean sediments (Gideon Henderson, Department of Earth Sciences, Oxford, *pers. comm.*, 2001), and on dust from the Cape Verde Islands (Jerome, 2001). As shown in section 5.2.7, this data can provide a very stern test of dust models. Unfortunately, this sort of calculation is expensive, as the time taken for the model to run varies approximately linearly with the number of tracers, and the model already takes three weeks to run a ten year integration. However, it is felt that the benefits outweigh this computer problem, and future model runs will include this more expensive, but important, provenance information. As explained in section 1.2.1, this provenance information is also very important when attempting to calculate radiative effects, due to the strong dependence of optical properties of dust with source location.

Figure 4.22 shows the modelled dust source of North America, as each successive source parameterisation is applied to the region. This, and also figure 5.6, which applies on a global scale, implies that the extent of the snow cover is having a significant effect on the dust source, at both the present day and LGM, and also on the ratio of LGM to present day total dust emissions. However, this snow cover is predominantly in regions of high soil moisture, and so if the source parameterisations were calculated in a different order, with snow cover last, then it would appear to be a very small effect. In the future, it is necessary to investigate the effect of the order of the calculation in more detail; it may be more sensible to calculate the sources in a different order, with the most important first, and the least important last.

Except in the early stages of the model development, the vertical structure of the dust concentration has not been investigated in great detail. A good framework in which this could be investigated is the Asian dust case study of section 4.3.2. There are numerous data, principally from lidar measurements, of the vertical structure of the dust cloud, at various stages of its evolution (eg Murayama *et al.*, 2001). It is important to get the vertical structure of the dust correct, so that the horizontal advection is also well simulated. However, it is especially important if the dust fields are to be used for radiative calculations in the long wave, where the effect of dust is particularly sensitive to height.

### 6.3.3 Suggestions for improved observations

Throughout this thesis, a recurring theme has been how ill-constrained the model is by observations, both at a process level, and on a global scale. One of the natural extensions of this work is to make suggestions of specific observations, which would help to constrain the model parameterisations and results.

The simulation of dust entrainment could be improved greatly if it was known how the threshold friction velocity for particle entrainment,  $u_t^*$ , is dependent on the particle size distribution of the parent soil. To date, observational work has concentrated on monotonic parent soils (eg Marticorena and Bergametti, 1995), and so in this model, a constant value is taken for  $u_t^*$ . This leads to an over-estimation of the amount of dust in the sub-micron size range. The dependence of particle entrainment on soil moisture is also badly constrained. Studies are needed to investigate the effects of winds blowing for long periods of time over moist soil, and possibly drying out the uppermost layer. Also, the soil moisture itself which is simulated by the GCM is very hard to validate, due to a lack of observations. A global soil-moisture dataset would be a very useful tool to aid this validation. Similarly, a global dataset of soil size distribution, including information on the particle size distribution of sub-micron particles, would be a great improvement to the extrapolation method which is carried out in this, and all, dust models. Another parameter for which there is a dearth of observations, is the scavenging coefficient for dust particles of various sizes, shape, and mineralogy. It would be a great help to have extensive observations of below-cloud, and in-cloud scavenging of dust particles, including the effects of different types of precipitation, *i.e.* convective and large-scale, and the effect of solid, compared to liquid, precipitation. This would enable a better representation of wet-deposition in the dust model.

It has been found that the observations of dust concentration, and dust deposition, have aided in the validation of the model results. However, the information obtained from the provenance data (eg Basile *et al.*, 1997), proved to be an even more stringent test of the model's ability to correctly simulate the dust cycle. This suggests that more of this analysis should be carried out, especially in regions where the origin of the dust is uncertain. Examples are the northern Atlantic, and north-east Pacific, where provenance information, obtained from dust in sediment cores, could help constrain the strength of the North American dust source relative to the Saharan and East Asian sources. Furthermore, this sort of observational data represents an average over several decades, and is more suited to the climate simulations of the dust cycle which have been carried out in this thesis, rather than true present day observations, like the Miami Network, or satellite data, which include anthropogenic land-use changes.

### 6.3.4 Extending the dust cycle modelling work

In the short term, the modified version of the model, including the threshold moisture parameterisation, and increased scavenging coefficient, will be run for a further ten years, at both LGM and present day, to bring them into line with the standard ten year runs. This would ensure that the results were not sensitive to interannual variability. In addition to this, more sensitivity studies could be carried out, particularly on the LGM experiment. These could point to further improvements which could be made to the model, for example to the value of  $L_{max}$ . The previous section mentioned that the source strength diagnostics are dependent on the order in which they are calculated, and are dependent on each other, and this causes some ambiguities on the relative importance of the changes in wind, source, moisture and precipitation in bringing about changes in dust concentration and deposition between the LGM and present day. These problems could be overcome by running several versions of the model, with different combinations of present day and LGM vegetation, winds, moisture and precipitation. These would be similar to the experiment carried out by Mahowald *et al.* (1999), in which, as well as the present day and LGM runs, they carried out an integration with present day potential source strength, and LGM winds. The sensitivity of the results to using a quicker, but less accurate advection scheme, has been shown to be low, at the present day. If this is the case at the LGM also, as seems likely, then the experiments above could be run with the quicker scheme. This would also allow the experiments to be carried out with a larger number of size bins, and allow, for example, a threshold friction velocity which varies with particle size.

So far in this thesis, and also for all previous dust work, concentration has focused on the present day and the LGM. It remains unknown how well models can reproduce other time periods, compared to data such as that in figure 1.3, from the Vostok ice core. This could be an important extra test of the model, especially because of potential 'tuning' of the model to get the correct LGM results. Different periods would act as an independent test of the model. The dust model has been developed in such a way that it is relatively simple to apply to other time periods. Indeed, the dust model has already been run for a year, under climate conditions from 15,000 years ago, from a COHMAP project members (1988)-style HadSM3 integration. The results from this initial study are not encouraging. Timeseries of dust deposition, such as that from the Vostok ice-core, show that one would expect the dust deposition at polar latitudes to be intermediate between the present day and LGM values. However, the model is simulating a higher deposition than the LGM over Greenland, and a lower deposition than the present day over Antarctica. Initial investigation shows that the BIOME4 model is very sensitive to the changed climate, and is predicting a large desert in Central Asia, which emits a huge amount of dust, and is predicting an increase in vegetation in Australia and Patagonia, greatly reducing the source strength. There clearly remains a vast amount of work to be done in this area. It may be that TRIFFID would perform better than BIOME4 at this time period. The problems may also result from errors in the GCM simulation of this time period, which also highlights another problem, namely the climate model. The simulations carried out in this thesis, and all published dust cycle modelling work, has used either prescribed SSTs, or slab ocean models. A more realistic test of the model would be to use a fully coupled atmosphere-ocean simulation (eg Hewitt *et al.*, 2001). Such runs, for several time periods, will soon be available.

In addition to other past climates, future climate scenarios could be investigated. This would be interesting in the context of the radiative forcing of dust. If the net effect of atmospheric dust is a cooling, and future anthropogenic land-use changes lead to increased desertification and therefore increased atmospheric dust loading, then the dust could result in a partial off-setting of the warming effects of increased greenhouse gases.

This leads on to the radiative effects of dust. These were discussed in section 1.2. The most obvious application of the dust model, is to use the resulting dust fields to calculate radiative forcings. To do this, estimates would be needed of the refractive index of dust across a wide range of wavelengths. Initially, Mie theory could be used to calculate extinction coefficients, single scattering albedo and asymmetry parameter, assuming spherical particles. The radiative forcings could be calculated using

a radiative code such as that of Edwards and Slingo (1996). This is the approach used by previous dust modellers (eg Tegen *et al.*, 1996, Woodward, 2001). The next step would be to run the dust model within the GCM, rather than off-line, so that the direct radiative effects of dust could feed back into the GCM. This would be most interesting with a coupled ocean-atmosphere GCM, such as HadCM3. The process of transferring to an in-line model would probably take some time, but would be made easier by the fact that the model has already been run with modelled winds from the GCM. Using the model to calculate radiative effects will also aid the comparison of modelled data with observations. Observational data of optical depth, such as that from the Aeronet network, could be used to further validate the model.

So far, little work has been carried out on modelling the indirect effects of dust on a global scale. At present, Watson *et al.* (2000) are using the fields of dust deposition from Mahowald *et al.* (1999), to estimate the indirect effect of dust on the productivity of marine phytoplankton, and the resulting implications for draw-down of atmospheric CO<sub>2</sub> at the LGM. However, it has been suggested that these dust deposition fields are too large, particularly over the Southern Ocean (Maher and Dennis, 2001). The fields of dust deposition predicted by the dust model developed in this thesis, agree better with data over Antarctica, and so are possibly more realistic over the Southern Ocean as well. These revised deposition fields may affect the results of the Watson *et al.* (2000) study.

A long term goal would be to include the dust model as part of a climate model which could be run over an entire glacial-interglacial cycle. It would be fascinating to investigate to what extent mineral dust could be reacting to, and controlling, the entire earth system.

---

## APPENDIX A

### Empirical expression for the collision efficiency, $E$

In the dust model, we use the expression described by Slinn (1983) for the collision efficiency,  $E$ , between a raindrop and an aerosol particle. It is based on dimensional analysis and some observational data.

$$\begin{aligned}
 E = & \frac{4}{ReSc} [1 + 0.4Re^{1/2}Sc^{1/3} + 0.16Re^{1/2}Sc^{1/2}] \\
 & + 4\phi[\omega^{-1} + (1 + 2Re^{1/2})\phi] \\
 & + \left(\frac{\rho_d}{\rho_p}\right)^{1/2} \left(\frac{St - S}{St - S + \frac{2}{3}}\right)^{3/2}
 \end{aligned} \tag{A.1}$$

where

$$\begin{aligned}
 S &= \frac{1.2 + \frac{1}{12} \ln(1 + Re)}{1 + \ln(1 + Re)} \\
 Re &= D_d U_d \rho_a / 2\mu_a && \text{Reynolds number of raindrop} \\
 Sc &= \mu_a / \rho_a D && \text{Schmidt number of collected particle} \\
 St &= 2\tau(U_d - u_p) / D_d && \text{Stokes number of collected particle} \\
 \phi &= d_p / D_d && \text{ratio of diameters} \\
 \omega &= \mu_d / \mu_a && \text{viscosity ratio} \\
 \tau &= \frac{D_p^2}{18\mu_a} && \text{relaxation time}
 \end{aligned}$$

and where  $D_d$  is the diameter of the droplet,  $d_p$  is the diameter of the aerosol particle,  $D$  is the aerosol diffusivity,  $U_d$  is the speed of the falling raindrop,  $u_p$  is the speed of the aerosol particle,  $\rho_a$  is the density of air,  $\rho_d$  is the density of the raindrop,  $\rho_p$  is the density of the aerosol particle,  $\mu_a$  is the viscosity of the air, and  $\mu_d$  is the viscosity of the raindrop.

The first term in equation A.1 is due to Brownian diffusion, the second is due to interception, and the third is due to inertial impaction.

---

## APPENDIX B

### Resistance analogue approach to dry deposition

Dry deposition at the surface can be characterised by considering a deposition velocity,  $v_d(z)$ , which relates the downwards flux of particles towards the surface,  $F(z)$ , to the particle concentration,  $C(z)$ . At a reference height,  $z_0$ ,

$$F(z_0) = v_d(z_0)C(z_0). \quad (\text{B.1})$$

The deposition velocity is equal to the sum of the Stoke's settling velocity,  $v_s$ , and a turbulent deposition velocity,  $v_t$

This appendix describes how  $v_t$  and  $v_d$  are calculated. It is based on the discussion and model of Seinfeld and Pandis (1998).

Turbulent deposition can be viewed as two separate processes; the transport of particles by diffusion through the surface layer, and transport by Brownian motion through the quasi-laminar sub-layer. Both these processes are driven by the gradient in particle concentration throughout the layers. This implies the utility of an analogue with electricity for modelling turbulent deposition, because in an electric circuit the flow of electricity is driven by gradients in potential. An electrical potential difference is analogous to a difference in particle concentration, and an electrical current is analogous to the particle flux. Furthermore, the surface layer is considered to have a characteristic resistance,  $r_a$ , and the laminar sub-layer to have a resistance  $r_b$ . These resistances have units of  $\text{sm}^{-1}$  and are equal to the reciprocals of the turbulent velocities in the two layers,  $v_a$  and  $v_b$ .

The method for parameterising dry deposition described here is based on this analogy. A circuit is constructed, representing the process of dry deposition, and consisting of resistances, particle concentrations (potentials) and fluxes (currents). The total resistance of the circuit,  $r_t$ , is then calculated. This total resistance is the reciprocal of the dry deposition velocity,  $v_d$ .

At the top of the surface layer, for the particle flux,  $T_2$ , we have that

$$T_2 = \frac{C_2 - C_1}{r_a} \quad (\text{B.2})$$

and at the top of the laminar sub-layer, for the particle flux,  $T_1$ , that

$$T_1 = \frac{C_1 - C_0}{r_b}. \quad (\text{B.3})$$

The total particle flux,  $F$  is equal to the sum of the flux due to the turbulence,  $T$ , and the flux due to sedimentation,  $S$ . Unlike transport due to turbulence, sedimentation is not driven by the gradient of particle concentration, but by the absolute value of concentration. Therefore we have the equivalent circuit shown in figure B.1a.

$T_1$  and  $T_2$  are given by equations B.2 and B.3. The sedimentation flux at the top of the surface layer,  $S_2$  is given by

$$S_2 = C_2 v_s. \quad (\text{B.4})$$

Similarly, at the top of the laminar sub-layer,

$$S_1 = C_1 v_s. \quad (\text{B.5})$$

Mass continuity gives that the total particle flux,  $F$ , must be constant throughout the surface layer and laminar sub-layer, so that

$$F = T_2 + S_2 = T_1 + S_1. \quad (\text{B.6})$$

The circuit in figure B.1a can be represented by an equivalent circuit consisting of one resistance,  $r_t$ , through which a particle flux  $F$  flows. This equivalent circuit is shown in figure B.1b. The resistance,

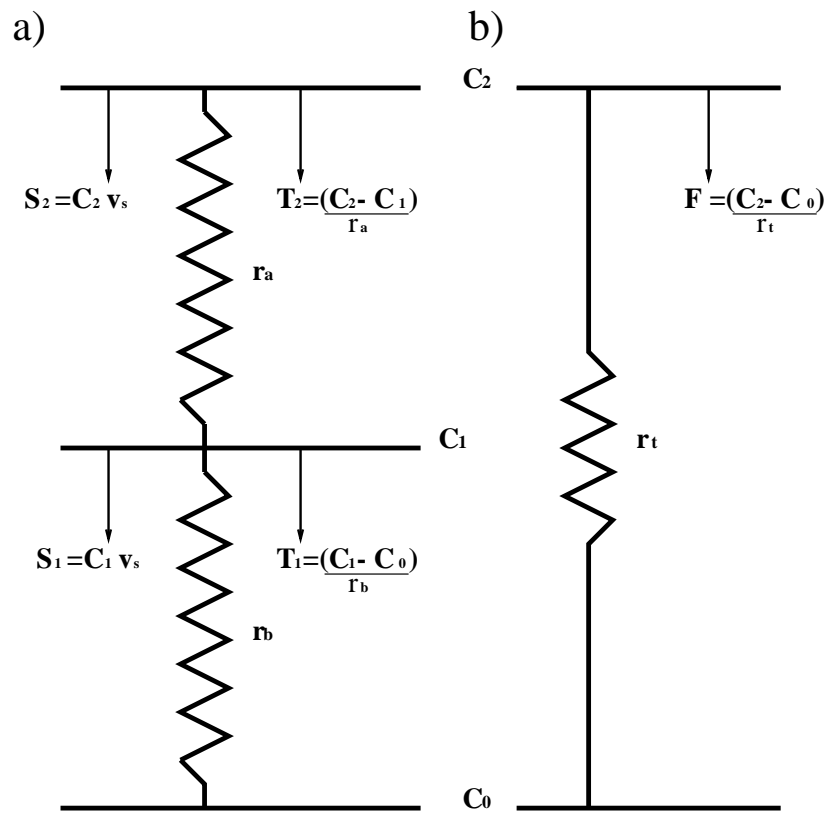


**Figure B.1:** (a) Circuit representing the process of dry deposition, showing the aerodynamic resistance,  $r_a$ , and the quasi laminar resistance,  $r_b$ .  $S_2$  and  $S_1$  are the sedimentation fluxes at the top of the surface and laminar sub-layers, respectively.  $T_2$  and  $T_1$  are the turbulent fluxes. (b) is the equivalent circuit, comprising of a single resistance,  $r_t$ , which is the reciprocal of the deposition velocity,  $v_d$ , and a single flux,  $F$ .

$r_t$  can be found by equating the particle fluxes in the two circuits.

$$\frac{C_2 - C_0}{r_t} = \frac{C_2 - C_1}{r_a} + C_2 v_s = \frac{C_1 - C_0}{r_a} + C_1 v_s \quad (\text{B.7})$$

It is assumed that all the particles which come into direct contact with the surface are deposited immediately, so that  $C_0 = 0$ . Then

$$\frac{1}{r_t} = \frac{1}{r_a + r_b + r_a r_b v_s} + v_s \quad (\text{B.8})$$

$r_t$  is equal to the reciprocal of the dry deposition velocity,  $v_d$ . All that remains is to obtain expressions for the resistances  $r_a$  and  $r_b$ .

$r_a$  can be calculated assuming a neutral atmosphere. This leads to

$$r_a = \frac{1}{\kappa u_*} \ln \left( \frac{z_0}{z} \right) \quad (\text{B.9})$$

where  $\kappa$  is the von Karman constant,  $z_0$  is the roughness length, and  $z$  is a reference height (the centre of the lowest model level).

$r_b$  can be related to Brownian diffusion and impaction at the surface due to gravity, via the semi-empirical expression given by Seinfeld and Pandis (1998).

$$r_b = \frac{1}{u_* (Sc^{-2/3} + 10^{-3}/St)} \quad (\text{B.10})$$

where  $Sc$  is the Schmidt number, and  $St$  is the Stokes number. The Stokes number can be written  $v_s u_*^2 / g\nu$ , the Schmidt number is defined by

$$Sc = \nu / D \quad (\text{B.11})$$

where  $\nu$  is the kinematic viscosity of air and  $D$  is the molecular diffusivity of the dust particles. The

diffusivity is calculated by

$$D = \frac{kTC_c}{6\pi\mu r_p} \quad (\text{B.12})$$

where  $k$  is Boltzmann's constant, and  $r_p$  is the particle radius.  $C_c$  is the Cunningham correction factor, which accounts for the relatively long mean free path at high altitudes (Seinfeld and Pandis, 1998):

$$C_c = 1 + \frac{\lambda}{r_p} (1.257 + 0.4e^{-1.1r_p/\lambda}) \quad (\text{B.13})$$

where  $\lambda$  is the mean free path of air molecules.

---

## References

- Andersen, K. K., Armengaud, A., and Genthon, C. (1998). Atmospheric dust under glacial and interglacial conditions. *Geophysical Research letters*, **25**, 2281–2284.
- Bagnold, R. A. (1941). *The physics of blown sand and desert dunes*. Methuen.
- Basile, I., Grousset, F. E., Revel, M., Petit, J. R., Biscaye, P. E., and Barkov, N. I. (1997). Patagonian origin of glacial dust deposited in East Antarctica (Vostok and Dome C) during glacial stages 2, 4 and 6. *Earth and Planet. Science Let.*, **146**, 573–589.
- Berger, A. (1979). Insolation signatures of quaternary climatic changes. *Il Nuovo Cimento*, **2(c)**, 63–87.
- Bisal, F. and Nielsen, K. F. (1962). Movement of soil particles in saltation. *Can. J. Soil. Sci.*, **42**, 81–86.
- Biscaye, P. E., Grousset, F. E., Revel, M., Van der Gaast, S., Zielinski, G. A., Vaars, A., and Kukla, G. (1997). Asian provenance of glacial dust (stage 2) in the Greenland Ice Sheet Project 2 ice core, Summit, Greenland. *J. Geophys. Res.*, **102(C12)**, 26765–26781.
- Bohren, C. F. and Huffman, D. R. (1983). *Absorption and Scattering of light by small particles*. John Wiley and Sons.
- Boyd, P. W., Watson, A. J., and coauthors (1994). Testing the iron hypothesis in ecosystems of the equatorial Pacific Ocean. *Nature*, **371**, 123–129.
- Chatenet, B., Marticorena, B., Gomes, L., and Beegametti, G. (1996). Assessing the microped size distributions of desert soils erodible by wind. *Sedimentology*, **43(5)**, 901–911.
- Chepil, W. S. (1945). Dynamics of wind erosion. *Soil Science*, **60**, 305–320;397–411;475–480.
- Chepil, W. S. (1956). Influence of moisture on erodibility of soil by wind. In *Proceedings soil sci. soc. Am.* (20), pages 288–292.
- Chipperfield, M. P. and Nikiforakis, N. (1998). Implementation of the weighted average flux advection scheme in SLIMCAT. Technical Report 46, UGAMP.
- Chipperfield, M. P. and Simon, P. (1996). The TOMCAT offline transport model. part II: Dynamics and advection. Technical report, CGAM.
- Claquin, T. (1999). *Modelisation de la mineralogie et du forçage radiatif des poussières desertiques*. Ph.D. thesis, Paris University VI.
- Claquin, T., Sculz, M., and Balkanski, Y. J. (1999). Modeling the mineralogy of atmospheric dust sources. *J. Geophys. Res.*, **104**, 22243–22256.
- CLIMAP project members (1981). Seasonal reconstructions of the Earth's surface at the last glacial maximum. *Map and Chart Ser. MC-36*.

- COHMAP project members (1988). Climatic changes of the last 18,000 years: observations and model simulations. *Science*, **241**, 1043–1052.
- Connelley, W. M. and Cattle, H. (1994). The Antarctic climate of the Unified Model. *Antarctic Science*, **6**(1), 115–122.
- Cox, P. M., Betts, R. A., Bunton, C. B., Essery, R. L. H., Rowntree, P. R., and Smith, J. (1999). The impact of new land surface physics on the GCM simulation of climate and climate sensitivity. *Climate Dynamics*, **15**, 183–203.
- Cox, P. M., Betts, R. A., Jones, C. D., Spall, S. A., and Totterdell, I. J. (2000). Acceleration of global warming due to carbon-cycle feedbacks in a coupled climate model. *Nature*, **408**, 184–187.
- Crosta, X., Pichon, J. J., and Burckle, L. H. (1998). Reappraisal of Antarctic seasonal sea-ice at the last glacial maximum. *Geophysical Research letters*, **25**, 2703–2706.
- Cullen, M. (1993). The unified forecast/climate model. *Meteorological Magazine*, **122**, 81–94.
- de Noblet, N. I., Prentice, I. C., Joussaume, S., Texier, D., Botta, A., and Haxeltine, A. (1996). Possible role of atmosphere-biosphere interactions in triggering the last glaciation. *Geophysical Research letters*, **23**, 3191–3194.
- Deardorff, J. W. (1970). Convective velocity and temperature scales for the unstable planetary boundary layer and for Rayleigh convection. *Journal of Atmospheric Science*, **27**, 1211–1213.
- Dong, B. and Valdes, P. J. (1998). Simulations of the last glacial maximum climates using a general circulation model: Prescribed versus computed sea surface temperatures. *Climate Dynamics*, **14**, 571–591.
- Edwards, J. M. and Slingo, A. (1996). Studies with a flexible new radiation code. I: choosing a configuration for a large scale model. *Q. J. R. Meteorol Soc*, **122**, 689–719.
- FAO/UNESCO (1974). Soil map of the world. 1:5,000,000.
- Fecan, F., Marticorena, B., and Bergametti, G. (1999). Parameterisation of the increase of aeolian threshold wind friction velocity due to soil moisture for arid and semi-arid areas. *Annales Geophysicae*, **17**, 149–157.
- Gates, W. L. (1992). AMIP: The atmospheric intercomparison project. *Bull. Amer. Met. Soc.*, **73**, 1962–1970.
- Genthon, C. (1992). Simulations of desert dust and sea-salt aerosols in Antarctica with a general circulation model of the atmosphere. *Tellus B.*, **44**, 371–389.
- Gibson, J. K., Kallberg, P., Uppala, S., Hernandez, A., Nomura, A., and Serrano, E. (1997). ERA description. ECMWF Re-Analysis Project Series, 1, Reading, UK.
- Gillette, D. A., Adams, J., Muhs, D. R., and Khil, R. (1982). Threshold friction velocities and

- rupture moduli for crusted desert soils for the input of soil particles into the air. *J. Geophys. Res.*, **87**, 9003–9015.
- Greeley, R., Blumberg, D. G., and Williams, S. H. (1994). Field measurements of active windblown sand. In The Desert Research Institute, editor, *Abstract of the Workshop on Response of Eolian Processes to Global Change*. Occas Pap 2 Reno Nev 1994.
- Gregory, D. and Rowntree, P. (1990). A mass flux convection scheme with representation of cloud ensemble characteristics and stability dependent closure. *Monthly weather Review*, **118**, 1483–1506.
- Gregory, D., Kershaw, R., and Inness, P. (1997). Parameterization of momentum transport by convection. II: Tests in a single-column and general circulation models. *Q. J. R. Meteorol Soc.*, **123**, 1153–1183.
- Grousset, F. E., Biscaye, P. E., Revel, M., Petit, J. R., Pye, K., Joussaume, S., and Jouzel, J. (1992). Antarctic (Dome C) ice-core dust at 18 k.y. B.P.: Isotopic constraints on origins. *Earth and Planet. Science Let.*, **111**, 175–182.
- Hansen, J. E. and Travis, L. D. (1974). Light scattering in planetary atmospheres. *Space Science Review*, **16**, 527–610.
- Haxeltine, A. and Prentice, I. C. (1996). BIOME3: An equilibrium terrestrial biosphere model based on ecophysical constraints, resource availability, and competition among plant functional types. *Global Biogeochemical Cycles*, **10**, 693–710.
- Hays, J. D., Imbrie, J., and Shackleton, N. J. (1976). Variations in the Earth's orbit: Pacemaker of the ice ages. *Sedimentology*, **194**, 1121–1132.
- Haywood, J. M., Francis, P. N., Glew, M. D., and Taylor, J. P. (2001). Optical properties and direct radiative effect of Saharan dust: A case study of two Saharan dust outbreaks using aircraft data. *J. Geophys. Res.*, **106**(D16), 18417–18430.
- Herman, J. R., Bhartia, P. K., Torres, O., Hsu, C., Sefor, C., and Celarier, E. (1997). Global distribution of UV-absorbing aerosols from Nimbus 7/TOMS data. *J. Geophys. Res.*, **102**, 16911–16922.
- Hewitt, C. D., Broccoli, A. J., Mitchell, J. F. B., and Stouffer, R. J. (2001). A coupled model study of the last glacial maximum: Was part of the North Atlantic relatively warm? *Geophysical Research letters*, **28**, 1571–1574.
- Hostetler, S. W. and Mix, A. C. (1999). Reassessment of ice-age cooling of the tropical ocean and atmosphere. *Nature*, **399**, 673–676.
- Hotta, S., Kubota, S., Katori, S., and Horikawa, K. (1984). Sand transport by wind on a wet sand surface. In *Proceedings 19th Coastal Engineering Conference*, pages 1265–1281.
- Houghton, J. T., Ding, Y., Griggs, D. J., Noguer, M., v-d Linden, P. J., Dai, X., Maskell, K., and Johnson, C. A., editors (2001). *Climate Change 2001: The Scientific Basis*. Cambridge University

- Press.
- Husar, R. B., Prospero, J. M., and Stowe, L. L. (1997). Characterisation of tropospheric aerosols over the oceans with the advanced very high resolution radiometer optical thickness operation product, NOAA. *J. Geophys. Res.*, **102**, 16889–16901.
- Husar, R. B., Tratt, D. M., and coauthors (2001). Asian dust events of April 1998. *J. Geophys. Res.*, **106**(D16), 18317–18330.
- Iversen, J. D. and White, B. R. (1982). Saltation threshold on Earth, Mars and Venus. *Sedimentology*, **29**, 111–119.
- Jabouille, P., Redelsperger, J.-L., and Lafore, J. P. (1996). Modification of surface fluxes by atmospheric convection in the TOGA COARE region. *Monthly weather Review*, **111**, 308–319.
- Jerome, A. (2001). Oxygen isotopes in single dust grains: A proxy for the source area of Saharan dust events. Presented at the 8th Scientific Assembly of IAMAS.
- Joussaume, S. (1990). Three-dimensional simulations of the atmospheric cycle of desert dust particles using a general circulation model. *J. Geophys. Res.*, **95**(D2), 1909–1941.
- Joussaume, S. (1993). Paleoclimatic traces: An investigation using an atmospheric general circulation model under ice age conditions. I. Desert dust. *J. Geophys. Res.*, **98**, 2767–2805.
- Joussaume, S. and Taylor, K. E. (1995). Status of the Paleoclimate Modelling Intercomparison Project (PMIP). In *Proceedings of the first international AMIP scientific conference*, pages 425–430.
- Jouzel, J., Lorius, C., Petit, J. R., Genthon, C., Barkov, N. I., M., K. V., and Petrov, V. M. (1987). Vostok ice core: a continuous isotope temperature record over the last climatic cycle (160,000 years). *Nature*, **329**, 402–408.
- Jouzel, J., Barkov, N. I., Barnola, J. M., Bender, M., Chappelaz, J., Genthon, C., Kotlyakov, V. M., Lipenkov, V., Lorius, C., Petit, J. R., Raynaud, D., Raisbeck, G., Ritz, C., Sowers, T., Stievenard, M., Yiou, F., and Yiou, P. (1993). Extending the Vostok ice-core record of paleoclimate to the penultimate glacial period. *Nature*, **364**, 407–412.
- Kallberg, P. (1997). Aspects of the re-analyzed climate. ECMWF Re-Analysis Project Series, 2, Reading, UK.
- Kalshnikova, O. (2001). Modeling the scattering phase function of non-spherical dust particles for remote sensing applications. Presented at the 8th Scientific Assembly of IAMAS.
- Kaplan, J. O. (2001). *Geophysical Applications of Vegetation Modeling*. Ph.D. thesis, Department of Ecology, Lund University.
- Kohfeld, K. E. and Harrison, S. P. (2001). DIRTMAP: The geological record of dust. *Earth Science Reviews*, **54**, 81–114.

- Krinner, K. and Genthon, C. (2001). Tropospheric transport of continental tracers towards Antarctica under varying climatic conditions. submitted to *Tellus B*.
- Lawson, T. J. (1971). Haboob structure at Khartoum. *Weather*, **26**, 105–112.
- Leemans, R. and Cramer, W. P. (1991). The IIASA database for mean monthly values of temperature, precipitation and cloudiness of a global terrestrial grid. Technical Report 46, International Institute of Applied Systems Analyses, Laxenburg.
- Levin, Z. (2001). On the interactions of mineral dust particles and clouds. Presented at the 8th Scientific Assembly of IAMAS.
- Levin, Z., Ganor, E., and Gladstein, V. (1996). The effects of desert particles coated with sulfate on rain formation in the eastern Mediterranean. *Journal of Applied Meteorology*, **35**(9), 1511–1523.
- Liao, H. and Seinfeld, J. H. (1998). Radiative forcing by mineral dust aerosol: sensitivity to key variables. *J. Geophys. Res.*, **103**(D24), 31637–31645.
- Louis, J. F. (1979). A parametric model of vertical eddy fluxes in the atmosphere. *Boundary Layer meteorology*, **17**, 187–202.
- Lunt, D. J. and Valdes, P. J. (2000). Tracer transport to ice core sites at the LGM and present day. Presented at the 25th General Assembly of EGS.
- Lunt, D. J. and Valdes, P. J. (2001). Dust transport to Dome C, Antarctica, at the last glacial maximum and present day. *Geophysical Research letters*, **28**, 295–298.
- Maher, B. and Dennis, P. F. (2001). Evidence against dust-mediated control of glacial-interglacial changes in atmospheric CO<sub>2</sub>. *Nature*, **411**, 176–179.
- Mahowald, N., Kohfeld, K. E., Hansson, M., Balkanski, Y., Harrison, S. P., Prentice, I. C., Schulz, M., and Rodhe, H. (1999). Dust sources and deposition during the last glacial maximum and current climate: A comparison of model results with paleodata from ice cores and marine sediments. *J. Geophys. Res.*, **104**(D13), 15895–15916.
- Marticorena, B. and Bergametti, G. (1995). Modeling the atmospheric dust cycle: 1. Design of a soil-derived dust emission scheme. *J. Geophys. Res.*, **100**, 16415–16430.
- Marticorena, B., Bergametti, G., and Aumont, B. (1997). Modeling the atmospheric dust cycle: 2. Simulation of Saharan dust sources. *J. Geophys. Res.*, **102**, 4387–4404.
- Martin, J. H. (1990). Glacial-interglacial CO<sub>2</sub> change: The iron hypothesis. *Paleoceanography*, **5**(1), 1–13.
- Martin, J. H., Coale, K. H., and coauthors (1994). Testing the iron hypothesis in ecosystems of the equatorial Pacific Ocean. *Nature*, **371**, 123–129.
- McKendry, J. G., Hacker, J. P., Stull, R., Sakiyama, S., Mignacca, D., and Reid, K. (2001). Long-range transport of Asian dust to the Lower Fraser Valley, British Columbia, Canada. *J.*

- Geophys. Res.*, **106**(D16), 18361–18370.
- McKenna-Neumann, C. and Nickling, W. G. (1989). A theoretical and wind tunnel investigation of the effect of capillarity water on the entrainment of sediment by wind. *Can. J. Soil. Sci.*, **69**, 79–96.
- McTainsh, G. H. and Pitblado, J. R. (1987). Dust storms and related phenomena measured from meteorological records in Australia. *Earth Surface Processes and Landforms*, **12**, 415–424.
- Membery, D. A. (1983). Low level wind profiles during the Gulf Shamal. *Weather*, **38**, 18–24.
- Methven, J. (1997). Offline trajectories: calculation and accuracy. Technical Report 44, UGAMP.
- Milankovitch, M. (1941). *Canon of insolation and the ice age problem (in yugoslavian)*. Beograd: Kon. Serb. Akad. English translation by Israel Program for Scientific Translations, (1969).
- Murayama, T., Sugimoto, N., Uno, I., Kinoshita, K., Aoki, K., Hagiwara, N., Liu, Z., Matsui, I., Sakai, T., Shibata, T., Arao, K., Sohn, B.-J., Won, J.-G., Yoon, S.-C., Li, T., Zhou, J., Hu, H., Abo, M., Iokibe, K., Koga, R., and Iwasaka, Y. (2001). Ground-based network observation of Asian dust events of April 1998 in east Asia. *J. Geophys. Res.*, **106**(D16), 18345–18359.
- Nickovic, S., Kallos, G., Papadopolous, A., and Kakaliagou, O. (2001). A model for prediction of desert dust cycle in the atmosphere. *J. Geophys. Res.*, **106**(D12), 18133–18129.
- Peltier, W. R. (1994). Ice-age paleotopography. *Science*, **265**, 195–201.
- Petit, J. R., Briat, M., and Royer, A. (1981). Ice age aerosol content from East Antarctic ice core samples and past wind strength. *Nature*, **293**, 391–394.
- Petit, J. R., Mounier, J., Jouzel, J., Korotkevitch, Y., Kotlyakov, V., and Lorius, C. (1990). Paleoclimatological implications of the Vostok core dust record. *Nature*, **343**, 56–58.
- Petit, J. R., Jouzel, J., Raynaud, D., Barkov, N. I., Barnola, J. M., Basile, I., Bender, M., Chappellaz, J., Davis, M., Delaygue, G., Delmotte, M., Kotlyakov, V. M., Legrand, M., Lipenkov, V. Y., Lorius, C., and Pepin, L. (1999). Climate and atmospheric history of the past 420,000 years from the Vostok ice core, Antarctica. *Nature*, **399**, 429–436.
- Pope, V. D., Gallani, M. L., Rowntree, P. R., and Stratton, R. A. (2000). The impact of new physical parametrizations in the Hadley Centre climate model: HadAM3. *Climate Dynamics*, **16**, 123–146.
- Prather, M. J. (1986). Numerical advection by conservation of second-order moments. *J. Geophys. Res.*, **91**, 6671–6681.
- Press, W., Flannery, B., Teukolsky, S., and Vetterling, W. (1992). *Numerical Recipes: The Art of Scientific Computing*. Cambridge.
- Prospero, J. M. (1999). Long-range transport of mineral dust in the global atmosphere: Impact of African dust on the environment of the southeastern United States. *Proc. Natl. Acad. Sci. USA*, **96**, 3396–3403.

- Prospero, J. M., Bonatti, E., Schubert, C., and Carlson, T. N. (1970). Dust in the Caribbean atmosphere traced to an African dust storm. *Earth and Planet. Science Let.*, **9**, 287–293.
- Prospero, J. M., Glaccum, R. A., and Nees, R. T. (1981). Atmospheric transport of soil dust from Africa to South America. *Nature*, **289**, 570–572.
- Pye, K. (1987). *Aeolian dust and dust deposits*. Academic Press.
- Reader, M., Fung, I., and McFarlane, N. (1999). The mineral dust aerosol cycle during the last glacial maximum. *J. Geophys. Res.*, **104**(D8), 9381–9398.
- Redelsperger, J.-L., Guichard, F., and Mondon, S. (2000). A parameterization of mesoscale enhancement of surface fluxes for large-scale models. *Journal of Climate*, **13**, 402–421.
- Royer, S., De Angelis, M., and Petit, J. R. (1983). A 30,000 year record of physical and optical properties of microparticles from an East Antarctic ice core and implications for paleoclimate reconstruction models. *Climate Change*, **5**, 381–412.
- Russell, G. L. and Lerner, J. A. (1981). A new finite-differencing scheme for the tracer transport equation. *Journal of Applied Meteorology*, **20**, 1483–1498.
- Seinfeld, J. H. and Pandis, S. N. (1998). *Atmospheric chemistry and physics: From air pollution to climate change*. Wiley.
- Shao, Y., Raupach, M. R., and Findlater, P. A. (1993). Effect of saltation bombardment on the entrainment of dust by wind. *J. Geophys. Res.*, **98**, 12719–12726.
- Shao, Y. P. and Leslie, L. M. (1997). Wind erosion prediction over the Australian continent. *J. Geophys. Res.*, **102**, 30091–30105.
- Sinclair, P. C. (1969). General characteristics of dust devils. *Journal of Applied Meteorology*, **8**, 32–45.
- Sirocko, F., Sarnthein, M., Lange, H., and Erlenkeuser, H. (1991). Atmospheric summer circulation and coastal upwelling in the Arabian Sea during the Holocene and the last glaciation. *Quaternary Research*, **36**, 72–93.
- Slingo, J., Blackburn, M., Betts, A., Brugge, R., Hodges, K., Hoskins, B., Miller, M., Steenman-Clark, L., and Thuburn, J. (1994). Mean climate and transience in the tropics of the UGAMP GCM: Sensitivity to convective parameterisations. *Q. J. R. Meteorol Soc.*, **120**, 881–992.
- Slinn, W. G. N. (1983). *Atmospheric Science and Power Production*, chapter 11. Division of Biomedical Environmental Research, US Department of Energy, Washington, DC.
- Steffensen, J. P. (1997). The size distribution of microparticles from selected segments of the Greenland Ice Core Project ice core representing different climatic periods. *J. Geophys. Res.*, **102**(C12), 26755–26763.

- Stockwell, D. Z. and Chipperfield, M. P. (1996). The TOMCAT offline transport model. part III: Convection and vertical diffusion. Technical report, CGAM, Cambridge.
- Stull, R. B. (1988). *An Introduction to Boundary Layer Meteorology*. Kluwer Academic Publishers.
- Sumner, M. E., editor (1998). *Handbook of Soil Science*. Boca Raton London : CRC Press.
- Swap, R., Garstang, M., Greco, S., Talbot, R., and Kallberg, P. (1992). Saharan dust in the Amazon basin. *Tellus B.*, **44**, 133–149.
- Tegen, I. (2001). The role of preferential source areas and vegetation in the global dust aerosol cycle. Presented at the 8th Scientific Assembly of IAMAS.
- Tegen, I. and Fung, I. (1994). Modelling of mineral dust in the atmosphere: Sources, transport and optical thickness. *J. Geophys. Res.*, **99**(D11), 22897–22914.
- Tegen, I. and Miller, R. (1998). A general circulation model study on the interannual variability of soil dust aerosol. *J. Geophys. Res.*, **103**(D20), 25975–25995.
- Tegen, I., Lacis, A. A., and Fung, I. (1996). The influence on climate forcing of mineral aerosols from disturbed soils. *Nature*, **380**, 419–422.
- Thompson, L. G. and Moseley-Thompson, E. (1981). Microparticle concentration variations linked with climatic change: Evidence from polar ice cores. *Science*, **212**, 812–815.
- Thompson, L. G., Moseley-Thompson, E., Davis, M. E., Bolzan, J., Dai, J., Yao, T., Gundestrup, N., Wu, X., Klein, L., and Xi, Z. (1989). Holocene-Late Pleistocene climatic ice core records from Qinhai-Tibetan Plateau. *Science*, **246**, 474–477.
- Thompson, L. G., Moseley-Thompson, E., Davis, M. E., Lin, P. N., Henderson, K. A., Cole-Dai, J., Bolzan, J. F., and Liu, K.-B. (1995). Late glacial stage and Holocene tropical ice core records from Huascaran, Peru. *Science*, **269**, 46–50.
- Tiedtke, M. (1989). A comprehensive mass flux scheme for cumulus parameterisation in large scale models. *Monthly weather Review*, **117**, 1779–1800.
- Toro, E. F. (1992). The weighted average flux method applied to the Euler equations. *Phil. Trans. R. Soc. Lond. A*, **341**, 499–530.
- Tratt, D. M., Frouin, R. J., and Westphal, D. L. (2001). April 1998 Asian dust event: A southern California perspective. *J. Geophys. Res.*, **106**(D16), 18371–18379.
- Volken, M. and Schumann, T. (1993). A critical review of below-cloud scavenging results on Mt. Rigi. *Water, Air and Soil Pollution*, **68**, 15–28.
- Watson, A. I., Bakker, D. C. E., Ridgwell, A. J., Boyd, P. W., and Law, C. S. (2000). Effect of iron supply on Southern Ocean CO<sub>2</sub> uptake and implications for glacial atmospheric CO<sub>2</sub>. *Nature*, **407**, 730–733.

- Webb, R. S., Rosenzweig, C. E., and Levine, E. R. (1991). A global data set of soil particle size properties. NASA Technical Memorandum 4286.
- White, B. R. (1979). Soil transport by winds on Mars. *J. Geophys. Res.*, **84**, 4643–4651.
- Wilson, M. F. and Henderson-Sellers, A. (1985). A global archive of land cover and soils data for use in general circulation models. *Journal of Climatology*, **5**, 119–143.
- Wiscombe, W. and Grams, G. (1976). The backscattered fraction in two-stream approximations. *Journal of Atmospheric Science*, **33**, 2440–2451.
- Woodward, S. (2001). Modelling the atmospheric life-cycle and radiative impact of mineral dust in the Hadley Centre climate model. *J. Geophys. Res.*, **106**(D16), 18155–18166.